

TECHNISCHE  
UNIVERSITÄT  
DRESDEN

---

# Phase-space structure of resonance eigenfunctions for chaotic systems with escape

Dissertation  
zur Erlangung des akademischen Grades  
Doctor rerum naturalium

vorgelegt von

Konstantin Clauß  
geboren am 09.06.1990 in Halle (Saale)

Institut für Theoretische Physik  
Fakultät Physik  
Bereich Mathematik und Naturwissenschaften  
Technische Universität Dresden  
2020

Eingereicht am 29. März 2020

Gutachter:

Prof. Dr. Roland Ketzmerick  
Technische Universität Dresden

Prof. Dr. Eduardo Altmann  
University of Sydney

## Abstract

Physical systems are usually not closed and insight about their internal structure is experimentally derived by scattering. This is efficiently described by resonance eigenfunctions of non-Hermitian quantum systems with a corresponding classical dynamics that allows for the escape of particles. For the phase-space distribution of resonance eigenfunctions in chaotic systems with partial and full escape we obtain a universal description of their semiclassical limit in terms of classical conditional invariant measures with the same decay rate. For partial escape, we introduce a family of conditionally invariant measures with arbitrary decay rates based on the hyperbolic dynamics and the natural measures of forward and backward dynamics. These measures explain the multifractal phase-space structure of resonance eigenfunctions and their dependence on the decay rate. Additionally, for the nontrivial limit of full escape we motivate the hypothesis that resonance eigenfunctions are described by conditionally invariant measures that are uniformly distributed on sets with the same temporal distance to the quantum resolved chaotic saddle. Overall we confirm quantum-to-classical correspondence for the phase-space densities, for their fractal dimensions, and by evaluating their Jensen–Shannon distance in a generic chaotic map with partial and full escape, respectively.

## Zusammenfassung

Typische physikalische Systeme sind nicht geschlossen, sodass ihre innere Struktur mit Hilfe von Streuexperimenten untersucht werden kann. Diese werden mit Hilfe einer nicht-Hermiteschen Quantendynamik und deren Resonanzeigenzuständen beschrieben. Die dabei zugrunde liegende klassische Dynamik berücksichtigt den Verlust von Teilchen. Für die semiklassische Phasenraumverteilung solcher Resonanzeigenzustände in chaotischen Systemen mit partieller und voller Öffnung entwickeln wir eine universelle Beschreibung mittels bedingt invarianter Maße gleicher Zerfallsrate. Für partiellen Zerfall stellen wir eine Familie bedingt invarianter Maße mit beliebiger Zerfallsrate vor, welche auf der hyperbolischen Dynamik und den natürlichen Maßen der vorwärts gerichteten und der invertierten Dynamik aufbauen. Diese Maße erklären die multifraktale Phasenraumstruktur der Resonanzzustände und deren Abhängigkeit von der Zerfallsrate. Darüber hinaus motivieren wir für den nicht trivialen Grenzfall voll geöffneter Systeme die Hypothese, dass Resonanzeigenzustände durch ein bedingt invariantes Maß beschrieben werden, welches gleichverteilt auf solchen Mengen ist, die den gleichen zeitlichen Abstand zum quantenunschärferen chaotischen Sattel haben. Insgesamt bestätigen wir die quantenklassische Korrespondenz für die Phasenraumdichten, deren fraktale Dimensionen und durch Auswertung ihres Jensen–Shannon Abstandes in einer generischen chaotischen Abbildung sowohl für partielle als auch für volle Öffnung.



# Contents

|          |  |           |
|----------|--|-----------|
| <b>1</b> | <b>Introduction</b>  | <b>1</b>  |
| <b>2</b> | <b>Chaotic scattering</b>                                  | <b>5</b>  |
| 2.1      | Quantum scattering . . . . .                               | 5         |
| 2.1.1    | Scattering matrix . . . . .                                | 5         |
| 2.1.2    | Non-Hermitian quantum mechanics . . . . .                  | 8         |
| 2.1.3    | Time-discrete quantum scattering . . . . .                 | 9         |
| 2.1.4    | Quantum maps with escape . . . . .                         | 10        |
| 2.1.4.1  | Spectrum and inverse quantum map . . . . .                 | 11        |
| 2.1.4.2  | Eigenfunctions of non-unitary $\mathcal{U}$ . . . . .      | 11        |
| 2.2      | Classical chaotic scattering . . . . .                     | 13        |
| 2.2.1    | Characterization of classical dynamics . . . . .           | 14        |
| 2.2.2    | Stroboscopic maps . . . . .                                | 16        |
| 2.2.3    | Classical maps with escape . . . . .                       | 19        |
| 2.2.4    | Classical maps with full escape . . . . .                  | 20        |
| 2.2.5    | Fractal structure . . . . .                                | 23        |
| 2.2.6    | Conditionally invariant measures . . . . .                 | 25        |
| 2.2.6.1  | Natural measure . . . . .                                  | 26        |
| 2.2.6.2  | Natural measure of the inverse map . . . . .               | 27        |
| 2.2.6.3  | Typical decay . . . . .                                    | 29        |
| 2.2.6.4  | Conditionally invariant measures for full escape . . . . . | 30        |
| <b>3</b> | <b>Eigenfunctions in closed maps</b>                       | <b>31</b> |
| 3.1      | Quantization of maps . . . . .                             | 31        |
| 3.1.1    | Quantized standard map . . . . .                           | 32        |
| 3.1.2    | Phase-space representation of quantum states . . . . .     | 33        |
| 3.2      | Structure of eigenfunctions . . . . .                      | 34        |
| 3.2.1    | Semiclassical eigenfunction hypothesis . . . . .           | 34        |
| 3.2.2    | Quantum ergodicity theorem . . . . .                       | 36        |

|          |  |           |
|----------|--|-----------|
| <b>4</b> | <b>Resonance eigenfunctions in maps with partial escape</b>    | <b>39</b> |
| 4.1      | Quantization of maps with partial escape . . . . .             | 39        |
| 4.1.1    | Correspondence principle for partial escape . . . . .          | 40        |
| 4.1.2    | Resonances in maps with partial escape . . . . .               | 41        |
| 4.2      | Phase-space distribution of resonance eigenfunctions . . . . . | 44        |
| 4.2.1    | Single resonance eigenfunctions . . . . .                      | 44        |
| 4.2.2    | Convergence of phase-space distribution . . . . .              | 46        |
| 4.2.2.1  | Expectation values of single eigenfunctions. . . . .           | 46        |
| 4.2.2.2  | Average expectation values. . . . .                            | 48        |
| 4.2.3    | Average phase-space distribution . . . . .                     | 51        |
| 4.2.4    | Fluctuations . . . . .   | 53        |
| 4.2.5    | Semiclassical expectation for iterations of $R$ . . . . .      | 55        |
| 4.2.6    | Conditional invariance of semiclassical measures . . . . .     | 58        |
| 4.3      | Conditionally invariant measures for partial escape . . . . .  | 60        |
| 4.3.1    | Construction of natural and inverse measure . . . . .          | 60        |
| 4.3.2    | Product measure . . . . .                                      | 63        |
| 4.3.3    | Periodic orbit measures . . . . .                              | 67        |
| 4.4      | Quantum-to-classical comparison . . . . .                      | 68        |
| 4.4.1    | Qualitative agreement . . . . .                                | 68        |
| 4.4.2    | Fractal dimensions . . . . .                                   | 71        |
| 4.4.3    | Jensen–Shannon divergence . . . . .                            | 75        |
| 4.4.4    | Semiclassical limit . . . . .                                  | 78        |
| 4.4.5    | Dependence on reflectivity function $R$ . . . . .              | 80        |
| 4.4.5.1  | Qualitative comparison . . . . .                               | 81        |
| 4.4.5.2  | Jensen–Shannon divergence . . . . .                            | 84        |
| 4.4.5.3  | Dependence on size of opening . . . . .                        | 87        |
| 4.4.6    | Baker map . . . . .  | 89        |
| 4.5      | Discussion and outlook . . . . .                               | 91        |
| <b>5</b> | <b>Resonance eigenfunctions in maps with full escape</b>       | <b>95</b> |
| 5.1      | Quantization for full escape . . . . .                         | 95        |
| 5.1.1    | Limit of full escape . . . . .                                 | 96        |
| 5.1.2    | Resonances in the limit of full escape . . . . .               | 96        |
| 5.2      | Phase-space distribution for full escape . . . . .             | 100       |
| 5.2.1    | Eigenfunctions in the limit of full escape . . . . .           | 100       |
| 5.2.2    | Long-lived resonance eigenfunctions . . . . .                  | 102       |
| 5.2.3    | Convergence of phase-space distribution . . . . .              | 104       |
| 5.2.3.1  | Expectation values of single eigenfunctions . . . . .          | 104       |
| 5.2.3.2  | Average expectation values . . . . .                           | 106       |

---

|          |   |            |
|----------|---|------------|
| 5.2.4    | Average distribution . . . . .                                      | 108        |
| 5.2.5    | Semiclassical expectation for iterations of $\Omega$ . . . . .      | 110        |
| 5.3      | Conditionally invariant measures for full escape . . . . .          | 114        |
| 5.3.1    | $\gamma$ -natural measures . . . . .                                | 114        |
| 5.3.2    | Limit of product measures . . . . .                                 | 115        |
| 5.3.3    | Resonance eigenfunction hypothesis for full escape . . . . .        | 116        |
| 5.3.3.1  | Simplified escape model . . . . .                                   | 116        |
| 5.3.3.2  | Implementation of $\mu_\gamma^h$ . . . . .                          | 118        |
| 5.3.3.3  | Illustration . . . . .  | 119        |
| 5.3.3.4  | Semiclassical limit of $\mu_\gamma^h$ . . . . .                     | 121        |
| 5.4      | Quantum-to-classical comparison . . . . .                           | 123        |
| 5.4.1    | Qualitative agreement . . . . .                                     | 123        |
| 5.4.2    | Fractal dimensions . . . . .  | 126        |
| 5.4.3    | Jensen–Shannon divergence . . . . .                                 | 130        |
| 5.4.4    | Semiclassical limit . . . . .                                       | 133        |
| 5.4.5    | Dependence on opening $\Omega$ . . . . .                            | 136        |
| 5.5      | Discussion and outlook . . . . .                                    | 141        |
| <b>6</b> | <b>Summary</b>  | <b>143</b> |
|          | <b>Appendices</b>   | <b>145</b> |
| <b>A</b> | <b>Generalized baker map</b>  | <b>147</b> |
| A.1      | Classical baker map . . . . .                                       | 147        |
| A.2      | Baker map with escape . . . . .                                     | 148        |
| A.3      | Quantized baker map . . . . .                                       | 149        |
| <b>B</b> | <b>Additional numerical results</b>                                 | <b>151</b> |
| B.1      | Distribution of eigenphases . . . . .                               | 151        |
| B.1.1    | Partial escape. . . . .   | 151        |
| B.1.2    | Full escape. . . . .  | 152        |
| B.2      | Quantum expectation of observables . . . . .                        | 152        |
| B.2.1    | Partial escape . . . . .  | 152        |
| B.2.2    | Full escape . . . . .   | 153        |
| B.3      | Effective information dimension . . . . .                           | 155        |
| B.4      | Jensen–Shannon divergence for different scales $\epsilon$ . . . . . | 156        |
| B.4.1    | Partial escape . . . . .  | 156        |
| B.4.2    | Full escape . . . . .   | 157        |

|          |  |            |
|----------|--|------------|
| <b>C</b> | <b>Miscellaneous proofs</b>  | <b>159</b> |
| C.1      | Expectation for iterations of $R$ for c-measures . . . . .         | 159        |
| C.2      | Comparison of natural and inverse decay rate . . . . .             | 160        |
| C.3      | Conditional invariance of product measures . . . . .               | 162        |
| C.3.1    | Generalized baker map . . . . .                                    | 162        |
| C.3.2    | Hyperbolic maps . . . . .  | 166        |
| C.3.3    | Construction and convergence of product measures . . . . .         | 168        |
| C.4      | Conditional invariance of periodic orbit measures . . . . .        | 170        |
| C.5      | Measures on arbitrary orbits . . . . .                             | 173        |
| C.5.1    | Approximation for typical measure . . . . .                        | 173        |
| C.5.2    | Conditional invariance . . . . .                                   | 174        |
| C.6      | Full escape . . . . .  | 176        |
| C.6.1    | Convergence of quantum map in limit of full escape . . . . .       | 176        |
| C.6.2    | Scaling of $\gamma$ -interval for fixed number of states . . . . . | 177        |
| C.6.3    | Conditional invariance of measures $\mu_\gamma^h$ . . . . .        | 177        |
|          | <b>List of Figures</b>   | <b>179</b> |
|          | <b>Bibliography</b>  | <b>183</b> |



# Chapter 1

## Introduction

One of the most fundamental concepts in theoretical physics is the correspondence principle between quantum and classical mechanics. In particular the semiclassical limit of large actions compared to Planck's constant relates observable properties of quantum systems to the classical dynamics. The field of quantum chaos examines this relation in systems with classical chaotic dynamics. In closed systems the presence of classical chaos has universal implications on the statistics of eigenvalues of the quantum system [1–4] and on the distribution of its eigenfunctions [5–7]. In particular, the semiclassical eigenfunction hypothesis relates the localization properties of regular and chaotic eigenfunctions to the phase-space structures which are typically explored by corresponding classical orbits. For fully chaotic systems this results in a uniform distribution for almost all eigenfunctions according to the quantum ergodicity theorem [8–15].

Experimentally accessible systems are often explored by scattering of waves and particles. In such a setup an initially prepared, incoming state interacts with the probed system and a subsequent measurement determines the properties of the outgoing state. Therefore scattering systems are not closed, which in classical dynamics is seen as an escape or capture of particles. Quantum mechanically, the energies and finite life times of eigenfunctions are described by complex resonances that appear as poles of the scattering matrix in the quantum scattering description [16, 17]. Chaotic scattering has a wide variety of applications [18], reaching from large scales in celestial mechanics [19, 20] to small scales in chemical reactions [21, 22], molecular [23], atomic [24] and nuclear physics [25], from fluid mechanics [26–28] to microwave resonators [29]. Scattering systems are often conveniently described by non-Hermitian Hamiltonians [30–32], which naturally appear in open quantum systems with dissipation [33–36] and recently have drawn a lot of attention especially in the context of topological phases and many-body systems [37–42]. In dynamical systems, one particularly interesting example are optical microcavities [43], which have a variety of applications and are experimentally and theoretically feasible. The classical ray dynamics in such a cavity is characterized by partial reflection and transmission at the boundary. This leads to a localization of resonance eigenfunctions which influences the emission patterns and lasing properties [43–55]. Thus, a

fundamental understanding of universal properties of resonances and resonance eigenfunctions in terms of the classical dynamics is desired, which generalizes the important results of closed chaotic systems to systems with escape.

The relation between quantum and classical properties is so far best understood in chaotic systems with full escape, in which particles are completely absorbed or escape to infinity [56–66]. These systems are typically characterized by a specific phase-space region which acts as a leak [67]. They model scattering systems, such as the three-disk scatterer [68] or potential scattering [69]. Classically, chaotic motion which is trapped for arbitrary long times takes place on a fractal invariant set, called the chaotic saddle. In hyperbolic systems this chaotic saddle has a stable and an unstable manifold of phase-space points that are trapped under forward and backward iteration, respectively [70]. The instability of the chaotic saddle leads to escape from the system, which is governed by the unstable direction: Typical smooth initial distributions asymptotically decay with a specific rate  $\gamma_{\text{nat}}$ , sometimes called classical or natural decay rate, and are described by a single classical measure, which is smooth along the unstable manifold of the saddle, the natural measure  $\mu_{\text{nat}}$  [71–74]. This measure is conditionally invariant, which means that it is invariant up to a global decay factor with rate  $\gamma_{\text{nat}}$ .

In contrast, quantum mechanically, the complex resonances imply a large range of quantum decay rates. The relation of their distribution to the fractal dimension of the classical chaotic saddle is well established in terms of a fractal Weyl law [56, 57, 69, 75–86]. Chaotic resonance eigenfunctions show fractal structures in a phase-space representation [87], which change according to their decay rate  $\gamma$  [59]. This structure is fundamentally related to the classical system with escape: Resonance eigenfunctions converge to some conditionally invariant measure with the corresponding decay rate [60]. For quantum decay rates close to the natural decay  $\gamma_{\text{nat}}$  this semiclassical limit is assumed to be the natural measure  $\mu_{\text{nat}}$  [87]. For resonance eigenfunctions with arbitrary decay rates in systems with full escape, an intuitive understanding of their localization properties is missing and there exists no analogue to the semiclassical eigenfunction hypothesis.

Even less investigated is the relation between quantum and classical dynamics in systems with partial escape, in which particles escape with some finite probability or the intensity is partially absorbed [67]. Classically, the natural conditionally invariant measure  $\mu_{\text{nat}}$  is multifractal and supported on the full phase space [88]. Quantum mechanically, partial escape implies finite decay rates, whose distribution is related to classical measures but not given by a simple fractal Weyl law [48, 89–92]. Again, the longest living resonance eigenfunctions are well described by the natural measure  $\mu_{\text{nat}}$ , which is also known as steady state probability distribution in the context of microcavities [47, 54, 55, 67]. Moreover, some aspects of resonance eigenfunctions are investigated in terms of classical periodic orbits [93, 94] and in the case of single-channel openings [95, 96]. In general, a complete understanding of resonance eigenfunctions for systems with partial escape is still missing.

---

In this thesis we investigate the semiclassical convergence of resonance eigenfunctions of systems with partial and full escape and present an intuitive description of their phase-space structure by simple properties of the classical system. The main results are already published in Refs. [66, 97]. The manuscript is organized as follows. In Chapter 2, based on a quantum scattering description, we first introduce resonance eigenfunctions of quantum maps with escape. Secondly, we present relevant aspects of classical chaotic scattering which leads to maps with escape and their invariant structures. Chapter 3 reviews fundamental results about the phase-space localization of eigenfunctions in closed systems. We consider partial escape in Chapter 4. First, an overview about spectral properties of quantum maps with partial escape is given. Secondly, we analyze the semiclassical convergence of resonance eigenfunctions numerically. We prove that the quantum-to-classical correspondence principle implies that resonance eigenfunctions in systems with partial escape converge to conditionally invariant measures with the corresponding decay rate. The third part introduces a new family of conditionally invariant measures of the classical map with escape. We finally analyze to which extent these measures are relevant as limit measures by means of fractal dimensions and quantifying their agreement with the Jensen-Shannon divergence. In Chapter 5 we discuss systems with full escape as a limiting case of partial escape. We perform the same analysis on the convergence of resonance eigenfunctions as for partial escape and review some well-established results regarding their localization. Furthermore, we discuss conditionally invariant measures of systems with full escape. We propose a resonance eigenfunction hypothesis for chaotic systems with full escape, which classically explains their phase-space structure and localization. This hypothesis is again tested quantitatively. The results are summarized and an outlook is given in Chapter 6.



# Chapter 2

## Chaotic scattering

Accessible physical systems are never truly closed. Instead, only by interaction it is possible to experimentally probe a given system. In many cases physical systems are explored using scattering experiments, where a beam of particles or electromagnetic waves collides with a sample of interest. For such systems a useful description is given by quantum scattering theory, which is introduced in Section 2.1. In Section 2.2 we discuss the corresponding classical scattering system and introduce all relevant properties of classical maps with escape.

### 2.1 Quantum scattering

Properties of matter are experimentally often accessed by scattering experiments with photons, electrons, nucleons, ions, or molecules [16, 17, 98, 99]. Scattering theory has been introduced initially to describe nuclear collisions with short-range interactions [99, 100]. In such systems initially free particles interact with the sample in a bounded region, e.g., in the vicinity of some atomic nucleus, and afterwards propagate freely until they are detected. This framework has been successfully applied to attracting or repelling potentials [69, 101], to describe excitations of atomic and nuclear states [102], and in chemical reactions of molecules [22, 103, 104].

In the following we briefly review the quantum mechanical scattering description in terms of the scattering matrix. This results in an effective non-Hermitian description of quantum mechanical time evolution in the system of interest, presented in Sec. 2.1.2. A simplified time-discrete scattering description is given in Sec. 2.1.3. This leads to quantum maps with escape as time-discrete model systems for resonance scattering in the last section (Sec. 2.1.4).

#### 2.1.1 Scattering matrix

The dynamics of non-relativistic quantum particles is generally described by the Schrödinger equation

$$i\hbar\partial_t\psi = \hat{H}\psi, \tag{2.1}$$

where the wavefunction  $\psi(q, t)$  describes the quantum state at position  $q \in \mathbb{R}^f$  (in systems with  $f$  degrees of freedom) and time  $t \in \mathbb{R}$ ,  $\hbar$  is Planck's constant and  $\hat{H}$  is the Hamilton operator of the considered collision system [16]. This Hamiltonian includes the interaction of the quantum particle with the system of interest. In contrast, the unperturbed particle propagates freely and is described by the free Hamiltonian, given by the kinetic term  $\hat{H}_0 = -\frac{\hbar^2}{2m}\nabla^2$ . Neglecting internal degrees of the scattering system, the physical meaning of  $\hat{H}$  and  $\hat{H}_0$  is that in the first case the interaction of the collision process is 'turned on' and in the other 'turned off', while the interaction is given by  $\hat{V} = \hat{H} - \hat{H}_0$  [16].

In the following we assume that the interaction can be described by a local potential  $V$ , which only depends on the position  $q$  of the particle such that  $\hat{V}$  is diagonal in position representation. Additionally, let us assume that the potential acts only in a finite region  $|q| < s$ , characterized by a typical scale  $s$ , or that  $V(q)$  decays to zero faster than  $1/|q|$ . This ensures that incoming and outgoing particles can be described by the free Hamiltonian  $\hat{H}_0$  for times  $t \rightarrow \pm\infty$ . Note that this condition is not satisfied for the long-ranged Coulomb potential, for which the mathematical description is more involved [105].

Experimentally the system is accessible indirectly, by measuring how the final state  $\phi_+$  depends on some initially prepared state  $\phi_-$ , when it is scattered at the potential  $\hat{V}$ , sketched in Fig. 2.1. These states are generally related by the scattering matrix according to [16, 17]

$$\phi_+ = \hat{S} \phi_-, \quad (2.2)$$

which was conceptually introduced for the first time by Heisenberg already in 1942 [106], and thoroughly developed by Lippmann and Schwinger [100]. For a time-independent Hamiltonian  $\hat{H}$ , the scattering  $S$ -matrix is given in terms of the unitary propagators  $\hat{U}(t) = e^{-i/\hbar \hat{H}t}$  of the full Hamiltonian  $\hat{H}$  and the free propagator  $\hat{U}_0(t) = e^{-i/\hbar \hat{H}_0 t}$  as

$$\hat{S} = \lim_{t \rightarrow \infty} \hat{U}_0(-t) \hat{U}(2t) \hat{U}_0(-t), \quad (2.3)$$

see e.g., Ref. [16] Chp. 5. In this representation it is clear that  $\hat{S}$  is itself unitary,  $\hat{S}\hat{S}^\dagger = \hat{S}^\dagger\hat{S} = \mathbb{1}$ , which expresses conservation of probability. Moreover, this operator includes the full

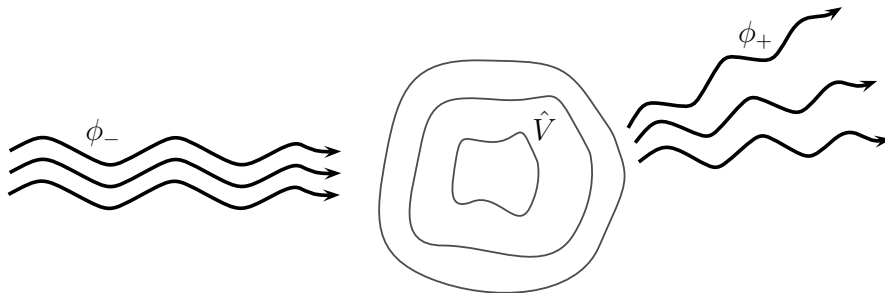


**Figure 2.1:** Sketch of scattering problem with incoming  $\phi_-$  and outgoing states  $\phi_+$ .

measurable information about the system, such as transition probabilities between incoming and outgoing channels, cross-sections, and delay times [16]. Let  $\phi_i, \phi_f$  be eigenfunctions of the free Hamiltonian  $\hat{H}_0$  with eigenvalues  $E_i, E_f$ , respectively. Considering a Lippmann–Schwinger equation for the relation of incoming and outgoing waves and using the Dyson perturbation expansion of the  $S$ -matrix [16, Chp. 6] it is possible to show that the matrix elements of  $\hat{S}$  are given in terms of the free eigenstates as

$$\hat{S}_{if} := \langle \phi_f | \hat{S} | \phi_i \rangle = \delta(E_i - E_f) \left[ \langle \phi_f | \phi_i \rangle - 2\pi i \langle \phi_f | \hat{T}^+(E) | \phi_i \rangle \right], \quad (2.4)$$

where  $\hat{T}^+(E)$  is the transition operator

$$\hat{T}^+(E) = \hat{V} + \hat{V} \frac{1}{E - \hat{H} + i0^+} \hat{V}. \quad (2.5)$$

Thus, restricting the scattering problem to the energy shell  $E_i = E_f = E$  the scattering operator reduces to

$$\hat{S}(E) = \mathbb{1} - 2\pi i \left( \hat{V} + \hat{V} \frac{1}{E - \hat{H} + i0^+} \hat{V} \right). \quad (2.6)$$

From Equation (2.6) follows, that poles of the scattering matrix are given by poles of the resolvent  $(E - \hat{H} + i0^+)^{-1}$ . Note that this operator is equivalent to the total Green operator of the scattering problem, see e.g., Ref. [16, 99]. These poles are typically complex valued. While the poles on the negative real axis,  $E \in \mathbb{R}_-$ , form a discrete spectrum and are associated with the bound eigenfunctions of  $\hat{H}$ , there also exist complex poles  $E_r - i\Gamma/2$  associated with resonant scattering solutions.

These poles with positive  $\Gamma > 0$  are related to resonances of finite width measured for example in cross sections. Consider the forward scattering amplitude  $f(E) = -(2\pi)^2 \hat{T}^+(E)$  as a function of some complex eigenvalue of  $\hat{H}$  [107, Sec. XI.7]. Assuming that  $f(E)$  has an analytic continuation, close to an isolated pole  $E_r - i\Gamma/2$  it can be written as  $f(E) = \frac{C}{E - (E_r - i\Gamma/2)} + f_b(E)$  [108, Sec. XII.6], with some constant  $C$  and where the background  $f_b(E)$  is determined by  $\hat{V}$  and is analytic at the pole. The cross section of forward scattering is proportional to  $|f(E)|^2$ , which is for small  $f_b(E_r)$  approximately given by [108]

$$|f(E)|^2 = \frac{|C|^2}{(E - E_r)^2 + \Gamma^2/4} + R. \quad (2.7)$$

Close to  $E = E_r$  the remainder  $R$  is negligible [108] and  $|f(E)|^2$  becomes equivalent to the Breit–Wigner resonance shape, which occurs exactly in the scattering of  $s$ -wave neutrons [98, Chp. 5.T]. Note that the width at half maximum for this profile is given by  $\Gamma$ . Hence, when the cross-section is measured experimentally depending on the energy  $E$  of incoming waves (or particles), Eq. (2.7) implies a peak at  $E = E_r$  with a width approximately given by  $\Gamma$ .

### 2.1.2 Non-Hermitian quantum mechanics

There are different methods to obtain the complex resonances for a system of interest, e.g., by complex scaling [109–119] or by means of non-Hermitian Hamiltonians [30–36]. The latter will be discussed in the following as it leads to time-discrete quantum maps with escape. So far the scattering problem is considered in terms of the asymptotic states of the free Hamiltonian. In certain situations it is convenient to decompose the phase space into a compact interaction region, which is related to the scattering potential  $V$ , and a set of open channels coupled to this region [31, 102, 120, 121]. Such a treatment has been applied to open billiards [122] and electron waveguides [123]. This yields a description of the scattering problem in terms of an effective non-Hermitian Hamiltonian, which describes time evolution in the interaction region.

Therefore consider a countable set of  $M$  open channels with an associated set of channel states  $\phi_{m,E}$ , with  $m \in \{1, \dots, M\}$ , which is continuous in the energy  $E$ , and a discrete set of states  $\psi_n$  with  $n \in \{1, \dots, N\}$ , associated with the compact interaction region [124]. The full Hamiltonian is decomposed into a self-adjoint Hamiltonian  $\hat{H}_{\text{cl}}$  describing the closed dynamics of internal states, a free Hamiltonian acting on channel states, and a coupling term  $\hat{W}$  between both. One advantage of this treatment is that the dimension of the problem reduces effectively to the  $N \times N$  matrix  $\hat{H}_{\text{cl}}$ , and the  $N \times M$  dimensional coupling term  $\hat{W}$ . The latter has to be chosen such that the full Hamiltonian is Hermitian [31]. A full derivation is given, e.g., in Ref [31] Sec. II.B, and in Ref. [121]. The main result is that the reactance matrix of the scattering problem is of the form [31]

$$\hat{K} = \pi \hat{W}^\dagger \frac{1}{E - \hat{H}_{\text{cl}}} \hat{W}, \quad (2.8)$$

which is related to the scattering matrix by [99]

$$\hat{S} = (\mathbb{1} - i\hat{K})(\mathbb{1} + i\hat{K})^{-1}. \quad (2.9)$$

Inserting Eq. (2.8) into Eq. (2.9) the scattering matrix is rewritten as

$$\hat{S}(E) = \mathbb{1} - 2i\pi \hat{W}^\dagger \frac{1}{E - \hat{H}_{\text{eff}}} \hat{W}. \quad (2.10)$$

Here an effective non-Hermitian Hamilton operator is introduced, which describes the time evolution of internal states,

$$\hat{H}_{\text{eff}} = \hat{H}_{\text{cl}} - i\hat{\Gamma}, \quad (2.11)$$

where  $\hat{\Gamma} := \pi \hat{W} \hat{W}^\dagger$  satisfies  $\hat{\Gamma}^\dagger = \hat{\Gamma}$ . Thus, the Hermitian operators  $\hat{H}_{\text{cl}}$  and  $\hat{\Gamma}$  decompose the effective Hamiltonian  $\hat{H}_{\text{eff}}$  into its real and imaginary part. We stress that, in contrast to the full Hamiltonian  $\hat{H}$  appearing in Eq. (2.6), the non-Hermitian  $\hat{H}_{\text{eff}}$  cannot be interpreted as



an observable. It nevertheless describes the time evolution and decay of any state  $\psi$  of the inner region, when there is no input through the coupled channel system. Apparently the complex eigenvalues  $E_m$  of the effective Hamiltonian,  $\hat{H}_{\text{eff}}\phi_m = E_m\phi_m$ , correspond to poles of the  $S$ -matrix in Eq. (2.10). Thus, these eigenvalues have the interpretation of resonances. The intermediate life times of the corresponding resonance eigenfunctions  $\phi_m$  are caused by the coupling as follows. Because  $\hat{\Gamma}$  is a positive operator the eigenvalues  $E_m$  are all located in the lower half of the complex plane, such that the imaginary part  $\text{Im}E_m = -\hbar\gamma_m/2$  is associated with a positive decay rate  $\gamma_m > 0$  of the norm of eigenfunctions as  $\|e^{-\frac{i}{\hbar}\hat{H}_{\text{eff}}t}\phi_m\|^2 = e^{-\frac{2}{\hbar}\text{Im}E_mt}\|\phi_m\|^2 = e^{-\gamma_mt}$ . This decay rate corresponds to the width of resonances as  $\Gamma = \hbar\gamma_m$ , which are discussed in Sec. 2.1.1.

### 2.1.3 Time-discrete quantum scattering

In this thesis, for simplicity, we consider time-discrete systems. Such dynamics is for example generated from mappings on Poincaré sections [125, 126] or from stroboscopic mappings of Hamiltonian systems with periodic driving [127], explained later in Sec. 2.2. Similar to the derivation in the previous section, it is possible to obtain a scattering matrix for time-discrete scattering systems using an input-output approach [124, 128, 129]. For this purpose the phase space is again divided into internal states  $\psi$  and incoming and outgoing states  $\phi_-$  and  $\phi_+$ . The scattering problem reduces in this context to a linear map [124]

$$\begin{pmatrix} \psi(n+1) \\ \phi_+ \end{pmatrix} = \hat{U} \begin{pmatrix} \psi(n) \\ \phi_- \end{pmatrix}, \quad (2.12)$$

where the full time-evolution operator  $\hat{U}$  is required to be unitary,  $\hat{U}\hat{U}^\dagger = \hat{U}^\dagger\hat{U} = \mathbb{1}$ . It is generally possible to parametrize this matrix as [124]

$$\hat{U} = \begin{pmatrix} \tilde{U}\mathcal{R} & -\tilde{U}\hat{W} \\ \hat{W}^\dagger & \sqrt{1 - \hat{W}^\dagger\hat{W}} \end{pmatrix}, \quad (2.13)$$

where  $\tilde{U}$  is unitary, we introduced  $\mathcal{R} := \sqrt{1 - \hat{W}^\dagger\hat{W}}$ , and the matrix  $\hat{W}$  can be chosen to be diagonal in a suitable basis as  $\hat{W}_{ij} = \delta_{ij}w_j$  for  $i \leq N$  and  $j \leq M$ . The values  $w_j \in [0, 1]$  describe how strong the channel  $j$  is coupled to the system. Conversely, the operator  $\mathcal{R}$  describes how internal states couple to the outgoing system by specifying the probability that remains in the system. Therefore  $\mathcal{R}$  is called reflection operator. Without coupling, i.e.,  $\hat{W} = 0$ , the reflection operator is the unit matrix on the inner system,  $\mathcal{R} = \mathbb{1}$ . In this case the time evolution of internal states  $\psi$  is given by  $\tilde{U}\psi$ , such that the unitary matrix  $\tilde{U}$  is identified as the quantum map of the closed system.

For a finite coupling,  $\hat{W} \neq 0$ , the scattering matrix is given by [124]

$$\hat{S}(\omega) = \sqrt{1 - \hat{W}^\dagger \hat{W}} - \hat{W}^\dagger \frac{1}{e^{-i\omega} - \tilde{\mathcal{U}}\mathcal{R}} \tilde{\mathcal{U}}\hat{W}, \quad (2.14)$$

relating incoming to outgoing states. The time evolution of any internal state is, according to Eqs. (2.12) and (2.13), given by  $\psi(n+1) = \tilde{\mathcal{U}}\mathcal{R}\psi(n) - \tilde{\mathcal{U}}\hat{W}\phi_-$ . Without input,  $\phi_- = 0$ , only propagation with the operator

$$\mathcal{U} := \tilde{\mathcal{U}}\mathcal{R} \quad (2.15)$$

takes place. First, probability escapes from the system according to the reflection operator  $\mathcal{R}$ , followed by the closed time evolution  $\tilde{\mathcal{U}}$ . Therefore the propagator  $\mathcal{U}$  is called quantum map with escape. A more detailed discussion of the stroboscopic scattering approach can be found in Ref. [129] Sec. III.D.

### 2.1.4 Quantum maps with escape

The quantum map with escape  $\mathcal{U} = \tilde{\mathcal{U}}\mathcal{R}$ , Eq. (2.15), consists of a unitary quantum map  $\tilde{\mathcal{U}}$  of a closed, time-discrete system and a reflection operator  $\mathcal{R}$ , which modifies the probability distribution of quantum states. In the following we assume that  $\tilde{\mathcal{U}}$  acts on an  $N$ -dimensional Hilbert space  $\mathbb{H}_N \simeq \mathbb{C}^N$ , and quantizes a classical map on a bounded phase space  $M: \Gamma \rightarrow \Gamma$ , as will be discussed in Chapter 3. The reflection operator is associated with a classical reflectivity function  $R: \Gamma \rightarrow \mathbb{R}_+$ , leading to a quantized map with partial escape, as explained in detail in Chapter 4. In the following we discuss some general properties of quantum maps with escape.

Let  $\mathcal{U}$  be a quantum map with escape as in Eq. (2.15) acting on the Hilbert space  $\mathbb{H}_N$ . The spectrum  $\sigma(\mathcal{U})$  consists of  $N$  eigenvalues  $\lambda \in \mathbb{C}$  satisfying the eigenvalue equation

$$\mathcal{U}\psi = \lambda\psi, \quad (2.16)$$

with the nonzero eigenfunctions  $\psi \in \mathbb{H}_N$ . The eigenvalues are often written as  $\lambda = e^{-i\theta - \gamma/2}$ , where  $\theta = \arg \lambda$  is the phase and  $\gamma = -2 \log |\lambda|$  characterizes the modulus. Comparing Eq. (2.16) to the definition of the scattering matrix for time-discrete systems, Eq. (2.14), it becomes evident that the eigenvalues of  $\mathcal{U}$  correspond to the poles of the scattering matrix. In particular, whenever one has  $\omega = \theta - i\gamma/2$ , a resonance condition is fulfilled in Eq. (2.14). In time-independent scattering systems the eigenphase  $\theta$  corresponds to the energy  $E$  and  $\gamma$  to the width  $\Gamma$  of the resonance, see Sec. 2.1.1. The norm of an eigenfunction  $\psi$  decays exponentially under time evolution as

$$\|\mathcal{U}^n \psi\|^2 = e^{-n\gamma} \|\psi\|^2, \quad (2.17)$$

such that  $\gamma$  is called the decay rate of  $\psi$ . In general  $\gamma$  can also become negative (leading to an exponential gain of the norm). If reflectivity functions without gain are considered, i.e.,  $R \leq 1$ , it follows that  $1 - \mathcal{U}^\dagger \mathcal{U} = 1 - \mathcal{R}^\dagger \mathcal{R} \geq 0$ , such that  $\mathcal{U}$  is a contraction with operator norm  $\|\mathcal{U}\|_\infty \leq 1$  [130, Sec. VI]. In these cases the modulus of all eigenvalues satisfies  $|\lambda| < 1$  and all decay rates are positive.

#### 2.1.4.1 Spectrum and inverse quantum map

In the following we discuss why the choice of order of closed propagation with  $\tilde{\mathcal{U}}$  and reflection  $\mathcal{R}$  is not important for the resonances. Therefore we show that the spectra of quantum maps with escape are the same for both choices,  $\sigma(\tilde{\mathcal{U}}\mathcal{R}) = \sigma(\mathcal{R}\tilde{\mathcal{U}})$ . Let  $\lambda \neq 0$  be an eigenvalue of  $\tilde{\mathcal{U}}\mathcal{R}$  with eigenfunction  $\psi$ . Then  $(\mathcal{R}\tilde{\mathcal{U}})\mathcal{R}\psi = \mathcal{R}(\tilde{\mathcal{U}}\mathcal{R}\psi) = \mathcal{R}\lambda\psi = \lambda\mathcal{R}\psi$ , such that  $\mathcal{R}\psi \neq 0$  is an eigenfunction of  $\mathcal{R}\tilde{\mathcal{U}}$  with the same eigenvalue. Since  $\tilde{\mathcal{U}}$  is unitary, for eigenvalues  $\lambda = 0$  of  $\tilde{\mathcal{U}}\mathcal{R}$  there must exist  $\phi \neq 0$  such that  $\mathcal{R}\phi = 0$ . In this case it is easy to see that  $\tilde{\mathcal{U}}^{-1}\phi \neq 0$  is an eigenvalue of  $\mathcal{R}\tilde{\mathcal{U}}$  with eigenvalue  $\lambda = 0$ . Thus  $\sigma(\tilde{\mathcal{U}}\mathcal{R}) \subseteq \sigma(\mathcal{R}\tilde{\mathcal{U}})$ . Conversely let  $\lambda \in \sigma(\mathcal{R}\tilde{\mathcal{U}})$  with eigenfunction  $\varphi$ . It then follows that  $(\tilde{\mathcal{U}}\mathcal{R})\tilde{\mathcal{U}}\varphi = \tilde{\mathcal{U}}(\mathcal{R}\tilde{\mathcal{U}}\varphi) = \tilde{\mathcal{U}}\lambda\varphi = \lambda\tilde{\mathcal{U}}\varphi$ , such that  $\tilde{\mathcal{U}}\varphi \neq 0$  is an eigenfunction of  $\tilde{\mathcal{U}}\mathcal{R}$  with the same eigenvalue  $\lambda$ . Thus  $\sigma(\mathcal{R}\tilde{\mathcal{U}}) \subseteq \sigma(\tilde{\mathcal{U}}\mathcal{R})$ .

In this thesis we consider the case  $\mathcal{U} = \tilde{\mathcal{U}}\mathcal{R}$  with classical reflectivity functions  $R \leq 1$  as the forward quantum map with escape. It turns out that this map is invertible if  $\mathcal{R}$  is invertible, which is the case for strictly positive  $R > 0$ . The inverse map is given by  $\mathcal{U}^{-1} = \mathcal{R}^{-1}\tilde{\mathcal{U}}^{-1}$ . The order of mapping and inverted reflection is exchanged in the inverse quantum map. Due to the above considerations we can thus think about  $\mathcal{U}_{\text{inv}} := \mathcal{U}^{-1}$  as a quantum map with gain  $\mathcal{R}_{\text{inv}} := \mathcal{R}^{-1}$  and closed time evolution  $\tilde{\mathcal{U}}^{-1} = \tilde{\mathcal{U}}^\dagger$ . Consider  $\lambda \in \sigma(\mathcal{U})$  with  $\lambda \neq 0$  and eigenfunction  $\psi \neq 0$ . It is easy to see that

$$\mathcal{U}_{\text{inv}}\psi = \mathcal{U}_{\text{inv}}\lambda^{-1}(\mathcal{U}\psi) = \lambda^{-1}(\mathcal{U}_{\text{inv}}\mathcal{U})\psi = \lambda^{-1}\psi. \quad (2.18)$$

This implies that  $\mathcal{U}$  and the inverse map  $\mathcal{U}_{\text{inv}}$  have the same eigenfunctions, and for each eigenvalue  $\lambda$  of  $\mathcal{U}$  there exists an eigenvalue  $\lambda^{-1}$  of  $\mathcal{U}_{\text{inv}}$ .

#### 2.1.4.2 Eigenfunctions of non-unitary $\mathcal{U}$

The non-unitarity of  $\mathcal{U}$  has important consequences for its spectrum and the nature of its eigenfunctions [30, 131]. Recall the unitary case  $\tilde{\mathcal{U}}^\dagger = \tilde{\mathcal{U}}^{-1}$  where the modulus of all eigenvalues  $\lambda_i$  is one and the set of eigenfunctions  $\{\phi_i\}$  of  $\mathcal{U}$  is an orthogonal basis of  $\mathbb{H}_N$ , i.e.,  $\mathbb{1} = \sum_i \frac{|\phi_i\rangle\langle\phi_i|}{\langle\phi_i|\phi_i\rangle}$ . This condition does not hold for the non-unitary operator  $\mathcal{U}$ .

Instead, the eigenvalue problem Eq. (2.16) must be considered for both  $\mathcal{U}$  and its adjoint, which is given by the hermitian conjugate operator  $\mathcal{U}^\dagger$  [131]. One ends with two different

eigenvalue problems,

$$\mathcal{U}\psi_i^{\text{R}} = \lambda_i\psi_i^{\text{R}} \quad \text{and} \quad \mathcal{U}^\dagger\psi_i^{\text{L}} = \nu_i\psi_i^{\text{L}}. \quad (2.19)$$

The states  $\psi^{\text{L}}$  and  $\psi^{\text{R}}$  are sometimes called left and right eigenstates of  $\mathcal{U}$ . Let us consider only non-degenerate spectra  $\sigma(\mathcal{U}) = \{\lambda_i\}$  and  $\sigma(\mathcal{U}^\dagger) = \{\nu_j\}$ . It follows for any  $i, j$  that  $\langle\psi_j^{\text{L}}|\mathcal{U}\psi_i^{\text{R}}\rangle = \lambda_i\langle\psi_j^{\text{L}}|\psi_i^{\text{R}}\rangle = \langle\mathcal{U}^\dagger\psi_j^{\text{L}}|\psi_i^{\text{R}}\rangle = \bar{\nu}_j\langle\psi_j^{\text{L}}|\psi_i^{\text{R}}\rangle$ , implying that  $\langle\psi_j^{\text{L}}|\psi_i^{\text{R}}\rangle = 0$  if  $\lambda_i \neq \bar{\nu}_j$  and conversely if  $\langle\psi_j^{\text{L}}|\psi_i^{\text{R}}\rangle \neq 0$  then  $\lambda_i = \bar{\nu}_j$  [131]. Non-degeneracy implies that there exists only one  $\nu_j \in \sigma(\mathcal{U}^\dagger)$  such that  $\lambda_i = \bar{\nu}_j$ . This shows that the spectra of  $\mathcal{U}$  and  $\mathcal{U}^\dagger$  are complex conjugate to each other. Relabeling the eigenvalues as  $\lambda_i = \bar{\nu}_i$  it follows that

$$\langle\psi_i^{\text{L}}|\psi_j^{\text{R}}\rangle = 0 \quad \text{for } i \neq j. \quad (2.20)$$

This is used to prove that the sets of all eigenfunctions  $\{\psi_i^{\text{R}}\}$ , as well as  $\{\psi_i^{\text{L}}\}$ , are linearly independent and thus form a basis, even though they are not orthogonal [131]. Thus, for any  $\varphi \in \mathbb{H}_N$  there exist coefficients  $\{c_i\}$  such that  $\varphi$  can be written as  $\varphi = \sum_i c_i\psi_i^{\text{R}}$ . Applying the scalar product with  $\psi_j^{\text{L}}$  from the left, it follows from Eq. (2.20) that  $\langle\psi_j^{\text{L}}|\varphi\rangle = c_j\langle\psi_j^{\text{L}}|\psi_j^{\text{R}}\rangle$  and

$$c_j = \frac{\langle\psi_j^{\text{L}}|\varphi\rangle}{\langle\psi_j^{\text{L}}|\psi_j^{\text{R}}\rangle}. \quad (2.21)$$

Altogether a representation of the unit matrix can be established in terms of the dual basis  $\{\psi_i^{\text{R}}, \psi_i^{\text{L}}\}$ , given by  $\mathbb{1} = \sum_i \frac{|\psi_i^{\text{R}}\rangle\langle\psi_i^{\text{L}}|}{\langle\psi_i^{\text{L}}|\psi_i^{\text{R}}\rangle} = \sum_i \frac{|\psi_i^{\text{L}}\rangle\langle\psi_i^{\text{R}}|}{\langle\psi_i^{\text{R}}|\psi_i^{\text{L}}\rangle}$ . Moreover the quantum map with escape and the inverse map are represented by

$$\mathcal{U} = \sum_i \lambda_i \frac{|\psi_i^{\text{R}}\rangle\langle\psi_i^{\text{L}}|}{\langle\psi_i^{\text{L}}|\psi_i^{\text{R}}\rangle}, \quad \mathcal{U}_{\text{inv}} = \sum_i \lambda_i^{-1} \frac{|\psi_i^{\text{R}}\rangle\langle\psi_i^{\text{L}}|}{\langle\psi_i^{\text{L}}|\psi_i^{\text{R}}\rangle}, \quad (2.22)$$

where  $\lambda_i \in \sigma(\mathcal{U})$ . Note that the second equation in Eq. (2.22) is not defined, if  $\mathcal{U}$  has the eigenvalue zero,  $0 \in \sigma(\mathcal{U})$ .

We emphasize that the adjoint propagator  $\mathcal{U}^\dagger = \mathcal{R}^\dagger\tilde{\mathcal{U}}^\dagger$  also corresponds to a quantum map with escape. In particular, the operator  $\mathcal{R}$  can be chosen Hermitian, such that  $\mathcal{R}^\dagger = \mathcal{R}$ . Thus  $\mathcal{U}^\dagger = \mathcal{R}\tilde{\mathcal{U}}^{-1}$  is the quantum map with escape, where the direction of time is reversed, but the reflection back into the system is the same (even though the order is switched). Since left eigenstates of  $\mathcal{U}$  are right eigenstates of  $\mathcal{U}^\dagger$ , this implies that a complete understanding of the right eigenstates of quantum maps with escape is sufficient to also understand the left ones. Therefore we focus on the right eigenfunctions in this thesis and aim to relate these to the underlying classical dynamics, which we introduce in the next section.

## 2.2 Classical chaotic scattering

In classical Hamiltonian mechanics the state of any particle with  $f$  degrees of freedom is described by a point  $(q, p) \in \Gamma$  in phase space, where  $q \in \mathbb{R}^f$  is the position and its conjugate is the momentum  $p \in \mathbb{R}^f$ . Dynamical time evolution is described by the Hamilton equations

$$\dot{p}_j(t) = -\frac{\partial H}{\partial q_j}(q(t), p(t), t), \quad \dot{q}_j(t) = \frac{\partial H}{\partial p_j}(q(t), p(t), t), \quad (2.23)$$

where the Hamilton function  $H$  characterizes the energy of the particle. In time-independent scattering processes  $H$  is typically of the form [126, Chp. 5]

$$H(q, p) = H_0(p) + V(q), \quad (2.24)$$

where  $H_0(p) = p^2/(2m)$  describes the free propagation of a non-relativistic particle and  $V$  is the scattering potential. As in quantum scattering, Sec. 2.1.1, the potential is supposed to vanish faster than  $1/|q|$  at large distances,  $\lim_{|q| \rightarrow \infty} |q|V(q) = 0$ . Thus, the dynamics of the particle before and after the collision can be described by free propagation with  $H_0$ . The equations of motion, Eq. (2.23), define the Hamiltonian flow  $\Phi^t(q_0, p_0) = (q(t, q_0, p_0), p(t, q_0, p_0))$  generated by the Hamilton function  $H$ . Similarly the free Hamiltonian  $H_0$  implicates a flow  $\Phi_0^t$  of particles not affected by  $V$ . Note that the phase-space volume is preserved under the Hamiltonian flow according to Liouville's theorem [132].

In analogy to the quantum scattering operator  $\hat{S}$ , Eq. (2.3), a classical scattering function  $\Sigma$  is defined, which maps incoming trajectories onto outgoing trajectories as

$$\mathbf{x}_{\text{out}} = \Sigma(\mathbf{x}_{\text{in}}) = \lim_{t \rightarrow \infty} \Phi_0^{-t} \circ \Phi^{2t} \circ \Phi_0^{-t}(\mathbf{x}_{\text{in}}) \quad (2.25)$$

for phase-space points  $\mathbf{x}_{\text{in}} = (q, p)$ , see e.g., Refs. [126, 133]. This is understood as follows. Consider some initial condition  $\mathbf{x}_{\text{in}}$  located inside the collision region. First,  $\Phi_0^{-t}(\mathbf{x}_{\text{in}})$  maps the starting point onto an incoming trajectory of a free particle at the time  $-t$ . This is taken as the starting point for time evolution with the full Hamiltonian flow for the time  $2t$ , leading finally to a free propagation when  $t$  is large enough. The endpoint is considered correspondingly as the endpoint of a free particle. Mapping this point backwards with the free flow  $\Phi_0$  for the time  $-t$  one obtains the initial point of the outgoing trajectory at time  $t = 0$ . Thus  $\mathbf{x}_{\text{out}}$  is again inside the collision region and corresponds to the initial condition of some outgoing particle which propagates freely. This establishes a map from the collision region onto itself.

Conceptually simple examples of classical scattering systems are spherical hard-disk scatterers [134, 135] or scattering at a periodic potential [136]. In both cases the continuous dynamics is effectively described by stroboscopic, time-discrete maps. Before discussing a particular class of such maps we introduce different characterizations of the classical dynamics.

### 2.2.1 Characterization of classical dynamics

Chaotic scattering is characterized by its invariant set  $\Gamma_s$  [126]. This set contains all phase-space points  $\mathbf{x} \in \Gamma$ , which never escape from the scattering system in both future and past times,  $t \rightarrow \pm\infty$ , and is constituted by unstable periodic orbits [137]. One defines stable  $\Gamma_f$  and unstable  $\Gamma_b$  manifolds of the invariant set as the sets of points that approach  $\Gamma_s$  under forward and backward time evolution, respectively. In general the invariant set may contain regions of regular motion on Kolmogorov–Arnold–Moser (KAM) tori [138–141]. If such regular regions exist, the scattering system is called non-hyperbolic [126]. In contrast, in hyperbolic scattering systems the dynamics close to the invariant set  $\Gamma_s$  is determined by motion on its unstable and stable manifolds. In this case the invariant set is called chaotic saddle. Chaotic dynamics is generally defined by sensitive dependence on initial conditions, a dense set of periodic points and the existence of a dense orbit [137, 142].

The sensitive dependence on initial conditions is quantified with the Lyapunov exponent, which is defined from the linearized dynamics as follows [137, Sec. 4.4]. For simplicity, we consider a map  $M: \Gamma \rightarrow \Gamma$  on a bounded phase space  $\Gamma$  in the following. Let  $\mathbf{x}_0 \in \Gamma$  with iterates  $\mathbf{x}_i := M^i(\mathbf{x}_0)$ , and let  $\mathbf{DM}(\mathbf{x})$  be the Jacobian of  $M$  at any phase-space point  $\mathbf{x}$ . An infinitesimal displacement  $\mathbf{y}_0$  from  $\mathbf{x}_0$  grows as  $\mathbf{y}_n = \mathbf{DM}(\mathbf{x}_{n-1}) \cdot \mathbf{y}_{n-1} = \mathbf{DM}^n(\mathbf{x}_0) \cdot \mathbf{y}_0$ , where  $\mathbf{DM}^n(\mathbf{x}_0) = \mathbf{DM}(\mathbf{x}_{n-1}) \cdot \mathbf{DM}(\mathbf{x}_{n-2}) \cdot \dots \cdot \mathbf{DM}(\mathbf{x}_0)$ . [137]. The Lyapunov exponents for any such  $\mathbf{x}_0$  in the direction  $\mathbf{u} = \mathbf{y}_0/|\mathbf{y}_0|$  is defined as

$$\lambda_L(\mathbf{x}_0, \mathbf{u}) = \lim_{n \rightarrow \infty} \frac{1}{n} \ln |\mathbf{DM}^n(\mathbf{x}_0) \cdot \mathbf{u}|, \quad (2.26)$$

which characterizes the average stretching or compression of the initial displacement. It is often convenient to consider the Lyapunov exponents in terms of the nonnegative, hermitian matrix  $\mathbf{L}_n(\mathbf{x}_0) := [\mathbf{DM}^n(\mathbf{x}_0)]^T \mathbf{DM}^n(\mathbf{x}_0)$  as  $\lambda_L(\mathbf{x}_0, \mathbf{u}) = \lim_{n \rightarrow \infty} \frac{1}{2n} \ln \mathbf{u}^T \cdot \mathbf{L}_n(\mathbf{x}_0) \cdot \mathbf{u}$  [137]. This allows choosing  $\mathbf{u}$  parallel to one of the real eigenvectors of  $\mathbf{L}_n$ , implying one approximate Lyapunov exponent for each eigenvector [137]. In the limit  $n \rightarrow \infty$  one thereby obtains  $d$  Lyapunov exponents  $\lambda_L^{(i)}$  for any  $d$ -dimensional phase space  $\Gamma$ . In two-dimensional hyperbolic systems there are only two Lyapunov exponents characterizing the stable and the unstable direction. If the map is volume-preserving on  $\Gamma$ , as in Hamiltonian systems, stretching and compressing have the same strength, such that  $\lambda_L^{(1)}(\mathbf{x}_0) = -\lambda_L^{(2)}(\mathbf{x}_0)$ .

We stress that in uniformly hyperbolic maps, the tangent space at arbitrary phase space points splits locally into stable and unstable subspaces,  $E_x^s \oplus E_x^u$  [143, Sec. 3.6]. They satisfy that stable and unstable subspaces of  $\mathbf{x}$  are mapped by the map  $M$  onto the stable and unstable subspaces of  $M(\mathbf{x})$ , respectively. In particular, there exists  $C > 0$  and  $\lambda \in (0, 1)$  such that  $\|\mathbf{DM}^n(\mathbf{x})\mathbf{y}\| < C\lambda^n\|\mathbf{y}\|$  for all  $\mathbf{y} \in E_x^s$  and  $\|\mathbf{DM}^{-n}(\mathbf{x})\mathbf{y}\| < C\lambda^n\|\mathbf{y}\|$  for all  $\mathbf{y} \in E_x^u$  [143, 144]. This means that all points  $\mathbf{y} \in E_x^s$  in the stable subspace of  $\mathbf{x}$  approach under forward iteration the forward iterates of  $\mathbf{x}$ ,  $\|M^n(\mathbf{y}) - M^n(\mathbf{x})\| \rightarrow 0$ . Conversely, points  $\mathbf{y} \in E_x^u$  approach under

backward iterations the backward iterates of  $\mathbf{x}$ ,  $\|M^{-n}(\mathbf{y}) - M^{-n}(\mathbf{x})\| \rightarrow 0$ . Thus, the stable direction on the phase space is given by the stable eigenvector of  $\mathbf{L}_n(\mathbf{x})$  with negative Lyapunov exponent, if  $n$  is large enough. On the other hand, stable and unstable direction interchange, when  $M$  is replaced with  $M^{-1}$ . This implies, that the unstable direction on the phase space  $\Gamma$  is characterized by the stable eigenvector of  $\mathbf{L}_{-n}(\mathbf{x})$  for large  $n$  and arbitrary  $\mathbf{x}$ .

The other conditions for chaos are the existence of a dense set of periodic points as well as a dense orbit on the phase space. They imply that the phase space of chaotic maps has only one dynamically independent component. In particular, chaotic maps are ergodic which is defined as follows. Let  $(\Gamma, \mathcal{B}, \mu)$  be a measure space with the Borel  $\sigma$ -algebra  $\mathcal{B}$  of measurable subsets  $A \subset \Gamma$  and probability measure  $\mu$ . A measure preserving map  $M: \Gamma \rightarrow \Gamma$ , i.e.,  $\mu[M^{-1}(A)] = \mu(A)$  for all  $A \in \mathcal{B}$ , is called ergodic with respect to  $\mu$ , if any invariant subset  $A \in \mathcal{B}$  has either zero or full measure,

$$M^{-1}(A) = A \quad \Rightarrow \quad \mu(A) \in \{0, 1\}. \quad (2.27)$$

This means, that there is no decomposition of the phase space in dynamically independent subsets, which are nontrivial in the sense that they have non-zero measure. For instance, any periodic orbit  $\mathbf{x}^* = M^p(\mathbf{x}^*)$  gives rise to such an invariant set  $A = \{M^i(\mathbf{x}^*) : 0 \leq i < p\}$ . This set consists of  $p$  isolated points, such that  $\mu(A) = 0$ .

In this thesis we consider maps, derived from Hamiltonian systems, which preserve the phase-space volume due to the symplectic structure [132]. This measure is given by the Lebesgue measure  $\mu_L$  on  $\Gamma$ , which is uniform on  $\Gamma$ . For any subset  $A \subset \Gamma$  it is defined by

$$\mu_L(A) := \int_A d\mu_L = \int_A dpdq. \quad (2.28)$$

One important consequence of ergodicity is the Birkhoff ergodic theorem, see e.g., Ref. [145]. Let  $M$  be ergodic with respect to the uniform measure  $\mu_L$  and  $f: \Gamma \rightarrow \mathbb{R}$  be a classical observable,  $f \in C^\infty(\Gamma, \mathbb{R})$ . The Birkhoff ergodic theorem [145, Sec. 1.6] states that for almost all initial conditions  $\mathbf{x} \in \Gamma$  the time average of the observable  $f$  converges to the phase-space average,

$$\lim_{n \rightarrow \infty} \frac{1}{n} \sum_{k=0}^{n-1} f[M^k(\mathbf{x})] = \int f d\mu_L. \quad (2.29)$$

It is generally difficult to prove ergodicity rigorously for specific maps. Systems with large degrees of freedom are expected to experience ergodic motion, which is known as Boltzmann ergodic hypothesis [146].

The following property is useful to numerically investigate ergodicity in dynamical systems. For any two measurable sets  $A, B \subset \Gamma$  ergodicity is equivalent to the convergence of

$\mu_L[M^{-k}(A) \cap B]$  in a Cesàro sense towards the product  $\mu_L(A)\mu_L(B)$ , i.e.,  $\frac{1}{n} \sum_{k=0}^{n-1} \mu_L[M^{-k}(A) \cap B] \xrightarrow{n \rightarrow \infty} \mu_L(A)\mu_L(B)$ . Thus, the overlap of two sets is on average given by their relative sizes. Chaotic systems often meet a stronger condition, where

$$\lim_{n \rightarrow \infty} \mu_L[M^{-n}(A) \cap B] = \mu_L(A)\mu_L(B) \quad (2.30)$$

holds not just on average. Such systems are called strong mixing [145]. Equation (2.30) means that the overlap of two regions converges directly towards the product of their relative sizes. This implies that for large  $n$  the iteration  $M^n(A)$  covers the phase space uniformly. Furthermore, if  $M$  is strong mixing with respect to  $\mu_L$ , any measure  $\mu$  which is absolutely continuous with respect to  $\mu_L$  converges weakly towards the Lebesgue measure  $\lim_{n \rightarrow \infty} \mu[M^{-n}(A)] = \mu_L$  [145, Sec. 6.3]. The mixing property, Eq (2.30), is simple to investigate numerically. Since mixing implies ergodicity, this can be used to deduce if a system is ergodic.

Ergodicity has further important consequences for the set of Lyapunov exponents  $\lambda_L^{(i)}(\mathbf{x})$ . In particular, the multiplicative ergodic theorem [145, Sec. 10.2] implies for almost all  $\mathbf{x} \in \Gamma$  the same Lyapunov exponents [137]. Therefore one usually drops the dependence on  $\mathbf{x}$  in the notation of  $\lambda_L^{(i)}$ . In two-dimensional, ergodic maps usually only the positive Lyapunov exponent is considered,  $\lambda_L := \lambda_L^{(u)} = -\lambda_L^{(s)} > 0$ .

### 2.2.2 Stroboscopic maps

In this thesis we consider time-discrete maps  $M: \Gamma \rightarrow \Gamma$  on a bounded phase-space  $\Gamma$ . Such maps emerge for example in two-dimensional billiards [125] or hard-disk scattering systems as a Poincaré section at the boundary of the disks [126, Sec. 5.2]. Considering scattering at a periodic potential also implicates an effective map containing the full dynamics [136]. Another way to obtain such maps are time-periodically driven systems with one degree of freedom. These systems are characterized by a Hamiltonian that satisfies  $H(q, p, t) = H(q, p, t + n\tau)$ . The Hamiltonian flow generates a stroboscopic map on the phase space  $\Gamma$  as  $\mathbf{x}(t_n) = \Phi_{t_n}(\mathbf{x}_0)$ , when discrete times  $t_n = t_0 + n\tau$  are considered for  $n \in \mathbb{Z}$ .

One particularly simple class of time-periodically driven systems are kicked systems, where the Hamilton function is given by

$$H(q, p, t) = T(p) + V(q) \sum_{n=-\infty}^{+\infty} \delta(t - n\tau). \quad (2.31)$$

The first term characterizes the kinetic energy, usually considered as  $T(p) = \frac{p^2}{2m}$ , which corresponds to free propagation with  $H_0$ . The second part corresponds to the kicking potential  $V$ , acting only at integer times  $n \in \mathbb{Z}$ . Thus, the Hamiltonian flow in these systems is equivalent to the free flow  $\Phi_0^t$  for all times in between the kicks,  $t \in (n + \epsilon, n + 1 - \epsilon)$  for  $n \in \mathbb{Z}$  and



all  $\epsilon > 0$ . The kicking potential  $V$  acts at times  $t = n \in \mathbb{Z}$  as a discontinuous jump in the  $p$ -coordinate.

One widely used example of such a kicked map is the Chirikov standard map [147], where the kicking potential  $V(q) = \frac{\kappa}{4\pi^2} \cos(2\pi q)$  depends on the so-called kicking strength  $\kappa$ . The resulting map on the two-dimensional phase space  $\Gamma$  is given in dimensionless coordinates  $(q, p) \in \Gamma$  at times half through the kick by

$$M(q, p) = (q + p^*, p^* - V'(q + p^*)/2), \quad \text{with } p^* = p - V'(q)/2, \quad (2.32)$$

where  $V'(q) = -\frac{\kappa}{2\pi} \sin(2\pi q)$ . We apply periodic boundary conditions, by restricting this map to the torus  $\Gamma := \mathbb{T}^2 = [0, 1) \times [0, 1)$ , leading to a bounded phase space. One major advantage of the standard map, Eq. (2.32), is that it allows to investigate different kinds of dynamical motion depending on the choice of the kicking strength  $\kappa$ .

Typical phase-space portraits of this map are illustrated in Fig. 2.2. At kicking strength  $\kappa = 0$  the momentum is conserved such that the system is integrable and all orbits are on regular tori, appearing as straight lines (a). The regular tori break up into chains of regular islands (elliptic shape) and chaotic layers (shown in blue) for small  $\kappa = 0.5$  (b), which follows from the Poincaré–Birkhoff theorem [137, 148, 149]. For larger  $\kappa = 2.5$ , shown in (c), the phase-space is divided into regular structures (red) surrounded by a large chaotic component (blue). For  $\kappa = 10$  no regular islands are found and the full phase space shows chaotic motion (d).

We further illustrate the local stable and unstable directions for the chaotic standard map with  $\kappa = 10$  in Fig. 2.3. These directions are calculated for phase-space points chosen on a grid as discussed in Sec. 2.2.1. For almost all phase-space points we find that the product of these directions locally spans a two dimensional space, i.e., they are not parallel, see closeup in (c). Note that the standard map for  $\kappa = 10$  is not uniformly hyperbolic and that ergodicity and

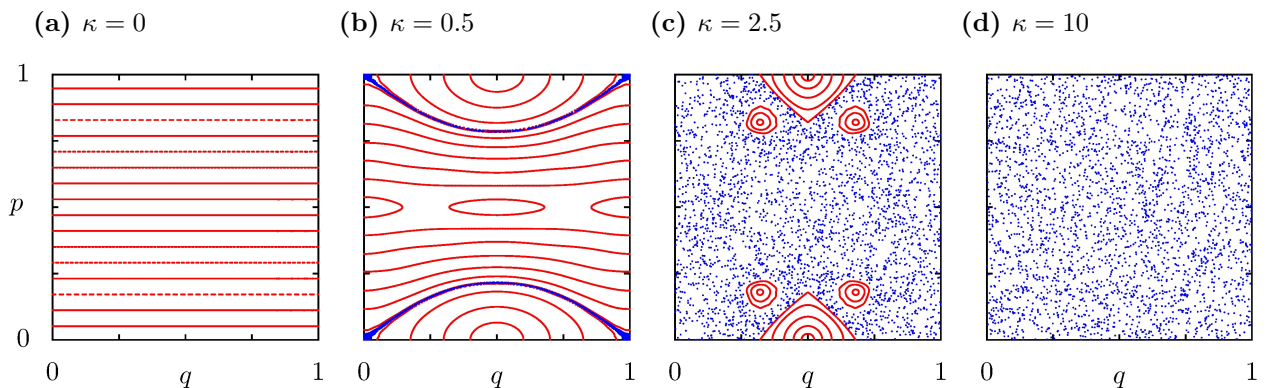


**Figure 2.2:** Phase-space portrait of the standard map with kicking strength (a)  $\kappa = 0$ , (b)  $\kappa = 0.5$ , (c)  $\kappa = 2.5$ , and (d)  $\kappa = 10$ . Illustrated are orbits  $\{M^i(x)\}_{i=0}^n$  belonging to regular motion (red,  $n = 800$ ) and to chaotic motion (blue,  $n = 3000$ ).

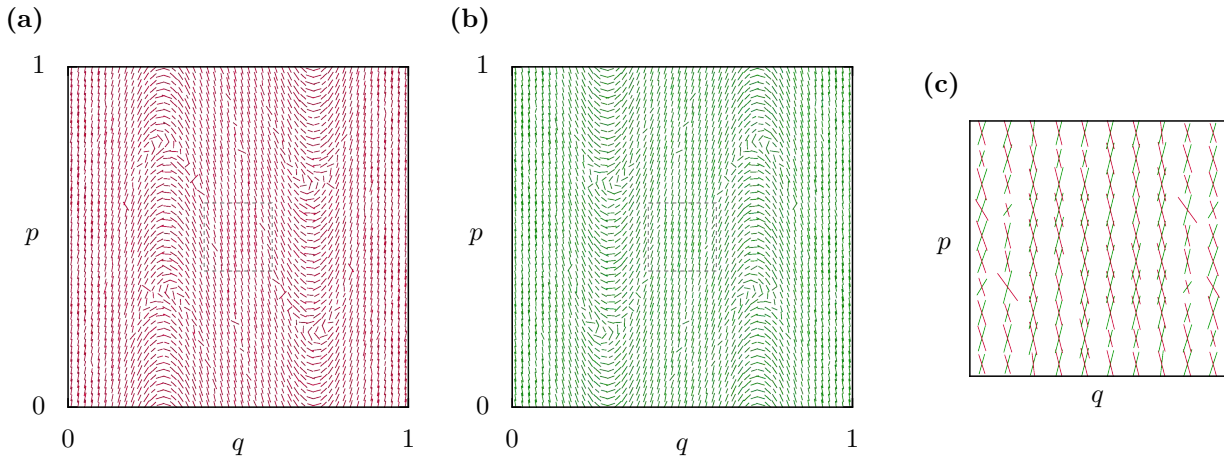


**Figure 2.3:** Illustrated are (a) local unstable and (b) local stable direction on phase space for the chaotic standard map with  $\kappa = 10$ . These directions are calculated choosing  $\mathbf{x} \in \Gamma$  on a  $50 \times 50$  grid from  $L_{\pm n}(\mathbf{x})$  with  $n = 20$  iterations as discussed in Sec. 2.2.1. The length indicates the local stretching  $e^{\lambda_L}$ . (c) Closeup of stable and unstable directions on the box  $(0.4, 0.6) \times (0.4, 0.6)$ , indicated by dashed lines in (a) and (b).

mixing property can only be observed numerically. These properties, however, are assumed in many rigorous results regarding the convergence of classical measures. Nevertheless, it is expected that these results also apply to generic 'chaotic' systems like the standard map at  $\kappa = 10$  and most numerical investigations will be performed for this system.

This behavior is contained in a minimalistic way in the so-called baker map [150–153], which obtains a simple phase-space structure. These maps implement stretching and folding of manifolds along the phase space and are used to model the horseshoe mechanism [143, Sec. 3.5]. The ternary baker map  $B_3: \mathbb{T}^2 \rightarrow \mathbb{T}^2$  is defined by

$$B_3(q, p) := \begin{cases} (3q, \frac{p}{3}) & \text{for } 0 \leq q < \frac{1}{3} \\ (3q - 1, \frac{p+1}{3}) & \text{for } \frac{1}{3} \leq q < \frac{2}{3} \\ (3q - 2, \frac{p+2}{3}) & \text{for } \frac{2}{3} \leq q < 1, \end{cases} \quad (2.33)$$

illustrated in Fig. 2.4. The phase space is divided into three rectangles, which are compressed

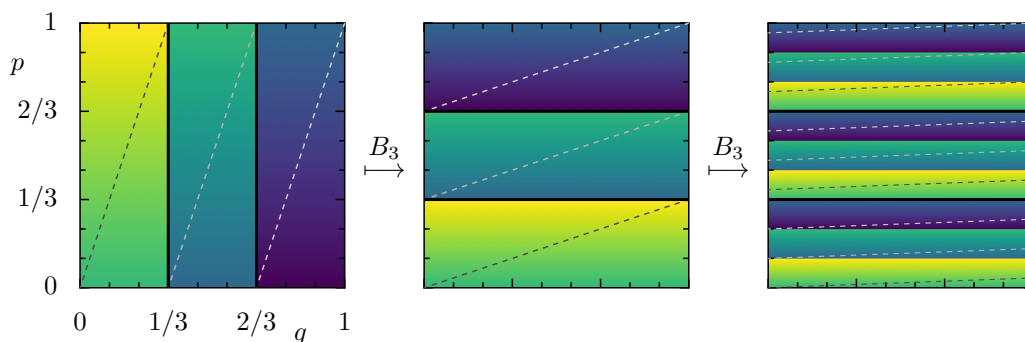


**Figure 2.4:** Time evolution of the ternary baker map  $B_3$  on phase space, see Eq. (2.33).

in the stable  $p$ -direction and stretched in unstable  $q$ -direction, each by a factor of three, and then stacked on top of each other. The general definition for an arbitrary number of differently sized stripes is given in App. A.1. Note that the baker map is equivalent to a shift on symbolic sequences, which allows for an analytical treatment, see Ref. [150] and App. A.1. It is easy to see that the baker map is uniformly hyperbolic and ergodic with respect to the uniform measure  $\mu_L$ . Its particularly simple structure preserves when escape is allowed from the stripes.

### 2.2.3 Classical maps with escape

In chaotic scattering systems almost all trajectories that are initially in a finite phase-space volume  $A \subset \Gamma$  eventually escape from this region. We consider a classical system similar to the considerations in Sec. 2.1.4, where the time evolution of internal states is effectively described by the closed map together with a coupling to the outside. This is realized in classical systems for example by introducing a leaky phase-space region  $\Omega$  [67], from which particles escape.

In analogy to the quantum map with escape, Eq. (2.15), we generally consider the closed map  $M$  together with a classical reflectivity function  $R: \Gamma \rightarrow \mathbb{R}_+$ , which implements a loss of intensity as follows. Each particle is considered to carry a weight or intensity  $J$ . We define the classical map with escape as the application of the reflectivity  $R$  on the intensity space, followed by the closed map  $M$ . In an extended phase-space  $\Gamma \times \mathbb{R}_+$  this is written as

$$(\mathbf{x}', J') = (M(\mathbf{x}), J \cdot R(\mathbf{x})). \quad (2.34)$$

The choice of order for mapping and reflection is chosen to match the order considered in the quantum case, see Eq. (2.15). Equation (2.34) can be viewed as the mapping of a localized phase-space density at  $\mathbf{x}$  with weight  $J$ . This is often written for arbitrary phase-space densities  $\rho: \Gamma \rightarrow \mathbb{R}_+$  in terms of the Perron-Frobenius operator

$$\mathcal{P}\rho(\mathbf{x}) = R[M^{-1}(\mathbf{x})] \cdot \rho[M^{-1}(\mathbf{x})]. \quad (2.35)$$

However, phase-space densities exist only for such probability measures  $\mu$  on  $\Gamma$ , which are absolutely continuous with respect to the Lebesgue measure  $\mu_L$  [145, Sec. 0.4]. For this reason, instead of densities, we consider the more general notion of time evolution for measures  $\mu$  in this thesis. For a closed map the time evolution  $\tilde{\mathcal{M}}$  of a measure  $\mu$  is given by the push-forward measure,

$$\tilde{\mathcal{M}}\mu(A) := M^*\mu(A) = \mu(M^{-1}(A)) \quad (2.36)$$

for all measurable  $A \subset \Gamma$ . For an arbitrary measurable function  $f$  on  $\Gamma$ , e.g., some observable, this implies  $\tilde{\mathcal{M}}\mu(f) = \mu(f \circ M)$ . Hence, the closed time evolution of observables is effectively given by  $f \mapsto f \circ M$ . This intuitively means that the iterated measure of some observable is

the same as the measure of the observable evaluated after one iteration  $M$  on the phase space. Note that for the characteristic function  $f = \mathbb{1}_A$  of some set  $A$  one recovers Eq. (2.36), since  $\mathbb{1}_A \circ M = \mathbb{1}_{M^{-1}(A)}$ .

The time evolution of the map with escape is generalized to measures in the following sense. We define the classical map with escape  $\mathcal{M} \equiv \mathcal{M}_{M,R}$  for any measure  $\mu$  on  $\Gamma$  as the push-forward measure modified by  $R$ ,

$$\mathcal{M}\mu(A) := \int_{M^{-1}(A)} R d\mu, \quad (2.37)$$

for all measurable  $A \subset \Gamma$ . It is sometimes useful to consider the map with escape  $\mathcal{M}$  for a measure applied to some measurable function  $f$ . In this case the definition in Eq. (2.37) implies

$$\mathcal{M}\mu(f) = \mu(R \cdot [f \circ M]), \quad (2.38)$$

such that application of the map with escape to observables is effectively given by  $f \mapsto R \cdot (f \circ M)$ . Note that in the closed limit,  $R(\mathbf{x}) = 1$ , the map with escape  $\mathcal{M}$  becomes equivalent to the closed map  $\tilde{\mathcal{M}}$ .

For a single phase-space point  $\mathbf{x} \in \Gamma$  the definition of  $\mathcal{M}$  ensures that the intensity is first reduced by  $R(\mathbf{x})$  and subsequently mapped with  $M$  as in Eq. (2.34). Thus, we have the same order of reflection  $R$  and mapping  $M$  as in the quantum map. In order to show this consider a so-called atomic measures  $\delta_{\mathbf{y}}$ , located solely at some phase-space point  $\mathbf{y} \in \Gamma$  [145, Sec. 6]. It is defined as

$$\delta_{\mathbf{y}}(A) = \int_A \delta(\mathbf{x} - \mathbf{y}) d\mu_L(\mathbf{x}) = \begin{cases} 1 & \mathbf{y} \in A, \\ 0 & \text{else.} \end{cases} \quad (2.39)$$

Applying the map with escape  $\mathcal{M}$  to the measure  $\delta_{\mathbf{y}}$  gives for volume preserving  $M$  on  $\Gamma$

$$\begin{aligned} \mathcal{M}\delta_{\mathbf{y}}(A) &\stackrel{(2.37)}{=} \int_{M^{-1}(A)} R(\mathbf{x}) \delta(\mathbf{x} - \mathbf{y}) d\mu_L(\mathbf{x}) \\ &= R(\mathbf{y}) \int_A \delta[M^{-1}(\mathbf{x}') - \mathbf{y}] d\mu_L(\mathbf{x}') = R(\mathbf{y}) \delta_{M(\mathbf{y})}(A). \end{aligned} \quad (2.40)$$

Hence the overall weight decreases by the factor  $R(\mathbf{y})$ , and the iterated measure is localized at the iterated phase-space point  $M(\mathbf{y})$ , as desired.

## 2.2.4 Classical maps with full escape

In many situations it is convenient to consider full escape, for example, when particles leave a bounded region indefinitely after entering a certain region  $\Omega$  [67, 69, 119]. Such maps naturally

arise in scattering systems, when the Hamiltonian flow is reduced to a finite phase-space volume  $\Gamma$ , which is not invariant. For chaotic dynamics almost all initial conditions within such a finite region eventually escape. After the escape they propagate freely and do not return to  $\Gamma$ . This occurs for example in the case of three-disk scattering systems [126]. Full escape is used to model ideally coupled channels between the system of interest and the surrounding.

In the framework of this thesis, full escape is characterized by a phase-space region  $\Omega$  with  $R(\mathbf{x} \in \Omega) = 0$ , while  $R(\mathbf{x} \notin \Omega) \neq 0$ . For simplicity we restrict to the simplest case where  $R(\mathbf{x} \notin \Omega) = 1$ . Thus we obtain a very simple form of the reflection function as  $R_\Omega(\mathbf{x}) := 1 - \mathbb{1}_\Omega(\mathbf{x})$ . The classical map with full escape is then defined as  $\mathcal{M}_\Omega := M^* R_\Omega^*$ . For any measure  $\mu$  on  $\Gamma$  this leads to

$$\mathcal{M}_\Omega \mu(A) = \mu[M^{-1}(A) \cap \Omega^c], \quad (2.41)$$

which follows immediately from Eq. (2.37) for partial escape.

In such maps there is usually a nontrivial set of points, which never fall into the opening  $\Omega$  under forward and backward iteration,

$$\Gamma_s = \{\mathbf{x} \in \Gamma : M^i(\mathbf{x}) \notin \Omega \forall i \in \mathbb{Z}\}. \quad (2.42)$$

This set has similar properties to the beforementioned chaotic saddle in scattering systems and is invariant under the map,  $M^{-1}(\Gamma_s) = \Gamma_s$ . Its stable manifold  $\Gamma_f$  consists of points that approach  $\Gamma_s$  in positive times, while the unstable manifold  $\Gamma_b$  approaches  $\Gamma_s$  in negative times,

$$\Gamma_f := \{\mathbf{x} \in \Gamma : \lim_{i \rightarrow \infty} M^i(\mathbf{x}) \in \Gamma_s\}, \quad \Gamma_b := \{\mathbf{x} \in \Gamma : \lim_{i \rightarrow -\infty} M^{-i}(\mathbf{x}) \in \Gamma_s\}. \quad (2.43)$$

Therefore  $\Gamma_f$  is called forward trapped set, and  $\Gamma_b$  is called backward trapped set of the map with escape. Their intersection is trapped in both directions, such that  $\Gamma_s = \Gamma_f \cap \Gamma_b$ . These sets are usually fractal sets with phase-space volume  $\mu_L(\Gamma_s) = \mu_L(\Gamma_b) = \mu_L(\Gamma_f) = 0$ . On the other hand, consider the sets of points, that fall onto the opening  $\Omega$  for the first time after  $n$  forward iterations,  $\Omega_0^+ = \Omega$ , and for  $n > 0$

$$\Omega_n^+ := M^{-n}(\Omega) \setminus \bigcup_{i=0}^{n-1} M^{-i}(\Omega). \quad (2.44)$$

These are the preimages of  $\Omega$  under the map with full escape, and they consist of all points escaping from the system in the next step after  $n$  iterations. Rewriting  $\Gamma_f = \{\mathbf{x} \in \Gamma : M^i(\mathbf{x}) \notin \Omega \forall i \in \mathbb{N}\}$ , it is easy to see that these sets partition the full phase space together with the forward trapped set,  $\Gamma = \bigcup_{n=0}^{\infty} \Omega_n^+ \cup \Gamma_f$ . Similarly one defines the sets, which fall into the

opening  $\Omega$  for the first time under backward iterations,  $\Omega_1^- = M(\Omega)$ , and for  $n > 1$

$$\Omega_n^- := M^n(\Omega) \setminus \bigcup_{i=1}^{n-1} M^i(\Omega). \quad (2.45)$$

This leads to the partition  $\Gamma = \bigcup_{i=0}^{\infty} \Omega_n^- \cup \Gamma_b$ .

We illustrate the relevant classical sets for the ternary baker map  $B_3$ , defined in Eq. (2.33), with full escape from the middle stripe,  $\Omega = [1/3, 2/3) \times [0, 1)$ , in Fig. 2.5. The sets of points escaping under forward iteration,  $\Omega_n^+$  shown in (a), and backward direction,  $\Omega_n^-$  shown in (b), cover almost the full phase space. The forward trapped set  $\Gamma_f$  is uniform along the  $p$ -coordinate, which is the stable direction on phase space (c). It is a fractal Cantor set along the unstable  $q$ -direction. Vice versa, the backward trapped set  $\Gamma_b$  is fractal in the  $p$ -direction and uniform in the  $q$ -direction (d). The chaotic saddle  $\Gamma_s$  inherits a combination of the fractal structures of forward and backward trapped sets, see (e), and is perfectly self-similar.

For the chaotic standard map with full escape from the opening  $\Omega = (0.3, 0.6) \times [0, 1)$  we illustrate the equivalent classical sets in Fig. 2.6. The escaping sets  $\Omega_n^\pm$  are stretched and folded along the phase space, see (a) and (b), and show a much richer structure than for the baker map. The forward trapped set  $\Gamma_f$  is stretched smoothly along the local stable direction, which depends on the phase-space point  $\boldsymbol{x}$  (c), and has a complex structure along the local unstable phase-space direction. The backward trapped set  $\Gamma_b$  is stretched along the local unstable direction on  $\Gamma$  (d), and is fractal in the stable direction. Again, the chaotic saddle  $\Gamma_s$

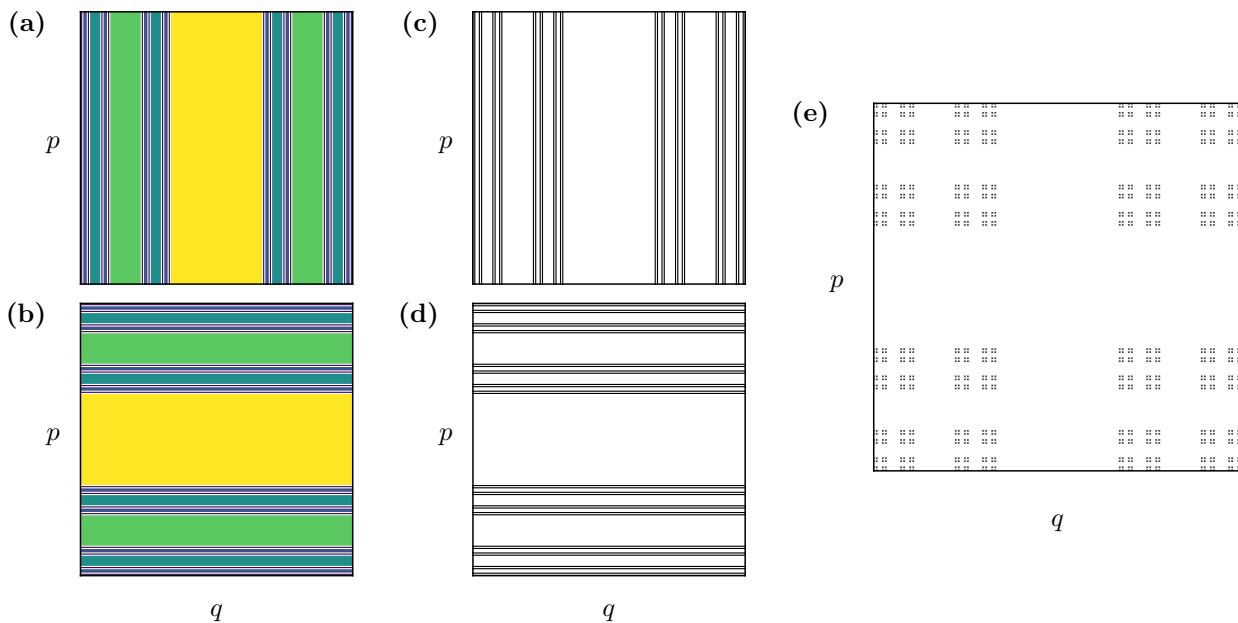


**Figure 2.5:** Classical sets of ternary baker map with escape from the middle strip. (a) Sets  $\Omega_n^+$  for  $0 \leq n \leq 4$  (light yellow to dark blue). (b) Sets  $\Omega_n^-$  for  $1 \leq n \leq 5$ . (c) Forward trapped set  $\Gamma_f$ , (d) backward trapped set  $\Gamma_b$ , and (e) chaotic saddle  $\Gamma_s$ , each approximated by points being trapped for five iterations (black stripes and points).

combines the fractal structures in both directions (e).

### 2.2.5 Fractal structure

Introducing escape to the system changes the nature of the chaotic set. In closed systems this set is equal to the whole phase space  $\Gamma$ . If full escape is considered through an opening  $\Omega$  the system shows transiently chaotic dynamics almost everywhere [67, 70, 154]. This means, that the sets of points escaping in future times  $\Omega_n^+$ , Eq. (2.44), cover almost the full phase space, i.e., its closure satisfies  $\Gamma = \overline{\bigcup_{n=0}^{\infty} \Omega_n^+}$ . The invariant chaotic set, the saddle  $\Gamma_s$ , usually has fractal properties and Lebesgue measure zero [137, Chp. 3], see Figs. 2.5(e) and 2.6(e).

In order to define the notion of a fractal it is necessary to consider the concept of generalized dimensions [155, 156], different from the usual topology dimension  $D_T$ , also known as Lebesgue covering dimension [157, Chp. 3]. The definition of  $D_T$  [157, Def. III.1] implies that it is always integer valued, and for any subset  $A \subset \mathbb{R}^n$  one has  $0 \leq D_T \leq n$ , where points are zero-dimensional, lines are one-dimensional, and so on. For metric spaces a more general concept is provided by the Hausdorff dimension  $D_H$  [157, Chp. VII]. The Hausdorff dimension for regular subsets of  $\mathbb{R}^n$ , such as points and lines, equals the topology dimension,  $D_H = D_T$ . However, in general  $D_H$  is not necessarily integer valued, and leads to the following definition of fractals [156]: A fractal is defined as a set for which the Hausdorff dimension is strictly larger than its topology dimension,  $D_H > D_T$ . This implies, that every set with non-integer

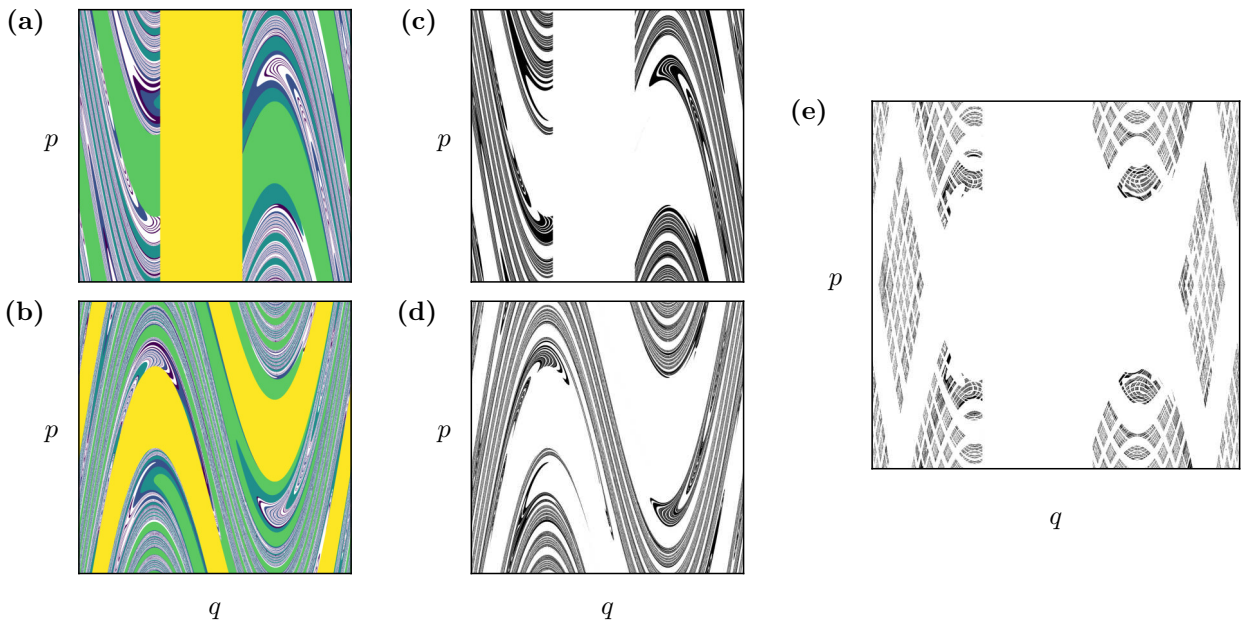


**Figure 2.6:** Classical sets of chaotic standard map with full escape from  $\Omega = (0.3, 0.6) \times [0, 1)$ . (a) Sets  $\Omega_n^+$  for  $0 \leq n \leq 4$  (light yellow to dark blue). Opening  $\Omega = \Omega_0^+$  is shown as the yellow region. (b) Sets  $\Omega_n^-$  for  $1 \leq n \leq 5$ . Iteration of opening,  $M(\Omega) = \Omega_0^-$ , is shown as the yellow region. (c) Forward trapped set  $\Gamma_f$ , (d) backward trapped set  $\Gamma_b$ , and (e) chaotic saddle  $\Gamma_s$ , each approximated by points being trapped for five iterations.

Hausdorff dimension is a fractal. The Hausdorff dimension  $D_H$  is thus referred to as the fractal dimension.

In order to estimate the Hausdorff dimension for subsets of  $\mathbb{R}^n$  one usually considers the conceptually simpler fractal box-counting dimension  $D_0$ , also known as Minkowski dimension [158]. Therefore let  $\mathcal{A}_\epsilon := \{A_i^\epsilon\}_{i=1}^{n_\epsilon}$  be a partition of the phase space,  $\Gamma = \bigcup_{i=1}^{n_\epsilon} A_i$ , dividing  $\Gamma$  into  $n_\epsilon$  boxes of size  $\epsilon$ . For any set  $B \subset \Gamma$  let  $N(B, \epsilon) \leq n_\epsilon$  be the least number of boxes within  $\mathcal{A}$  that are necessary to cover  $B$ . The box-counting dimension is then defined as the scaling of  $N(B, \epsilon)$  with  $\epsilon$  [158],

$$D_0(B) = -\lim_{\epsilon \rightarrow 0} \frac{\ln N(B, \epsilon)}{\ln \epsilon}. \quad (2.46)$$

Note that this limit not necessarily exists, such that strictly speaking upper and lower box-counting dimensions have to be considered by replacing the limit in Eq. (2.46) with limit superior (lim sup) and limit inferior (lim inf), respectively. For this thesis such a distinction is not considered, and fractal dimensions are only estimated numerically for finite grids.

It is possible to generalize the concept of the box-counting dimension, if not only the number of boxes  $A_i$  covering  $B$ , but also the proportion of their intersection  $B \cap A_i$  is taken into account. This proportion is given in terms of a probability measure  $\mu_B$  that is uniform on  $B$  and normalized on  $\Gamma$ . For arbitrary probability measures  $\mu$  on  $\Gamma$  one defines generalized dimensions of order  $q$ , also called Rényi dimensions, as [159, 160]

$$D_q(\mu) = -\lim_{\epsilon \rightarrow 0} \frac{\frac{1}{1-q} \ln \sum_{i=1}^{n_\epsilon} [\mu(A_i^\epsilon)]^q}{\ln \epsilon}. \quad (2.47)$$

The term in the nominator is sometimes called Rényi entropy of order  $q$  and denoted by  $S_q(\mu, \epsilon)$ . If  $\mu = \mu_B$  one obtains in the limit of  $q \rightarrow 0$ , where  $q > 0$ , that  $[\mu_B(A_i)]^q \rightarrow 1$ , if and only if  $B \cap A_i \neq \emptyset$ . Hence,  $\lim_{q \rightarrow 0} S_q(\mu_B, \epsilon) = \ln N(B, \epsilon)$  for all  $\epsilon$ , such that the box-counting dimension is obtained in this limit.

Another relevant dimension for dynamical systems is the information dimension, which is obtained in the limit  $q \rightarrow 1$ . In this limit the weight  $\mu(A_i)$  of each box is considered. Applying l'Hôpital's rule to the Rényi entropy of order  $q$  the usual information entropy of a probability measure  $\mu$  discretized on  $\mathcal{A}_\epsilon$  is obtained,

$$S_1(\mu, \epsilon) = -\sum_{i=1}^{n_\epsilon} \mu(A_i^\epsilon) \ln \mu(A_i^\epsilon), \quad (2.48)$$

where only terms with  $\mu(A_i^\epsilon) > 0$  contribute. This leads to the information dimension

$$D_1(\mu) = -\lim_{\epsilon \rightarrow 0} \frac{S_1(\mu, \epsilon)}{\ln \epsilon}. \quad (2.49)$$



Altogether, the parameter  $q$  of the generalized Rényi dimensions determines how the measure of the box  $\mu(A_i)$  is counted. For small  $q \rightarrow 0$  all contributing sets are weighted equally, while for large  $q$  only those boxes with the largest values of  $\mu(A_i)$  contribute.

Let us consider the fractal sets in maps with full escape, i.e., the chaotic saddle  $\Gamma_s$  as well as forward and backward trapped set  $\Gamma_f, \Gamma_b$ . The linearized hyperbolic dynamics on the saddle implies a local splitting into stable and unstable direction  $E^s \oplus E^u$ , as discussed in Sec. 2.2.1. Therefore the full fractal dimension of  $\Gamma_s$  decomposes into the partial fractal dimensions  $D_1^{(s),(u)}$  along stable and unstable direction [161, Sec. 6.3],

$$D_1(\Gamma_s) = D_1^{(s)}(\Gamma_s) + D_1^{(u)}(\Gamma_s). \quad (2.50)$$

Similarly, the product structure implies for  $\Gamma_f$  and  $\Gamma_b$  [67]

$$D_1(\Gamma_f) = 1 + D_1^{(u)}(\Gamma_f), \quad D_1(\Gamma_b) = D_1^{(s)}(\Gamma_b) + 1. \quad (2.51)$$

This follows from their definition, which implies that  $\Gamma_f$  and  $\Gamma_b$  are smooth along stable and unstable manifold of  $\Gamma_s$ , respectively, such that  $D_1^{(s)}(\Gamma_f) = D_1^{(u)}(\Gamma_b) = 1$ . These relations simplify further in time-reversal Hamiltonian systems, where all other partial dimensions coincide,  $D_1^{(u)}(\Gamma_f) = D_1^{(s)}(\Gamma_b) = D_1^{(s),(u)}(\Gamma_s)$  [67]. Hence, all partial dimensions are determined by the fractal dimension of the chaotic saddle  $D_1(\Gamma_s)$ , only.

The fractality of the chaotic saddle is related to the transient chaotic dynamics in systems with full escape by the Kantz–Grassberger relation [72, 161],

$$D_1^{(u)}(\Gamma_s) = 1 - \frac{\gamma_{\text{nat}}}{\lambda_L}. \quad (2.52)$$

Here, escape from the system is expressed in terms of the natural decay rate  $\gamma_{\text{nat}}$ , explained in the next section, while the chaotic motion is expressed by the typical Lyapunov exponent  $\lambda_L = \lambda_L(\Gamma_s)$  on the chaotic saddle, see 2.2.1. A generalization of this relation for systems with partial escape is given in Refs. [88, 162],

$$D_1^{(u)}(\Gamma_s) = 1 - \frac{\gamma_{\text{nat}} + \overline{\ln R}}{\lambda_L}, \quad (2.53)$$

where the average  $\overline{\ln R}$  has to be taken over the chaotic set. We apply the concepts of fractal dimension to resonance eigenfunctions and conditionally invariant measures of maps with partial escape in Sec. 4.4.2 and of maps with full escape in Sec. 5.4.2.

### 2.2.6 Conditionally invariant measures

As discussed in the context of ergodicity, we consider closed maps  $M$  for which the Lebesgue measure  $\mu_L$  is invariant,  $\tilde{\mathcal{M}}\mu_L(A) = \mu_L[M^{-1}(A)] = \mu_L(A)$  for all measurable  $A \subset \Gamma$ . This

means that  $\mu_L$  is an eigenmeasure of the operator  $\tilde{\mathcal{M}}$  with eigenvalue one. Recall that in strongly mixing maps, Eq. (2.30), the uniform measure appears as the weak limit of any smooth initial measure  $\mu$ , as  $\lim_{n \rightarrow \infty} \tilde{\mathcal{M}}^n \mu(A) = \mu_L(A)$ . Similarly the uniform measure  $\mu_s$  on the invariant set  $\Gamma_s$  is an invariant measure of the map with escape. However, this fractal measure is unstable under time evolution due to the hyperbolic nature of  $\Gamma_s$ . Taking the limit of  $\mathcal{M}^n \mu$  for any smooth initial measure does not converge towards  $\mu_s$ . Thus, a more general concept is required to describe asymptotic behavior in maps with escape.

For this purpose one generalizes the concept of invariant measures to conditionally invariant measures [71, 74]. Let  $\mathcal{M}$  be a map with escape as defined in Eq. (2.37). A measure  $\mu$  is called a conditionally invariant measure of  $\mathcal{M}$  (or c-measure), if and only if there exists  $\gamma \in \mathbb{R}$ , such that for any measurable  $A \subset \Gamma$

$$\mathcal{M}\mu(A) = e^{-\gamma} \mu(A). \quad (2.54)$$

Thus, any c-measure is an eigenmeasure of the operator  $\mathcal{M}$  with eigenvalue  $e^{-\gamma} \in \mathbb{R}_+$ . Applying the map with escape  $n$  times to a c-measure  $\mu$  one finds an exponential decay of the norm,  $\|\mathcal{M}^n \mu\| = e^{-n\gamma} \|\mu\|$ , where  $\|\mu\| := \mu(\Gamma)$ . Therefore  $\gamma$  is called the decay rate of  $\mu$ . Classically, possible values of decay rates  $\gamma$  are strictly bounded by minimal and maximal values of the reflectivity as [89]

$$-\ln \max_{\mathbf{x} \in \Gamma} \{R(\mathbf{x})\} \equiv \gamma_{\min} \leq \gamma \leq \gamma_{\max} \equiv -\ln \min_{\mathbf{x} \in \Gamma} \{R(\mathbf{x})\}. \quad (2.55)$$

This implies strictly positive decay rates  $\gamma \in \mathbb{R}_+$  for the typical case of  $R < 1$  on some phase-space regions, leading to an exponential decay of the norm of  $\mu$  under the map  $\mathcal{M}$ . Conversely, if  $R > 1$  on some phase-space regions there occurs an exponential gain [162], which is expressed here in terms of negative decay rates.

### 2.2.6.1 Natural measure

In chaotic systems with escape the sensitivity on initial conditions induces transient chaos [163]. Nevertheless it is interesting to understand the asymptotic behavior for long times, particularly the decay mechanism. It is desired to find a classical measure for maps with escape, which emerges from time evolution similar to  $\mu_L$  in closed systems [74]. In particular, the question arises, if there exists a unique measure  $\mu_{\text{nat}}$  describing the asymptotic behavior of  $\mathcal{M}^n \mu$  for any smooth initial measure  $\mu$ . In this sense, such a measure would emerge *naturally* from the time evolution and will therefore be called natural measure.

Even though in general it is not possible to prove such a statement, there are some cases for which the existence of such a unique measure is shown. For example in Anosov maps with full escape from rectangular [164] or small holes [165] such a measure exists and is supported on the backward trapped set  $\Gamma_b$ . In general, this limit is not necessarily unique [74].

For systems with partial escape, there are much less rigorous mathematical results, regarding uniqueness of the limiting measure. Thus, typically the definition of the natural measure is given in terms of the uniform distribution  $\mu_L$  in the following sense [74]. The natural measure  $\mu_{\text{nat}}$  of the map with escape  $\mathcal{M}$  is defined as the weak limit

$$\mu_{\text{nat}}(A) = \lim_{n \rightarrow \infty} \frac{\mathcal{M}^n \mu_L(A)}{\|\mathcal{M}^n \mu_L\|}, \quad (2.56)$$

for any measurable  $A \subset \Gamma$ . The decay rate  $\gamma_{\text{nat}}$  of  $\mu_{\text{nat}}$  is given by  $\gamma_{\text{nat}} = - \lim_{n \rightarrow \infty} \log \frac{\|\mathcal{M}^{n+1} \mu_L\|}{\|\mathcal{M}^n \mu_L\|}$ , and is called natural decay rate of the map  $\mathcal{M}$ . If the limit in Eq. (2.56) exists, it is easy to see, that  $\mu_{\text{nat}}$  is conditionally invariant with decay rate  $\gamma_{\text{nat}}$ . Moreover, for full escape this definition implies that the natural measure is uniform on the unstable manifold  $\Gamma_b$  of the chaotic saddle. We emphasize, however, that this manifold is not uniformly distributed on the phase space, as seen in Fig. 2.5 and Fig. 2.6, leading to a fractal measure  $\mu_{\text{nat}}$ .

There are several ways to construct the measure  $\mu_{\text{nat}}$  other than time-evolution as in Eq. (2.56). For example, in the Ulam method [166, 167] the Perron-Frobenius operator, Eq. (2.35), is discretized on a finite phase-space partition, which yields a nonnegative matrix acting on discrete density vectors. The Perron-Frobenius theorem [145] ensures that the largest eigenvalue of this matrix is positive and real, and the corresponding eigenvector is nonnegative. Thus it is interpreted as a probability density. The largest eigenvalue is related to the natural decay rate as  $e^{-\gamma_{\text{nat}}}$ , while the eigenvector corresponds to the natural measure  $\mu_{\text{nat}}$  evaluated on a finite grid.

### 2.2.6.2 Natural measure of the inverse map

The classical map with escape  $\mathcal{M}$  is invertible, if the closed map  $M$  is invertible and if the reflectivity function satisfies  $R > 0$  almost everywhere on the phase space  $\Gamma$  [162]. Such reflectivity functions arise for example in models of optical microcavities, where Fresnel's laws of transmission and reflection determine the escape at the boundary [43, 47, 48, 54, 67]. In the following we use the inverse map to identify another important classical c-measure of the map with escape  $\mathcal{M}$  and its decay rate.

The inverse  $\mathcal{M}^{-1}$  of the map with escape is given by application of the inverse closed map  $M^{-1}: \Gamma \rightarrow \Gamma$ , followed by application of the inverse reflectivity  $R^{-1} := 1/R$  [162]. The inverse  $\mathcal{M}^{-1}$  is defined as the push-forward operator of  $M^{-1}$  followed by application of the inverse reflectivity, which implies for measures  $\mu$  on  $\Gamma$

$$\mathcal{M}^{-1} \mu(A) = \int_{M(A)} R^{-1} \circ M^{-1} d\mu \quad (2.57)$$

for all measurable  $A \subset \Gamma$ . Rewriting Eq. (2.57) in terms of measurable functions  $f$  on  $\Gamma$  yields

$$\mathcal{M}^{-1}\mu(f) = \mu([R^{-1} \circ M^{-1}] \cdot [f \circ M^{-1}]). \quad (2.58)$$

In this notation it is easy to see that

$$\mathcal{M}^{-1}\mathcal{M}\mu(f) \stackrel{(2.38)}{=} \mathcal{M}^{-1}\mu(R \cdot [f \circ M]) \stackrel{(2.58)}{=} \mu([R^{-1} \circ M^{-1}] \cdot ([R \cdot f \circ M] \circ M^{-1})) \quad (2.59)$$

$$= \mu(\underbrace{[R^{-1} \circ M^{-1}] \cdot [R \circ M^{-1}]}_{=1} \cdot \underbrace{f \circ M \circ M^{-1}}_{=f}) = \mu(f) \quad (2.60)$$

for all measurable  $f$ , and similarly  $\mathcal{M}\mathcal{M}^{-1}\mu(f) = \mu(f)$ . This shows that  $\mathcal{M}^{-1}$  is indeed the inverse of  $\mathcal{M}$ .

We emphasize that Eqs. (2.57) and (2.58) are equivalent to Eqs. (2.37) and (2.38), when we replace  $M$  with  $M^{-1}$  and  $R$  with  $R^{-1} \circ M^{-1}$ . Thus the inverse map itself is a chaotic map with escape, determined by  $\mathcal{M}^{-1} = \mathcal{M}_{M^{-1}, R^{-1} \circ M^{-1}}$ . Hence, results for  $\mathcal{M}$  are similarly valid for  $\mathcal{M}^{-1}$ . It follows that there exists a natural measure of the inverse map

$$\mu_{\text{inv}} := \mu_{\text{nat}}[\mathcal{M}^{-1}], \quad (2.61)$$

which we call the inverse measure of  $\mathcal{M}$ . This measure is, according to Eq. (2.56), determined by the weak limit

$$\mu_{\text{inv}}(A) = \lim_{m \rightarrow \infty} \frac{\mathcal{M}^{-m}\mu_{\text{L}}(A)}{\|\mathcal{M}^{-m}\mu_{\text{L}}\|}, \quad (2.62)$$

for any  $A \subset \Gamma$ . The inverse measure is conditionally invariant under the inverse map  $\mathcal{M}^{-1}$  and it grows exponentially with the rate  $\gamma_{\text{nat}}[\mathcal{M}^{-1}] = -\log \lim_{n \rightarrow \infty} \frac{\|\mathcal{M}^{-(n+1)}\mu_{\text{L}}\|}{\|\mathcal{M}^{-n}\mu_{\text{L}}\|}$ . Furthermore,  $\mu_{\text{inv}}$  is conditionally invariant under the map with escape  $\mathcal{M}$  with decay rate

$$\gamma_{\text{inv}} := -\gamma_{\text{nat}}[\mathcal{M}^{-1}]. \quad (2.63)$$

For the last statement assume that  $\mu$  is a c-measure of  $\mathcal{M}^{-1}$  with decay rate  $\gamma$ , i.e.,  $\mathcal{M}^{-1}\mu(A) = e^{-\gamma}\mu(A)$  for all  $A \subset \Gamma$ , cf. Eq. (2.54). Then for all  $A \subset \Gamma$  one obtains

$$\mathcal{M}\mu(A) = \mathcal{M}[e^{\gamma}\mathcal{M}^{-1}\mu](A) = e^{-(\gamma)}\mu(A), \quad (2.64)$$

such that  $\mu$  is also a c-measure of  $\mathcal{M}$  with decay rate  $-\gamma$  and vice versa. This further implies that the natural decay rate is the inverse decay rate of the inverse map with escape,  $\gamma_{\text{nat}} = -\gamma_{\text{inv}}[\mathcal{M}^{-1}]$ . Note that natural  $\gamma_{\text{nat}}$  and inverse decay rate  $\gamma_{\text{inv}}$  of the map with escape  $\mathcal{M}$  are independent [162].

We remark that  $\mu_{\text{inv}}$  can also be obtained using the Ulam method [166,167] from a discretized

Perron-Frobenius operator of the inverse map. As discussed for the natural measure, the largest eigenvalue of this finite approximation is given by  $e^{-\gamma_{\text{nat}}[\mathcal{M}^{-1}]}$ . Thus one likes to argue, that it is also larger than the corresponding eigenvalue  $e^{-\gamma_{\text{inv}}[\mathcal{M}^{-1}]}$ , which implies  $\gamma_{\text{nat}}[\mathcal{M}^{-1}] < \gamma_{\text{inv}}[\mathcal{M}^{-1}]$  and, in general,  $\gamma_{\text{nat}} < \gamma_{\text{inv}}$ . This statement is proven in App. C.2.

### 2.2.6.3 Typical decay

Another important classical decay rate is the average decay of typical orbits. This decay rate is relevant for the distribution of quantum decay rates in the semiclassical limit [89]. Consider some phase-space point  $x \in \Gamma$  and its iterations under the map with escape. This is realized by iterating the normalized initial measure  $\delta_x$ . The weight after  $n$  iterations is given by

$$\|\mathcal{M}^n \delta_x\| = R(\mathbf{x}) \cdot R[M(\mathbf{x})] \cdot \dots \cdot R[M^{n-1}(\mathbf{x})] \|\delta_{M^n(\mathbf{x})}\| = \prod_{i=0}^{n-1} R[M^i(\mathbf{x})], \quad (2.65)$$

which follows from iterative application of Eq. (2.40). Let  $\langle \gamma \rangle_n(\mathbf{x})$  be the average decay rate after  $n$  steps for this orbit, which is defined by  $\|\mathcal{M}^n \delta_x\| = e^{-n \langle \gamma \rangle_n(\mathbf{x})}$ . It follows that

$$\langle \gamma \rangle_n(\mathbf{x}) = -\frac{1}{n} \ln \prod_{i=0}^{n-1} R[M^i(\mathbf{x})] = -\frac{1}{n} \sum_{i=0}^{n-1} \ln R[M^i(\mathbf{x})] \quad (2.66)$$

is the time average of the function  $f(\mathbf{x}) = -\ln R(\mathbf{x})$  for initial condition  $\mathbf{x}$ . For chaotic maps Birkhoffs ergodic theorem, Eq. (2.29), implies that this time average converges towards the same limit for almost all  $\mathbf{x} \in \Gamma$  and is given by the phase-space average of  $f$ ,

$$\gamma_{\text{typ}} := \lim_{n \rightarrow \infty} \langle \gamma \rangle_n(\mathbf{x}) = - \int_{\Gamma} \ln R \, d\mu_L. \quad (2.67)$$

Thus, almost everywhere on the phase space one obtains the same decay rate for single initial conditions. This might seem counterintuitive, since we just argued for the natural measure in Sec. 2.2.6.1 that almost all classical initial measures decay with the natural decay rate. However, this only holds for smooth initial measures, which corresponds to averaging over an ensemble of initial points in each iteration. Therefore, the natural decay rate behaves like  $e^{-\gamma_{\text{nat}}} \approx \int_{\Gamma} R \, d\mu_L$ , which implies  $\gamma_{\text{nat}} \approx -\ln \int_{\Gamma} R \, d\mu_L$  [67], which contrasts Eq. (2.67). Hence the difference between natural and typical decay rate lies in the nature of the considered average.

We remark that the definition of the typical decay rate  $\gamma_{\text{typ}}$  in Eq. (2.67) can also be applied to the inverse map  $\mathcal{M}^{-1}$ , where the reflectivity function is given by  $R^{-1} \circ M^{-1}$ . This implies that the typical decay rate of the inverse map equals  $\gamma_{\text{typ}}[\mathcal{M}^{-1}] = \int_{\Gamma} \ln R \, d\mu_L$ . Consequently, the typical decay rate of the inverse map is just the negative of the typical decay rate of the forward map,  $\gamma_{\text{typ}}[\mathcal{M}^{-1}] = -\gamma_{\text{typ}}$ . This expresses the fact that the average decay under

the forward map  $\mathcal{M}$  must be compensated by its inverse. Even though the typical escape plays an important role for single trajectories, a relevant conditionally invariant measure  $\mu_{\text{typ}}$  characterizing this typical decay is not found in the literature. In the outlook of Chap. 4 we claim the existence of such a measure and outline a definition based on conditionally invariant measures localizing on typical periodic orbits, introduced in Sec. 4.3.3.

#### 2.2.6.4 Conditionally invariant measures for full escape

In the limit of full escape where  $R = 1 - \mathbb{1}_\Omega$ , the structure of any conditionally invariant measure is determined by its structure on the opening  $\Omega$ , only [74]. This indicates, how c-measures with arbitrary decay rates can be constructed. Consider a probability measure  $\nu_\Omega$  supported on  $\Gamma_b \cap \Omega$  and any  $\gamma \in \mathbb{R}_+$ . For any  $\gamma \in \mathbb{R}_+$  a conditionally invariant measure  $\mu$  with decay rate  $\gamma$  is given by [60, 74]

$$\mu(A) = (1 - e^{-\gamma}) \sum_{i=0}^{\infty} e^{-i\gamma} \nu_\Omega[M^i(A)]. \quad (2.68)$$

Vice versa, any conditionally invariant measure  $\mu$  of the map with full escape  $\mathcal{M}_\Omega$  with  $\gamma < \infty$  can be decomposed accordingly by its restriction to  $\Omega$ ,  $\nu_\Omega(A) := \frac{\mu(A \cap \Omega)}{\mu(\Omega)}$ . We emphasize, that for maps with partial escape such a decomposition of conditionally invariant measures does not exist.

Furthermore, let us remark that in systems with full escape the integral on the right hand side of Eq. (2.67) diverges,

$$\gamma_{\text{typ}} = - \int_\Gamma \ln R \, d\mu_L = - \underbrace{\int_\Omega \ln R \, d\mu_L}_{=\infty} - \int_{\Gamma \setminus \Omega} \ln R \, d\mu_L = \infty, \quad (2.69)$$

such that typical orbits decay arbitrarily fast. This is consistent with the discussion in Sec. 2.2.4 that almost all phase-space points eventually escape through the opening  $\Omega$ .

# Chapter 3

## Eigenfunctions in closed maps

This chapter reviews fundamental results about the semiclassical localization of eigenfunctions in closed chaotic systems with a focus on chaotic quantum maps. In the first section we introduce the concept of quantization of maps and the phase-space distribution of quantum states. The second section reviews the semiclassical structure of eigenfunctions in closed systems, namely the semiclassical eigenfunction hypothesis and the quantum ergodicity theorem.

### 3.1 Quantization of maps

In general, there exist no unique quantization procedure for time discrete maps  $M: \Gamma \rightarrow \Gamma$  on some phase space  $\Gamma$ . The correspondence principle between quantum and classical dynamics, however, leads to certain necessary axioms of quantization, which are given for maps, e.g., in Refs. [168–170]. In the particular case of a periodic phase space,  $\Gamma = \mathbb{T}^2$ , one usually considers a series of finite dimensional Hilbert spaces  $\{\mathbb{H}_N\}_{N \in \mathbb{N}}$  with  $\mathbb{H}_N = \mathbb{C}^N$ . The dimension  $N$  of the Hilbert space corresponds to the number of Planck cells of size  $h = 1/N$ , into which the phase space  $\Gamma$  is divided. Hence, the parameter  $h$  is an effective Planck's constant in dimensionless units, which determines the semiclassical limit as  $h \rightarrow 0$  (or equivalently  $N \rightarrow \infty$ ). The quantization of a classical observable, i.e., a smooth function  $a \in C^\infty(\Gamma, \mathbb{C})$ , is given by a sequence of linear maps  $\{\text{Op}_N(a)\}_{N \in \mathbb{N}}$  acting on  $\mathbb{H}_N$ , satisfying asymptotically for  $N \rightarrow \infty$  [170]

$$\begin{aligned} \text{(a)} \quad & \text{Op}_N(\bar{a}) \sim \text{Op}_N(a)^\dagger, \\ \text{(b)} \quad & \text{Op}_N(ab) \sim \text{Op}_N(a)\text{Op}_N(b), \quad \text{and} \\ \text{(c)} \quad & \lim_{N \rightarrow \infty} \frac{1}{N} \text{tr} [\text{Op}_N(a)] = \int a \, d\mu_L. \end{aligned} \tag{3.1}$$

Here, any two sequences of operators  $\{A_N\}$  and  $\{B_N\}$  are defined to be semiclassically equivalent,  $A_N \sim B_N$ , if  $\|A_N - B_N\|_\infty \xrightarrow{N \rightarrow \infty} 0$  with the usual operator norm  $\|A_N\|_\infty = \sup_{\varphi \in \mathbb{H}_N} \frac{\|A_N \varphi\|}{\|\varphi\|}$ .

This allows to define a suitable correspondence condition for the quantization of maps as

follows. The sequence  $\{\tilde{\mathcal{U}}_N\}_{N \in \mathbb{N}}$  of unitary operators  $\tilde{\mathcal{U}}_N: \mathbb{H}_N \rightarrow \mathbb{H}_N$  quantizes the closed map  $M$ , if for any smooth observable  $a$  on  $\Gamma$  the Egorov property holds, that is

$$\tilde{\mathcal{U}}_N^\dagger \text{Op}_N(a) \tilde{\mathcal{U}}_N \sim \text{Op}_N(a \circ M). \quad (3.2)$$

This relation ensures that classical and quantum time evolution of observables commute in the semiclassical limit. Even though quantization is not unique for a given map  $M$ , it is usually possible to define a quantum propagator  $\tilde{\mathcal{U}}_N$  by taking the classical action as a generating function, see e.g., Ref. [171] and [172] Sec. 8.2. For certain systems, such as the bakers map, there are more adapted methods like geometric quantization [151, 152, 174]. In time-periodically kicked systems a quantization can be obtained by the Floquet approach [175].

### 3.1.1 Quantized standard map

The standard map is derived from a time-periodically kicked Hamiltonian, Eq. (2.31), where the kicking potential  $V(q)$  acts only at discrete times and the particle propagates freely between the kicks. The propagator for the freely moving particle is given by  $e^{-\frac{i}{2\hbar}\hat{p}^2}$ , while a full kick corresponds to  $e^{-\frac{i}{\hbar}V(\hat{q})}$  for position and momentum operators  $\hat{q}$  and  $\hat{p}$ . Considering the observation time in the middle of the kick, the Floquet propagator [175, 176] for this system is given by

$$\tilde{\mathcal{U}} = e^{-\frac{i}{2\hbar}V(\hat{q})} e^{-\frac{i}{2\hbar}\hat{p}^2} e^{-\frac{i}{2\hbar}V(\hat{q})}. \quad (3.3)$$

This operator acts on a Hilbert space corresponding to the full plane  $\mathbb{R}^2$ . In order to obtain a quantum map on the torus  $\Gamma = \mathbb{T}^2$  one applies Fourier transformation to the kinetic term  $e^{-\frac{i}{2\hbar}\hat{p}^2}$  and periodic boundary conditions in  $q$  and  $p$ , see e.g. Ref. [169]. This automatically implies discrete lattice points

$$q_k = 2\pi\hbar(k + \vartheta_p), \quad p_k = 2\pi\hbar(k + \vartheta_q), \quad k \in \mathbb{Z}, \quad (3.4)$$

with the so-called Bloch phases  $\vartheta_q, \vartheta_p$ . The number of lattice points within the interval  $[0, 1)$  determines the dimension of the Hilbert space and is given by  $N = 1/(2\pi\hbar) = 1/h$ . Moreover, periodicity further restricts the choices of  $\vartheta_q$ , which is either  $\vartheta_q = 0$  for  $N$  even, or  $\vartheta_q = 1/2$  for  $N$  odd. Throughout this thesis we always use  $\vartheta_p = 0$ . The quantized standard map on the torus follows in position representation as follows, for a detailed derivation see for example Ref. [176],

$$\langle q_n | \tilde{\mathcal{U}} | q_k \rangle = \frac{1}{N} e^{-\frac{i}{2\hbar}V(q_n)} \sum_{m=0}^{N-1} e^{\frac{i}{\hbar}p_m(q_n - q_k)} e^{-\frac{i}{2\hbar}p_m^2} e^{-\frac{i}{2\hbar}V(q_k)}. \quad (3.5)$$



### 3.1.2 Phase-space representation of quantum states

Quantum classical correspondence is often investigated on the phase space. There are different types of phase-space representations, e.g., the Wigner-representation [177], or the Glauber–Sudarshan representation [178, 179]. In this thesis we consider the so-called Husimi representation [180, 181], which has the intuitive interpretation as a phase-space density. The Husimi function  $\mathcal{H}_\psi$  of any quantum state  $\psi \in \mathbb{H}_N$  is defined by

$$\mathcal{H}_\psi(\mathbf{x}) := h^{-1} \langle \alpha_{\mathbf{x}} | \psi \rangle \langle \psi | \alpha_{\mathbf{x}} \rangle, \quad (3.6)$$

where  $\alpha_{\mathbf{x}}$  is a coherent state with minimal uncertainty  $\Delta q \Delta p = \hbar/2$  localized at the phase-space point  $\mathbf{x} = (q, p) \in \Gamma$ . We consider the simplest case of equal uncertainty in  $p$  and  $q$ , such that  $\Delta q = \Delta p = \sqrt{\hbar/2}$ . The coherent states  $\alpha_{\mathbf{x}}$  are eigenstates of the annihilation operator  $\hat{a} = \frac{1}{\sqrt{2}}(\hat{q} + i\hat{p})$ , where  $\hat{a}\alpha_{\mathbf{x}} = (q + ip)\alpha_{\mathbf{x}}$ , see, e.g., [182]. They are given in position representation on  $\mathbb{R}^2$  in dimensionless units by

$$\alpha_{\mathbf{x}}(q') = (2h)^{1/4} e^{-\frac{1}{2h}[(q-q')^2 - 2ipq']} \quad (3.7)$$

and have to be restricted to the torus phase space  $\Gamma = \mathbb{T}_2$  by application of suitable boundary conditions [182]. Note that it is also possible to consider stretched or tilted coherent states with  $\Delta p \neq \Delta q$ . The specific choice changes the resulting phase-space distributions on the scale of order  $h$ .

Based on coherent states is the anti-Wick quantization of some observable  $a : \Gamma \rightarrow \mathbb{R}$  [183],

$$\text{Op}_N^{\text{aw}}(a) := h^{-1} \int_{\Gamma} a(\mathbf{x}) |\alpha_{\mathbf{x}}\rangle \langle \alpha_{\mathbf{x}}| d\mu_L(\mathbf{x}). \quad (3.8)$$

This definition means that for all phase-space points  $\mathbf{x} \in \Gamma$  a projector on the localized coherent state  $|\alpha_{\mathbf{x}}\rangle \langle \alpha_{\mathbf{x}}|$  is considered, which is weighted with the value of the observable in  $\mathbf{x}$ . Recall that the quantization of observables is not unique and needs to satisfy certain asymptotic conditions, see Eq. (3.1). Due to the close relation to coherent states, we only consider the Anti-Wick quantization in this thesis. In particular, the expectation value of the observable  $a$  in some quantum state  $\psi \in \mathbb{H}_N$ ,

$$\mathbb{E}_\psi[a] := \langle \psi | \text{Op}_N(a) | \psi \rangle, \quad (3.9)$$

is for the anti-Wick quantization directly related to the Husimi distribution  $\mathcal{H}_\psi$  as

$$\mathbb{E}_\psi[a] = h^{-1} \int_{\Gamma} a(\mathbf{x}) \langle \psi | \alpha_{\mathbf{x}} \rangle \langle \alpha_{\mathbf{x}} | \psi \rangle d\mu_L(\mathbf{x}) = \int_{\Gamma} a(\mathbf{x}) \mathcal{H}_\psi(\mathbf{x}) d\mu_L(\mathbf{x}). \quad (3.10)$$

This further illustrates that the Husimi distribution is a density on the phase space  $\Gamma$ , which

implies for each  $\psi \in \mathbb{H}_N$  the Husimi measure

$$\mu_\psi(A) := \int_A \mathcal{H}_\psi(\mathbf{x}) \, d\mu_L(\mathbf{x}). \quad (3.11)$$

Altogether, the Husimi phase-space representation is a versatile tool to investigate the structure of eigenfunctions in terms of expectation values of classical observables.

## 3.2 Structure of eigenfunctions

In this section we review the main results for the localization of eigenfunctions of closed quantum maps, which are the semiclassical eigenfunction hypothesis [5–7, 184, 185] and the quantum ergodicity theorem [8–15]. Both are based on the correspondence principle between quantum and classical time evolution. These fundamental statements specify the semiclassical phase-space structure of eigenfunctions in terms of the set of semiclassical limit measures.

A semiclassical limit measure is defined as follows. Consider a quantization  $\{\tilde{\mathcal{U}}_N\}_{N \in \mathbb{N}}$  of a classical map  $M: \Gamma \rightarrow \Gamma$  acting on the Hilbert space  $\mathbb{H}_N$  and let  $\mathcal{E}_N$  be the set of eigenfunctions of  $\tilde{\mathcal{U}}_N$ . A classical measure  $\mu$  on the phase space  $\Gamma$  is called semiclassical limit measure of the quantum map, if there exists a sequence of eigenfunctions  $\{\psi_N\}_{N \in \mathbb{N}}$  of  $\tilde{\mathcal{U}}_N$  such that the expectation values  $\mathbb{E}_\psi[a]$  of any smooth observable  $a: \Gamma \rightarrow \mathbb{R}$  converge towards the classical expectation value  $\mu(a)$ ,

$$\langle \psi_N | \text{Op}_N(a) | \psi_N \rangle \xrightarrow{N \rightarrow \infty} \mu(a) = \int_\Gamma a \, d\mu. \quad (3.12)$$

### 3.2.1 Semiclassical eigenfunction hypothesis

The semiclassical eigenfunction hypothesis [5–7, 184, 185] relates the structure of resonance eigenfunctions to classical invariant sets. It is formulated in Ref. [7] as follows: *Each semiclassical eigenstate has a Wigner function concentrated on the region explored by a typical orbit over infinite times.* The Wigner function of some quantum state  $\psi$  on a two-dimensional phase space is defined as the Fourier transformation of the product of  $\psi$  and its complex conjugate  $\psi^*$  in position representation, separated by the distance  $Q$  [177],

$$\mathcal{W}_\psi(q, p) = \frac{1}{2\pi\hbar} \int dQ \, e^{-ipQ/\hbar} \psi^*(q - Q/2) \psi(q + Q/2). \quad (3.13)$$

The Wigner function can become negative and is thus a quasi probability density. A convolution of the Wigner function with a Gaussian distribution in  $q$  and  $p$  with standard deviations  $\sigma_q \sigma_p \geq \hbar/2$ , however, always yields a non-negative distribution [186]. If the width of the Gaussian is minimal with respect to the uncertainty principle and symmetric in  $p$  and  $q$ ,  $\sigma_p = \sigma_q = \sqrt{\hbar/2}$ , the usual Husimi phase-space distribution for symmetric coherent states is

recovered,  $\mathcal{H}_\psi(q, p) = \iint dq' dp' (h/2) \exp \left[ -\frac{(p-p')^2}{h} - \frac{(q-q')^2}{h} \right] \mathcal{W}_\psi(q', p')$ .

The semiclassical eigenfunction hypothesis leads to a distinction between regular and chaotic eigenfunctions. Regular eigenfunctions are concentrated on regular tori  $C_m$ , which satisfy a quantization condition of the action [7],  $I_m = \frac{1}{2\pi} \oint_{C_m} p \cdot dq = (m + \frac{\alpha}{4})\hbar$ , where  $\alpha$  is the Maslov index of the torus [187]. The semiclassical Wigner function of such a regular eigenfunction is given by [5, 184]

$$\mathcal{W}_m(q, p) \approx \frac{1}{2\pi} \delta[I(q, p) - I_m], \quad (3.14)$$

where  $I(q, p)$  is the action of the regular torus at  $(q, p)$ . The  $\delta$ -function restricts the Wigner function to the classical torus with action  $I_m$ , which is typically explored by classical orbits over infinite times [7]. In contrast, in chaotic and thus ergodic systems classical orbits usually explore complete surfaces of fixed energy determined by the Hamilton function,  $H(q, p) = E$ . For chaotic eigenfunctions the semiclassical Wigner function of an eigenfunction with energy  $E$  is given by [5, 6]

$$\mathcal{W}(q, p) \approx \frac{\delta[E - H(q, p)]}{\iint dq dp \delta[E - H(q, p)]}, \quad (3.15)$$

which is a uniform distribution on the energy shell.

In systems with a mixed phase space there exist both regular and chaotic motion. This implies usually a set of regular eigenfunctions concentrated on the regular tori of the system, and a set of chaotic eigenfunctions spread over the ergodic component of the system. In both cases, the Wigner functions localize on classical phase-space regions that are invariant under the closed map  $M$ . Thus, the eigenfunction hypothesis implies that any semiclassical limit measure  $\mu$  must be invariant under  $M$ , and that any two different of these measures localize on dynamically independent regions on  $\Gamma$ .

This is illustrated for the quantized standard map, Eq. (3.5), for  $\kappa = 2.5$  in Fig. 3.1. The classical phase space at  $\kappa = 2.5$  inherits regular and chaotic motion as illustrated in (a). The bottom panel shows a single orbit that is trapped around the regular island chain of period four. The Husimi distributions of four considered eigenfunctions for  $h = 1/1000$  are shown in (b). The first two panels show regular eigenfunctions, concentrated on classical tori highlighted in (a). The chaotic eigenfunction in the third panel localizes on the ergodic component of the classical phase space with fluctuations on the scale of order  $h$ . In the fourth panel we show an eigenfunction localizing on the boundary between regular and chaotic region, which reminds of classically trapped orbits, see bottom panel in (a). Similar Husimi distributions as in (b) are shown in (c) for  $h = 1/16000$ . As predicted by the semiclassical eigenfunction hypothesis, the regular eigenfunctions are much more concentrated on a single torus while the chaotic eigenfunction spreads uniformly over the chaotic region. Note that one always expects

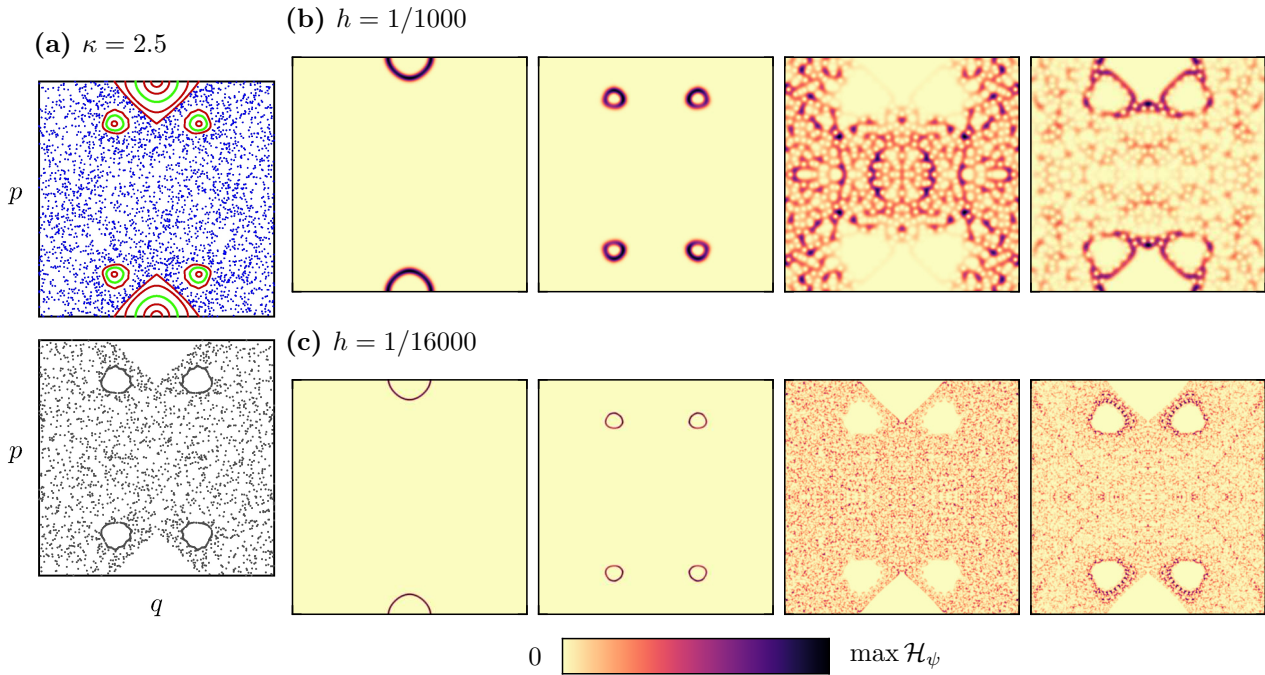


**Figure 3.1:** Semiclassical eigenfunction hypothesis for mixed phase space  $\Gamma$ . (a) Classical phase-space portrait of standard map with  $\kappa = 2.5$ . The bottom panel shows a single trajectory, which is trapped around the island chain of period four. (b) Husimi distribution  $\mathcal{H}_\psi$  of eigenfunction  $\psi$  of the quantized standard map for  $h = 1/1000$ . Shown are two regular eigenfunctions, a chaotic eigenfunction, and a trapped eigenfunction (from left to right). The regular eigenfunctions localize on classical tori highlighted in top panel of (a). (c) Same as (b) for  $h = 1/16000$ . The maximum of the colormap is taken for each  $\mathcal{H}_\psi$  individually in (b) and (c), as indicated by the colorbar below.

trapped eigenfunctions at the boundary between regular islands and chaotic sea, even though their relative number decreases for larger  $N$ .

### 3.2.2 Quantum ergodicity theorem

The uniform distribution of chaotic eigenfunctions is rigorously proven for specific systems with ergodic dynamics in terms of the quantum ergodicity theorem [8–15], which applies to eigenfunctions of the Laplacian on compact hyperbolic surfaces [9, 10], to ergodic billiards [11], and to arbitrary smooth ergodic maps on the torus [12].

The quantum ergodicity theorem for ergodic maps is formulated as follows [13, 15]. Let  $\{\tilde{\mathcal{U}}_N\}_{N \in \mathbb{N}}$  be a quantization of the classical map  $M: \Gamma \rightarrow \Gamma$  acting on the Hilbert space  $\mathbb{H}_N$ , and let  $M$  be ergodic with respect to the uniform Lebesgue measure  $\mu_L$ . Let  $\mathcal{E}_N$  denote the set of eigenfunctions of  $\tilde{\mathcal{U}}_N$  for each  $N \in \mathbb{N}$ . Then, the semiclassical limit measure of almost any subsequence  $\{\psi_N\}_{N \in \mathbb{N}}$  of eigenfunctions  $\psi_N \in \mathcal{E}_N$  is given by the Lebesgue measure  $\mu_L$ . In other words, there exist subsets  $\mathcal{E}'_N \subset \mathcal{E}_N$  of eigenfunctions, satisfying  $\lim_{N \rightarrow \infty} \frac{|\mathcal{E}'_N|}{|\mathcal{E}_N|} = 1$ , such

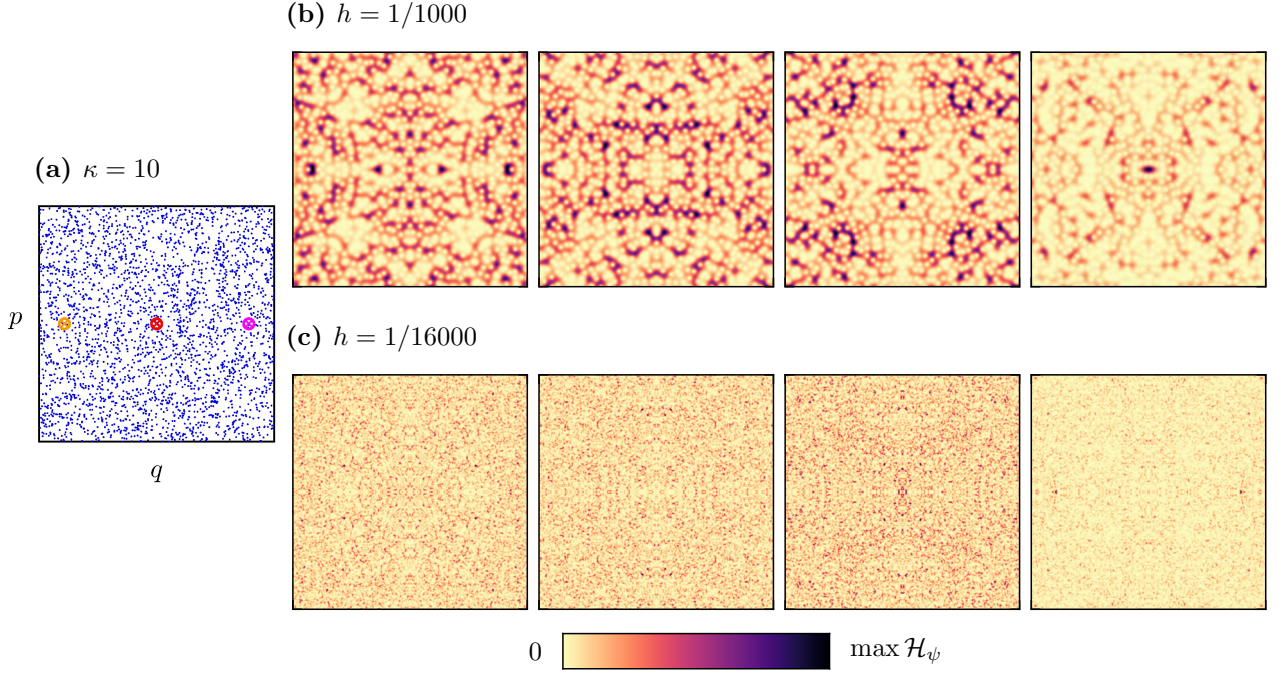


**Figure 3.2:** Quantum ergodicity for chaotic map. (a) Typical trajectory of the chaotic standard map with  $\kappa = 10$  on the phase space (blue). Colored markers indicate three different classical fixed points  $(q^*, p^*)$ . (b) Husimi distribution  $\mathcal{H}_\psi$  of chaotic eigenfunctions  $\psi$  of quantized standard map for  $h = 1/1000$ . The last panel shows an eigenfunction that is enhanced on the fixed point  $(q^*, p^*) = (0.5, 0.5)$ , see red marker in (a). (c) Same as (b) for  $h = 1/16000$ . The eigenfunction in the last panel is enhanced on two fixed points of  $M$ , see pink and orange marker in (a).

that for any smooth observable  $a$

$$\langle \psi'_N | \text{Op}_N(a) | \psi'_N \rangle \xrightarrow{N \rightarrow \infty} \mu_L(a) = \int_{\Gamma} a \, d\mu_L, \quad (3.16)$$

where  $\{\psi'_N\}_{N \in \mathbb{N}}$  is any sequence of eigenfunctions with  $\psi'_N \in \mathcal{E}'_N$ .

In consequence, the only relevant semiclassical limit measure for chaotic maps is the uniform distribution  $\mu_L$ . Furthermore, Eq. (3.16) implies that the Husimi densities  $\mathcal{H}_{\psi'_N}$  of the eigenfunctions  $\psi'_N$  converge in a weak sense towards the uniform measure, i.e., the Husimi measure defined in Eq. (3.11) satisfies  $\mu_{\psi'_N}(A) \xrightarrow{N \rightarrow \infty} \mu_L(A)$  for all measurable  $A \subset \Gamma$ . We emphasize that such a convergence does not hold point-wise,  $\mathcal{H}_{\psi'_N}(q, p) \not\rightarrow 1$ , since the Husimi distribution fluctuates on scales of order  $h$ .

Figure 3.2 illustrates Husimi distributions  $\mathcal{H}_\psi$  of eigenfunctions  $\psi$  of the chaotic standard map for  $\kappa = 10$  and Planck's constant  $h \in \{1/1000, 1/16000\}$ . The classical phase space is shown in (a) with a typical orbit. In addition, three fixed points of the standard map, Eq. (2.32), are highlighted. In (b) and (c) we show for both values of  $h$  three chaotic eigenfunctions, that cover the phase space uniformly, and one exceptional eigenfunction, which is enhanced on periodic orbits. We observe that individual Husimi distributions of chaotic eigen-

functions always fluctuate on scales of order  $h$  illustrating why the convergence in Eq. (3.16) only holds on average, e.g., over some phase-space region  $A \subset \Gamma$ .

Semiclassical convergence in ergodic systems is investigated often using the distribution of quantum expectation values  $\mathbb{E}_\psi[a]$  of some observable  $a$  at finite  $h = 1/N$  around the classical expectation value  $\mu_L(a)$  [14, 188–190]. Quantum ergodicity is expressed in the convergence of the sums

$$S_k(N, a) = \frac{1}{N} \sum_{\psi \in \mathcal{E}_N} \left| \mathbb{E}_\psi[a] - \mu_L(a) \right|^k \xrightarrow{N \rightarrow \infty} 0 \quad (3.17)$$

for  $k \geq 1$ . Note that convergence of Eq. (3.17) for  $k = 1$  is equivalent to the quantum ergodicity theorem Eq. (3.16), which follows from Ref. [145] Theorem 1.20. The rate of quantum ergodicity is defined as the asymptotic scaling  $S_k \sim N^{\kappa_k} = h^{-\kappa_k}$  for  $N \rightarrow \infty$ . This has been investigated in particular for the second moment  $S_2(N, a)$ , relating it to classical autocorrelation functions [191]. Note that the second moment has a similar form to the variance of the distribution of  $\mathbb{E}_\psi[a]_N$  around the mean value  $\mu(a)$ , which is evaluated for a finite sample of size  $N$ . In this sense  $S_2(N, a) \approx \text{Var}(a_N)$ . In chaotic maps one usually expects and observes an asymptotic scaling of  $S_1 \sim N^{-1/2} = h^{1/2}$  and  $S_2 \sim N^{-1} = h$  [182], which is the same as for random matrices [192].

# Chapter 4

## Resonance eigenfunctions in maps with partial escape

In this chapter we investigate the phase-space structure of resonance eigenfunctions in systems with partial escape. This chapter is divided in four main sections. In the first section the quantization of maps with partial escape is reviewed and resonance eigenvalues of the considered example system are discussed. In the second section, Sec. 4.2, we analyze resonance eigenfunctions of the quantum system. Therefore we present numerical support for the convergence of resonance eigenfunctions to fractal phase-space structures. We briefly discuss their fluctuations around the quantum average. We further derive a semiclassical expression for expectation values of specific phase-space functions generalizing the results of Ref. [59]. Finally we prove that semiclassical limit measures for quantum maps with partial escape must be conditionally invariant, generalizing the results of Ref. [60]. Section 4.3 deals with conditional invariant measures of the classical map with partial escape. First we present a well-known construction of the natural measure and the inverse measure. Based on this construction, we introduce a family of conditionally invariant measures for arbitrary decay rates in systems with partial escape. We also derive another class of conditionally invariant measures for partial escape which are based on periodic orbits. The fourth section is used to compare resonance eigenfunctions and classical product measures. We first compare their phase-space distributions qualitatively on the phase space. Secondly we analyze their effective fractal dimensions. We further apply the Jensen–Shannon divergence as a quantitative distance between resonance eigenfunctions and classical measures. Finally, we investigate the dependence on the reflectivity of the system, by going from an almost closed system to a system with almost full escape. The results of this chapter have been published in Ref. [97].

### 4.1 Quantization of maps with partial escape

In systems with partial escape the classical time evolution is given by application of some reflectivity function  $R: \Gamma \rightarrow \mathbb{R}_+$  followed by the closed map  $M$  as introduced in Sec. 2.2.3.

The classical maps with escape considered in this thesis are as a map  $\mathcal{M}$  of measures  $\mu$  in Eq. (2.38) which usually leads to a loss of probability. Hence, the correspondence principle between quantum and classical maps with escape is slightly different from the Egorov property for closed maps, Eq. (3.2).

### 4.1.1 Correspondence principle for partial escape

In analogy to Ref. [60, Axiom 2] the following correspondence principle is required for maps with escape. Let  $\mathcal{M}$  be a classical map with escape for the closed map  $M$  with reflectivity function  $R$ . The sequence  $\{\mathcal{U}_N\}_{N \in \mathbb{N}}$  of linear operators  $\mathcal{U}_N: \mathbb{H}_N \rightarrow \mathbb{H}_N$  quantizes the map with escape  $\mathcal{M}$ , if for any smooth observable  $a: \Gamma \rightarrow \mathbb{R}$  classical and quantum time-evolution are equivalent in the limit  $N \rightarrow \infty$ ,

$$\mathcal{U}_N^\dagger \text{Op}_N(a) \mathcal{U}_N \sim \text{Op}_N(R \cdot (a \circ M)). \quad (4.1)$$

Note that if the map  $M$  is discontinuous on  $\Gamma$  it is additionally required that  $a$  is compactly supported on the set  $C(M^{-1})$  where  $M^{-1}$  is continuous, i.e.,  $a \in C_c^\infty(C(M^{-1}))$  [60]. In contrast to the Egorov property for closed maps, Eq (3.2), the propagator  $\mathcal{U}_N$  appearing on the left hand side of Eq. (4.1) is not unitary,  $\mathcal{U}_N^\dagger \neq \mathcal{U}_N$ . Moreover, the observable on the right hand side in Eq. (4.1) corresponds to the time-evolved observable  $a$  under the map with escape  $\mathcal{M}$  according to Eq. (2.38). Hence, Eq. (4.1) ensures that classical and quantum time-evolution of observables commute in the semiclassical limit.

Let  $\{\tilde{\mathcal{U}}_N\}_{N \in \mathbb{N}}$  be a quantization of the closed map  $M$  and consider the quantization of the reflectivity operator

$$\mathcal{R}_N := \text{Op}_N(R^{1/2}), \quad (4.2)$$

which can be chosen to be hermitian,  $\mathcal{R}_N^\dagger = \mathcal{R}_N$ , for real valued reflectivity functions  $R$ . The Egorov property for closed maps, Eq (3.2), and the quantization condition for observables, Eq. (3.1), imply that Eq. (4.1) holds for quantum maps with escape as considered in Sec. 2.1.4,  $\mathcal{U}_N = \tilde{\mathcal{U}} \cdot \mathcal{R}_N$ , since for  $N \rightarrow \infty$

$$\mathcal{U}_N^\dagger \text{Op}_N(a) \mathcal{U}_N = \mathcal{R}_N^\dagger \tilde{\mathcal{U}}_N^\dagger \text{Op}_N(a) \tilde{\mathcal{U}}_N \mathcal{R}_N \quad (4.3)$$

$$\stackrel{\text{Eq. (3.2)}}{\sim} \text{Op}_N(R^{1/2}) \text{Op}_N(a \circ M) \text{Op}_N(R^{1/2}) \quad (4.4)$$

$$\stackrel{\text{Eq. (3.1)(b)}}{\sim} \text{Op}_N(R^{1/2} \cdot a \circ M \cdot R^{1/2}) = \text{Op}_N(R \cdot (a \circ M)). \quad (4.5)$$

Hence, any closed quantization gives rise to a quantization for partial escape when the reflectivity operator is suitably chosen.

Furthermore it is desirable to achieve the usual Egorov property for the map with escape,



when the inverse time evolution is considered instead of the hermitian conjugate. Therefore assume that  $R > 0$  is strictly positive, such that  $R^{-1}$  is defined on  $\Gamma$ . The second quantization condition for observables, Eq. (3.1)(b), implies that  $\text{Op}_N(R^{1/2})\text{Op}_N(R^{-1/2}) \sim \text{Op}_N(1) = \mathbb{1}_N$ , such that asymptotically  $\mathcal{R}_N^{-1} = [\text{Op}_N(R^{1/2})]^{-1} \sim \text{Op}_N(R^{-1/2})$ . Altogether we consistently obtain with  $\mathcal{U}_N^{-1} = \mathcal{R}_N^{-1}\tilde{\mathcal{U}}_N^{-1}$  the asymptotic relation

$$\mathcal{U}_N^{-1} \text{Op}_N(a) \mathcal{U}_N \sim \text{Op}_N(a \circ M), \quad (4.6)$$

for  $N \rightarrow \infty$ , which follows similar to Eqs. (4.3)–(4.5). In the following we omit the suffix  $N$  whenever suitable.

### 4.1.2 Resonances in maps with partial escape

In contrast to closed chaotic systems the propagator  $\mathcal{U}$  of the quantum map with escape is in general subunitary for  $R \leq 1$ , as discussed in Sec. 2.1.4. Recall that the eigenvalue equation,  $\mathcal{U}\psi = \lambda\psi$ , see Eq. (2.16), leads to eigenvalues  $\lambda = e^{-i\theta - \gamma/2}$  with modulus less than one. Therefore the decay rates  $\gamma$  are all positive. In this section we investigate these eigenvalues for the chaotic standard map with partial escape. We consider kicking strength  $\kappa = 10$  and escape from a leaky region  $\Omega \subset \Gamma$  in terms of the reflectivity function

$$R(q, p) = 1 - (1 - R_\Omega)\mathbb{1}_\Omega(q, p) = \begin{cases} R_\Omega & (q, p) \in \Omega \\ 1 & \text{else,} \end{cases} \quad (4.7)$$

choosing a strip parallel to the  $p$ -direction,  $\Omega = (0.3, 0.6) \times [0, 1)$ . The parameter  $R_\Omega$  controls the amount of escape from  $\Omega$ . If not stated otherwise, in the following we consider the reflectivity parameter  $R_\Omega = 0.2$ , which is considered 'far' from the closed limit ( $R_\Omega = 1$ ) and 'far' from the limit of full escape ( $R_\Omega = 0$ ).

We illustrate eigenvalues of the standard map with escape in the  $\theta$ - $\gamma$  plane for different values of effective Planck's constant  $h \in \{1/250, 1/1000, 1/4000, 1/16000\}$  in Fig. 4.1, where the dimension of the corresponding Hilbert space is  $N = 1/h$ . The horizontal lines indicate the classical natural decay rates of forward and inverse map,  $\gamma_{\text{nat}}$  (red) and  $\gamma_{\text{inv}}$  (green), and the typical decay rate  $\gamma_{\text{typ}}$  (blue). This representation resembles the spectra of chaotic optical microcavities in the complex frequency plane [48], where  $\theta$  is identified as the energy and  $\gamma$  corresponds to the width of the resonance, see also discussion in Sec. 2.1. We make two remarkable observations. First, almost all of the resonances fall into a relatively narrow band of decay rates,  $\gamma_{\text{nat}} \lesssim \gamma \lesssim \gamma_{\text{inv}}$ , where  $\gamma_{\text{nat}}$  and  $\gamma_{\text{inv}}$  are the natural decay rates of forward and inverse map, see Sec. 2.2.6. Let us remark that there also exists a strict spectral gap related to the topological pressure of the classical chaotic map [89, 126], where no quantum resonances are found in classically allowed regions [91, 193]. However, the relative number of

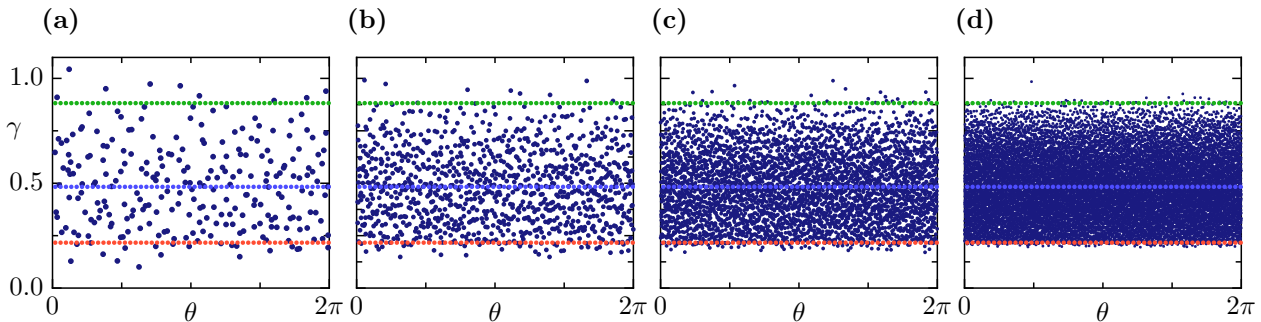


**Figure 4.1:** Eigenvalues of the chaotic standard map with partial escape for  $R_\Omega = 0.2$  and  $\Omega = (0.3, 0.6) \times [0, 1)$ . Shown is the spectrum of  $\mathcal{U}$  in  $\theta$ - $\gamma$  plane for (a)  $h = 1/250$ , (b)  $h = 1000$  (c)  $h = 4000$ , and (d)  $h = 16000$ . Horizontal lines indicate classical decay rates  $\gamma_{\text{nat}} \approx 0.22$  (red),  $\gamma_{\text{typ}} \approx 0.48$  (blue), and  $\gamma_{\text{inv}} \approx 0.88$  (green).

supersharp resonances with  $\gamma < \gamma_{\text{nat}}$  goes to zero for  $h \rightarrow 0$  and they are unlikely to be found far from  $\gamma_{\text{nat}}$  [194]. Since the same can be expected for resonances with  $\gamma > \gamma_{\text{inv}}$ , we expect semiclassically almost all decay rates in the range  $\gamma_{\text{nat}} \leq \gamma \leq \gamma_{\text{inv}}$ . We secondly observe no gaps within the interval  $[\gamma_{\text{nat}}, \gamma_{\text{inv}}]$ . Hence we expect that the spectrum  $\sigma(\mathcal{U})$  becomes dense on this interval in the semiclassical limit, even though the distribution visibly depends on  $\gamma$ .

We reveal the distribution of the decay rates by illustrating the probability  $P(\gamma)$  in Fig. 4.2 for the same values of  $h$  as before. This distribution is clearly not uniform. The probability at  $\gamma_{\text{nat}}$  is significantly larger than at  $\gamma_{\text{inv}}$ . For decreasing values of  $h$  the histogram develops a maximum close to  $\gamma_{\text{typ}}$ . We also confirm that for (a)  $h = 1/250$  and (b)  $h = 1/1000$  there is a significantly larger probability to find exceptional resonances with  $\gamma < \gamma_{\text{nat}}$  and  $\gamma > \gamma_{\text{inv}}$  than for (d)  $h = 1/16000$ . We additionally investigate the distribution of the spectrum with respect to the angle  $\theta$  and observe that  $P(\theta)$  becomes uniformly distributed for small  $h$ , shown in App. B.1.

These observations are consistent with the results of Refs [89, 195] that in the semiclassical

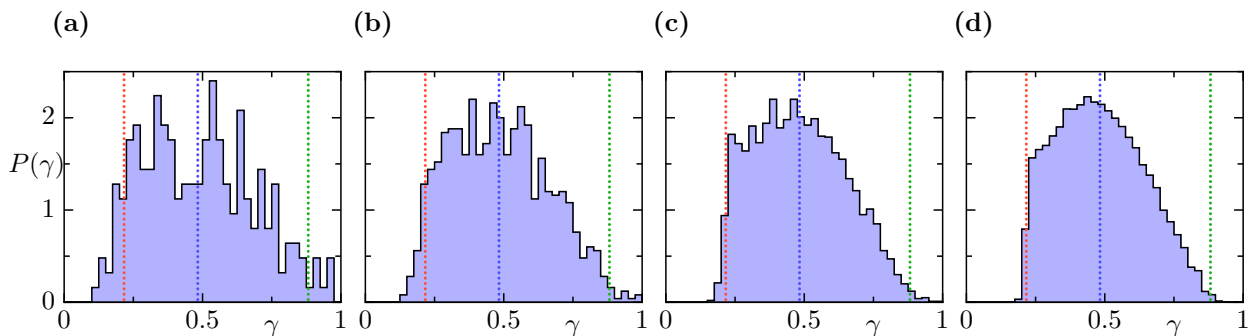


**Figure 4.2:** Distribution of decay rates  $\gamma$  for the chaotic standard map with partial escape for  $R_\Omega = 0.2$ . Shown is the normalized probability  $P(\gamma)$  to find the decay rate  $\gamma$  for (a)  $h = 1/250$ , (b)  $h = 1/1000$  (c)  $h = 1/4000$ , and (d)  $h = 1/16000$ . Vertical lines indicate classical decay rates  $\gamma_{\text{nat}} \approx 0.22$  (red),  $\gamma_{\text{typ}} \approx 0.48$  (blue), and  $\gamma_{\text{inv}} \approx 0.88$  (green).

limit almost all resonance eigenfunctions have decay rate  $\gamma = \gamma_{\text{typ}}$ , even though the emerging peak is not very prominent. The slow convergence has already been noted in Ref. [89], and the uniform distribution with respect to  $\theta$  has been proven for decay rates close to  $\gamma_{\text{typ}}$  in Ref. [195]. We remark that the shape of the probability distribution at the edges  $\gamma_{\text{nat}}$  and  $\gamma_{\text{inv}}$  is understood in the context of open quantum graphs [91]. Moreover, the distribution of decay rates at the lower edge  $\gamma_{\text{nat}}$  is related to multifractal properties of the natural measure  $\mu_{\text{nat}}$  [92].

We additionally show the spectra for two other choices of  $R_\Omega$  in Figs. 4.3 and 4.4. When less escape from  $\Omega$  is considered,  $R_\Omega = 0.8$ , the resonances concentrate on a band which is narrower than before, see Fig. 4.3. Note that here  $\gamma_{\text{nat}}$  and  $\gamma_{\text{inv}}$  are much smaller and closer to each other. There are also significantly more exceptionally small and large resonances outside of the interval  $[\gamma_{\text{nat}}, \gamma_{\text{inv}}]$ , which is seen for example at  $h = 1/1000$  comparing Fig. 4.3(a) to Fig. 4.1(b). The corresponding distribution of decay rates is almost symmetric around  $\gamma_{\text{typ}}$ , see Fig. 4.3(c,d).

In contrast, for more escape,  $R_\Omega = 0.05$ , the spectrum is much broader than before, see

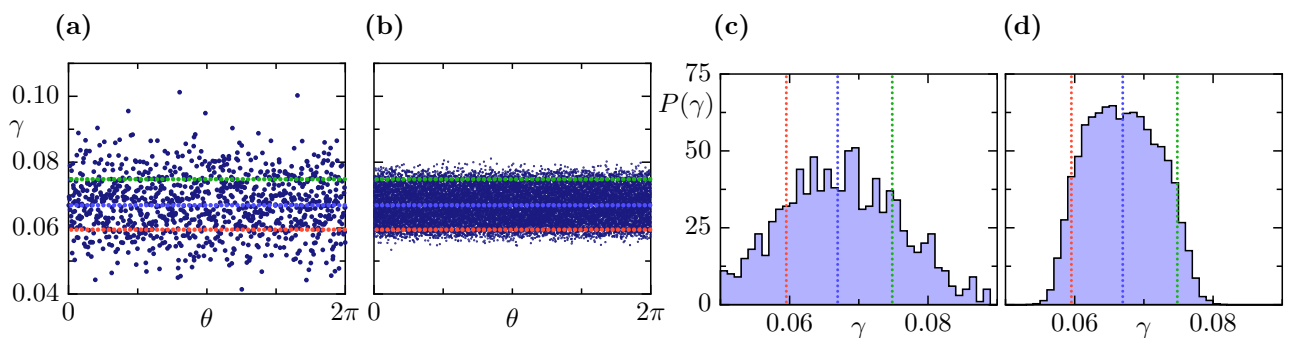


**Figure 4.3:** Eigenvalues and distribution of decay rates for the chaotic standard map with partial escape for  $R_\Omega = 0.8$ . Shown is the spectrum for (a)  $h = 1/1000$ , and (b)  $h = 1/16000$  as in Fig. 4.1. Probability distribution  $P(\gamma)$  is shown in (c) and (d) for the same  $h$ , respectively. Horizontal (a,b) and vertical (c,d) lines indicate classical decay rates  $\gamma_{\text{nat}} \approx 0.060$ ,  $\gamma_{\text{typ}} \approx 0.063$ , and  $\gamma_{\text{inv}} \approx 0.075$ .

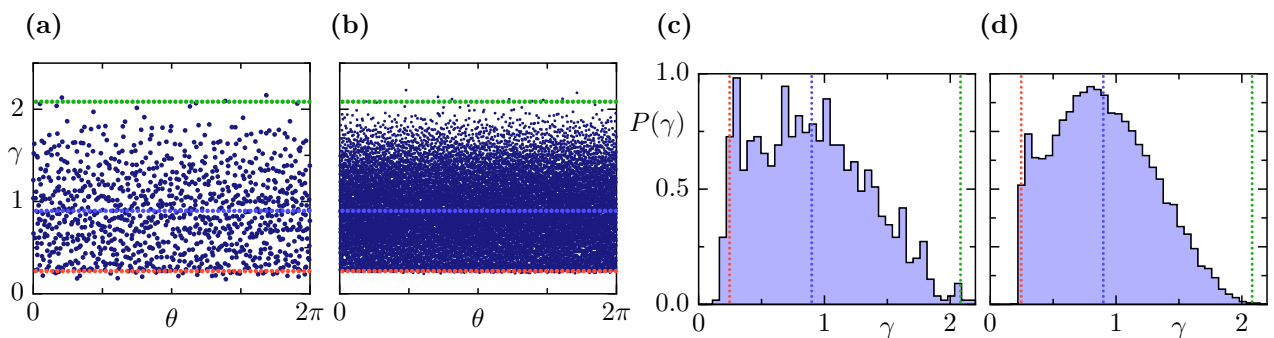


**Figure 4.4:** Eigenvalues and distribution of decay rates for the chaotic standard map with partial escape for  $R_\Omega = 0.05$  as in Fig. 4.3. Horizontal (a,b) and vertical (c,d) lines indicate classical decay rates  $\gamma_{\text{nat}} \approx 0.25$ ,  $\gamma_{\text{typ}} \approx 0.90$ , and  $\gamma_{\text{inv}} \approx 2.1$  (red, blue, green).

Fig. 4.4. We notice that here  $\gamma_{\text{inv}}$  is larger than for  $R_\Omega = 0.2$ , but  $\gamma_{\text{nat}}$  is of the same order. The number of resonances close to  $\gamma_{\text{inv}}$  is significantly smaller than before, such that this region is sparsely filled even for  $h = 1/16000$  (b). The distribution of decay rates is again peaked around  $\gamma_{\text{typ}}$ , but there is also a small peak at  $\gamma_{\text{nat}}$ , see Fig. 4.4(c,d). In contrast, close to the inverse decay rate the probability to find resonances is almost zero.

We conclude that the quantum mechanically relevant region of decay rates is the interval between the classical decay rates  $\gamma_{\text{nat}}$  and  $\gamma_{\text{inv}}$ . The phase-space distribution of the corresponding resonance eigenfunctions are investigated in the following section. For an investigation of the spectrum of quantum maps in the limit of full escape we refer to Sec. 5.1.2 in the next chapter.

## 4.2 Phase-space distribution of resonance eigenfunctions

In this section we investigate resonance eigenfunctions for systems with partial escape on the phase space. The objective is to answer the following questions: Is there convergence of resonance eigenfunctions to one semiclassical limit measures? Is it meaningful to average over eigenfunctions in order to reveal their underlying structure?

### 4.2.1 Single resonance eigenfunctions

For this purpose we first illustrate Husimi distributions  $\mathcal{H}_\psi$ , defined in Eq. (3.6), of single resonance eigenfunctions  $\psi$  with increasing decay rates closest to  $\gamma \in \{\gamma_{\text{nat}} \approx 0.22, 0.35, \gamma_{\text{typ}} \approx 0.48, 0.75, \gamma_{\text{inv}} \approx 0.88\}$  in Fig. 4.5. The decay rate increases from left to right as indicated. The top row, Fig. 4.5 (a), shows results for  $h = 1/250$ . There are two immanent observations. First, the resonance eigenfunctions are not uniformly distributed. Secondly, their distribution depends on the decay rate  $\gamma$ , which is seen as a qualitative change of the regions with large probability between  $\gamma_{\text{nat}}$  and  $\gamma_{\text{inv}}$ . We decrease Planck's constant to  $h = 1/1000$  in Fig. 4.5 (b) confirming both observations. There additionally emerge finer patterns in the phase-space structure for all  $\gamma$ . Further decreasing  $h$  in Fig. 4.5 (c) and (d) to  $h = 1/4000$  and  $h = 1/16000$  reveals that the Husimi distributions resolves filamentary structures always on scales of order  $h$ . This reminds of the behavior of classical fractals. For small  $h$  the dependence on the decay rate  $\gamma$  is clearly visible, indicating its persistence in the semiclassical limit.

This already leads to the conclusion, that the decay rate  $\gamma$  is one relevant parameter for the semiclassical phase-space structure. Hence, if resonance eigenfunctions converge to classical measures, these measures must depend on the limiting decay rate  $\gamma$ . For any  $\gamma \in [\gamma_{\text{nat}}, \gamma_{\text{inv}}]$  there are, however, many eigenfunctions with decay rates close to  $\gamma$ , which is seen in the spectra, see Fig. 4.1. Thus it is necessary to examine, if the phase-space structure is the same for all those eigenfunctions. We emphasize that this can at most be expected to hold semiclassically and in a weak sense, only. Comparing the phase-space distribution of single

resonance eigenfunctions with almost the same decay rate is therefore not conclusive, as is shown in Fig. 4.6. Here, the five resonance eigenfunctions with decay rates  $\gamma$  closest to  $\gamma_{\text{typ}}$  for  $h = 1/1000$  are presented. They show strong fluctuations on the scale of  $h$ . Therefore such a qualitative comparison is not sufficient to confirm (or to rule out) the same semiclassical limit measure for the same decay rate  $\gamma$ .

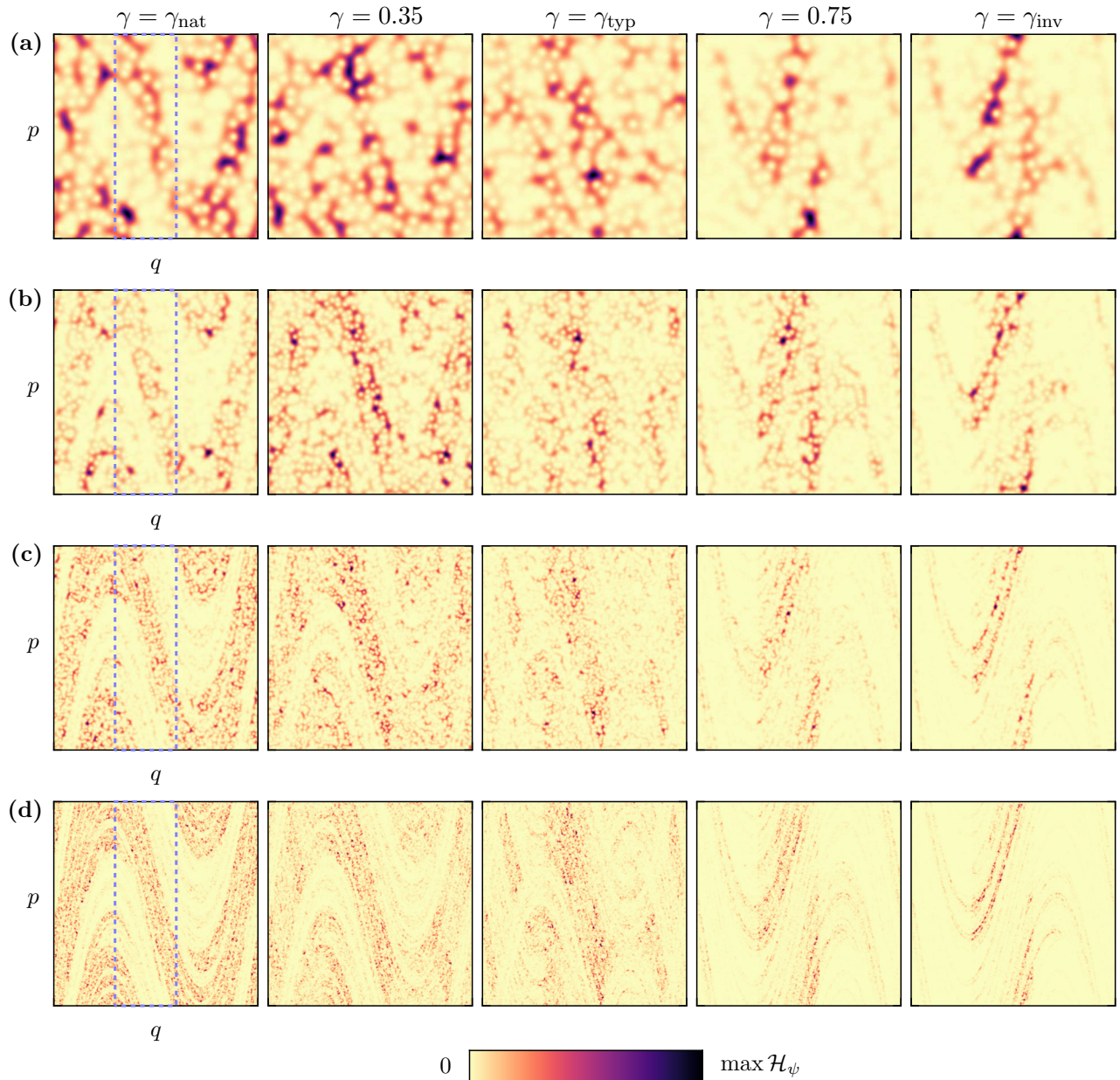


**Figure 4.5:** Husimi distribution  $\mathcal{H}_\psi$  of single resonance eigenfunctions  $\psi$  with decay rate closest to  $\gamma \in \{\gamma_{\text{nat}}, 0.35, \gamma_{\text{typ}}, 0.88, \gamma_{\text{inv}}\}$  for the chaotic standard map with partial escape and decreasing Planck's constant (a)  $h = 1/250$ , (b)  $h = 1/1000$ , (c)  $h = 1/4000$ , and (d)  $h = 1/16000$ . An individual colormap is used in each panel. Dashed blue line indicates the position of the opening  $\Omega$ .

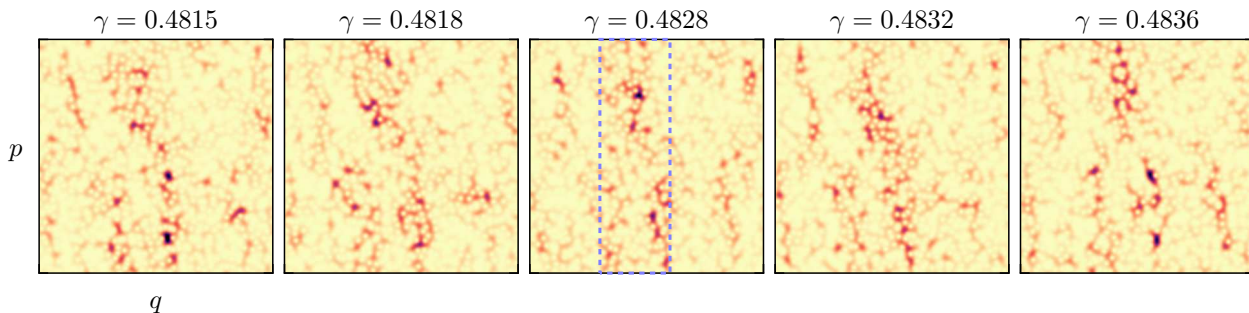


**Figure 4.6:** Husimi distribution of the five resonance eigenfunctions with decay rate  $\gamma$  closest to  $\gamma_{\text{typ}} \approx 0.4828$  for chaotic standard map with partial escape and  $h = 1/1000$ . Dashed blue line indicates the position of the opening  $\Omega$ . Same colormap for all panels with maximum taken from  $\gamma \approx \gamma_{\text{typ}}$  (middle panel).

## 4.2.2 Convergence of phase-space distribution

In order to show that resonance eigenfunctions with the same decay rate  $\gamma$  have the same semiclassical phase-space structure we investigate expectation values of classical observables on phase space. Recall that weak convergence of resonance eigenfunctions with the same decay rate  $\gamma$  implies, that for a fixed observable  $a: \Gamma \rightarrow \mathbb{R}$  the expectation values  $\mathbb{E}_\psi[a]$ , defined in Eq. (3.9), must converge to the same value. We stress that this value is a priori not known. Due to the observations in the previous section a dependence on  $\gamma$  is expected.

### 4.2.2.1 Expectation values of single eigenfunctions.

Let us consider four different observables on the phase space  $\Gamma$ : The indicator functions  $a_{1,2,3}(q, p) = \mathbb{1}_{A,B,C}(q, p)$  of some phase-space areas  $A = (0.3, 0.5) \times (0.6, 0.8)$ ,  $B = (0.7, 0.9) \times (0.1, 0.3)$ , and  $C = (0.3, 0.5) \times (0.1, 0.3)$  and the smooth observable  $a_4(q, p) = \sin^2(2\pi q) \cos^2(\pi p)$ . They are chosen such that  $A, C \subset \Omega$  and  $B \subset \Gamma \setminus \Omega$ , see illustration in Fig. 4.7. Expectation values  $\mathbb{E}_\psi[a_i]$  are computed for all resonance eigenfunctions  $\psi$  of the chaotic standard map

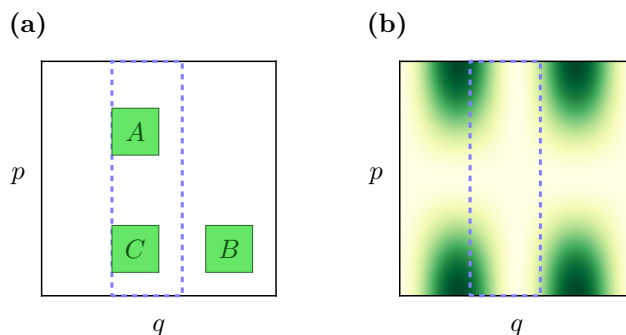


**Figure 4.7:** Illustration of the considered observables on the phase space. (a) Indicator functions of areas  $A = (0.3, 0.5) \times (0.1, 0.3)$ ,  $B = (0.7, 0.9) \times (0.1, 0.3)$ ,  $C = (0.3, 0.5) \times (0.6, 0.8)$ . (b) Smooth observable  $a_4(q, p) = \sin^2(2\pi q) \cos^2(\pi p)$  as a density between zero (white) and one (dark green). Dashed blue line indicates position of the considered opening  $\Omega$ .

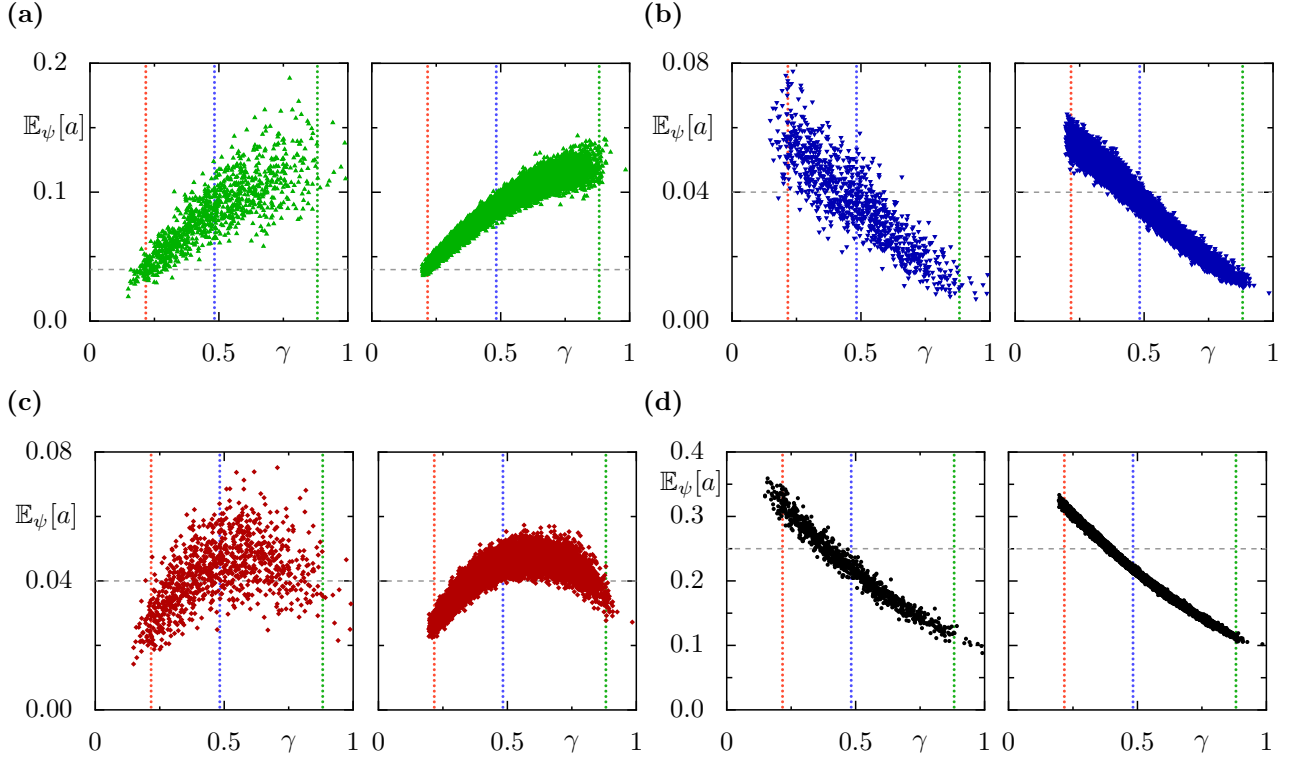


**Figure 4.8:** Expectation values  $\mathbb{E}_\psi[a]$  of different observables  $a$  on  $\Gamma$  for single resonance eigenfunctions  $\psi$  as a functions of their decay rate  $\gamma$ . Considered are observables as shown in Fig. 4.7, (a)  $a_1 = \mathbb{1}_A$ , (b)  $a_2 = \mathbb{1}_B$ , (c)  $a_3 = \mathbb{1}_C$ , and (d) smooth  $a_4(q, p) = \sin^2(2\pi q) \cos(\pi p)$ . Planck's constant is  $h = 1/1000$  (left) and  $h = 1/16000$  (right). Gray dashed line indicates  $\mu_L(a_i)$  for each observable which is expected in closed systems from Eq. (3.16).

with partial escape by integrating their Husimi distribution  $\mathcal{H}_\psi$ , see Eq. (3.10). Note that for the indicator functions, the expectation value  $\mathbb{E}_\psi[\mathbb{1}_{A,B,C}]$  is equal to the probability of the eigenfunction  $\psi$  on the sets  $A, B, C \subset \Gamma$ .

The results are illustrated in Fig. 4.8 for two different values of Planck's constant,  $h \in \{1/1000, 1/16000\}$ . For  $a_1$  the expectation values of all eigenfunctions are shown in (a). The dotted vertical lines indicate the natural decay rate  $\gamma_{\text{nat}}$  (red), the typical decay rate  $\gamma_{\text{typ}}$  (blue) and the inverse decay rate  $\gamma_{\text{inv}}$  (green) of the considered system, while the horizontal gray dashed line indicates the expectation in the closed chaotic system,  $\mathbb{E}_{\text{cl}}[a_1] = \mu_L(A) = 0.04$ , see Eq. 3.16. At  $h = 1/1000$  the obtained values for  $\mathbb{E}_\psi[a_1]$  deviate clearly from the closed uniform expectation (left panel) and quantify the dependence on  $\gamma$ , already seen in Fig. 4.5. The expectation values increase with  $\gamma$  while they increasingly fluctuate. Considering  $h = 1/16000$  the expectation values seem to accumulate around a  $\gamma$ -dependent curve (right panel). Compared to  $h = 1/1000$  the fluctuations around this curve become smaller. For  $a_2$  we observe that the expectation values decrease with the decay rate  $\gamma$ , while the fluctuations also become smaller, see (b). For  $a_3$  we find that the expectation  $\mathbb{E}_\psi[a_3]$  first increases with  $\gamma$  up to  $\gamma \approx 0.6$ , and then decreases again for larger decay rates (c). These three examples show that in systems with partial escape the expectation values of different observables can have a

completely distinct dependence on  $\gamma$ .

Additionally for the smooth observable  $a_4$  we obtain a decrease of the expectation value  $\mathbb{E}_\psi[a_4]$  similar to  $a_2$ , but with overall larger values. The decrease is related to the localization of  $a_4$  mostly outside of the opening  $\Omega$ , see Fig. 4.7. The larger values are related to the larger size of the observable, i.e.,  $\mathbb{E}_{\text{cl}}[a_4] = \int a_4 d\mu_L = 0.25$ . This shows that for both smooth and non-smooth observables we get comparable results. In all cases the spreading of the observed values becomes smaller for  $h = 1/16000$ , which is compatible with the same semiclassical limit measure for all eigenfunctions with the same decay rate  $\gamma$ .

#### 4.2.2.2 Average expectation values.

In order to quantify these observations we consider for a fixed decay rate  $\gamma$  the set of  $S$  closest eigenfunctions, from which  $S/2$  eigenfunctions have decay rate smaller and larger than  $\gamma$ . In order to formally define this set for fixed  $h = 1/N$  let  $\{\gamma_i\}_{i=1}^N$  be the set of decay rates of the quantum map  $\mathcal{U}_N$  which is ordered like  $\gamma_i \leq \gamma_j$  for  $i \leq j$ . We define for given decay rate  $\gamma$  and  $S \in 2\mathbb{N}$  the set

$$\mathcal{I}_\gamma^S := \left\{ n - \frac{S}{2}, n - \frac{S}{2} + 1, \dots, n, \dots, n + \frac{S}{2} - 1 \right\} \cap \{1, \dots, N\}, \quad (4.8)$$

where  $n$  is such that  $\gamma_{n-1} < \gamma \leq \gamma_n$ . This set is used to index the  $S$  closest quantum decay rates to  $\gamma$  with  $S/2$  being larger and  $S/2$  being smaller. Let us remark, that for small  $\gamma$  there can be less than  $S/2$  resonances with smaller decay rates, and vice versa for large  $\gamma$ . For example, if  $\gamma \leq \gamma_0$  we have  $\mathcal{I}_\gamma^S = \{1, \dots, \frac{S}{2}\}$  and similarly for  $\gamma > \gamma_N$  we get  $\mathcal{I}_\gamma^S = \{N - \frac{S}{2} + 1, \dots, N\}$ , such that in these cases  $|\mathcal{I}_\gamma^S| < S$ . Therefore the considered indices are restricted to values between 1 and  $N$ . We implicitly refer to this restriction throughout this thesis whenever an average over the  $S$  closest resonances is considered.

We use this restricted index set  $\mathcal{I}_\gamma^S$  to define the average over  $S$  eigenfunctions with respect to the decay rate  $\gamma$  for expectation values of observables as

$$\langle a \rangle_\gamma := \frac{1}{|\mathcal{I}_\gamma^S|} \sum_{i \in \mathcal{I}_\gamma^S} \mathbb{E}_{\psi_i}[a]. \quad (4.9)$$

The sample standard deviation of the values  $\mathbb{E}_{\psi_i}[a]$  is given by

$$\sigma_\gamma(a) = \left( \frac{1}{|\mathcal{I}_\gamma^S| - 1} \sum_{i \in \mathcal{I}_\gamma^S} \left| \mathbb{E}_{\psi_i}[a] - \langle a \rangle_\gamma \right|^2 \right)^{1/2}, \quad (4.10)$$

where division with  $|\mathcal{I}_\gamma^S| - 1$  ensures an unbiased estimator. Similarly for given  $\gamma$  and  $S$  the



average decay rate of the sample is defined as

$$\langle \gamma \rangle_\gamma := \frac{1}{|\mathcal{I}_\gamma^S|} \sum_{i \in \mathcal{I}_\gamma^S} \gamma_i \quad (4.11)$$

with standard deviation  $\Delta_\gamma$ .

We first confirm that the average decay rate  $\langle \gamma \rangle_\gamma$  converges to the considered one in Fig. 4.9. For  $\gamma \in \{\gamma_{\text{nat}}, 0.35, \gamma_{\text{typ}}, 0.75, \gamma_{\text{inv}}\}$  the average decay rate for  $S = 50$  is illustrated over  $h$  in (a). Additionally the standard deviation  $\Delta_\gamma$  is shown as a shaded region for each  $\gamma$ . As expected, the average approaches the considered decay rate  $\gamma$  for small  $h$ . For  $\gamma = \gamma_{\text{inv}}$  we observe a slower convergence, which is due to the significantly lower number of resonances around  $\gamma_{\text{inv}}$ , see Fig. 4.2. This becomes more clear in Fig. 4.9(b), where the standard deviation  $\Delta_\gamma$  is shown over  $h$ . We find a power-law scaling of approximately  $\Delta_\gamma \sim h$  for all decay rates except  $\gamma_{\text{inv}}$ . This is not surprising, since the total number of resonances grows as  $1/h$  within a finite  $\gamma$ -interval. For  $\gamma_{\text{typ}}$  this result is semiclassically exact [89, 195]. For smaller decay rates the scaling of their number with  $h$  is non-trivially related to classical fractals [92]. Applying the considerations in Ref. [92] to much larger decay rates could explain the scaling at  $\gamma = \gamma_{\text{inv}}$ .

In order to numerically test the convergence of expectation values of observables we present the mean expectation value  $\langle a \rangle_\gamma$  and the standard deviation  $\sigma_\gamma(a)$  for the smooth observable  $a = a_4$  as a function of  $h$  in Fig. 4.10. The considered decay rates are the same as in Fig. 4.9. We observe that the mean expectation value remains almost constant when  $h$  becomes smaller (a). Again we find that for  $\gamma_{\text{inv}}$  there are some stronger fluctuations and a larger standard deviation. This is related to the before-mentioned larger standard deviation  $\Delta_\gamma$  for  $\gamma_{\text{inv}}$ , see Fig. 4.9(b), which decreases slower than for the other decay rates. We also observe that the standard deviation decreases with  $h$ , indicated by the shaded regions in (a) and in Fig. 4.9(b).

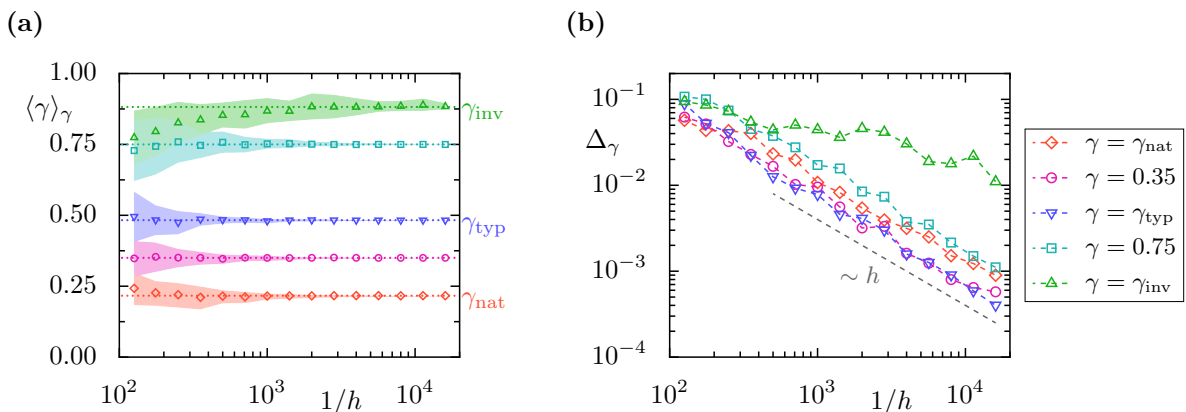


**Figure 4.9:** (a) Average decay rate  $\langle \gamma \rangle_\gamma$  vs.  $h$  for  $\gamma \in \{\gamma_{\text{nat}}, 0.35, \gamma_{\text{typ}}, 0.75, \gamma_{\text{inv}}\}$  (diamonds, circles, lower triangles, squares, upper triangles). The average is taken over  $S = 50$  resonances. Shaded regions indicate standard deviation  $\Delta_\gamma$ . Dotted lines indicate selected  $\gamma$ . (b) Standard deviation  $\Delta_\gamma$  vs.  $h$  for same  $\gamma$  as in (a). Gray dashed line shows approximate scaling  $\Delta_\gamma \sim h$ .

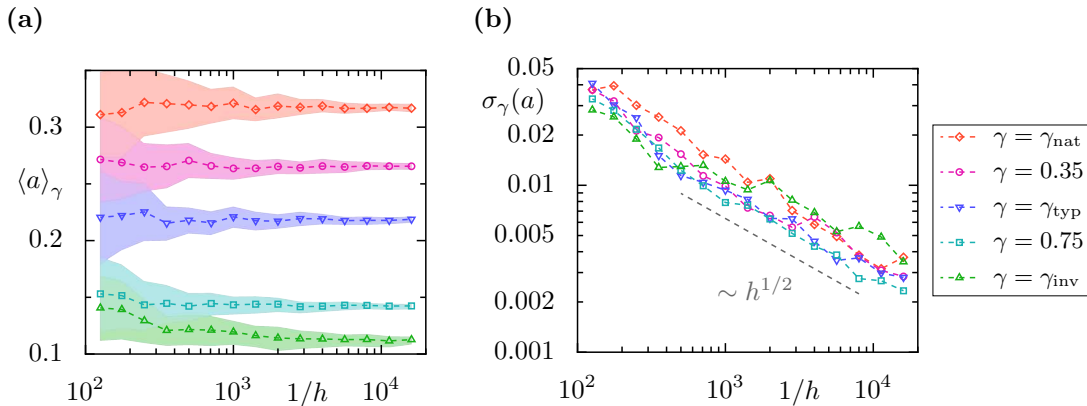


**Figure 4.10:** (a) Mean expectation value  $\langle a \rangle_\gamma$  vs.  $h$  for  $\gamma \in \{\gamma_{\text{nat}}, 0.35, \gamma_{\text{typ}}, 0.75, \gamma_{\text{inv}}\}$  and smooth observable  $a = a_4$ . The average is taken over  $S = 50$  resonance eigenfunctions. Shaded regions indicate the corresponding standard deviation  $\sigma_\gamma(a)$ . (b) Standard deviation  $\sigma_\gamma(a)$  vs.  $h$  for same  $\gamma$  as in (a). Gray dashed line shows approximate scaling  $\sigma_\gamma(a) \sim h^{1/2}$ .

Here we find a power law which is approximately given by  $\sigma_\gamma(a) \sim h^{1/2}$ . For  $\gamma = \gamma_{\text{nat}}$  there is a surprising increase of  $\sigma_\gamma(a)$  for the smallest considered  $h$ . Even though this seems to spoil the power-law decay, similar fluctuations are seen for different values of  $\gamma$  and  $h$ . This is confirmed for the other observables in Appendix B.2. This suggests semiclassical convergence of the  $\mathbb{E}_\psi[a]$  for resonance eigenfunctions  $\psi$  towards a  $\gamma$ -dependent value. Altogether these observations justify to consider some unknown semiclassical limit measures  $\mu_\gamma^{\text{sc}}$ , which only depends on the decay rate  $\gamma$ .

It is desirable to quantify this convergence in terms of a similar quantity as for the  $k$ -th moment  $S_k(N, a)$  of the distribution around  $\mu_L$  in closed systems, see Eq. (3.17). This could be achieved by

$$\tilde{S}_k(N, a) = \frac{1}{N} \sum_{i=1}^N |\mathbb{E}_{\gamma_i}[a] - \mu_{\gamma_i}^{\text{sc}}(a)|^k, \quad (4.12)$$

which is for  $k = 2$  similar to the average variance of individual eigenfunctions around the expectation value of their semiclassical limit. The crucial difference is that in contrast to Eq. (3.17) the semiclassical limit measure depends on the decay rate. Since these measures are not known, we approximate Eq. (4.12) with

$$\tilde{S}_k(N, a) \approx \frac{1}{N} \sum_{i=1}^N |\mathbb{E}_{\gamma_i}[a] - \langle a \rangle_{\gamma_i}|^k. \quad (4.13)$$

This quantity can be seen as the squared standard deviation  $\sigma_\gamma^2(a)$  averaged over all decay rates. Figure 4.11 illustrates the dependence of  $\tilde{S}_2(N, a)$  on Planck's constant  $h = 1/N$  for all considered observables  $a_i$  in a double-logarithmic scaling. In all cases we observe a power law dependence like  $\tilde{S}_2(N, a) \sim h$ , confirming that fluctuations of single resonance eigenfunctions

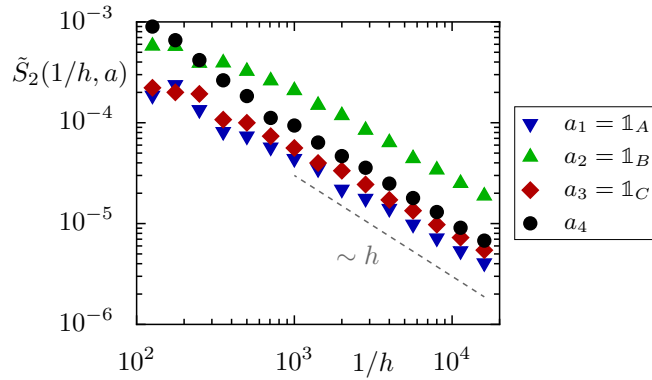


**Figure 4.11:** Convergence of resonance eigenfunctions in terms of the second moment  $\tilde{S}_2(N, a)$ , see Eq. (4.13), shown as a function of  $h$  for the considered observables  $a_{1,2,3,4}$  as in Fig. 4.7.

on average go to zero semiclassically for all considered observables. The observed speed of convergence deviates only little from the expectation in closed systems.

In conclusion, for resonance eigenfunctions in systems with partial escape we expect that the semiclassical limit measures depend on the decay rate  $\gamma$ , only. Most importantly, our numerical findings suggest that individual eigenfunctions converge weakly to their average phase-space structure. Hence, in order to obtain a complete description of resonance eigenfunctions it is sufficient to understand the limit of their average structure and the fluctuations around this average.

### 4.2.3 Average phase-space distribution

The results from the previous section imply that it is sufficient to understand and reasonable to investigate the average phase-space distribution of resonance eigenfunctions. For any decay rate  $\gamma$  we define the average Husimi distribution as

$$\langle \mathcal{H} \rangle_\gamma^S(x) := \frac{1}{|\mathcal{I}_\gamma^S|} \sum_{i \in \mathcal{I}_\gamma^S} \mathcal{H}_i(x), \quad (4.14)$$

using the restricted index set  $\mathcal{I}_\gamma^S$  as in Eq. (4.8) and the Husimi distribution  $\mathcal{H}_i$  of the eigenfunction  $\psi_i$  with decay rate  $\gamma_i$ , see Eq. (3.6). In the following we always fix the number of considered eigenfunctions to  $S = 50$  as in the previous section and omit this index. The average Husimi distribution  $\langle \mathcal{H} \rangle_\gamma$  is intuitively related to the mean expectation value  $\langle a \rangle_\gamma$  of an observable  $a$ ,

$$\langle a \rangle_\gamma = \frac{1}{|\mathcal{I}_\gamma^S|} \sum_{i \in \mathcal{I}_\gamma^S} \mathbb{E}_{\psi_i}[a] \stackrel{(3.10)}{=} \frac{1}{|\mathcal{I}_\gamma^S|} \sum_{i \in \mathcal{I}_\gamma^S} \int_\Gamma a(x) \mathcal{H}_i(x) dx \stackrel{(4.14)}{=} \int_\Gamma a(x) \langle \mathcal{H} \rangle_\gamma(x) dx. \quad (4.15)$$

It thus defines the probability density for the average expectation value.

With the aim of obtaining an intuitive picture of the phase-space localization of resonance eigenfunctions we illustrate average Husimi distributions  $\langle \mathcal{H} \rangle_\gamma$  in Fig. 4.12 for increasing decay rates and different values of  $h$ , as in Fig. 4.5. In this representation the dependence on  $\gamma$  is revealed much clearer even for large values of  $h = 1/250$ , see Fig. 4.12(a). The high-density filaments at decay rates  $\gamma_{\text{nat}}$  and  $\gamma_{\text{inv}}$  are concentrated on distinct directions on the phase space, which we identify as the stable and unstable direction of the classical dynamics, see Fig. 2.3. For intermediate decay rates there is a transition between both densities. For decreasing values of  $h$  the average phase-space distribution shows repeatedly finer scales, seen from top to bottom

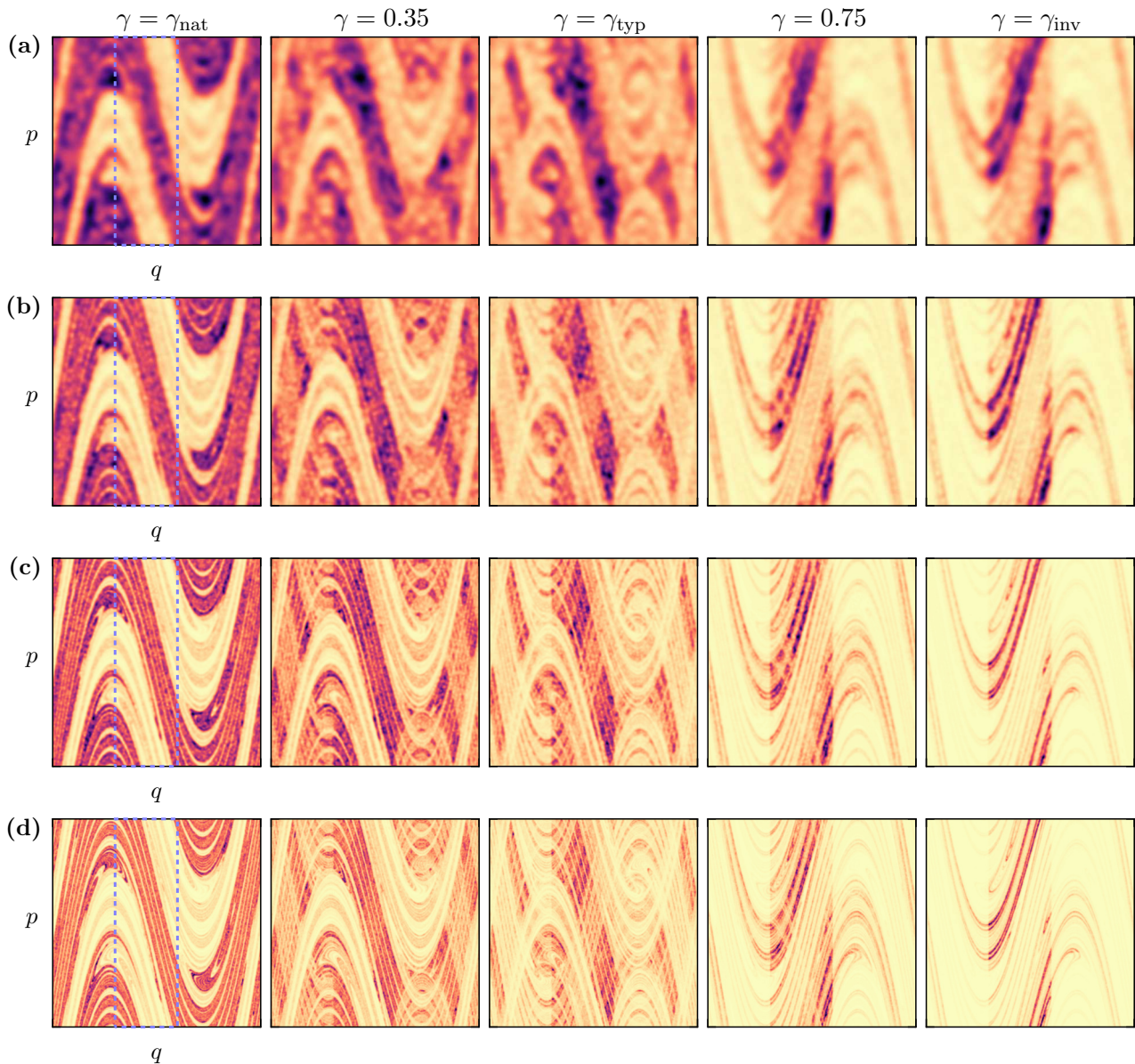


**Figure 4.12:** Average Husimi distribution  $\langle \mathcal{H} \rangle_\gamma$  of resonance eigenfunctions with decay rate closest to  $\gamma \in \{\gamma_{\text{nat}}, 0.35, \gamma_{\text{typ}}, 0.75, \gamma_{\text{inv}}\}$  (from left to right) for chaotic standard map with partial escape and decreasing Planck's constant (a)  $h = 1/250$ , (b)  $h = 1/1000$ , (c)  $h = 1/4000$ , and (d)  $h = 1/16000$ . An individual colormap is used in each panel. Dashed blue line indicates the position of the opening.

in Fig. 4.12. On these scales the finest filaments reveal a fractal phase-space structure, where a transition of the high-density filaments takes place between  $\gamma_{\text{nat}}$  and  $\gamma_{\text{inv}}$ . We conclude that the semiclassical limit measure has fractal properties. Note that due to the finite sample size of  $S = 50$  fluctuations of single eigenfunctions do not vanish completely.

#### 4.2.4 Fluctuations

The following results are obtained together with Felix Kunzmann during his Bachelor thesis [196]. As discussed before, single eigenfunctions fluctuate around their average phase-space structure. The phase-space structure of single eigenfunctions is fully understood from the average structure and from the nature of their fluctuations. Even without a-priori knowledge of the semiclassical limit measure, it is thus an interesting question to understand these fluctuations.

For this purpose we define the rescaled Husimi distribution of an eigenfunction  $\psi$  with decay rate  $\gamma$  as

$$\tilde{\mathcal{H}}_{\psi} = \mathcal{H}_{\psi} / \langle \mathcal{H} \rangle_{\gamma}, \quad (4.16)$$

which rescales a single Husimi distribution with the average such that it fluctuates around a constant value of one. An illustration of these distributions is given in Fig. 4.13 for (a)  $h = 1/1000$  and (b)  $h = 1/16000$ . The considered decay rates are the same as in Fig. 4.5 (showing the corresponding single Husimi distributions) and in Fig. 4.12 (showing the corresponding

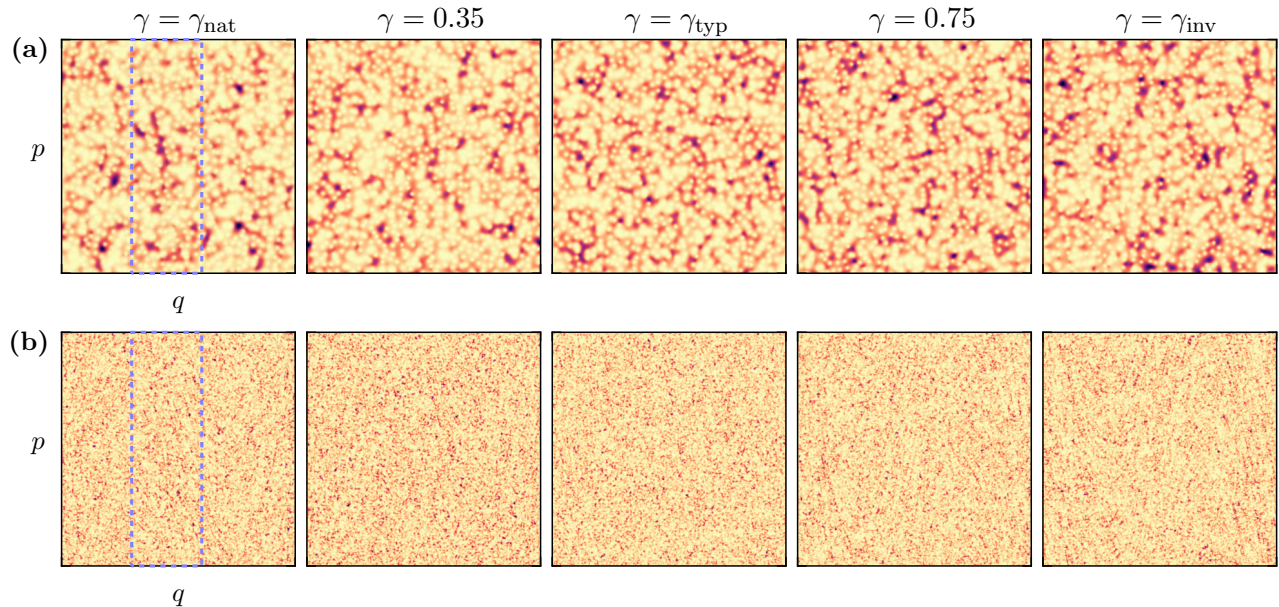


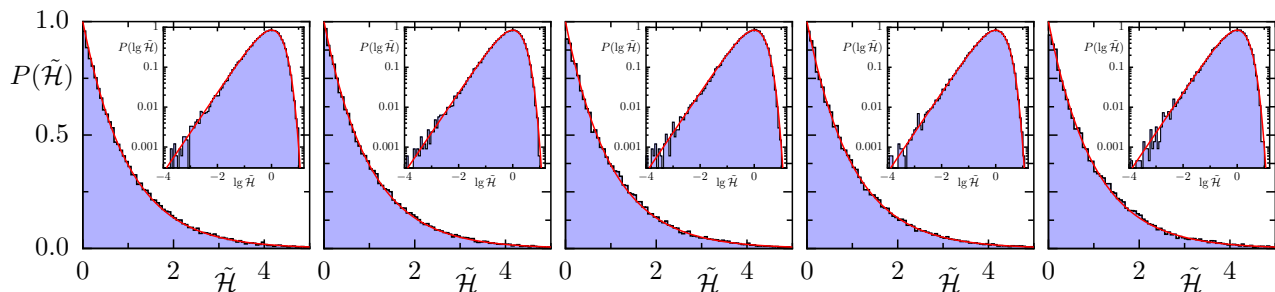
**Figure 4.13:** Rescaled Husimi distribution  $\tilde{\mathcal{H}}_{\psi} = \mathcal{H}_{\psi} / \langle \mathcal{H} \rangle_{\gamma}$  of resonance eigenfunctions  $\psi$  with decay rate closest to  $\gamma \in \{\gamma_{\text{nat}}, 0.35, \gamma_{\text{typ}}, 0.88, \gamma_{\text{inv}}\}$  (from left to right) for chaotic standard map with partial escape and decreasing Planck's constant (a)  $h = 1/1000$  and (b)  $h = 1/16000$ . The average Husimi distribution is calculated using 50 resonances. Dashed blue line indicates the position of the opening  $\Omega$ .

average Husimi distributions). In fact, Fig. 4.13 can be obtained by dividing the densities in Fig. 4.5 with those in Fig. 4.12 for the two values of  $h$ , respectively. The rescaled Husimi distributions show an almost uniform distribution of the fluctuations for all  $\gamma$ . There is no visible dependence on the decay rate  $\gamma$ . The obtained distributions qualitatively resemble the Husimi phase-space distributions observed in closed systems, see Fig. 3.2, where the statistics of fluctuations is explained by a random wave model [13].

We are interested in the probability distribution  $P(\tilde{\mathcal{H}})$ , i.e., the probability that the rescaled Husimi distribution obtains a certain value. Therefor consider the rescaled Husimi distribution  $\tilde{\mathcal{H}}_\gamma$  for some decay rate  $\gamma$ , evaluated at the mid points of a grid of size  $32 \times 32$ ,  $(q_i, p_j) = (\frac{i+1/2}{32}, \frac{j+1/2}{32})$  with  $0 \leq i, j < 32$ . We choose this large number of points in order to obtain a better statistics. Investigations for single phase-space points and regions avoiding symmetry lines can be found in Ref. [196]. For a chosen decay rate  $\gamma$  the probability distribution is calculated considering  $S = 50$  resonance eigenfunctions and for all values  $\tilde{\mathcal{H}}_\gamma(q_i, p_j)$ .

The results for  $P(\tilde{\mathcal{H}})$  are presented in Fig. 4.14 for (a)  $h = 1/1000$  and (b)  $h = 1/16000$  and for the five different decay rates  $\gamma$  as before. We find very good agreement with the exponential distribution  $P(x) = e^{-x}$  (red line), which is the semiclassical expectation in closed systems [13]. This holds equally well for all decay rates  $\gamma$ . The agreement becomes better if  $h$  is considered

(a)  $h = 1/1000$



(b)  $h = 1/16000$

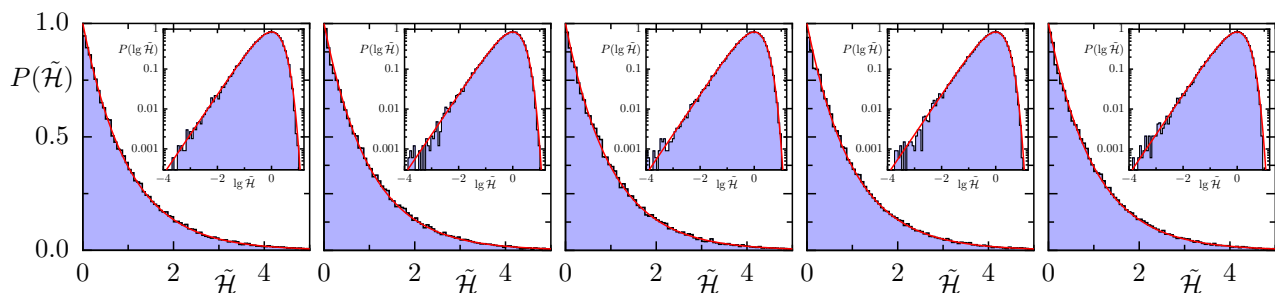


**Figure 4.14:** Distribution of rescaled Husimi values  $\tilde{\mathcal{H}}_\gamma$  of the 50 eigenfunctions with decay rate closest to  $\gamma \in \{\gamma_{\text{nat}}, 0.35, \gamma_{\text{typ}}, 0.88, \gamma_{\text{inv}}\}$  (from left to right). Considered are all values  $\tilde{\mathcal{H}}(q, p)$  at the mid points on a grid of size  $32 \times 32$ ,  $(q_i, p_j) = (\frac{i+1/2}{32}, \frac{j+1/2}{32})$  for  $0 \leq i, j < 32$ . Planck's constant is chosen as (a)  $h = 1/1000$  and (b)  $h = 1/16000$ . Red line shows the exponential distribution  $P(x) = e^{-x}$  for random states [13]. Inset shows the distribution  $P(\lg \tilde{\mathcal{H}})$  for the same set of data.

smaller, see (b). The insets show a similar statistics obtained from the same data for the logarithm  $\lg \tilde{\mathcal{H}} = \log_{10}(\tilde{\mathcal{H}})$  in double logarithmic representation. This distribution is more sensitive to small values of  $\tilde{\mathcal{H}}$ . It perfectly agrees with the expected exponential distribution (red line).

We conclude that fluctuations of values of the rescaled Husimi  $\tilde{\mathcal{H}}(q, p)$  are distributed exponentially [196] for all decay rates. Hence, for fixed  $\gamma$ , values of the usual Husimi distribution  $\mathcal{H}_\gamma(q, p)$  at a given point  $(q, p)$  are also exponentially distributed, but with a different mean value. The mean values considered here are chosen as the average distribution  $\langle \mathcal{H} \rangle_\gamma(q, p)$ . In general these fluctuations are expected around a value which is given by the semiclassical limit measure  $\mu_\gamma^{\text{sc}}$ .

### 4.2.5 Semiclassical expectation for iterations of $R$

In this section we derive properties of the semi-classical limit measures of resonance eigenfunctions in analogy to the results in Ref. [59] which were obtained for systems with full escape. They derive an equation for the semiclassical weight on the sets of points, which fall into the opening  $\Omega$  under forward iteration for the first time after  $m$  steps. These sets are defined as  $\Omega_m^+ = M^{-m}(\Omega) \setminus \bigcup_{i=0}^{m-1} M^{-i}(\Omega)$ , see Eq. (2.44). For full escape, the expectation values of these sets for eigenfunctions with decay rate  $\gamma$  converge semiclassically to  $\mathbb{E}_{\psi_\gamma}[\Omega_m] \xrightarrow{h \rightarrow 0} e^{-m\gamma} (1 - e^{-\gamma})$  [59].

In the following we generalize this to maps with partial escape, considering both forward and backward time evolution. First, recall the reflectivity function for full escape  $R_0 = 1 - \mathbb{1}_\Omega$ . The characteristic function of the sets  $\Omega_m^+$  can be expressed in terms of the reflectivity function  $R_0$  by  $\mathbb{1}_{\Omega_0^+} = 1 - R_0$  and  $\mathbb{1}_{\Omega_m^+} = (1 - R_0 \circ M^m) \cdot \prod_{i=0}^{m-1} R_0 \circ M^i$ . This is shown by applying the relation  $\mathbb{1}_A \circ M = \mathbb{1}_{M^{-1}(A)}$ . These characteristic functions are immediately generalizable to arbitrary  $R$ , and we define the analogue expression to the sets  $\Omega_m^+$  as

$$T_m^+ := (1 - R \circ M^m) \cdot \prod_{i=0}^{m-1} R \circ M^i = \prod_{i=0}^{m-1} R \circ M^i - \prod_{i=0}^m R \circ M^i. \quad (4.17)$$

The interpretation of these functions is simple and analogue to full escape: The function  $T_m^+$  characterizes the phase-space distribution, which escapes from the system after exactly  $m + 1$  steps.

In order to determine the expectation value  $\mathbb{E}_{\psi_\gamma}[T_m]$  in analogy to the result for full escape we first rewrite the  $n$ -fold application of the propagator  $\mathcal{U} = \tilde{\mathcal{U}}\mathcal{R}$  as

$$\mathcal{U}^n = \tilde{\mathcal{U}}\mathcal{R} \cdot \tilde{\mathcal{U}}\mathcal{R} \cdot \dots \cdot \tilde{\mathcal{U}}\mathcal{R} \cdot \tilde{\mathcal{U}}\mathcal{R} \quad (4.18)$$

$$= \tilde{\mathcal{U}}^n \cdot \tilde{\mathcal{U}}^{-(n-1)}\mathcal{R}\tilde{\mathcal{U}}^{n-1} \cdot \tilde{\mathcal{U}}^{-(n-2)}\mathcal{R}\tilde{\mathcal{U}}^{n-2} \cdot \dots \cdot \tilde{\mathcal{U}}^{-1}\mathcal{R}\tilde{\mathcal{U}} \cdot \mathcal{R} \quad (4.19)$$

$$= \tilde{\mathcal{U}}^n \cdot \mathcal{R}_{n-1} \cdot \dots \cdot \mathcal{R}_0, \quad (4.20)$$

where the operators  $\mathcal{R}_0 := \mathcal{R}$  and  $\mathcal{R}_{m+1} := \tilde{\mathcal{U}}^{-1}\mathcal{R}_m\tilde{\mathcal{U}}$  are introduced. The semiclassical correspondence of quantum and classical time evolution of the closed map, Egorov property Eq. (3.2), ensures that for the observable  $\sqrt{R}$  with quantization  $\mathcal{R} = \text{Op}_N(\sqrt{R})$  we have  $\mathcal{R}_m \sim \text{Op}_N(\sqrt{R} \circ M^m)$  for  $N \rightarrow \infty$ . This allows the evaluation of expectation values of the products  $\prod_{i=0}^m R \circ M^i$  asymptotically for  $N \rightarrow \infty$  as

$$\mathbb{E}_{\psi_\gamma} \left[ \prod_{i=0}^{m-1} R \circ M^i \right] = \langle \psi_\gamma | \text{Op}_N \left( \prod_{i=0}^{m-1} R \circ M^i \right) \psi_\gamma \rangle \quad (4.21)$$

$$\sim \langle \psi_\gamma | \mathcal{R}_0^\dagger \cdot \dots \cdot \mathcal{R}_{m-1}^\dagger \mathcal{R}_{m-1} \cdot \dots \cdot \mathcal{R}_0 \psi_\gamma \rangle \quad (4.22)$$

$$= \langle \psi_\gamma | \mathcal{R}_0^\dagger \cdot \dots \cdot \mathcal{R}_{m-1}^\dagger \cdot (\tilde{\mathcal{U}}^\dagger)^m \tilde{\mathcal{U}}^m \cdot \mathcal{R}_{m-1} \cdot \dots \cdot \mathcal{R}_0 \psi_\gamma \rangle \quad (4.23)$$

$$= \langle \mathcal{U}^m \psi_\gamma | \mathcal{U}^m \psi_\gamma \rangle = e^{-m\gamma}, \quad (4.24)$$

where the first asymptotic relation follows from Eq. (3.1) for real valued  $R$  and Eq. (4.20) has been used in the last line. Hence, for  $T_m^+$  follows with Eq. (4.17) that  $\mathbb{E}_{\psi_\gamma}[T_m^+] \sim e^{-m\gamma} - e^{-(m+1)\gamma}$  and

$$\mathbb{E}_{\psi_\gamma}[T_m^+] \xrightarrow{h \rightarrow 0} e^{-m\gamma} (1 - e^{-\gamma}), \quad (4.25)$$

which generalizes the expression in Ref. [59] to arbitrary reflectivity functions. Equation (4.25) gives a semiclassical expression for the expected loss of weight in the  $m$ -th time step. Hence, the total weight  $w_n$  after  $n$  iterations is given by  $w_n = 1 - \sum_{m=0}^n e^{-m\gamma} (1 - e^{-\gamma}) = e^{-n\gamma}$ , which corresponds to the overall decay of resonance eigenfunctions, Eq. (2.17).

If the reflectivity function is strictly positive,  $R > 0$ , the quantum map with escape  $\mathcal{U}$  is invertible. In this case we find a similar relation for the functions  $T_m^- := (R^{-1} \circ M^{-m} - 1) \cdot \prod_{i=1}^{m-1} R^{-1} \circ M^{-i}$ , by applying similar considerations towards  $\mathcal{U}^{-1}$ . We obtain asymptotically  $\mathbb{E}_{\psi_\gamma}[T_m^-] \sim e^{m\gamma} - e^{(m-1)\gamma}$  such that

$$\mathbb{E}_{\psi_\gamma}[T_m^-] \xrightarrow{h \rightarrow 0} e^{m\gamma} (1 - e^{-\gamma}). \quad (4.26)$$

An illustration of these expectation values for  $T_n^+$  and  $T_m^-$  is given in Figs. 4.15 and 4.16 for the chaotic standard map with partial escape  $R_\Omega = 0.2$  from the phase-space region  $\Omega$  as before. The expectation values at the decay rate  $\gamma$  are calculated as in Eq. (3.10), by integrating the Husimi distribution  $\mathcal{H}_\psi$  of each resonance eigenfunction on a  $1024 \times 1024$  grid, multiplied with  $T_n^+$  and  $T_m^-$ , respectively. For comparison the expectation values  $\mu_L(T_n)$  of the closed systems are shown (gray vertical lines). For  $T_0^+$  the values fall directly onto the theoretical prediction, Eq. (4.25), for all values of  $h$ , see Fig. 4.15(a). This is not surprising, since the expectation values  $\langle \psi_\gamma | \mathbb{1} - \mathcal{R} | \psi_\gamma \rangle$  are exactly given by  $1 - e^{-\gamma}$ . The differences, e.g., for  $h = 1/250$ , are due to the finite width of coherent states in the definition of the Husimi distribution. This leads effectively to a smoothing of the function  $T_0^+$  which vanishes for



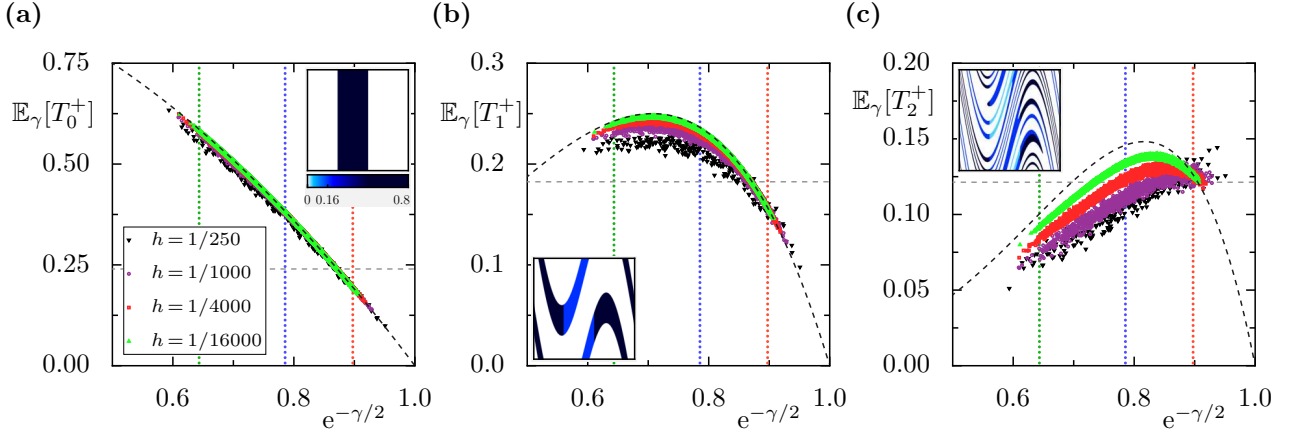


**Figure 4.15:** Expectation values of observables  $T_n^+$  for (a)  $n = 0$ , (b)  $n = 1$  and (c)  $n = 2$  vs. modulus of eigenvalue  $e^{-\gamma/2}$  for single eigenfunctions at  $h \in \{1/250, 1/1000, 1/4000, 1/16000\}$  (black, violet, red, green) compared to the semiclassical prediction, Eq. (4.25) (dashed black lines), and to uniform expectation from closed system,  $\mu_L(T_0^+) = 0.24$ ,  $\mu_L(T_1^+) \approx 0.18$ ,  $\mu_L(T_2^+) \approx 0.12$  (gray horizontal lines). Dotted vertical lines indicate  $e^{-\gamma/2}$  for classical decay rates  $\gamma_{\text{inv}}$  (green),  $\gamma_{\text{typ}}$  (blue) and  $\gamma_{\text{nat}}$  (red). Insets show phase-space distribution of  $T_n^+$  with same colormap for all  $n$ , see (a).

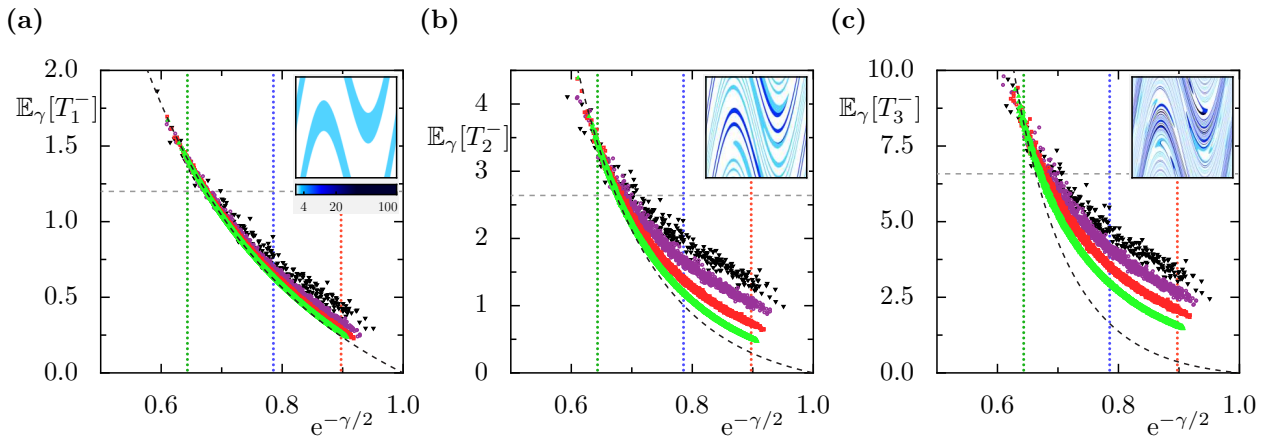


**Figure 4.16:** Same as Fig. 4.15, but showing expectation values of  $T_m^-$  for (a)  $m = 1$ , (b)  $m = 2$  and (c)  $m = 3$ , compared to semiclassical prediction Eq. (4.26) (dashed black lines) and to uniform expectation from closed system,  $\mu_L(T_0^-) = 1.2$ ,  $\mu_L(T_1^-) \approx 2.6$ ,  $\mu_L(T_2^-) \approx 6.6$  (gray horizontal lines). Inset shows phase-space distribution  $T_m^-$  with same colormap for all  $m$ , see (a).

smaller  $h$ . For  $T_1^+$  we observe larger deviations from the semiclassical curve for  $h = 1/250$  and  $h = 1/1000$  (b). These deviations almost vanish when  $h$  is decreased to  $h = 1/16000$ . For  $T_2^+$  we observe large deviations (c), even though the expectation values get closer to the prediction for smaller values of  $h$ . We notice, that around  $\gamma_{\text{nat}}$  the expectation values are already close to the prediction, even for large  $h$ .

Similar results are shown in Fig. 4.16 for  $T_m^-$ . For  $T_1^-$  we observe a comparable good agreement between the semiclassical prediction, Eq. (4.26), and the quantum expectation values as observed for  $T_1^+$ , compare Fig. 4.16(a) with Fig. 4.15(b). For large  $h$  there are visible

deviations, which almost vanish at  $h = 1/16000$ . For  $T_2^-$  and  $T_3^-$  the deviations from the semiclassical curve are much stronger. Again, for smaller values of  $h$  the expectation values become closer to the prediction, but in the numerically explored range do not yet fit to the expectation for all decay rates. Here we notice that, surprisingly, for decay rates around  $\gamma_{\text{inv}}$  the expectation values are already close to the prediction, even for large values of  $h$ .

The observed deviations are due to the limited resolution of phase-space structures. Recall that the Husimi distribution is smooth on scales of order  $h$ . Therefore at the considered values of  $h$  the fine filaments of  $T_2^+$  and  $T_2^-$  are not completely resolved. This obviously causes even larger deviations for  $T_3^-$ .

So far, we evaluated the semiclassical limit of the expectation value for very specific observables,  $T_n^\pm$ , related to forward and backward iterations of  $R$ . Thus, the right-hand side of Eqs. (4.25) and (4.26) restricts the possible semiclassical limit measures of resonance eigenfunctions. In the following we show more generally that all semiclassical limit measures must be conditionally invariant. Such measures satisfy Eqs. (4.25) and (4.26), as shown in App. C.1.

#### 4.2.6 Conditional invariance of semiclassical measures

In systems with full escape the semiclassical limit measures are proven to be conditionally invariant [60]. In the following we generalize Theorem 1 of Ref. [60] to systems with partial escape. Hereby we use the correspondence principle for the quantization, given in Sec. 3.1 and Sec. 4.1, see also Refs. [60, 170].

**Theorem 4.1** (Semiclassical limit measures). *Consider a sequence of eigenfunctions  $\{\psi_N\}_{N \in \mathbb{N}}$  of the quantization  $\{\mathcal{U}_N\}_{N \in \mathbb{N}}$  of a map with escape  $\mathcal{M} = \mathcal{M}_{M,R}$  with corresponding eigenvalues  $\{\lambda_N\}_{N \in \mathbb{N}}$  satisfying  $\gamma_N := -2 \log |\lambda_N| \leq \nu < \infty$  for some  $\nu$ . Assume that this sequence converges to the classical measure  $\mu$  on  $\Gamma$ . Let  $C(M^{-1}) \subset \Gamma$  be the set where  $M^{-1}$  is continuous and  $D(M^{-1}) = \Gamma \setminus C(M^{-1})$ . Then*

(i) *If  $\mu[C(M^{-1})] > 0$ , there exists  $\gamma \in [0, \nu]$  such that the eigenvalues  $\lambda_N$  satisfy*

$$|\lambda_N|^2 \xrightarrow{N \rightarrow \infty} e^{-\gamma}.$$

*For any measurable  $A \subset \Gamma$  with  $A \cap D(M^{-1}) = \emptyset$  one has  $\mathcal{M}\mu(A) = e^{-\gamma}\mu(A)$ .*

(ii) *If  $\mu[D(M^{-1})] = \mathcal{M}\mu[D(M^{-1})] = 0$ , then  $\mu$  is a conditionally invariant measure of the map with escape  $\mathcal{M}$ , with decay rate  $\gamma$ .*

*In particular, if  $M$  is smooth on the full phase space  $\Gamma$ , the limiting measure  $\mu$  is conditionally invariant.*

The first condition means that the measure has positive weight on the continuity set of the inverse map  $M^{-1}$ , i.e., on all points  $x \in \Gamma$  on which  $M^{-1}$  is continuous. Note that if  $M$  is

continuous on the full phase-space this condition is always satisfied, e.g., for the standard map. The proof of Theorem 4.1 follows closely the proof of Theorem 1 of Ref. [60] for quantum maps with full escape and is given here for completeness.

*Proof of Theorem 4.1.* The first statement (i) follows from the eigenvalue equation and the correspondence principle between quantum and classical time evolution, Eq. (4.1). We obtain from the eigenvalue equation

$$|\lambda_N|^2 \langle \psi_N | \text{Op}_N(a) | \psi_N \rangle = \langle \psi_N | \mathcal{U}^\dagger \text{Op}_N(a) \mathcal{U} | \psi_N \rangle \quad (4.27)$$

Since  $\mu[C(M^{-1})] > 0$  we can find some smooth observable defined on this set,  $a \in C_c^\infty[C(M^{-1})]$ , such that  $\mu(a) = \int a d\mu > 0$ . Thus we can apply Eq. (4.1) to the right hand side of Eq. (4.27) and obtain asymptotically for  $N \rightarrow \infty$

$$|\lambda_N|^2 \langle \psi_N | \text{Op}_N(a) | \psi_N \rangle \sim \langle \psi_N | \text{Op}_N(R \cdot (a \circ M)) | \psi_N \rangle. \quad (4.28)$$

Recall that  $\psi_N$  converges to  $\mu$  on  $\Gamma$ , i.e., for any smooth observable  $a$  the expectation values converge as  $\lim_{N \rightarrow \infty} \langle \psi_N | \text{Op}_N(a) | \psi_N \rangle = \mu(a)$ . Thus  $\mu(a) > 0$  implies that for  $N$  large enough  $\langle \psi_N | \text{Op}_N(a) | \psi_N \rangle > 0$  becomes larger than zero. This allows to divide Eq. (4.28) by  $\langle \psi_N | \text{Op}_N(a) | \psi_N \rangle$ . We obtain

$$|\lambda_N|^2 \sim \frac{\langle \psi_N | \text{Op}_N(R \cdot (a \circ M)) | \psi_N \rangle}{\langle \psi_N | \text{Op}_N(a) | \psi_N \rangle} \quad (4.29)$$

which asymptotically implies

$$|\lambda_N|^2 \xrightarrow{N \rightarrow \infty} \frac{\mu(R \cdot (a \circ M))}{\mu(a)} = \frac{\mathcal{M}\mu(a)}{\mu(a)}. \quad (4.30)$$

This limit is independent of  $a$  and we denote it by  $e^{-\gamma}$ . Since the indicator function  $\mathbb{1}_A$  of any Borel subset  $A \subset C(M^{-1})$  can be approximated by smooth functions supported in  $C(M^{-1})$  this further proves that  $\mathcal{M}\mu(A) = e^{-\gamma} \mu(A)$ .

The second statement is proven in full analogy to statement (iii) of Theorem 1 in Ref. [60]. First we split any Borel set  $A$  into disjoint  $A \cap D(M^{-1})$  and  $A_c \equiv A \setminus D(M^{-1}) \subset C(M^{-1})$ . This gives

$$\mathcal{M}\mu(A) = \mathcal{M}\mu(A_c) + \underbrace{\mathcal{M}\mu[A \cap D(M^{-1})]}_{=0} = e^{-\gamma} \mu(A_c) \quad (4.31)$$

$$= e^{-\gamma} (\mu(A_c) + \underbrace{\mu[A \cap D(M^{-1})]}_{=0}) = e^{-\gamma} \mu(A) \quad (4.32)$$

which proves that the semiclassical limit measure  $\mu$  is conditionally invariant.  $\square$

The interpretation of Theorem 4.1 is quite simple for continuous maps. This is for example the case for the standard map on the torus. In this case Theorem 4.1 tells us that the limit of any semiclassically convergent sequence of resonance eigenfunctions of a quantum map with escape has to be a conditionally invariant measure of the corresponding classical map with escape  $\mathcal{M}$ . This can be understood intuitively: Resonance eigenfunctions are invariant under time-evolution up to a global decay with rate  $\gamma$  (and some phase). In the semiclassical limit, the quantum time evolution corresponds to the classical one. Thus the limit of resonance eigenfunctions has to be invariant under classical time evolution up to a global decay with the same rate  $\gamma$ .

In this section we showed that convergent sequences of resonance eigenfunctions have conditionally invariant semiclassical limit measures with the same decay rate. Moreover, our numerical investigations in the first subsection suggest that resonance eigenfunctions with decay rates close to each other converge to their average and thus have the *same* semiclassical limit measure. For a fixed decay rate there may exist, however, many different classical conditionally invariant measures. Furthermore, so far only for the natural and the inverse decay rate conditionally invariant measures are constructed, Sec. 2.2.6, but not for arbitrary decay rates  $\gamma$ . The next section deals with these problems and introduces a family of such measures, based on the construction of the natural and inverse measures. These are valuable candidates for the semiclassical limit measures of resonance eigenfunctions.

## 4.3 Conditionally invariant measures for partial escape

In this section we investigate conditionally invariant measures for systems with partial escape, in order to understand the semiclassical behavior of resonance eigenfunctions by classical means. For this purpose we introduce a family of classical conditionally invariant measures which depend only on the decay rate  $\gamma$ . First, we introduce a construction for the natural measure and the inverse measure based on time evolution. In the second section we combine the structure of natural and inverse measure to define a conditionally invariant measure for arbitrary classical decay rates. We finally present another class of conditionally invariant measures based on periodic orbits.

### 4.3.1 Construction of natural and inverse measure

Recall the defining property of the natural measure  $\mu_{\text{nat}}$ : If the dynamics on phase-space is ergodic and hyperbolic, smooth initial distributions asymptotically decay with the same characteristic rate  $\gamma_{\text{nat}}$  and approach the natural measure  $\mu_{\text{nat}}$ . We refer to Sec. 2.2.6 for a more general discussion. In the definition of  $\mu_{\text{nat}}$  we restrict to the uniform initial measure  $\mu_L$ , see Eq. (2.56), which leads to a construction of  $\mu_{\text{nat}}$  by time evolution. Applying the classical

map with escape  $n$  times to  $\mu_L$  gives

$$\mathcal{M}^n \mu_L(A) = \int_A \prod_{i=1}^n R[M^{-i}(\mathbf{x})] d\mu_L(\mathbf{x}). \quad (4.33)$$

Equation (4.33) follows from successive application of the time evolution of measures, Eq. (2.37),  $\mathcal{M}\mu_L(A) = \int_{M^{-1}(A)} R d\mu_L = \int_A R \circ M^{-1} |\det(\mathbf{D}M^{-1})| d\mu_L$ , where integral transformation is used. The determinant of the Jacobian equals one,  $|\det(\mathbf{D}M^{-1})| = 1$ , because the considered maps  $M$  are volume preserving. The natural measure is then given by normalizing  $\mathcal{M}^n \mu_L$  for each  $n$  and taking the limit  $n \rightarrow \infty$ , see Eq. (2.56).

Numerically only finite approximations of  $\mu_{\text{nat}}$  can be obtained for generic systems. Lets call  $\mu_{\text{nat}}^n := \mathcal{M}^n \mu_L / \|\mathcal{M}^n \mu_L\|$  the  $n$ -step approximation of the natural measure  $\mu_{\text{nat}}$ . Contrary to the limit measure  $\mu_{\text{nat}}$ , the finite approximation is absolutely continuous with respect to the Lebesgue measure  $\mu_L$  for all  $n \in \mathbb{N}$ , which trivially follows from Eq. (4.33). In particular, its density  $\rho_{\text{nat}}^n$  is given up to normalization by  $\rho_{\text{nat}}^n(q, p) \propto \prod_{i=1}^n R[M^{-i}(q, p)]$ . Thus the density at a phase-space point  $(q, p)$  is proportional to the average decay of its backward iterates  $\{(q, p), \dots, M^{-n}(q, p)\}$  during the  $n$  time steps. This leads to the following intuitive interpretation: Phase-space points which experience the same average decay under  $n$  backward iterations have the same weight for the natural measure. Thus we call  $\mu_{\text{nat}}$  uniformly distributed on sets with the same average decay under backward iteration.

We now apply the same arguments to the inverse measure  $\mu_{\text{inv}}$ , which is defined as the natural measure of the inverse map  $\mathcal{M}^{-1}$ , see Sec. 2.2.6.2. The inverse time evolution of the uniform distribution yields

$$\mathcal{M}^{-n} \mu_L(A) = \int_A \prod_{i=0}^{n-1} R^{-1}[M^i(\mathbf{x})] d\mu_L(\mathbf{x}), \quad (4.34)$$

which follows from Eq. (2.57). The inverse measure  $\mu_{\text{inv}}$  is then obtained by normalizing  $\mathcal{M}^{-n} \mu_L$  for each  $n$  and taking the limit  $n \rightarrow \infty$ , as in Eq. (2.62). Defining the  $n$ -step approximation of the inverse measure as  $\mu_{\text{inv}}^n := \mathcal{M}^{-n} \mu_L / \|\mathcal{M}^{-n} \mu_L\|$ , we again obtain a measure with density with respect to  $\mu_L$ . This density,  $\rho_{\text{inv}}^n(q, p) \propto \prod_{i=0}^{n-1} R^{-1}[M^i(q, p)]$ , is proportional to the average gain of the forward iterations of the phase-space point  $(q, p)$  under  $R^{-1}$ . Thus phase-space points with the same average gain under  $n$  forward iterations have the same weight. Hence, in contrast to  $\mu_{\text{nat}}$ , the inverse measure  $\mu_{\text{inv}}$  is uniformly distributed on sets with the same average gain under forward iteration.

In Fig. 4.17 the construction of  $\mu_{\text{nat}}$  and  $\mu_{\text{inv}}$  is illustrated for the chaotic standard map with partial escape  $R_\Omega = 0.2$ . By construction, the densities of  $\mu_{\text{nat}}^n$  are reduced on the iterates of the opening,  $M^i(\Omega)$ . Due to the chaotic phase space, after only a few iterations the densities become stretched along the unstable phase-space direction, compare with Fig. 2.3. Conversely, the densities of  $\mu_{\text{inv}}^n$  are enhanced on the opening  $\Omega$  and its preimages  $M^{-i}(\Omega)$ .

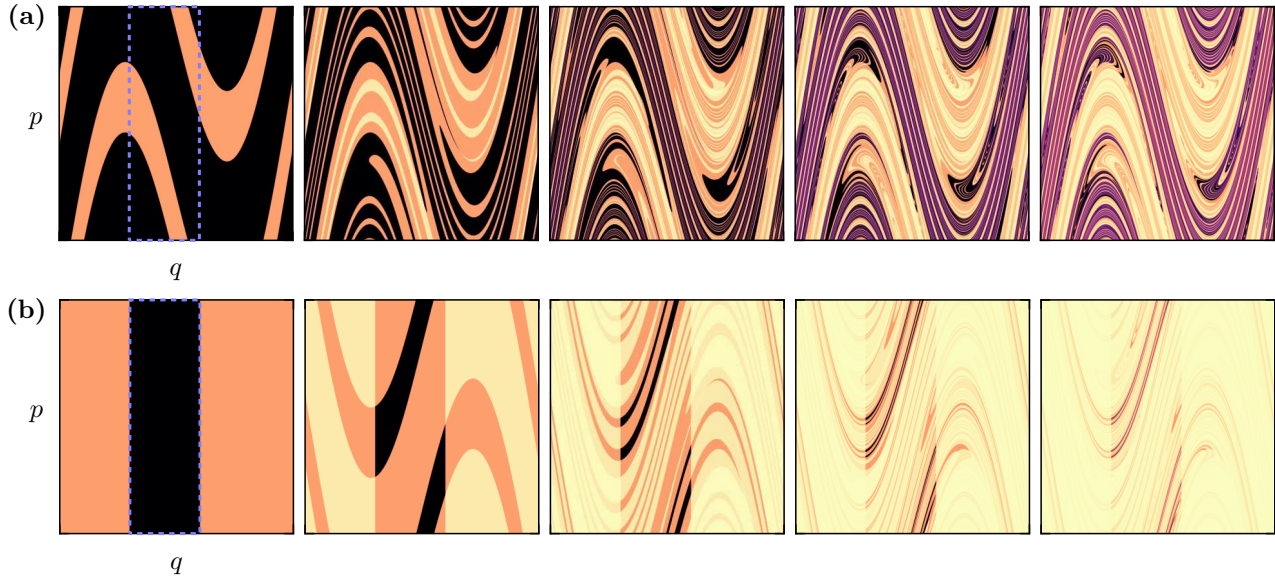


**Figure 4.17:** Finite approximations of (a) natural measure  $\mu_{\text{nat}}^n$  and (b) inverse measure  $\mu_{\text{inv}}^n$  for  $1 \leq n \leq 5$  (from left to right) and the chaotic standard map with partial escape. Shown are the densities evaluated on a grid of size  $1024 \times 1024$ . Dashed blue lines in first panel indicate opening  $\Omega$ . Individual colormap is used for each panel going from zero (light yellow) to the maximum value (black).

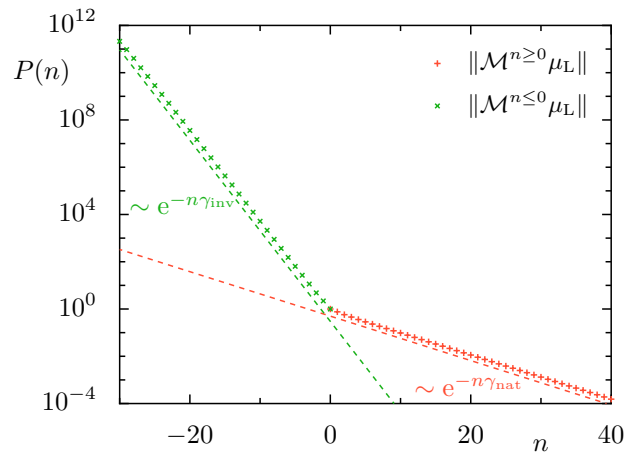


**Figure 4.18:** Weight of forward and backward iteration  $\mathcal{M}\mu_{\text{L}}$  and  $\mathcal{M}^{-1}\mu_{\text{L}}$  of uniform distribution over time step  $n$ . Considered are  $10^8$  uniform initial points on the phase space  $\Gamma$ . The asymptotic scaling  $P(n) \sim e^{-\gamma_{\text{nat}}n}$  and  $P(n) \sim e^{-\gamma_{\text{inv}}n}$  are shown as dashed lines of the same colors, where  $\gamma_{\text{nat}} \approx 0.2165$  and  $\gamma_{\text{inv}} \approx 0.8820$ .

The inverse measure stretches along the unstable phase-space direction of  $M^{-1}$ , which is the stable direction of  $M$ , compare with Fig. 2.3. Both measures have a nontrivial multifractal phase-space structure, which is revealed for larger  $n$ . Note that the filaments of largest intensity become exponentially thin with increasing  $n$ . This construction converges weakly to the natural measure  $\mu_{\text{nat}}$  and the inverse measure  $\mu_{\text{inv}}$ .

The corresponding decay rates  $\gamma_{\text{nat}}$  and  $\gamma_{\text{inv}}$  are obtained from the asymptotic scaling of  $\|\mathcal{M}^n \mu_{\text{L}}\|$  and  $\|\mathcal{M}^{-n} \mu_{\text{L}}\|$  for large  $n$ . We illustrate the exponential decay under the forward

map and the exponential gain under the inverse map for a fixed number of uniform initial conditions on the phase space in Fig. 4.18. The exponential scalings are used to determine natural  $\gamma_{\text{nat}}$  and inverse decay rate  $\gamma_{\text{inv}}$ .

These measures are relevant for quantum mechanics in the following sense. The natural measure  $\mu_{\text{nat}}$  is conjectured to be the semiclassical limit measure of resonance eigenfunctions with decay rate  $\gamma_{\text{nat}}$  [87]. We conjecture that similarly the semiclassical limit measure of resonance eigenfunctions with decay rate  $\gamma_{\text{inv}}$  is given by the inverse measure  $\mu_{\text{inv}}$  [97].

### 4.3.2 Product measure

In the following we use the natural and the inverse measure to construct conditionally invariant measures with arbitrary decay rate  $\gamma$  as presented in Ref. [97]. This is motivated by the following considerations. Assume there exist two conditionally invariant measures which have a density with respect to the Lebesgue measure,  $\mu_{1,2}(A) = \int_A \rho_{1,2} d\mu_{\text{L}}$ . (We emphasize that in general for maps with escape, such measures do not exist and we only use it as a motivation for the following approach.) For such measures we obtain

$$\mathcal{M}\mu_{1,2}(A) \stackrel{\text{Eq. (2.37)}}{=} \int_A (R \circ M^{-1}) \cdot (\rho_{1,2} \circ M^{-1}) d\mu_{\text{L}} \stackrel{\text{Eq. (2.54)}}{=} e^{-\gamma_{1,2}} \int_A \rho_{1,2} d\mu_{\text{L}} \quad (4.35)$$

from time evolution and conditional invariance. Since this holds for all  $A$  and the integrands are all positive, we conclude that for almost all  $\mathbf{x} \in \Gamma$  we have  $R[M^{-1}(\mathbf{x})] \cdot \rho_{1,2}[M^{-1}(\mathbf{x})] = e^{-\gamma_{1,2}} \rho_{1,2}(\mathbf{x})$ . Now consider the product density  $\rho_{\xi} := \rho_1^{1-\xi} \rho_2^{\xi}$  for some  $\xi \in \mathbb{R}$  and the corresponding measure  $\mu_{\xi}(A) = \int_A \rho_{\xi} d\mu_{\text{L}}$ . Time evolution yields

$$\mathcal{M}\mu_{\xi}(A) \stackrel{\text{Eq. (2.37)}}{=} \int_A (R \circ M^{-1}) \cdot (\rho_{\xi} \circ M^{-1}) d\mu_{\text{L}} \quad (4.36)$$

$$= \int_A [(R \circ M^{-1}) \cdot (\rho_1 \circ M^{-1})]^{1-\xi} [(R \circ M^{-1}) \cdot (\rho_2 \circ M^{-1})]^{\xi} d\mu_{\text{L}} \quad (4.37)$$

$$= \int_A [e^{-\gamma_1} (\rho_1 \circ M^{-1})]^{1-\xi} [e^{-\gamma_2} (\rho_2 \circ M^{-1})]^{\xi} d\mu_{\text{L}} \quad (4.38)$$

$$= e^{-[(1-\xi)\gamma_1 + \xi\gamma_2]} \mu_{\xi}(A), \quad (4.39)$$

such that it is conditionally invariant with decay rate  $\gamma_{\xi} = (1 - \xi)\gamma_1 + \xi\gamma_2$ . This implies, that any two conditionally invariant measures with different decay rates  $\gamma_1 \neq \gamma_2$ , that have a density with respect to  $\mu_{\text{L}}$  could be used to construct conditionally invariant measures  $\mu_{\xi}$  with arbitrary decay rates  $\gamma_{\xi}$ . The problem with this approach is, however, that in the considered systems conditionally invariant measures usually are fractal and do not have a density. Nevertheless, this motivates us to look for a similar construction of product measures between the natural measure  $\mu_{\text{nat}}$  and the inverse measure  $\mu_{\text{inv}}$ .

The main idea is to use the local phase-space structure of stable and unstable directions in

hyperbolic maps, discussed in Sec. 2.2.1. While  $\mu_{\text{nat}}$  is smooth along the unstable direction and fractal along the stable direction,  $\mu_{\text{inv}}$  is fractal along the unstable and smooth along the stable direction. This fractal distribution is responsible for fulfilling conditional invariance, i.e., the partial escape with  $R$  and iteration with  $M$  leads to the global decay factors  $e^{-\gamma_{\text{nat}}}$  and  $e^{-\gamma_{\text{inv}}}$ , respectively.

We factorize the reflectivity as  $R = R^{1-\xi}R^\xi$  for any  $\xi \in \mathbb{R}$ . Consider the natural measure for the same map  $M$  but with reflectivity function  $R^{1-\xi}$ , denoted in the following as  $\mu_{\text{nat}}[R^{1-\xi}]$ . The measures  $\mu_{\text{nat}}[R^{1-\xi}]$  all have similar structure to the usual  $\mu_{\text{nat}}$ , which is obtained for  $\xi = 0$ , illustrated in Fig. 4.19(a). Note that for  $\xi = 1$  the uniform measure  $\mu_{\text{L}}$  is obtained. Secondly we define the inverse measure for the reflectivity function  $R^\xi$ , denoted as  $\mu_{\text{inv}}[R^\xi]$ . These measures have similar structure to  $\mu_{\text{inv}}$ , which is obtained for  $\xi = 1$ , while for  $\xi = 0$  we get the uniform distribution, see Fig. 4.19(b).

The hyperbolic phase-space structure implies a local decomposition of  $\mu_{\text{nat}}[R^{1-\xi}]$  as the product of a uniform measure along the unstable, and a fractal measure along the stable direction, as motivated in App. C.3.2. Similarly  $\mu_{\text{inv}}[R^\xi]$  is written locally as the product of a fractal measure in the unstable, and a uniform measure in the stable direction. These considerations lead to a local product measure of the form  $\mu_\xi = \mu_{\text{inv}}[R^\xi] \times \mu_{\text{nat}}[R^{1-\xi}]$ , along unstable and stable direction. The obtained measures are heuristically shown to be conditionally invariant under the map with escape  $\mathcal{M}$  and have decay rate

$$\gamma_\xi = \gamma_{\text{nat}}[R^{1-\xi}] + \gamma_{\text{inv}}[R^\xi], \quad (4.40)$$

see App. C.3.2. For the special case of the generalized bakers map Eq. (4.40) is exact and a rigorous proof of conditional invariance is given in App. C.3.1.

The explicit construction of the product measures  $\mu_\xi$  using time evolution is given by [97]

$$\mu_\xi(A) = \lim_{n \rightarrow \infty} \frac{\tilde{\mu}_\xi^n(A)}{\|\tilde{\mu}_\xi^n\|}, \quad \text{with} \quad (4.41)$$

$$\tilde{\mu}_\xi^n(A) = \int_A \prod_{i=1}^n R^{1-\xi}[M^{-i}(\mathbf{x})] \prod_{j=0}^{n-1} R^{-\xi}[M^j(\mathbf{x})] d\mu_{\text{L}}(\mathbf{x}). \quad (4.42)$$

Apparently these measures are uniformly distributed on sets with the same average decay under backward iteration and the same average gain under forward iteration. For any  $\mathbf{x} \in \Gamma$  the final weight is determined only by the overall decay in  $n$  backward iterations, and does not depend at which time step the decay takes places (and similarly for the forward iterations).

We illustrate the construction of the measures  $\mu_\xi$  for five different values of  $\xi$ , increasing between  $\xi = 0$  to  $\xi = 1$  from left to right, in Fig. 4.19. For each  $\xi$  we show the approximation  $\mu_{\text{nat}}^n[R^{1-\xi}]$  in (a) and  $\mu_{\text{inv}}^n[R^\xi]$  in (b) considering  $n = 5$  iterations. The corresponding normalized product measures  $\mu_\xi^n = \tilde{\mu}_\xi^n / \|\tilde{\mu}_\xi^n\|$ , Eq. (4.42), are illustrated in (c). For  $\xi = 0$  just the first



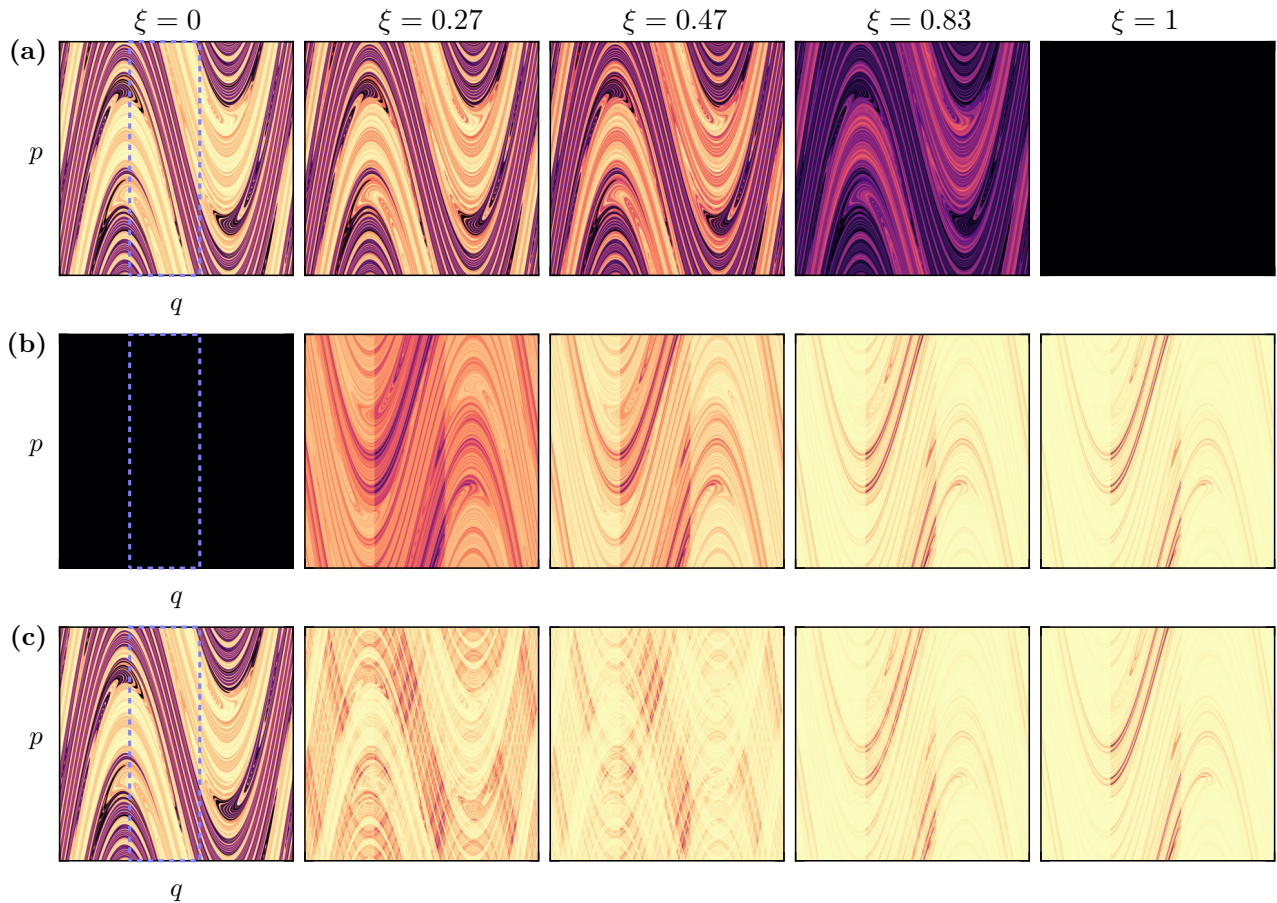


**Figure 4.19:** Construction of product measures  $\mu_\xi$ . Illustrated are finite approximations of (a)  $\mu_{\text{nat}}[R^{1-\xi}]$ , (b)  $\mu_{\text{inv}}[R^\xi]$ , and (c)  $\mu_\xi$ , using  $n = 5$  steps in the construction for  $\xi \in \{0, 0.266, 0.4695, 0.825, 1.0\}$  (from left to right). Each density is shown on a grid of size  $1024 \times 1024$ . The densities in (c) result from multiplying the densities in (a) and (b). For  $\xi = 0$  we have  $\mu_{\text{inv}}[R^\xi] = \mu_L$  (b) and  $\mu_\xi = \mu_{\text{nat}}$ , see (a) and (c). For  $\xi = 1$  we have  $\mu_{\text{nat}}[R^{1-\xi}] = \mu_L$  (a) and  $\mu_\xi = \mu_{\text{inv}}$ , see (b) and (c). Dashed blue line indicates the position of the opening  $\Omega$  in the first panel. Individual colormaps are used for each density going from zero (light yellow) to the maximum value (black).

factor contributes in Eq. (4.42), such that the natural measure is recovered,  $\mu_{\xi=0} = \mu_{\text{nat}}$ , see Eqs. (4.33), with decay rate  $\gamma_{\text{nat}}$ . This follows from Eq. (4.40) as  $\gamma_{\xi=0} = \gamma_{\text{nat}}[R] + \gamma_{\text{inv}}[R^0] = \gamma_{\text{nat}}[R]$ . For  $\xi = 1$  we similarly obtain  $\mu_{\xi=1} = \mu_{\text{inv}}$  see Eq. (4.34), with decay rate  $\gamma_{\xi=1} = \gamma_{\text{inv}}$ . For intermediate values of  $\xi \in (0, 1)$  we observe a transition between  $\mu_{\text{nat}}$  and  $\mu_{\text{inv}}$ . The phase-space densities inherit structures of both measures, with their strength depending on  $\xi$ , see middle panels of Fig. 4.19(c). These finite approximations already reveal a non-trivial multifractal distribution on the underlying hyperbolic structure of the dynamics.

For the same values of  $\xi$  the decay of the measures  $\mu_\xi$  is shown in Fig. 4.20. Here, the measures  $\mu_\xi$  are evaluated on a finite grid of initial conditions using  $n = n_c = 8$  forward and backward iterations in Eq. (4.42). This choice of the construction time  $n_c$  for a given number of initial conditions is discussed in App. C.3.3. We observe an exponential decay of  $\mu_\xi$  proportional to  $\sim e^{-\gamma_\xi n}$  for number of iterations  $n \leq n_c$  (colored lines). The decay rate

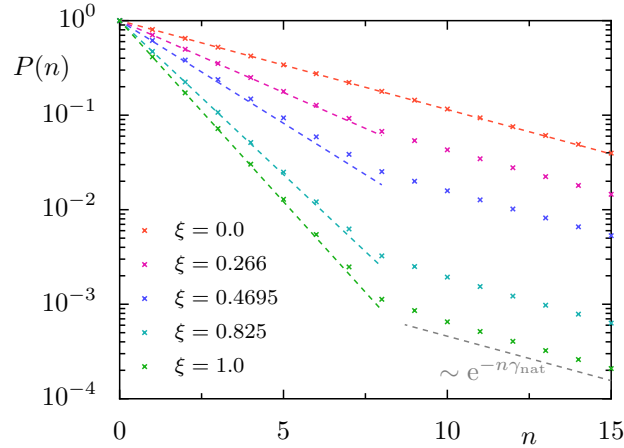


**Figure 4.20:** Decay of product measures,  $P(n) = \|\mathcal{M}^n \mu_\xi\|$ , approximated by  $\mu_\xi^{n_c}$  with  $n_c = 8$  and  $N_c = 8196 \times 8196$  initial conditions on a grid. Considered are the same values of  $\xi$  as in Fig. 4.19 corresponding to  $\gamma_\xi \in \{\gamma_{\text{nat}}, 0.35, \gamma_{\text{typ}}, 0.75, \gamma_{\text{inv}}\}$  (red, violet, blue, cyan, green). For comparison, the expected scaling  $P(n) = e^{-n\gamma_\xi}$  is shown up to  $n \leq n_c$ . For more iterations the scaling converges to the natural decay, see gray dashed line.

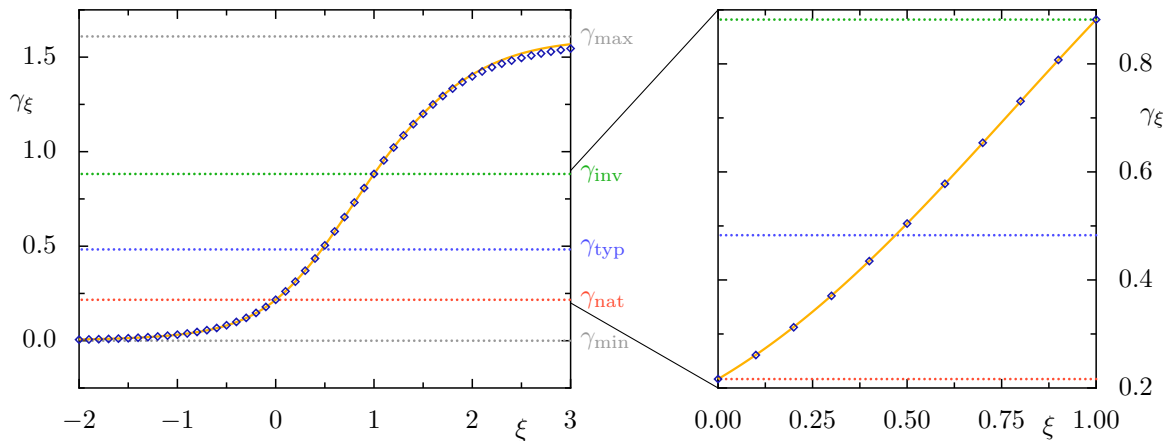


**Figure 4.21:** Classical decay rates  $\gamma_\xi$  as a function of  $\xi$ . Shown is the decay rate  $\gamma_\xi = -\log \mathcal{M} \mu_\xi(\Gamma)$  based on conditional invariance, Eq. (2.54), evaluated for numerically constructed  $\mu_\xi$  (blue diamonds). For comparison a numerical evaluation of Eq. (4.40) is plotted (orange), where decay rates of corresponding natural and inverse measures are used. A closeup of the region with  $\xi \in [0, 1]$  is shown. For the numerical approximation of  $\mu_\xi$ , Eq. (4.42),  $N_c = 8192 \times 8192$  initial conditions on a grid and  $n = 8$  are used. Horizontal lines indicate classical decay rates  $\gamma \in \{\gamma_{\text{min}}, \gamma_{\text{nat}}, \gamma_{\text{typ}}, \gamma_{\text{inv}}, \gamma_{\text{max}}\}$  as indicated.

$\gamma_\xi$  is here evaluated from the first iteration as  $\gamma_\xi = -\log \|\mathcal{M} \mu_\xi\|$  based on Eq. (2.54). If we iterate further than the number of iterations  $n_c$  used to construct  $\mu_\xi$ , the scaling converges to the natural decay rate  $\gamma_{\text{nat}}$  (gray line).

In order to test Eq. (4.40) we evaluate the dependence of  $\gamma_\xi$  on  $\xi$  numerically for the measures  $\mu_\xi$  and compare with the result obtained from  $\mu_{\text{nat}}[R^{1-\xi}]$  and  $\mu_{\text{inv}}[R^\xi]$ . This is illustrated in Fig. 4.21 and we find very good agreement between the theoretical prediction (orange line) and the numerical results for  $\mu_\xi$  (blue diamonds). Here, the measures  $\mu_\xi$  are numerically approximated as before. The theoretical prediction is calculated from the asymptotic scaling

of  $\mu_{\text{nat}}$  and  $\mu_{\text{inv}}$ , when the reflectivity function is adapted accordingly. The decay rate  $\gamma_\xi$  continuously increases with  $\xi$  from  $\gamma_{\text{min}}$  (approached for  $\xi \rightarrow -\infty$ ) to  $\gamma_{\text{max}}$  (approached for  $\xi \rightarrow \infty$ ), while for  $\xi = 0$  and  $\xi = 1$  we obtain  $\gamma_{\text{nat}}$  and  $\gamma_{\text{inv}}$ , respectively. There is perfect agreement in the quantum mechanical relevant region of  $\xi \in [0, 1]$  (magnified plot). Note that the dependence is not linear, as suggested by the motivational considerations, Eq. (4.39).

Let us further remark that the measures  $\mu_\xi$  are defined for reflectivity functions  $R > 0$ , only. In the limit of a closed map, i.e., when  $R(\mathbf{x}) = 1$ , there is no escape and we consistently obtain  $\gamma_\xi = 0$  and the uniform distribution  $\mu_\xi = \mu_{\text{L}}$  for all  $\xi$ . On the other hand, the limit of full escape is not trivial and will be discussed later in Sec. 5.3.2.

### 4.3.3 Periodic orbit measures

In the following we present another class of conditionally invariant measures for partial escape with arbitrary reflectivity functions  $R$ , but which obtain only very specific decay rates. These measures are based on periodic orbits and localize only on a few points in phase space. Therefore recall the atomic measure  $\delta_{\mathbf{y}}$ , defined in Eq. (2.39), which localize on  $\mathbf{y} \in \Gamma$ .

The simplest of these measures localize on fixed points of the closed map. Let  $\mathbf{y} \in \Gamma$  be a fixed point of the closed map  $M$ , i.e.,  $M(\mathbf{y}) = \mathbf{y}$ . Then the atomic measure  $\delta_{\mathbf{y}}$  is a c-measure of the open map  $\mathcal{M}$  with decay rate  $\gamma_{\mathbf{y}} = -\ln R(\mathbf{y})$  which is seen as follows. For all  $A \subset \Gamma$  we have  $\mathcal{M}\delta_{\mathbf{y}}(A) \stackrel{(2.40)}{=} R(\mathbf{y})\delta_{M(\mathbf{y})}(A) = R(\mathbf{y})\delta_{\mathbf{y}}(A) = e^{-\gamma_{\mathbf{y}}}\delta_{\mathbf{y}}(A)$ .

Thus, for all fixed points there exists a conditionally invariant measure of  $\mathcal{M}$  whose decay is given by the reflectivity function  $R$  evaluated at the fixed point. In particular this means, that such a measure exists for a very specific set of decay rates only,  $\gamma \in \{-\ln R(\mathbf{y}) : M(\mathbf{y}) = \mathbf{y}\}$ . For example, if there exists a fixed point  $\mathbf{y}$  with  $R(\mathbf{y}) = \max_{\Gamma} R$ , the corresponding measure  $\delta_{\mathbf{y}}$  has the minimal classically allowed decay rate  $\gamma_{\text{min}}$  (with  $\gamma_{\text{min}} = 0$  if  $\max_{\Gamma} R = 1$ ). Conversely if  $R(\mathbf{y}) = \min_{\Gamma} R$ , the corresponding measure has the maximal decay rate  $\gamma_{\text{max}}$ .

Secondly, consider a periodic orbit  $\underline{\mathbf{p}} = \{\mathbf{y}_0, \mathbf{y}_1\}$  with period  $p = 2$ , such that  $M(\mathbf{y}_0) = \mathbf{y}_1$  and  $M(\mathbf{y}_1) = \mathbf{y}_0$ . Let  $R_0 := R(\mathbf{y}_0)$  and  $R_1 := R(\mathbf{y}_1)$ . Then the measure

$$\mu_{\underline{\mathbf{p}}}(A) := c_0 \delta_{\mathbf{y}_0}(A) + c_1 \delta_{\mathbf{y}_1}(A) \quad (4.43)$$

with  $c_0 = \frac{\sqrt{R_1}}{\sqrt{R_0} + \sqrt{R_1}}$  and  $c_1 = \frac{\sqrt{R_0}}{\sqrt{R_0} + \sqrt{R_1}}$  is a conditionally invariant measure of  $\mathcal{M}$  with decay rate  $\gamma_{\underline{\mathbf{p}}} = -\ln(R_0 R_1)^{1/2}$ . In order to prove this consider for some  $A \subset \Gamma$

$$\mathcal{M}\mu_{\underline{\mathbf{p}}}(A) = c_0 \mathcal{M}\delta_{\mathbf{y}_0}(A) + c_1 \mathcal{M}\delta_{\mathbf{y}_1}(A) = c_0 R(\mathbf{y}_0)\delta_{\mathbf{y}_1}(A) + c_1 R(\mathbf{y}_1)\delta_{\mathbf{y}_0}(A) \quad (4.44)$$

$$= \frac{\sqrt{R_1}R_0}{\sqrt{R_0} + \sqrt{R_1}} \delta_{\mathbf{y}_1}(A) + \frac{\sqrt{R_0}R_1}{\sqrt{R_0} + \sqrt{R_1}} \delta_{\mathbf{y}_0}(A) \quad (4.45)$$

$$= \sqrt{R_0 R_1} [c_1 \delta_{\mathbf{y}_1}(A) + c_0 \delta_{\mathbf{y}_0}(A)] = e^{-\gamma_{\underline{\mathbf{p}}}} \mu_{\underline{\mathbf{p}}}(A), \quad (4.46)$$

which proves that  $\mu_{\underline{p}}$  is conditionally invariant under  $\mathcal{M}$ .

This can be generalized to periodic orbits of arbitrary length. Therefore, consider a periodic orbit  $\underline{p} := \{\mathbf{y}_0, \dots, \mathbf{y}_{p-1}\}$  of period  $p$ , such that  $M(\mathbf{y}_i) = \mathbf{y}_{i+1}$  for  $i < p-1$  and  $M(\mathbf{y}_{p-1}) = \mathbf{y}_0$ . Let  $R_i := R(\mathbf{y}_i)$  as above. Then the measure

$$\mu_{\underline{p}}(A) := \frac{1}{C} \sum_{i=0}^{p-1} c_i \delta_{\mathbf{y}_i}, \quad \text{with} \quad c_i = \left( \prod_{j=0}^{p-1} R_j^{[(j-i) \bmod p]} \right)^{1/p} \quad (4.47)$$

and normalization  $C = \sum_{i=0}^{p-1} c_i$  is a conditionally invariant measure of the map with partial escape  $\mathcal{M}$  and has decay rate  $\gamma_{\underline{p}} := -\ln \prod_{j=0}^{p-1} R_j^{1/p}$ . We emphasize that the decay rate is the average decay rate of the periodic orbit,  $\gamma_{\underline{p}} = -\frac{1}{p} \sum_{j=0}^{p-1} \ln R_j$ . A proof of conditional invariance and uniqueness of  $\mu_{\underline{p}}$  is given in Appendix C.4.

These measures, however, localize on individual periodic orbits. Only in the limit of infinitely large periods  $p$  one thereby achieves measures localizing on the full phase space. Since we do not observe a localization of resonance eigenfunctions on only a few phase-space points we conclude that for small periods  $p$  these measures individually do not play a role for the semiclassical localization of resonance eigenfunctions. We will discuss an outlook in the end of this chapter, how the average over many of these measures could be used to determine the semiclassical limit of resonance eigenfunctions for specific decay rates.

## 4.4 Quantum-to-classical comparison

In this section we compare resonance eigenfunctions with the proposed classical measures  $\mu_{\xi}$ . The goal is to analyze to which extent the measures  $\mu_{\xi}$  describe the phase-space structure of resonance eigenfunctions and if they are possible semiclassical limit measures.

Therefore we first qualitatively compare the phase-space representations of resonance eigenfunctions and classical measures depending on their decay rate. Secondly, we investigate their fractal dimensions using effective entropies of coarse grained phase-space densities. Furthermore we quantify the distance between resonance eigenfunctions and classical measures using the Jensen–Shannon divergence. This distance is used to investigate if the proposed measures  $\mu_{\xi}$  are possible semiclassical limit measures of systems with partial escape. Finally, we modify the amount of escape through the opening  $\Omega$  in terms of the considered reflectivity and also consider openings of different sizes.

### 4.4.1 Qualitative agreement

We illustrate and compare average Husimi distributions  $\langle \mathcal{H} \rangle_{\gamma}$  of resonance eigenfunctions and classical measures  $\mu_{\xi}$  in Fig. 4.22 for the standard map with partial escape. Note that the measures  $\mu_{\xi}$  are illustrated on phase space by considering expectation values of Gaussian

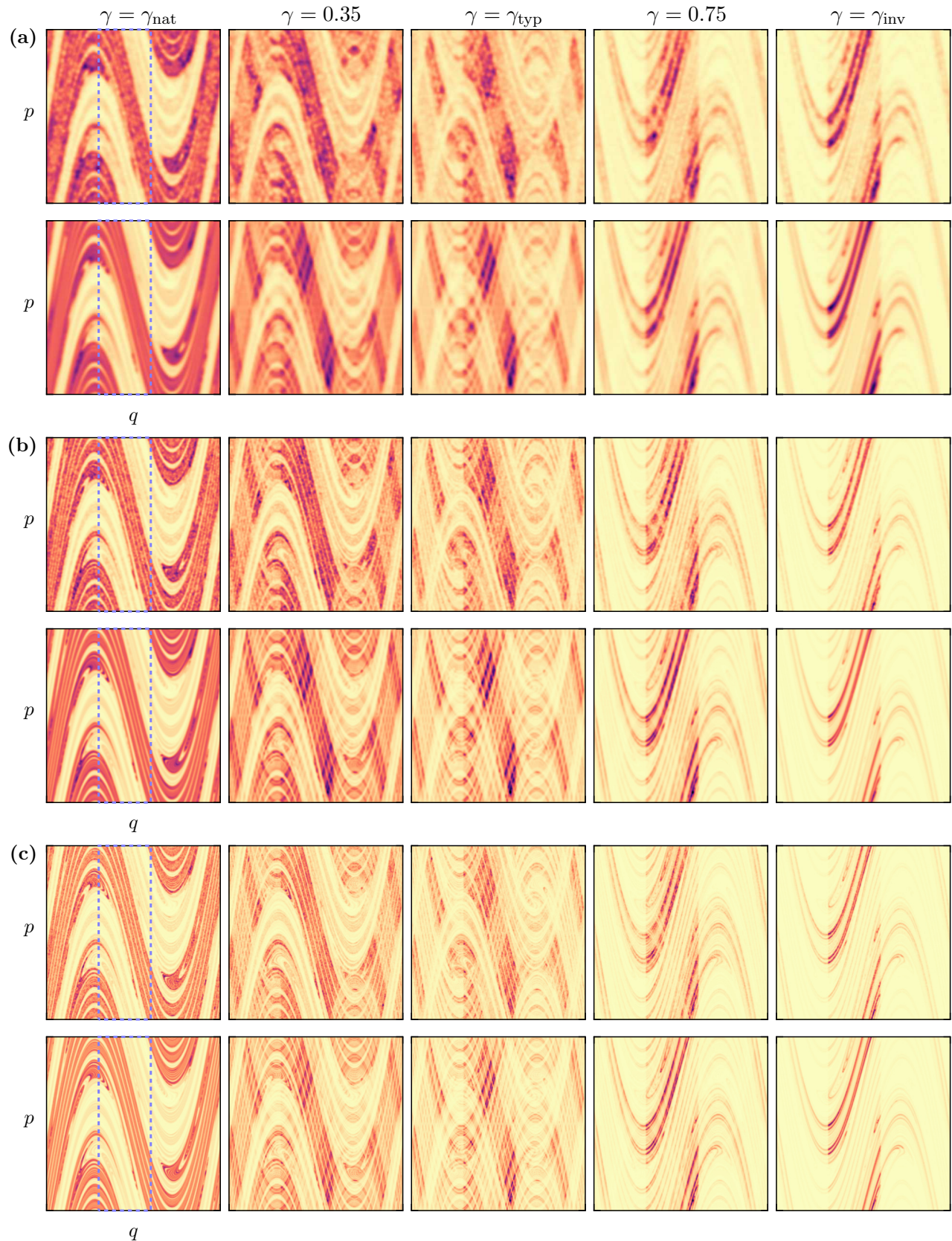


**Figure 4.22:** Quantum-to-classical correspondence for standard map with partial escape. Shown are average Husimi distributions  $\langle \mathcal{H} \rangle_\gamma$  of resonance eigenfunctions averaged over 50 resonances for  $\gamma \in \{\gamma_{\text{nat}}, 0.35, \gamma_{\text{typ}}, 0.75, \gamma_{\text{inv}}\}$  and (a)  $h = 1/1000$ , (b)  $h = 1/4000$ , and (c)  $h = 1/16000$  (top row). Bottom row shows Gaussian smoothed phase-space distribution of c-measures  $\mu_\xi$  for  $\xi \in \{0, 0.266, 0.470, 0.825, 1\}$  corresponding to same  $\gamma$ . Same colormap for quantum and classical densities, with maximum given by  $1.25 \max \langle \mathcal{H} \rangle_\gamma^h$ .

distributions  $g_{\mathbf{x},\sigma}$ , centered at  $\mathbf{x} \in \Gamma$  with width  $\sigma = \sqrt{\hbar/2}$ . This is the classical equivalent to the Husimi distribution  $\mathcal{H}_\psi(\mathbf{x})$ , Eq. (3.6), which is defined as the projection of the quantum state  $\psi$  onto coherent states  $\alpha_{\mathbf{x}}$  centered at  $\mathbf{x} \in \Gamma$  with minimal uncertainty  $\Delta q = \Delta p = \sqrt{\hbar/2}$ . This allows for a meaningful qualitative comparison.

For  $h = 1/1000$ , shown in Fig. 4.22(a), we observe a remarkable similarity between quantum (top) and classical (bottom) distributions. Both show the same multifractal structure, which changes dramatically with  $\gamma$ . We confirm for the natural decay rate  $\gamma_{\text{nat}}$  that the average Husimi distribution of resonance eigenfunctions agrees perfectly with the natural measure  $\mu_{\text{nat}}$ . The distributions at  $\gamma_{\text{nat}}$  are stretched along the unstable direction for regions with high intensity (dark red), but also for the lowest intensities (light yellow). Conversely, the distributions for the inverse decay rate  $\gamma_{\text{inv}}$  concentrate along the stable direction and the maximal values are found inside the opening  $\Omega$ . There is very good agreement between resonance eigenfunctions at  $\gamma_{\text{inv}}$  and the inverse measure  $\mu_{\text{inv}}$ . For intermediate values of  $\gamma$  the densities inherit a structure on both, stable and unstable directions, which reveals the hyperbolic structure on phase space. Recall that the definition of the classical measures  $\mu_\xi$  is based on this product structure, see Sec. 4.3.2. The product structure of the Husimi distributions resembles that of the classical densities. There are, however, visible differences in the strength of this effect: For example, at  $\gamma = \gamma_{\text{typ}}$  (middle panels) a careful inspection reveals stronger peaks along the stable direction for the classical measures (dark-red diagonal central structure) than for the resonance eigenfunctions.

We present the same qualitative comparison for  $h = 1/4000$  (b) and  $h = 1/16000$  (c), in order to check if the observations persist further towards the semiclassical limit. We confirm this on a qualitative level: For natural decay rate  $\gamma_{\text{nat}}$  and inverse decay rate  $\gamma_{\text{inv}}$  there is excellent quantum-to-classical agreement. (left and right panels). The hyperbolic structure is revealed for the intermediate decay rates on a scale which depends on  $h$  (middle panels). The Husimi distributions change with increasing decay rate  $\gamma$  similar to the classical measures. The observed over-enhancement of the classical measures  $\mu_\xi$  compared to the Husimi distributions is still visible in specific phase-space regions, e.g., for  $\gamma_{\text{typ}}$  in the diagonal central structure. However, these differences occur on smaller scales due to the finer phase-space resolution.

Altogether the qualitative similarity of quantum and classical distributions confirms that the main structure of resonance eigenfunctions has a classical origin. In particular, the dependence of this structure on the decay rate  $\gamma$  follows the classical structures of  $\mu_\xi$  from the unstable to the stable direction on the phase space. Classically this dependence is understood from the definition of  $\mu_\xi$ , see Sec. 4.3.2. However, a close inspection shows that there are small but still visible differences between the classical and quantum results for all  $h$ , e.g., for  $\gamma = \gamma_{\text{typ}}$  in the region around  $(q, p) = (0.5, 0.75)$ , see Fig. 4.22. From this qualitative comparison it is not clear, if these differences vanish in the semiclassical limit. This motivates to pursue more quantitative comparisons between resonance eigenfunctions and classical measures.

### 4.4.2 Fractal dimensions

In order to find a quantitative comparison between quantum and classical phase-space distribution we first investigate their fractal properties. These are characterized by non-integer fractal dimensions, see Sec. 2.2.5. Since the support of resonance eigenfunctions for any  $\gamma$  is given by the full phase space  $\Gamma$ , their box-counting dimension, Eq. (2.46), must be equal to the dimension of the phase-space,  $D_0 = 2$ . This also holds for the classical product measures  $\mu_\xi$  at least in the relevant region for  $\xi \in [0, 1]$ . Therefore we consider the full spectrum of generalized Rényi-dimensions  $D_q$ , Eq. (2.47), and in particular the information dimension  $D_1$ , Eq. (2.49).

In order to quantify fractality of resonance eigenfunctions, let us apply the definition of the information entropy  $S_1(\mu, \epsilon)$ , Eq. (2.48), to the Husimi measure  $\mu_\psi$  which is implied by the Husimi density  $\mathcal{H}_\psi$ , see (3.11). Recall that  $\epsilon > 0$  is the size of the boxes that partition the phase space, and assume it to be fixed. Any weakly convergent sequence of resonance eigenfunctions  $\psi_\gamma^h$  as in Theorem 4.1, with limiting decay rate  $\gamma$  can be used to define the semiclassical limit of this entropy as

$$S_1^{\text{sc}}(\gamma, \epsilon) := \lim_{h \rightarrow 0} S_1(\mu_{\psi_\gamma^h}, \epsilon). \quad (4.48)$$

The semiclassical information dimension of this sequence follows from  $S_1^{\text{sc}}(\gamma, \epsilon)$  by taking the limit

$$D_1^{\text{sc}}(\gamma) = - \lim_{\epsilon \rightarrow 0} \frac{S_1^{\text{sc}}(\gamma, \epsilon)}{\ln \epsilon} \quad (4.49)$$

as in Eq. (2.49). We emphasize that this only leads to non-trivial results, however, if the limit  $h \rightarrow 0$  (in the definition of  $S_1^{\text{sc}}$ ) is taken before considering  $\epsilon \rightarrow 0$ . It is not possible to interchange these limits, because for finite  $h$  the information content of the Husimi measure  $\mu_\psi$  does not increase on scales of order  $\epsilon \lesssim \sqrt{\hbar}$  due to the smoothness of  $\mathcal{H}_\psi^h$ . Therefore taking the limit  $\epsilon \rightarrow 0$  for finite  $h$  results in the trivial dimension  $D_1 = 2$  for all resonance eigenfunctions. These considerations are similarly valid for the generalized Rényi entropies  $S_q(\mu, \epsilon)$  and dimensions  $D_q(\mu)$ , Eq. (2.47), by considering arbitrary  $q$  in Eqs. (4.48) and (4.49).

Nevertheless, we want to quantify the fractality of resonance eigenfunctions at finite values of  $h$  as an effective approximation for the limiting case. For this purpose, let us consider the effective entropies  $S_q(\mu_{\psi_\gamma^h}, \epsilon)$  for fixed values of  $h$ . Because the phase-space density is smooth on the order of  $h$  this quantity is only reasonable to consider for  $\epsilon \gtrsim \sqrt{\hbar}$ . With this in mind we define an effective generalized dimension in terms of the local scaling of  $S_q(\mu, \epsilon)$  with  $\ln \epsilon$  as

$$D_q(\mu, \epsilon) := - \frac{\partial S_q(\mu, \epsilon)}{\partial \ln \epsilon} \approx - \frac{S_q(\mu, \epsilon) - S_q(\mu, \epsilon + \Delta\epsilon)}{\ln \epsilon - \ln(\epsilon + \Delta\epsilon)}, \quad (4.50)$$

for small  $\Delta\epsilon$ . This is equivalent to the local fractal dimensions discussed for classical measures in Refs. [92,197]. It obtains non-trivial values only in the regime of relatively large  $\epsilon \gtrsim \sqrt{h}$ . In the following we apply this quantity to resonance eigenfunctions  $\psi_\gamma$  and reveal their fractal properties effectively for finite values of  $\epsilon$ . Numerically we consider the scaling in Eq. (4.50) for a finite interval of  $\epsilon \in [1/16, 1/4]$ . This choice gives numerically reasonable results. For other choices of  $\epsilon$  we refer to App. B.3.

In Figure 4.23 we illustrate the effective fractal dimensions  $D_q(\gamma, \epsilon) := D_q(\mu_{\psi_\gamma}, \epsilon)$  of all resonance eigenfunctions of the standard map with partial escape as a function of their decay rate  $\gamma$  at decreasing values of  $h \in \{1/250, 1/1000, 1/4000, 1/16000\}$  and compare them to the classical result for the product measures  $\mu_\xi$  with the same decay rate for  $q \in \{1, \dots, 4\}$ . For all  $q$  we observe a nontrivial dependence of  $D_q(\gamma, \epsilon)$  on  $\gamma$ . This illustrates the multifractal nature of resonance eigenfunctions in maps with partial escape, and most importantly, that it depends strongly on the decay rate. Panel (a) shows the information dimension. We notice that smaller values of  $h$  lead to larger effective  $D_1$  for all decay rates, which is explained by quantum fluctuations on the order of  $\epsilon$ , further analyzed in App. B.3. The shape of the progression, however, does not change much for different  $h$ . First, the dimension increases slightly with  $\gamma$  up to a maximum value, and then decreases for decay rates with  $\gamma \gtrsim 0.4$  up to minimal values around  $\gamma_{\text{inv}}$ . For  $h \rightarrow 0$  the obtained effective dimensions of the eigenfunctions will semiclassically converge to the corresponding effective dimension of the limit measure. Here, the numerical values for  $h = 1/16000$  (green markers) are closest to this limit and should be compared to the classical result for  $\mu_\xi$  (dashed blue line). The agreement between the obtained effective quantum and classical information dimensions is excellent. The maximum of the classical dimensions is around  $\gamma \approx 0.35$  continuously decreasing for larger and smaller decay rates, with  $D_1(\mu_{\text{nat}}, \epsilon) \approx 1.9$  and  $D_1(\mu_{\text{inv}}, \epsilon) \approx 1.7$ .

Furthermore, the effective generalized Rényi dimensions  $D_q(\gamma, \epsilon)$  are illustrated in (b)  $q = 2$ , (c)  $q = 3$ , and (d)  $q = 4$ . In all cases the dependence on  $\gamma$  is nontrivial and changes with  $q$ . This supports the claim, that resonance eigenfunctions have a multifractal character. The position of the maximum moves closer to  $\gamma_{\text{nat}}$  for larger  $q$ , and we also observe overall smaller values. The effective dimensions have a similar dependence on  $h$  as for  $q = 1$ . For the smallest value,  $h = 1/16000$ , we find that the effective dimensions of resonance eigenfunctions agree very well with those of the proposed measures  $\mu_\xi$ . This holds for all considered  $q$ .

So far we considered single resonance eigenfunctions. Let us also consider effective fractal dimensions of average Husimi distributions  $\langle \mathcal{H} \rangle_\gamma$ , which are similarly defined by Eq. (4.50). This will be denoted by the same symbol  $D_q(\gamma, \epsilon)$  in the following and, whenever necessary, it will be explicitly stated if single or average eigenfunctions are used. The results are illustrated in Fig. 4.24 considering  $\langle \mathcal{H} \rangle_\gamma$  for  $\gamma \in [\gamma_{\text{nat}}, \gamma_{\text{inv}}]$  and taking the average over 50 eigenfunctions as in Sec. 4.2.3. The quantum results are shown as straight lines using the same colors as in Fig. 4.23, while the classical results for  $\mu_\xi$  again are shown for comparison as a dashed blue



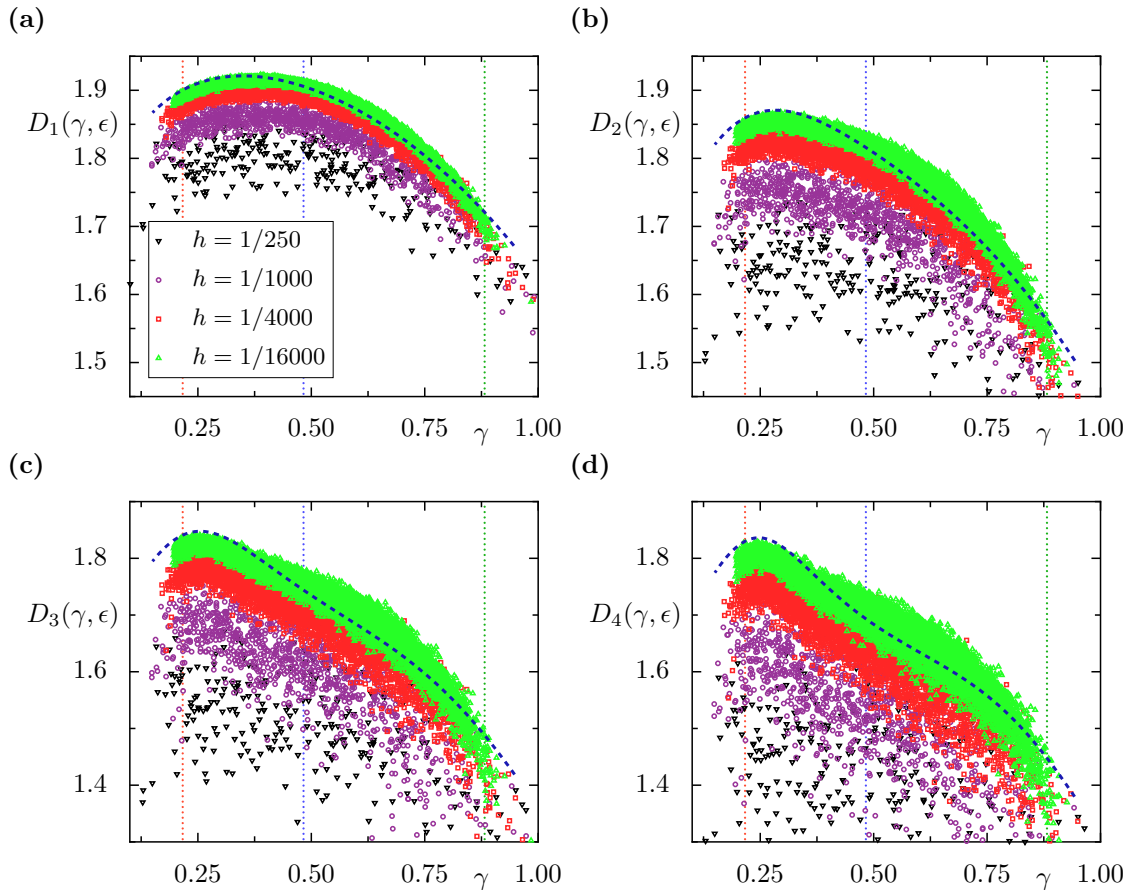


**Figure 4.23:** Fractal dimensions of single resonance eigenfunctions and classical measures for partial escape. Shown are effective Rényi-dimensions  $D_q(\gamma, \epsilon)$  of Husimi distributions  $\mathcal{H}_\gamma$  of resonance eigenfunctions as a function of  $\gamma$  for  $h \in \{1/250, 1/1000, 1/4000, 1/16000\}$  (black, violet, red, green). Considered are dimensions for (a)  $q = 1$ , (b)  $q = 2$ , (c)  $q = 3$ , and (d)  $q = 4$ , while  $\epsilon \in [1/4, 1/16]$ . Results for the classical measures  $\mu_\xi$  are shown for comparison (dashed line). Vertical dotted lines indicate  $\gamma_{\text{nat}}$ ,  $\gamma_{\text{typ}}$  and  $\gamma_{\text{inv}}$  (red, blue, green).

line. Comparing quantum and classical results for  $D_1(\gamma, \epsilon)$  in Fig. 4.24(a), we find excellent agreement for decay rates between  $\gamma_{\text{nat}}$  and  $\gamma \approx 0.35$  and also close to  $\gamma_{\text{inv}}$ . However, for intermediate decay rates the information dimension of the quantum system are systematically larger than the classical ones. Corresponding results for the effective Rényi dimensions  $D_q$  with  $q \in \{2, \dots, 3\}$  are shown in (b)–(d). Again we observe generally smaller dimensions for larger  $q$ , while the position of the maximum moves towards  $\gamma_{\text{nat}}$ . The results of the quantum system closely resemble the curve for  $\mu_\xi$  for decay rates around  $\gamma_{\text{nat}}$  and  $\gamma_{\text{inv}}$ . For intermediate decay rates similar differences are seen as for  $q = 1$ .

We emphasize that there are two main differences between Fig. 4.24 and Fig. 4.23. First, the averaged Husimis generally show larger fractal dimensions due to the reduction of quantum fluctuations. Secondly, for  $h \geq 1/1000$  the obtained quantum results fall almost on top of each other. The second observation implies, that taking first the average of Husimi distributions seemingly leads to a much faster convergence of the effective dimensions than for single eigenfunctions. Thus it is very likely that these results are already very good approximations of the

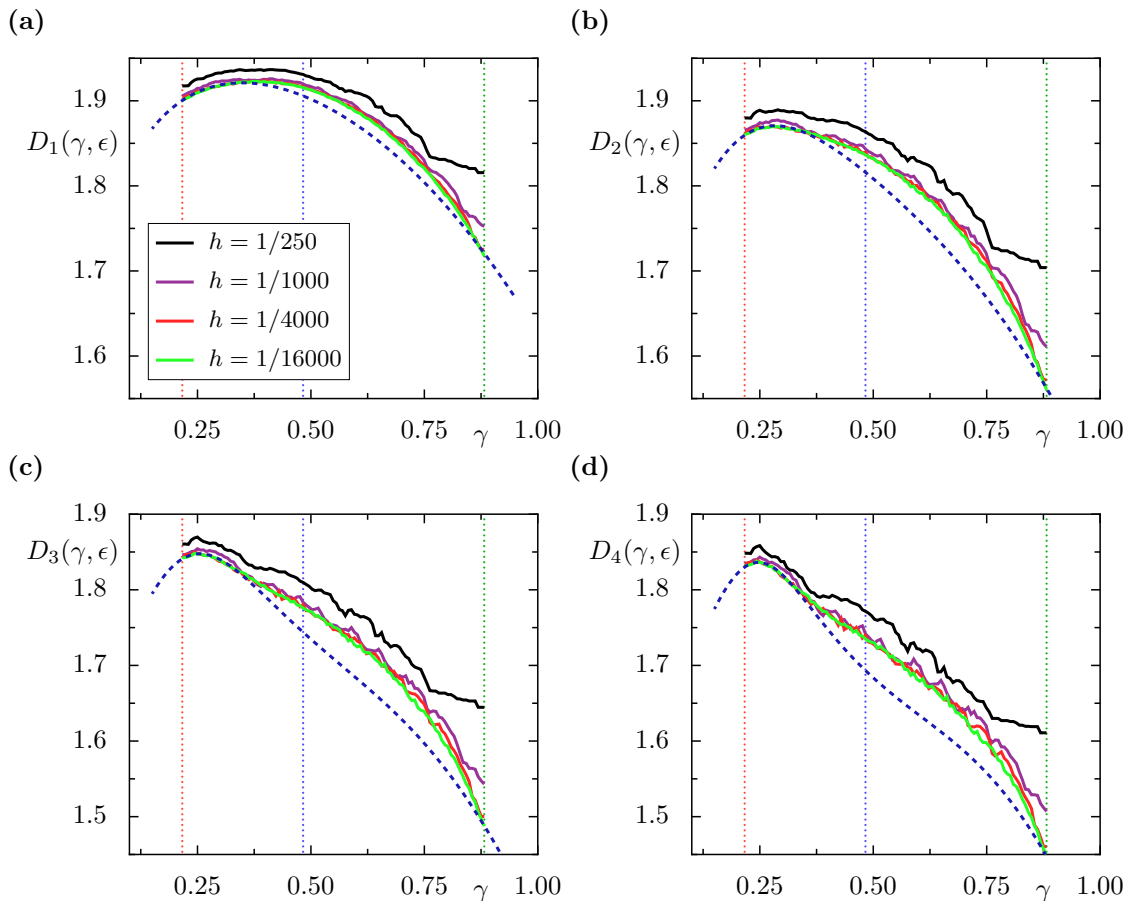


**Figure 4.24:** Fractal dimensions of average resonance eigenfunctions and classical measures for partial escape. Shown are effective Rényi-dimensions  $D_q(\gamma, \epsilon)$  as a function of  $\gamma$  considering average Husimi distributions  $\langle \mathcal{H} \rangle_\gamma$  of 50 eigenfunctions for  $h \in \{1/250, 1/1000, 1/4000, 1/16000\}$  (black, violet, red, green). The parameter  $q$  is chosen as (a)  $q = 1$ , (b)  $q = 2$ , (c)  $q = 3$ , and (d)  $q = 4$ , while  $\epsilon \in [1/4, 1/16]$ . Results for the classical measures  $\mu_\xi$  are shown for comparison (dashed line). Vertical dotted lines indicate  $\gamma_{\text{nat}}$ ,  $\gamma_{\text{typ}}$  and  $\gamma_{\text{inv}}$  (red, blue, green).

semiclassical limit, at least for  $h = 1/16000$ .

Finally we illustrate the spectrum of effective Rényi dimensions  $D_q(\gamma, \epsilon)$  as a function of  $q$  considering the averaged Husimi distributions  $\langle \mathcal{H} \rangle_\gamma$  for  $h = 1/16000$  in Fig. 4.25 (open colored symbols). We chose the same decay rates  $\gamma \in \{\gamma_{\text{nat}}, 0.35, \gamma_{\text{typ}}, 0.75, \gamma_{\text{inv}}\}$  as in Fig. 4.22, and compare to the classical results for the corresponding  $\mu_\xi$  (filled blue symbols). For the box-counting dimension,  $q = 0$ , we obtain the trivial result  $D_0 = 2$  for all  $\gamma$ , as expected for both quantum and classical densities. Increasing  $q$  leads to smaller effective dimensions  $D_q(\gamma, \epsilon)$  which seem to saturate at finite values. This is observed for the resonance eigenfunctions as well as for the classical measures. The limit for large  $q$  depends on the decay rate  $\gamma$ . This quantum-to-classical comparison shows once again that at the natural decay rate  $\gamma_{\text{nat}}$  the effective Rényi spectra show perfect agreement. This supports the conjecture, that the semiclassical limit measure at  $\gamma_{\text{nat}}$  is the natural measure. We also find excellent agreement at the inverse decay rate  $\gamma_{\text{inv}}$ , which is a strong indication that the semiclassical limit measure

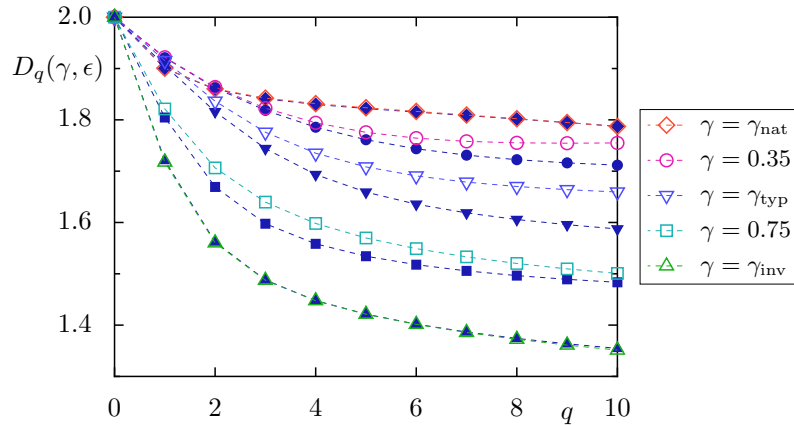


**Figure 4.25:** Fractal dimensions of resonance eigenfunctions and classical measures. Shown are effective Rényi dimensions  $D_q(\gamma, \epsilon)$  as a function of  $q$  for five different decay rates  $\gamma \in \{\gamma_{\text{nat}}, 0.35, \gamma_{\text{typ}}, 0.75, \gamma_{\text{inv}}\}$  (diamond, circle, lower triangle, square, upper triangle) considering average Husimis  $\langle \mathcal{H} \rangle_\gamma$  of 50 eigenfunctions for  $h = 1/16000$  (open symbols) and the classical measures  $\mu_\xi$  (filled symbols).

is  $\mu_{\text{inv}}$  for this decay rate, as we conjectured in Ref. [97]. Interestingly, for  $\gamma = 0.35$  quantum and classical effective dimensions agree up to  $q = 3$  (circles). Only for larger  $q$  we clearly see deviations. On the other hand, for the typical decay rate  $\gamma_{\text{typ}}$  and for  $\gamma = 0.75$  there are visible deviations for all values of  $q$ , which is consistent with the observations in Fig. 4.24.

Altogether this shows, that we are able to effectively quantify multifractal properties of resonance eigenfunctions. The numerical results strongly support the claim, that the semiclassical limit measures also have nontrivial fractal dimensions, which depend on the decay rate  $\gamma$ , and are indeed multifractals. Furthermore, the proposed measures  $\mu_\xi$  lead to very good approximations for the multifractal spectrum of Rényi dimensions, with excellent agreement for  $\gamma_{\text{nat}}$  and  $\gamma_{\text{inv}}$ , but showing slight deviations for intermediate decay rates. This motivates us to further investigate a quantitative distance between resonance eigenfunctions and the proposed measures  $\mu_\xi$ .

### 4.4.3 Jensen–Shannon divergence

The distance between quantum and classical measures can be quantified using any metric on the sets of probability measures. In this thesis we consider the Jensen–Shannon divergence [76], which quantifies the similarity of two measures. It has various applications, e.g., for image recognition [198], in information theory [199], and for the analysis of correlations of DNA segments [200], symbolic sequences [201], citation networks [202], or decision making problems [203].

Assume a partition of the phase space into sets  $\mathcal{A}_\epsilon = \{A_i^\epsilon\}$  with  $\mu(A_i^\epsilon) = \epsilon^2$  as introduced in Sec. 2.2.5. For any two probability measures  $\mu_1$  and  $\mu_2$  the Jensen–Shannon divergence  $d_{\text{JS}}^\epsilon$

on the partition  $\mathcal{A}_\epsilon$  is defined as [76]

$$d_{\text{JS}}^\epsilon(\mu_1, \mu_2) = S_1\left(\frac{\mu_1 + \mu_2}{2}, \epsilon\right) - \frac{S_1(\mu_1, \epsilon) + S_1(\mu_2, \epsilon)}{2}, \quad (4.51)$$

in terms of the information entropy  $S_1(\mu, \epsilon)$  evaluated for the discretized measures  $\mu_{1,2}(A_i^\epsilon)$ , see definition in Eq. (2.48). The Jensen–Shannon divergence is the difference of the information entropy of the mean  $(\mu_1 + \mu_2)/2$  of both measures and the mean of their individual entropies. In the following we always write  $d_{\text{JS}}$  without the superscript  $\epsilon$ . The square root of  $d_{\text{JS}}$  is a metric [204], such that it can be used to evaluate the distance between two measures. This also implies that  $d_{\text{JS}}(\mu_1, \mu_2) \geq 0$  with equality if and only if  $\mu_1 = \mu_2$ . The scale  $\epsilon$  introduced in the definition of  $d_{\text{JS}}$  defines the considered coarseness on the phase-space. This is required, because semiclassical convergence of resonance eigenfunctions is expected only weakly, see Sec. 4.2.2, e.g., for observables of fixed size  $\epsilon$ . For quantum-to-classical comparison the calculated difference is only meaningful if  $\epsilon \gtrsim \sqrt{\hbar}$ . In the following we consider  $\epsilon = 1/16$ , which approximately satisfies  $\epsilon \approx \sqrt{\hbar}$  for  $h = 1/250$ .

The Jensen–Shannon divergence between individual Husimi distributions  $\mathcal{H}_\gamma$  and several classical measures is illustrated in Fig. 4.26 for all quantum decay rates  $\gamma$  at different values of  $h$ . We consider classically the uniform measure  $\mu_L$  (gray circles), the natural measure  $\mu_{\text{nat}}$  (red boxes), the inverse measure  $\mu_{\text{inv}}$  (green triangles), and the proposed measures  $\mu_\xi$  (blue diamonds) with  $\xi$  adapted to the respective  $\gamma$ , see Sec. 4.3.2. Apparently, the distance of resonance eigenfunctions to the natural measure  $\mu_{\text{nat}}$  has a pronounced minimum at  $\gamma = \gamma_{\text{nat}}$  and increases significantly with  $\gamma$ , see Fig. 4.26(a). This quantifies the observation, that the structure of resonance eigenfunctions at  $\gamma_{\text{nat}}$  agrees well with  $\mu_{\text{nat}}$ , but changes with  $\gamma$ . Simi-

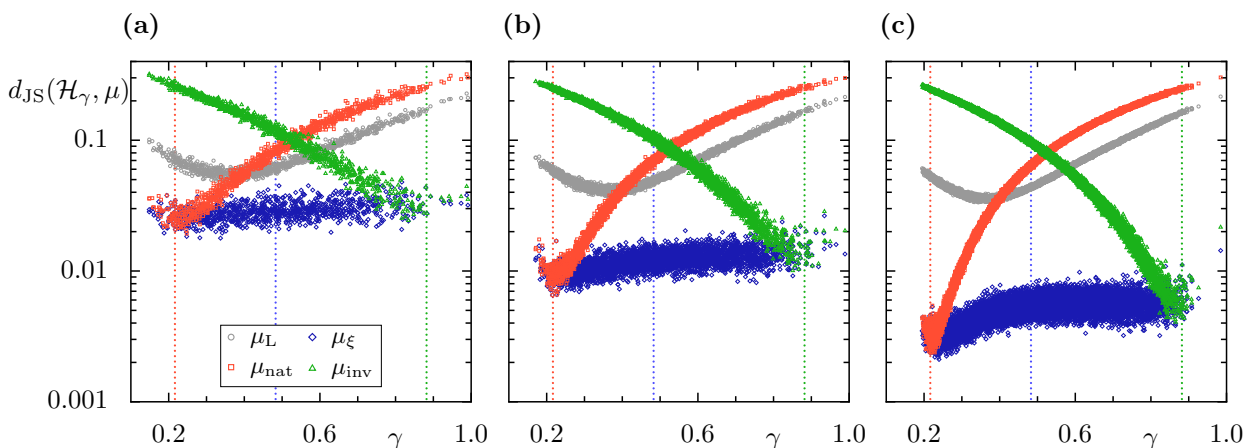


**Figure 4.26:** Jensen–Shannon divergence between single quantum Husimi distributions  $\mathcal{H}_\gamma$  and different classical measures as a function of the decay rate  $\gamma$  for (a)  $h = 1/1000$ , (b)  $h = 1/4000$ , and (c)  $h = 1/16000$ . The symbols correspond to the considered measures  $\mu_\xi$  (blue diamonds),  $\mu_{\text{nat}}$  (red boxes),  $\mu_{\text{inv}}$  (green triangles), and  $\mu_L$  (gray circles). Dotted vertical lines indicate  $\gamma_{\text{nat}}$ ,  $\gamma_{\text{typ}}$ , and  $\gamma_{\text{inv}}$  (red, blue, green).

larly the distance to  $\mu_{\text{inv}}$  is minimal at  $\gamma_{\text{inv}}$  and increases significantly for smaller decay rates. The distance to the uniform measure  $\mu_{\text{L}}$  obtains values between these limits and is minimal at around  $\gamma \approx 0.35$ . This shows that in the considered system resonance eigenfunctions at this decay rate are closer to uniformity, which is also seen in the maximum of the information dimension in Fig. 4.23. The distances  $d_{\text{JS}}$  between eigenfunctions and the conditionally invariant measures  $\mu_{\xi}$  are much smaller than for the other measures. We emphasize on the fact that there is almost no dependence on  $\gamma$ . This means that for the considered phase-space resolution  $\epsilon$  and Planck's constant  $h$  the proposed measures  $\mu_{\xi}$  are equally suitable to describe the Husimi distribution  $\mathcal{H}_{\gamma}$  irrespective of  $\gamma$ .

Reducing  $h$  in Fig. 4.26(b) and (c) we confirm that the Jensen–Shannon divergence between quantum and classical measures reduces significantly for all  $\gamma$  only for  $\mu_{\xi}$ . For  $\mu_{\text{nat}}$  and  $\mu_{\text{inv}}$  such a decrease is observed at  $\gamma_{\text{nat}}$  and  $\gamma_{\text{inv}}$ , respectively, while the distance remains almost constant for other decay rates. There is no qualitative change of the distances for the uniform measure  $\mu_{\text{L}}$ . Note that variation of  $\epsilon > \sqrt{h}$  leads to similar results with overall smaller distances for larger  $\epsilon$  and vice versa, see Appendix B.4.

We additionally confirm that the proposed measures  $\mu_{\xi}$  agree very well with resonance eigenfunctions in Fig. 4.27, where the Jensen–Shannon divergence  $d_{\text{JS}}$  between average Husimis  $\langle \mathcal{H} \rangle_{\gamma}$  and classical measures is shown for the same parameters as in Fig. 4.26. For  $h = 1/1000$  the distance between  $\langle \mathcal{H} \rangle_{\gamma}$  and  $\mu_{\xi}$  is approximately one magnitude smaller than between  $\langle \mathcal{H} \rangle_{\gamma}$  and  $\mu_{\text{L}}$ , see Fig. 4.27(a). For  $\mu_{\text{nat}}$  and  $\mu_{\text{inv}}$  a sharp minimum is observed at  $\gamma_{\text{nat}}$  and  $\gamma_{\text{inv}}$ , respectively. For smaller  $h = 1/4000$  and  $1/16000$  the distances for  $\mu_{\text{L}}$  do not decrease, while for  $\mu_{\text{nat}}$  and  $\mu_{\text{inv}}$  the minimum becomes sharper, see Fig. 4.27(b) and (c). The distances for the product measures  $\mu_{\xi}$  decrease for all decay rates  $\gamma$  when  $h$  becomes smaller. However, for

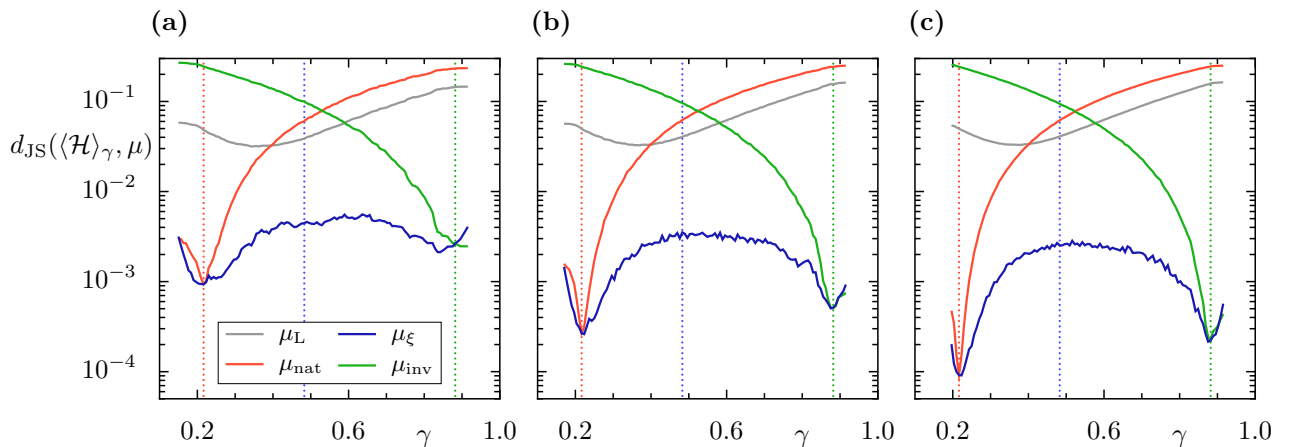


**Figure 4.27:** Jensen–Shannon divergence between average Husimi distributions and different classical measures as a function of the decay rate  $\gamma$  for (a)  $h = 1/1000$ , (b)  $h = 1/4000$ , and (c)  $h = 1/16000$ . The average in  $\langle \mathcal{H} \rangle_{\gamma}$  is taken over 50 eigenfunctions. The considered classical measures are  $\mu_{\xi}$  (blue),  $\mu_{\text{nat}}$  (red),  $\mu_{\text{inv}}$  (green), and  $\mu_{\text{L}}$  (gray). Dotted vertical lines indicate  $\gamma_{\text{nat}}$ ,  $\gamma_{\text{typ}}$ , and  $\gamma_{\text{inv}}$  (red, blue, green).

intermediate decay rates this is barely visible between  $h = 1/4000$  and  $h = 1/16000$ .

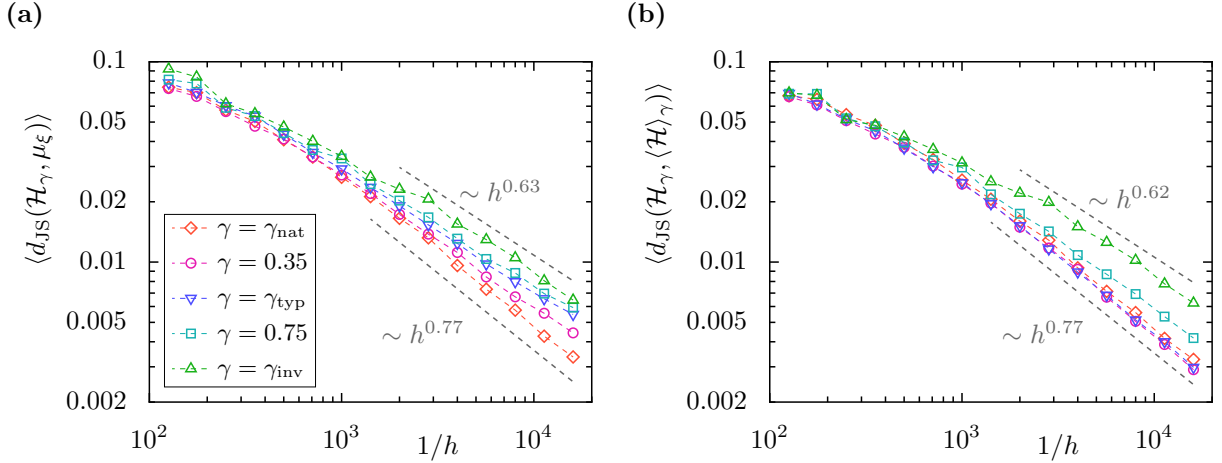
Altogether, if the considered classical measure at a given decay rate  $\gamma$  is not the semiclassical limit measure, as for  $\mu_L$ ,  $\mu_{\text{nat}}$  (large  $\gamma$ ) and  $\mu_{\text{inv}}$  (small  $\gamma$ ), we see a very fast saturation of the Jensen–Shannon divergence at finite values. This is independent of the choice of single or averaged Husimi distributions. On the other hand, the numerical results agree with the conjectures that  $\mu_{\text{nat}}$  and  $\mu_{\text{inv}}$  are the semiclassical limit measures at  $\gamma_{\text{nat}}$  and  $\gamma_{\text{inv}}$ , respectively. In the next section we investigate the dependence of  $d_{\text{JS}}$  with  $h$  in order to quantify to which extent the product measures  $\mu_\xi$  are suitable as semiclassical limit measures of resonance eigenfunctions with arbitrary decay rates.

#### 4.4.4 Semiclassical limit

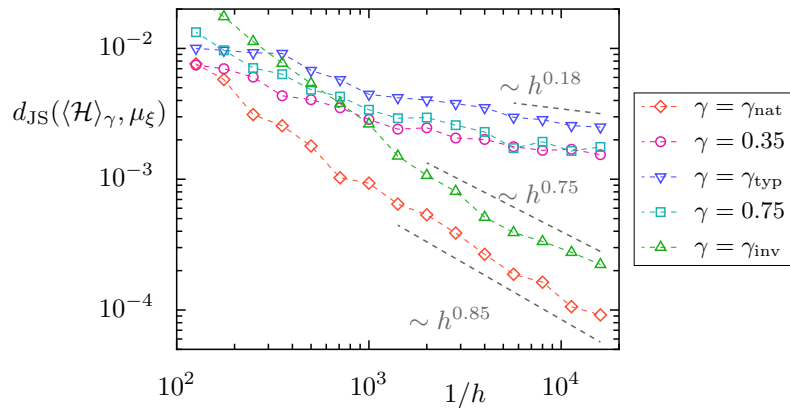
Since resonance eigenfunctions converge weakly towards their semiclassical limit measure, their distance  $d_{\text{JS}}$ , defined on a finite partition of the phase space in Eq. (4.51), converges to zero in the semiclassical limit. Therefore we consider the dependence of  $d_{\text{JS}}$  between Husimi distributions and the proposed measures  $\mu_\xi$  in order to test if these measures are compatible with a distance  $d_{\text{JS}} \rightarrow 0$  in the limit  $h \rightarrow 0$ . We consider  $\epsilon = 1/16$  as in the previous section.

Figure 4.28(a) illustrates the average Jensen–Shannon divergence  $\langle d_{\text{JS}}(\mathcal{H}_\gamma, \mu_\xi) \rangle$  for five different decay rates  $\gamma$ , comparing individual Husimi distributions  $\mathcal{H}_\gamma$  and the classical measures  $\mu_\xi$ . For the average 50 eigenfunctions are considered. We observe a power-law decay  $d_{\text{JS}} \sim h^\delta$  with exponents  $0.6 \lesssim \delta \lesssim 0.8$  where larger exponents are observed for smaller decay rates  $\gamma$ . Distances of the same order and scaling are found when individual Husimi distributions  $\mathcal{H}_\gamma$  are compared to average Husimi distributions  $\langle \mathcal{H} \rangle_\gamma$  at the same decay rates, shown in Fig. 4.27(b). This has two remarkable implications: First, there exists a large regime of  $h$ , where a single resonance eigenfunction is equally well described by the classical measure  $\mu_\xi$  and the average Husimi distribution  $\langle \mathcal{H} \rangle_\gamma$ . Secondly, the observed decay of the distance  $d_{\text{JS}}(\mathcal{H}_\gamma, \mu_\xi)$  is of the same order as the decay of fluctuations of single eigenfunctions around the average. Combining the knowledge about the distribution of the fluctuations, discussed in Section 4.2.4, and the fractal properties of the semiclassical limit measure could be used to establish an explanation for the exponent  $\delta$ , but this is not attempted here. Altogether, the results of Fig. 4.28(a) lead to the conclusion that the classical measures  $\mu_\xi$  are indeed compatible with a semiclassical distance of  $d_{\text{JS}} \rightarrow 0$ .

In order to obtain a more sensitive test to this hypothesis we additionally consider the Jensen–Shannon divergence between averaged Husimi distributions  $\langle \mathcal{H} \rangle_\gamma$  and the proposed measures  $\mu_\xi$  as a function of  $h$  in Fig. 4.29. This reduces quantum fluctuations and leads to overall smaller distances for all considered  $\gamma$ . For  $\gamma_{\text{nat}}$  and  $\gamma_{\text{inv}}$  we again find a power-law decay of the form  $d_{\text{JS}} \sim h^\delta$ , where the exponents  $\delta \approx 0.85$  and  $\delta \approx 0.75$  are slightly larger than for single eigenfunctions, Fig. 4.28. This indicates that resonance eigenfunctions with decay rates  $\gamma_{\text{nat}}$  and  $\gamma_{\text{inv}}$  converge semiclassically towards the natural measure  $\mu_{\text{nat}}$  and the inverse



**Figure 4.28:** Quantum-to-classical and quantum-to-average comparison in the semiclassical limit. (a) Shown is the averaged Jensen–Shannon divergence  $d_{\text{JS}}$  between single Husimi distributions  $\mathcal{H}_\gamma$  and the classical measures  $\mu_\xi$  as a function of  $h$  for  $\gamma \in \{\gamma_{\text{nat}}, 0.35, \gamma_{\text{typ}}, 0.75, \gamma_{\text{inv}}\}$ . (b) Same as (a) considering the averaged  $d_{\text{JS}}$  between single  $\mathcal{H}_\gamma$  and average Husimi distributions  $\langle \mathcal{H} \rangle_\gamma$ . All averages are taken over 50 resonances. Gray lines indicate numerical scaling for  $\gamma_{\text{nat}}$  (lower) and  $\gamma_{\text{inv}}$  (upper).



**Figure 4.29:** Quantum-to-classical comparison in the semiclassical limit for average Husimi distributions. Shown is the Jensen–Shannon divergence  $d_{\text{JS}}$  between average Husimi distributions  $\langle \mathcal{H} \rangle_\gamma$  and the classical measures  $\mu_\xi$  as a function of  $h$  for  $\gamma \in \{\gamma_{\text{nat}}, 0.35, \gamma_{\text{typ}}, 0.75, \gamma_{\text{inv}}\}$ . Gray lines indicate numerical scaling for  $\gamma_{\text{nat}}$ ,  $\gamma_{\text{inv}}$ , and  $\gamma_{\text{typ}}$  (from lower to upper).

measure  $\mu_{\text{inv}}$ , respectively. Thus we verify the expectation for the natural measure  $\mu_{\text{nat}}$  [47,87] on a quantitative level for systems with partial escape. Moreover this provides strong evidence for our conjecture about the inverse measure  $\mu_{\text{inv}}$ , see Sec. 4.3.1.

The observed exponents  $\delta$  for the average Husimi distribution are larger than the exponents for the single Husimi distributions in Fig. 4.28(a). In both cases the Jensen–Shannon divergence  $d_{\text{JS}}$  decreases, because the fluctuating, fractal Husimi distributions are integrated over the fixed scale  $\epsilon$ , which converges semiclassically. Additionally, the considered interval of decay rates used for the average converges towards the considered  $\gamma$ , as discussed in Fig. 4.10. This has a strong impact on the average Husimi distribution mostly for large values of  $h$ , where the

decrease of  $d_{\text{JS}}$ , e.g., for  $\gamma_{\text{nat}}$ , is much faster in Fig. 4.29 than in Fig. 4.28(a). Let us further remark, that in Ref. [97] Fig. 6(b) instead of fixing the number of resonances fixed intervals around  $\gamma$  are considered, which implies an increasing number of resonances with smaller  $h$ . This number depends on the distribution of decay rates, see Sec. 4.1.2, and therefore leads to an additional modification of the exponent  $\delta$ , which depends non-trivially on  $\gamma$ . Another problem of this method is, that there is an unknown finite distance between eigenfunctions (and measures) at the boundary of the considered interval in  $\gamma$ , which becomes relevant in the semiclassical limit. For this reason, in this thesis we consider only a fixed number of resonances, under the price to deal with changing intervals in  $\gamma$ . Here we do not investigate the exponents  $\delta$  any further.

The Jensen–Shannon divergence for intermediate values of  $\gamma$ , shown in Fig. 4.29, show a much slower decrease with  $h$ . There seems to be a very slow power-law decay for  $\gamma_{\text{typ}}$  with a small exponent  $\delta \approx 0.18$ , which is much smaller than for  $\gamma_{\text{nat}}$  and  $\gamma_{\text{inv}}$ . Furthermore, this decay is even smaller than the observed exponents for single eigenfunctions. Note that the opposite is observed for  $\gamma_{\text{nat}}$  and  $\gamma_{\text{inv}}$ . For  $\gamma = 0.35$  and  $\gamma = 0.75$  the distance is almost constant for the smallest values of  $h$ . This suggests a saturation towards a finite distance between Husimi distributions and classical measures for intermediate decay rates  $\gamma$  in the semiclassical limit,  $d_{\text{JS}}(\gamma, \mu_\xi) = \lim_{h \rightarrow 0} d_{\text{JS}}(\langle \mathcal{H} \rangle_\gamma^h, \mu_\xi) > 0$ . We expect a similar saturation also for the individual Husimi distributions in Fig. 4.28(a). However, this saturation can only be seen, when  $d_{\text{JS}}(\mathcal{H}_\gamma, \mu_\xi)$  is of the order of the semiclassical distance  $d_{\text{JS}}(\gamma, \mu_\xi)$ , for which much larger values of  $h$  than currently possible would be required.

In conclusion, we obtain that the product measures  $\mu_\xi$  are well-suited as an approximation of single resonance eigenfunctions for finite values of  $h$  and all  $\gamma$ . We also find strong numerical evidence, that for small decay rates around  $\gamma_{\text{nat}}$  and large decay rates  $\gamma_{\text{inv}}$  the semiclassical limit measure is given by  $\mu_{\text{nat}}$  and  $\mu_{\text{inv}}$ . For intermediate decay rates  $\gamma$ , however, our numerical findings suggest that the measures  $\mu_\xi$  are not the semiclassical limit measures of the resonance eigenfunctions.

#### 4.4.5 Dependence on reflectivity function $R$

In this section we qualitatively and quantitatively investigate the dependence on the amount of escape from the system, i.e., the dependence on the reflectivity  $R$ . For this purpose we consider the same chaotic map as before with escape from the opening  $\Omega = (0.3, 0.6) \times [0, 1)$ , and using the reflectivity function  $R(\mathbf{x}) = R_\Omega$  if  $\mathbf{x} \in \Omega$  and else  $R(\mathbf{x}) = 1$ , see Eq. (4.7). Changing the parameter  $R_\Omega$  from unity to zero allows to investigate the transition from a closed system to a system with full escape. Here we restrict to partial escape with  $R_\Omega \in (0, 1)$ . For the limit of full escape,  $R_\Omega = 0$ , we refer to Chapter 5. Considering different  $R_\Omega$  not only changes the range and distribution of quantum decay rates, see Sec. 4.1.2, but also the classically relevant decay rates. In the following we consider  $R_\Omega \in \{0.8, 0.4, 0.2, 0.1, 0.05, 0.01\}$ , and give an overview



about the classical decay rates corresponding to these reflectivity parameters in Table 4.1.

#### 4.4.5.1 Qualitative comparison

We illustrate average Husimi distributions  $\langle \mathcal{H} \rangle_\gamma$  considering 50 resonances and the classical measures  $\mu_\xi$  for  $h = 1/4000$  for decreasing  $R_\Omega$  in Fig. 4.30. For the considered decay rates  $\gamma$  see Table 4.1. If there is almost no escape from the system,  $R_\Omega = 0.8$ , we find excellent agreement between quantum and classical densities (a). Between  $\gamma_{\text{nat}}$  and  $\gamma_{\text{inv}}$  we observe a transition of the phase-space structure from unstable to stable direction. It is remarkable how closely the structure of resonance eigenfunctions follows the classical measures  $\mu_\xi$ , even though the range of decay rates is much smaller than for  $R_\Omega = 0.2$ , see Table 4.1. Moreover, the distributions are close to the uniform distribution, which is seen in the overall darker colors without approaching zero (light yellow). Recall that in the closed limit  $R_\Omega \rightarrow 1$  the uniform distribution is obtained for all eigenfunctions as well as for the measures  $\mu_\xi$ .

Allowing more escape from the opening,  $R_\Omega = 0.4$  and  $R_\Omega = 0.2$ , we still find very good qualitative agreement for all decay rates  $\gamma$ , Fig. 4.30(b) and (c). We notice that the phase-space densities for different values of  $R_\Omega$  change only in the intensity distribution but not in their structure, when the classical decay rates are chosen accordingly, e.g., considering  $\gamma_{\text{typ}}$  for all  $R_\Omega$ . Surprisingly, this holds not only for the classical measures  $\mu_\xi$ , where such a behavior is implied by their definition Eq. (4.42), but also for the Husimi distributions. Nevertheless, it is already possible to distinguish some qualitative differences between quantum and classical densities at such large values of  $R_\Omega$  for the intermediate decay rates, as discussed for  $R_\Omega = 0.2$  in Sec. 4.4.1.

| $R_\Omega$ | $\gamma_{\text{min}}$ | $\gamma_{\text{nat}}$ | $\gamma_{(n+t)/2}$ | $\gamma_{\text{typ}}$ | $\gamma_{(t+i)/2}$ | $\gamma_{\text{inv}}$ | $\gamma_{\text{max}}$ |
|------------|-----------------------|-----------------------|--------------------|-----------------------|--------------------|-----------------------|-----------------------|
| 0.8        | 0                     | 0.05952               | 0.06323            | 0.06694               | 0.07089            | 0.07483               | 0.2231                |
| 0.4        | 0                     | 0.1700                | 0.2224             | 0.2749                | 0.3428             | 0.4108                | 0.9163                |
| 0.2        | 0                     | 0.2165                | 0.3497             | 0.4828                | 0.6842             | 0.8820                | 1.609                 |
| 0.1        | 0                     | 0.2368                | 0.4638             | 0.6908                | 1.071              | 1.450                 | 2.303                 |
| 0.05       | 0                     | 0.2461                | 0.5724             | 0.8987                | 1.490              | 2.082                 | 2.996                 |
| 0.01       | 0                     | 0.2532                | 0.8174             | 1.382                 | 2.514              | 3.647                 | 4.602                 |

**Table 4.1:** Relevant classical decay rates for the chaotic standard map with escape from  $\Omega = [0.3, 0.6) \times [0, 1)$  and different  $R_\Omega$ . The relevant classical decay rates are minimal and maximal decay rates  $\gamma_{\text{min}}, \gamma_{\text{max}}$ , Eq. (2.55), natural decay rate  $\gamma_{\text{nat}}$ , typical decay rate  $\gamma_{\text{typ}}$ , and inverse decay rate  $\gamma_{\text{inv}}$ . Additionally  $\gamma_{(n+t)/2} := (\gamma_{\text{nat}} + \gamma_{\text{typ}})/2$  and  $\gamma_{(t+i)/2} := (\gamma_{\text{typ}} + \gamma_{\text{inv}})/2$  are specified, as considered in Fig. 4.30. Natural and inverse decay rates are computed numerically from  $8192^2$  initial conditions using  $n = 8$  time steps. The typical decay rate results from  $\gamma_{\text{typ}} = -|\Omega| \ln R_\Omega$  with  $|\Omega| = 0.3$ .

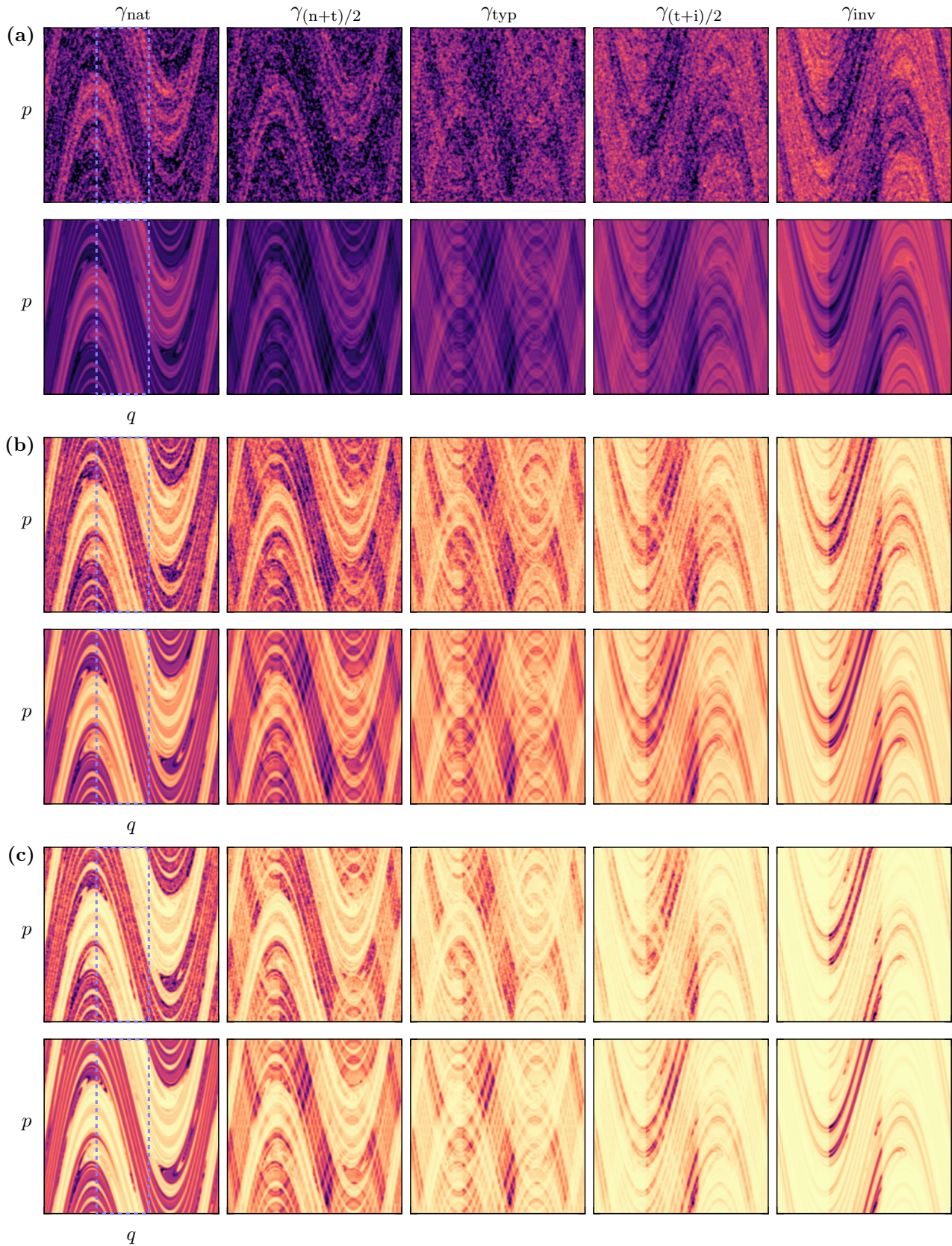


**Figure 4.30:** Quantum-to-classical correspondence for standard map with partial escape considering (a)  $R_\Omega = 0.8$ , (b)  $R_\Omega = 0.4$ , (c)  $R_\Omega = 0.2$ , (d)  $R_\Omega = 0.1$ , (e)  $R_\Omega = 0.05$ , and (f)  $R_\Omega = 0.01$ . The top row in each subplot shows averaged Husimi distributions  $\langle \mathcal{H} \rangle_\gamma$  using 50 resonances for  $h = 1/4000$  and with decay rates  $\gamma \in \{\gamma_{nat}, \gamma_{(n+t)/2}, \gamma_{typ}, \gamma_{(t+i)/2}, \gamma_{inv}\}$ , see Table 4.1 and ...

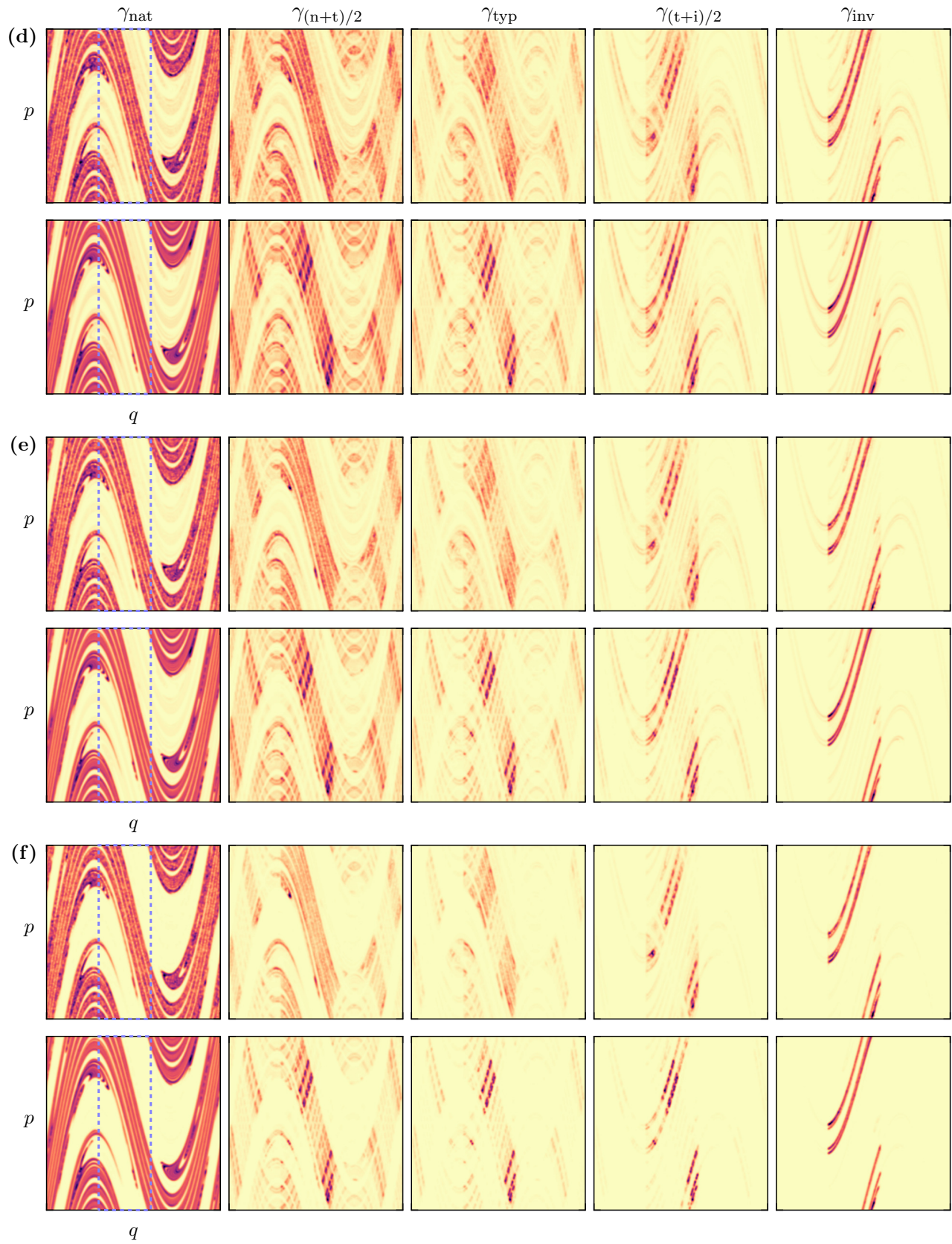


**Figure 4.30 (cont.):** ... bottom row shows Gaussian smoothed phase-space distribution of the product measures  $\mu_\xi$ . Individual colormap for each  $R_\Omega$  and  $\gamma$  with maximum given by the classical density. Dashed blue line indicates the position of the opening  $\Omega$ .

Further decreasing  $R_\Omega$  to  $R_\Omega = 0.1$  and below, this effect becomes more pronounced, see Fig 4.30(b)–(c): While for  $\gamma_{\text{nat}}$  and  $\gamma_{\text{inv}}$  the quantum-to-classical agreement is overwhelming, the quantum and classical phase-space distributions for intermediate decay rates become more distinct. Even though there still is a product structure visible in the intermediate resonance eigenfunctions, it is much broader than classically predicted by  $\mu_\xi$ . For these measures we apparently obtain strong peaks in the region of  $\Omega$ , where both natural measure  $\mu_{\text{nat}}$  and inverse measure  $\mu_{\text{inv}}$  have large values, see e.g., for the smallest considered  $R_\Omega = 0.01$  in 4.30(f) (bottom row). This indicates that in the limit of small  $R_\Omega$  the product measures  $\mu_\xi$  are not suitable approximations for the semiclassical limit of resonance eigenfunctions.

#### 4.4.5.2 Jensen–Shannon divergence

This leads to the question if it is possible to distinguish these different behaviors quantitatively using the Jensen–Shannon divergence. Therefore we first calculate the averaged Jensen–Shannon divergence  $\langle d_{\text{JS}}(\mathcal{H}_\gamma, \mu_\xi) \rangle$  between single eigenfunctions and the measures  $\mu_\xi$  for different values of  $h$ , as in Fig. 4.28. This is shown together with the averaged Jensen–Shannon divergence  $\langle d_{\text{JS}}(\mathcal{H}_\gamma, \langle \mathcal{H} \rangle_\gamma) \rangle$  between single and average Husimi distributions in Fig. 4.31 for  $R_\Omega \in \{0.8, 0.4, 0.1, 0.01\}$ . We secondly illustrate the Jensen–Shannon divergence  $d_{\text{JS}}(\langle \mathcal{H} \rangle_\gamma, \mu_\xi)$  between average Husimi distributions and the classical measures  $\mu_\xi$  in Fig. 4.32 for the same values of  $R_\Omega$ .

Figure 4.31(a) shows the Jensen–Shannon divergence for  $R_\Omega = 0.8$  as a function of  $h$  for the same decay rates as considered before, see Tab. 4.1. For all decay rates we observe a power-law decay  $d_{\text{JS}} \sim h^\delta$  with  $\delta \approx 0.9$ . Indeed, the obtained values fall almost perfectly on top of each other for all  $\gamma$ . Moreover, when single and average Husimi distributions are compared (right panel), the Jensen–Shannon divergence has almost exactly the same dependence on  $h$  for all decay rates. Similar observations are made for  $R_\Omega = 0.4$  in Fig. 4.31(b). Again the scaling of both comparisons are very similar with an exponent of  $\delta \approx 0.8$ . This leads to the conclusion that for systems with large  $R_\Omega$  the product measures are excellent approximations for the semiclassical structure of resonance eigenfunctions.

In contrast, for more escape with  $R_\Omega = 0.1$  in Fig. 4.31(c) the observations are similar as for  $R_\Omega = 0.2$ , see Fig. 4.28. Comparing left and right panel in Fig. 4.31(c) it becomes obvious that the scaling of the Jensen–Shannon divergence with  $h$  for intermediate decay rates is much slower when single eigenfunctions are compared to  $\mu_\xi$  instead (left) of the average  $\langle \mathcal{H} \rangle_\gamma$  (right). This means that single eigenfunctions converge faster to their average than to the classical measures  $\mu_\xi$ . From this one concludes that the measures  $\mu_\xi$  are not the semiclassical limit measures for intermediate decay rates under the assumption that  $\langle \mathcal{H} \rangle_\gamma$  is already close to this limit. Note that this is not seen for  $\gamma_{\text{nat}}$  and  $\gamma_{\text{inv}}$  and that for  $\gamma_{\text{inv}}$  the absolute difference to  $\mu_\xi$  is much larger for large values of  $h$ . For even smaller  $R_\Omega = 0.01$  these observations are validated and become more evident, shown in (d).

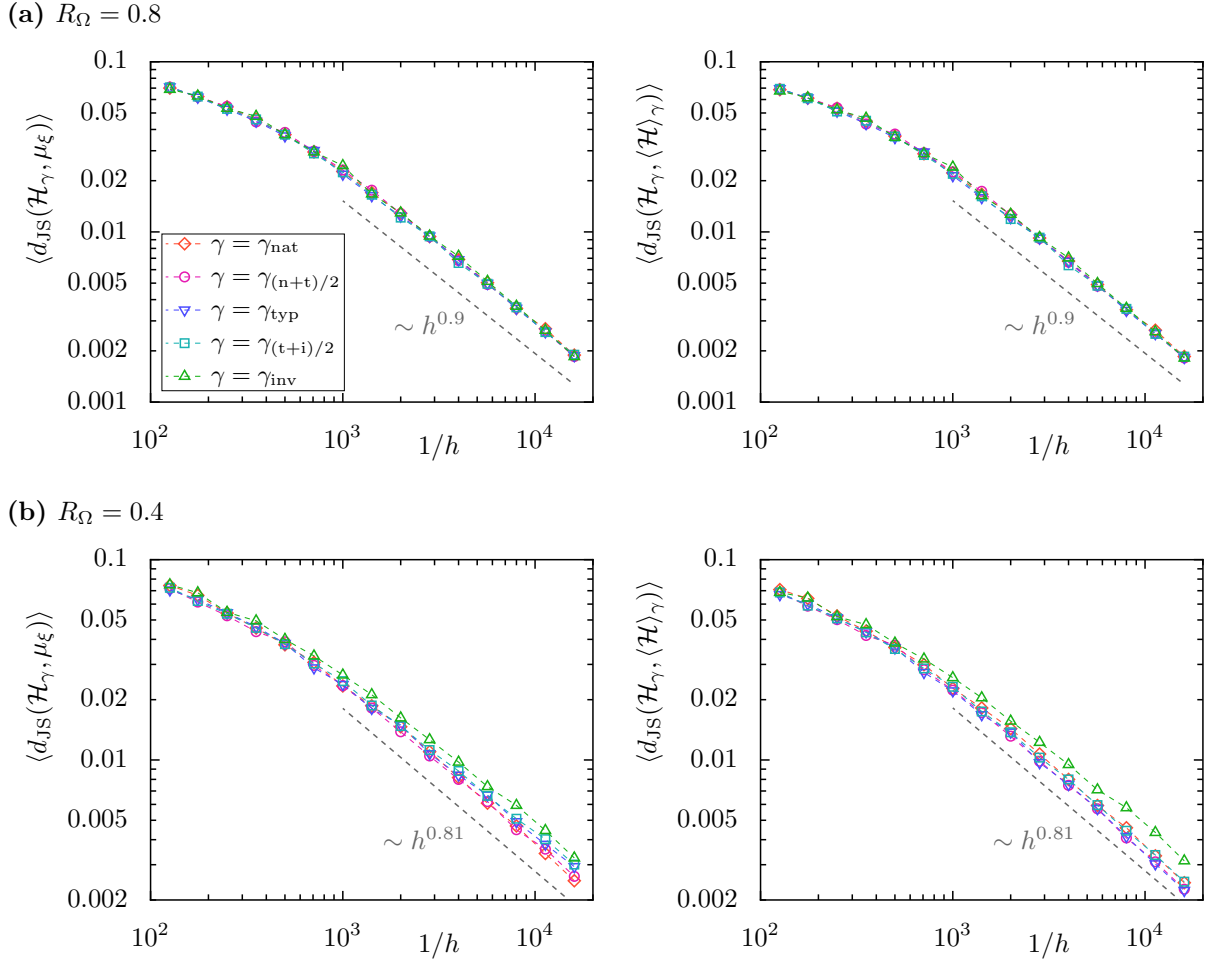


**Figure 4.31:** Quantum-to-classical and quantum-to-average comparison in the semiclassical limit depending on the amount of escape from the opening. Considered are (a)  $R_\Omega = 0.8$ , (b)  $R_\Omega = 0.4$ , (c)  $R_\Omega = 0.1$ , and (d)  $R_\Omega = 0.01$  (for (c) and (d) see next page). Left panels show the averaged Jensen–Shannon divergence  $d_{\text{JS}}$  between single Husimi distributions  $\mathcal{H}_\gamma$  and the classical measures  $\mu_\xi$  as a function of  $h$  for  $\gamma$  as indicated in (a). Right panels show the averaged Jensen–Shannon divergence  $d_{\text{JS}}$  between single  $\mathcal{H}_\gamma$  and averaged Husimi distributions  $\langle \mathcal{H} \rangle_\gamma$ . All averages are taken over 50 resonances. Gray lines indicate numerical scaling for  $\gamma_{\text{nat}}$  (lower) and in (c) and (d) also for  $\gamma_{\text{inv}}$  (upper). For classical decay rates see Tab. 4.1.

These observations are further confirmed in Fig. 4.32 for the comparison of average Husimi distributions  $\langle \mathcal{H} \rangle_\gamma$  and  $\mu_\xi$ . For  $R_\Omega = 0.8$ , even in this much more sensitive test, we find the same power-law decay for all decay rates (a). The exponent  $\delta \approx 0.95$  is slightly larger than in Fig. 4.31(a), which is consistent with the observations in Sec. 4.4.4. For  $R_\Omega = 0.4$  shown in (b), however, we make similar observations as for  $R_\Omega = 0.2$  in Fig. 4.28. For  $\gamma_{\text{nat}}$  and  $\gamma_{\text{inv}}$  a larger exponent of the power law is observed than in Fig. 4.31(b), while the exponent for intermediate decay rates is much smaller than before. This effect becomes stronger if more escape is considered in (c)  $R_\Omega = 0.1$  and (d)  $R_\Omega = 0.01$ . In all cases, the Jensen–Shannon divergence between the average Husimi distributions and the classical measures, shown in Fig. 4.32(b)–(d), is consistent with a semiclassical distance of zero for  $\gamma_{\text{nat}}$  and  $\gamma_{\text{inv}}$ , only. For

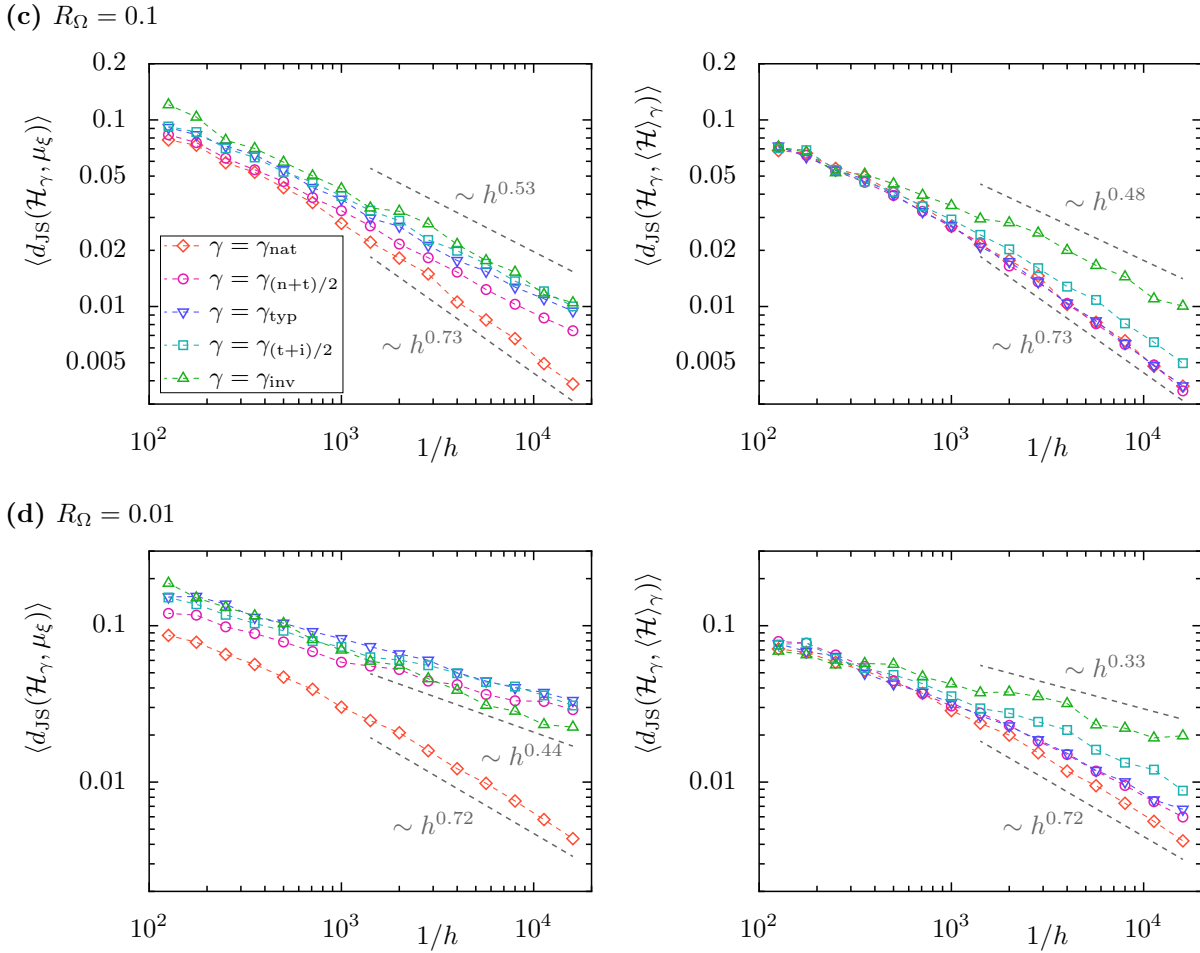


**Figure 4.31 (cont.):** Quantum-to-classical and quantum-to-average comparison in the semiclassical limit depending on the escape from the opening.

the other decay rates the distance  $d_{\text{JS}}$  almost remains constant for the smallest values of  $h$ .

This is consistent with the qualitative observations in Fig. 4.30, where excellent agreement between resonance eigenfunctions and the proposed measures  $\mu_\xi$  is seen for  $\gamma_{\text{nat}}$  and  $\gamma_{\text{inv}}$  independent of the considered  $R_\Omega$ . The numerical investigation of the Jensen–Shannon divergence, presented in Figs. 4.31 and 4.32, confirms that in systems with more escape, for small  $R_\Omega$ , there is no semiclassical agreement between the product measures  $\mu_\xi$  and the phase-space distribution of resonance eigenfunctions. Conversely, in the closed limit there is excellent quantum-to-classical agreement. This is seen for  $R_\Omega = 0.8$ , where for all considered decay rates the Jensen–Shannon divergence  $d_{\text{JS}}$  shows the same dependence on  $h$  for all decay rates  $\gamma$ . We conclude that in the regime of almost closed systems the proposed measures  $\mu_\xi$  are convenient approximations of resonance eigenfunctions at finite values of  $h$ . The opposite limit of full escape,  $R_\Omega \rightarrow 0$ , is investigated in Chapter 5.

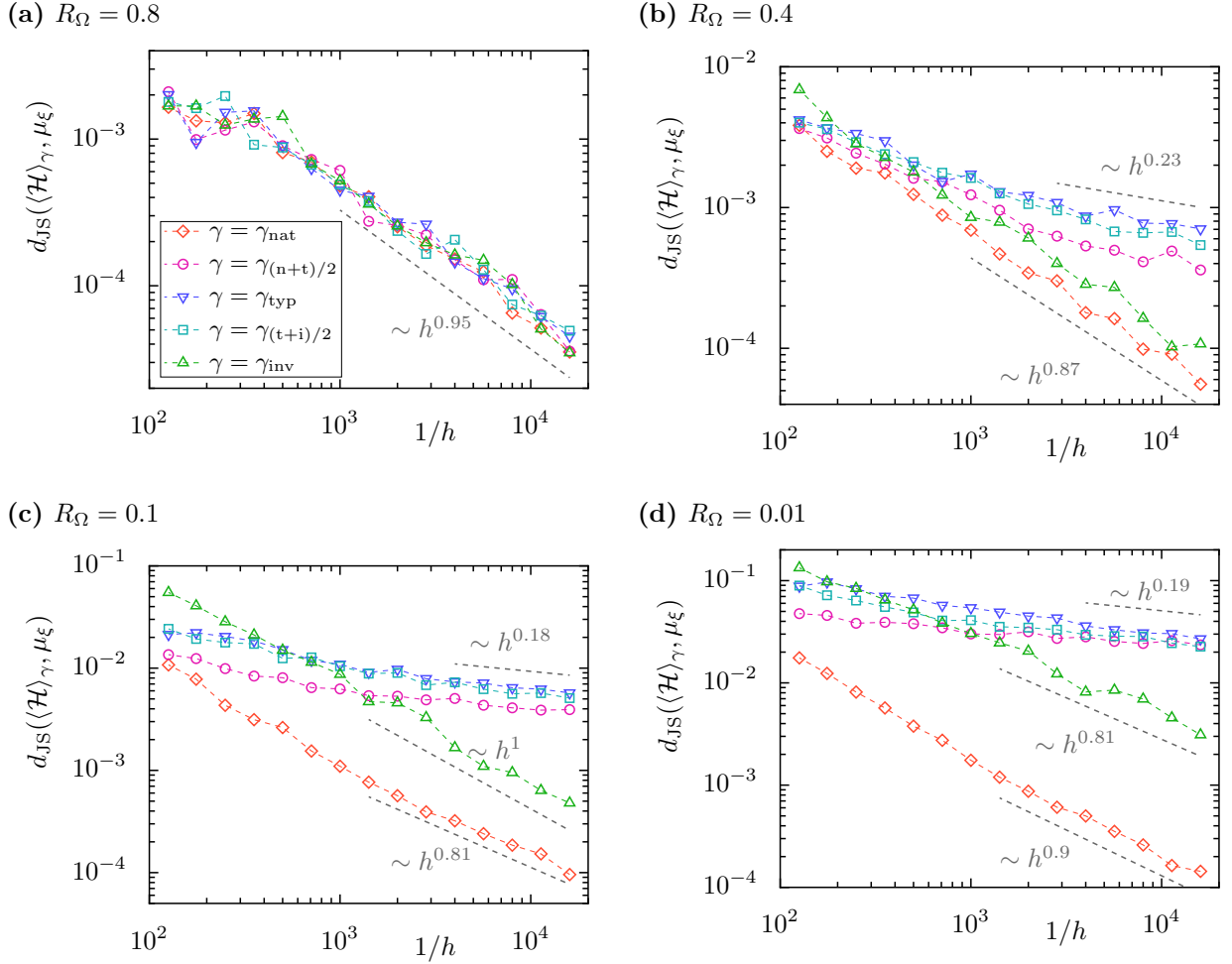


**Figure 4.32:** Quantum-to-classical comparison in the semiclassical limit for average Husimi distributions depending on the amount of escape from the opening. Considered are (a)  $R_\Omega = 0.8$ , (b)  $R_\Omega = 0.2$  and (c)  $R_\Omega = 0.05$ . Shown is the Jensen–Shannon divergence  $d_{\text{JS}}$  between average Husimi distributions  $\langle \mathcal{H} \rangle_\gamma$  and the classical measures  $\mu_\xi$  as a function of  $h$  for  $\gamma$  as indicated in (a). Gray lines indicate numerical scaling for  $\gamma_{\text{nat}}$ ,  $\gamma_{\text{inv}}$ , and  $\gamma_{\text{typ}}$  (from lower to upper).

#### 4.4.5.3 Dependence on size of opening

In the following we change the reflectivity function by considering escape from smaller and larger regions  $\Omega$  for the same escape with  $R_\Omega$ . For this purpose we consider the chaotic standard map as before with partial escape from two different regions,  $\Omega_1 = [0.2, 0.4) \times [0, 1)$  and  $\Omega_2 = [0.2, 0.7) \times [0, 1)$ , where  $R_\Omega = 0.2$ . The relevant classical decay rates for these openings are shown in Tab. 4.2.

We illustrate quantum and classical phase-space densities for both maps with escape in Fig. 4.33. For both openings we observe a very good qualitative agreement, similar as before. Especially at  $\gamma_{\text{nat}}$  and  $\gamma_{\text{inv}}$  there is perfect agreement. For intermediate decay rates we find deviations between quantum and classical densities, which are still present further in the semiclassical limit (not shown). Interestingly we notice, that the visual agreement is similar

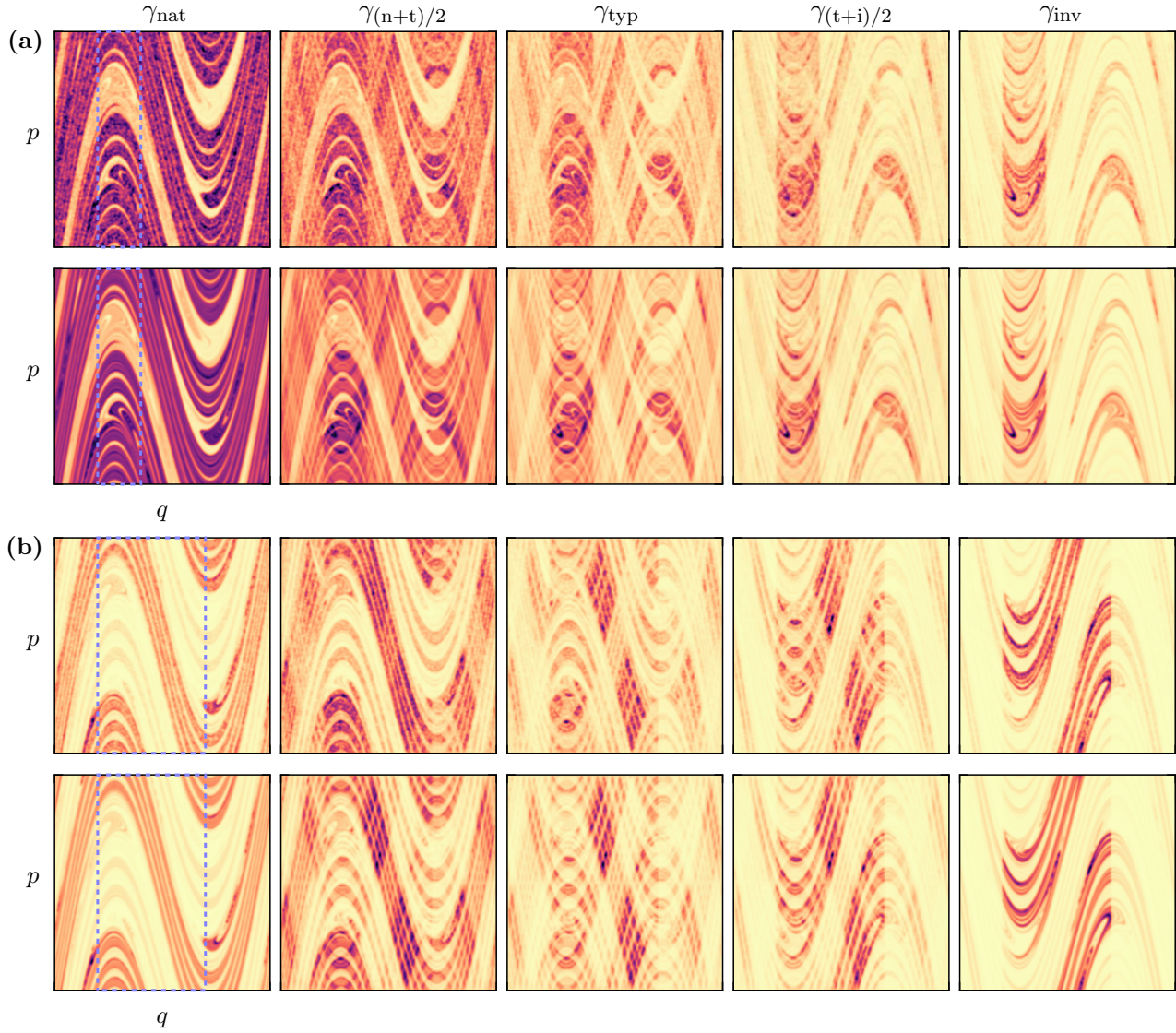


**Figure 4.33:** Quantum-to-classical correspondence for standard map with partial escape considering (a)  $\Omega_1 = (0.2, 0.4) \times [0, 1)$  and (b)  $\Omega_2 = (0.2, 0.7) \times [0, 1)$  with each  $R_\Omega = 0.2$ . The top row in each subplot shows averaged Husimi distributions  $\langle \mathcal{H} \rangle_\gamma$  using 50 resonances for  $h = 1/4000$  and with decay rates  $\gamma \in \{\gamma_{\text{nat}}, \gamma_{(n+t)/2}, \gamma_{\text{typ}}, \gamma_{(t+i)/2}, \gamma_{\text{inv}}\}$ , see Table 4.2. The bottom row shows Gaussian smoothed phase-space distribution of the corresponding product measures  $\mu_\xi$ . Individual colormap for each  $R_\Omega$  and  $\gamma$  with maximum given by the classical density. Dashed blue line indicates the position of the opening  $\Omega$ .

| $\Omega$   | $\gamma_{\min}$ | $\gamma_{\text{nat}}$ | $\gamma_{(n+t)/2}$ | $\gamma_{\text{typ}}$ | $\gamma_{(t+i)/2}$ | $\gamma_{\text{inv}}$ | $\gamma_{\max}$ |
|------------|-----------------|-----------------------|--------------------|-----------------------|--------------------|-----------------------|-----------------|
| $\Omega_1$ | 0               | 0.1704                | 0.2461             | 0.3219                | 0.4133             | 0.5047                | 1.609           |
| $\Omega_2$ | 0               | 0.4195                | 0.6121             | 0.8047                | 1.027              | 1.249                 | 1.609           |

**Table 4.2:** Relevant classical decay rates for the chaotic standard map with partial escape from  $\Omega_1 = [0.2, 0.4) \times [0, 1)$  and  $\Omega_2 = [0.2, 0.7) \times [0, 1)$  for  $R_\Omega = 0.2$  as in Tab. 4.1. Natural and inverse decay rates are computed numerically. The typical decay rate results from  $\gamma_{\text{typ}} = -|\Omega| \ln R_\Omega$ .



between the smaller opening, shown in (a), and the larger opening (b). Thus, more escape through a larger opening has not the same effect on the predictive quality of the measures  $\mu_\xi$  as allowing more escape by decreasing  $R_\Omega$ , see Sec. 4.4.5.

#### 4.4.6 Baker map

In the following we qualitatively compare product measures  $\mu_\xi$  and resonance eigenfunctions obtained for the baker map. For this purpose we consider the ternary baker map  $B_3$  and

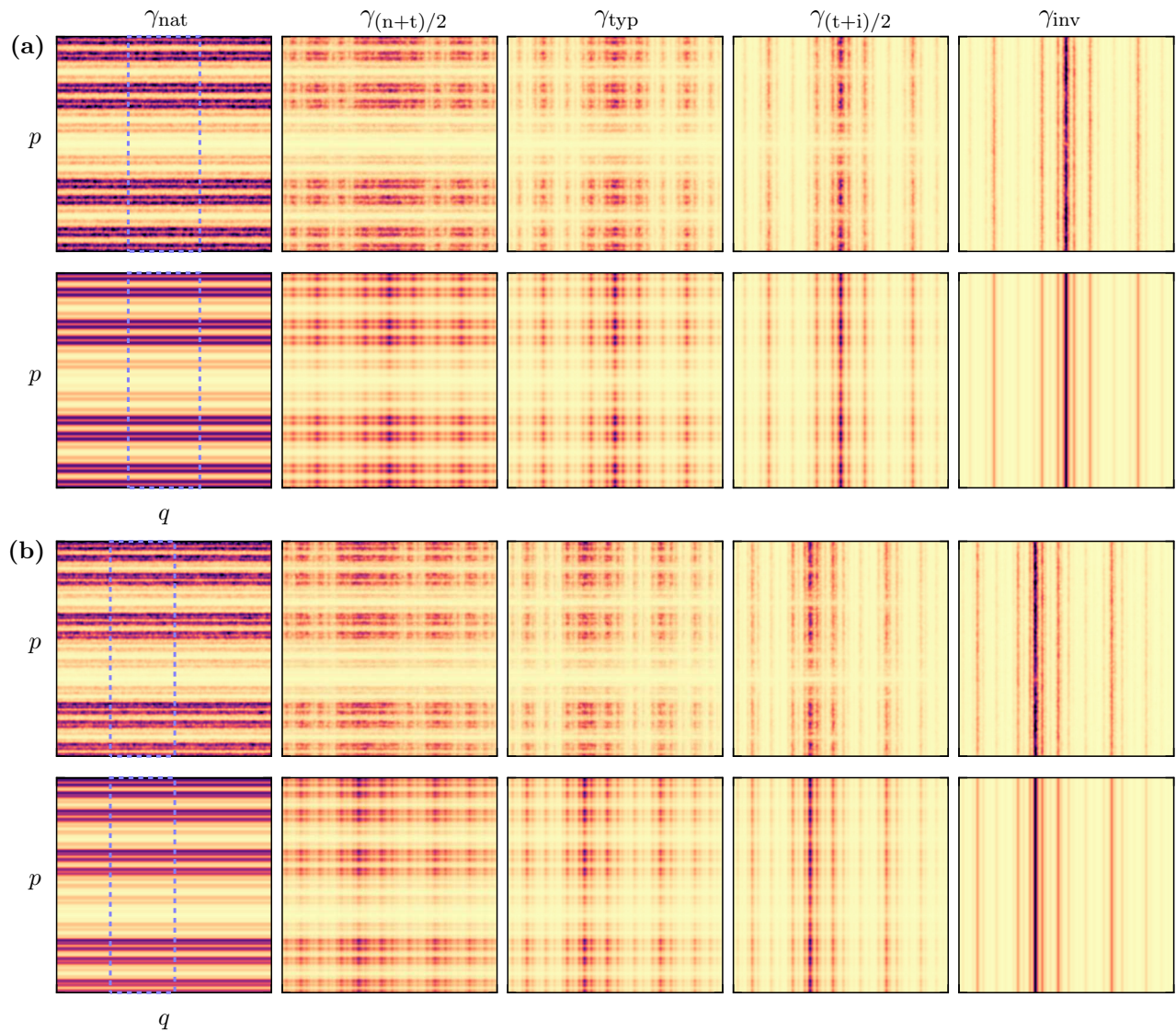


**Figure 4.34:** Quantum-to-classical correspondence for baker map with partial escape. (a) Triadic baker map  $B_3$  for  $h = 1/3999$  and (b) asymmetric baker map  $B_r$  with  $\mathbf{r} = (0.25, 0.3, 0.45)$  for  $h = 1/4000$ . Escape is considered from the middle strip,  $\mathbf{R} = (1, 0.2, 1)$ . The top row in each subplot shows averaged Husimi distributions  $\langle \mathcal{H} \rangle_\gamma$  using 50 resonances for decay rates  $\gamma \in \{\gamma_{\text{nat}}, \gamma_{(n+t)/2}, \gamma_{\text{typ}}, \gamma_{(t+i)/2}, \gamma_{\text{inv}}\}$ , see Table 4.3. The bottom row shows Gaussian smoothed phase-space distribution of the product measures  $\mu_\xi$ . Individual colormap for each  $R_\Omega$  and  $\gamma$  with maximum given by the classical density. Dashed blue line indicates the position of the opening  $\Omega$ .

| $\mathbf{r}$        | $\gamma_{\min}$ | $\gamma_{\text{nat}}$ | $\gamma_{(n+t)/2}$ | $\gamma_{\text{typ}}$ | $\gamma_{(t+i)/2}$ | $\gamma_{\text{inv}}$ | $\gamma_{\max}$ |
|---------------------|-----------------|-----------------------|--------------------|-----------------------|--------------------|-----------------------|-----------------|
| $(1/3, 1/3, 1/3)$   | 0               | 0.3102                | 0.4233             | 0.5365                | 0.6919             | 0.8473                | 1.609           |
| $(0.25, 0.3, 0.45)$ | 0               | 0.2744                | 0.3786             | 0.4828                | 0.6356             | 0.7885                | 1.609           |

**Table 4.3:** Relevant classical decay rates for the baker map  $B_{\mathbf{r}}$  with two different  $R$  and escape with  $\mathbf{R} = (1, 0.2, 1)$ . The relevant classical decay rates are minimal and maximal decay rates  $\gamma_{\min}, \gamma_{\max}$ , Eq. (2.55), natural decay rate  $\gamma_{\text{nat}}$ , typical decay rate  $\gamma_{\text{typ}}$ , and inverse decay rate  $\gamma_{\text{inv}}$ , which are all computed analytically.

an asymmetric baker map  $B_{\mathbf{r}}$  with  $\mathbf{r} = (0.25, 0.3, 0.45)$  with escape from the middle strip as  $\mathbf{R} = (1, 0.2, 1)$ , see App. C.3.1. The quantized baker map is defined in App. A.3.

For five decay rates between  $\gamma_{\text{nat}}$  and  $\gamma_{\text{inv}}$ , see Tab. 4.3, we present for both baker maps average Husimi distributions  $\langle \mathcal{H} \rangle_{\gamma}$  and the corresponding classical measures in Fig. 4.34. Results for the ternary baker map are shown in (a) and show symmetric phase-space densities. For  $\gamma_{\text{nat}}$  and  $\gamma_{\text{inv}}$  we confirm quantum-to-classical agreement. For intermediate decay rates the agreement is similarly good as observed for the standard map in Fig. 4.22, with the same limitations. This is also observed for the asymmetric baker map in (b). Note that if escape takes place only from the middle strip, the product measures  $\mu_{\xi}$  for the triadic baker map are the same as discussed in Ref. [205], where a more detailed qualitative quantum-to-classical comparison for this setting is found.

## 4.5 Discussion and outlook

In this chapter we gather detailed insight about the semiclassical localization of resonance eigenfunctions in maps with partial escape. The investigations and observations lead to the following conclusions.

We observe that resonance eigenfunctions in systems with partial escape converge towards a class of semiclassical limit measures depending only on their decay rate  $\gamma$ . These limit measures are conditionally invariant with the same decay rate. For  $\gamma_{\text{nat}}$  we numerically confirm the expectation [87] that resonance eigenfunctions converge towards the natural measure  $\mu_{\text{nat}}$ . We identify that the opposite edge of the quantum mechanical spectrum is characterized by the inverse decay rate  $\gamma_{\text{inv}}$ . We equivalently conjecture and find numerical support that the inverse measure  $\mu_{\text{inv}}$  is the relevant semiclassical limit measure for this decay rate. In addition we present a family of conditionally invariant measures for arbitrary decay rates which is based on the hyperbolic phase-space structure and which exhibits a simple numerical construction. These measures qualitatively agree very well with resonance eigenfunctions for all decay rates. This is shown for different reflectivity functions by varying the strength of escape and the size of the opening. We find very good agreement in systems with less escape, i.e., with reflectivity functions  $R$  close to one, but we do not find equally convincing agreement if  $R$  becomes very small in certain regions. For the generic case, we observe that the Jensen–Shannon divergence semiclassically does not converge to zero for intermediate decay rates. Even though the proposed product measures  $\mu_\xi$  are very good approximations for resonance eigenfunctions this indicates that they are not the true semiclassical limit measures for arbitrary decay rates.

This leaves the question open about the semiclassical limit measures of resonance eigenfunctions. The particular case of full escape is separately investigated in the next chapter, where we present an entirely different approach to construct classical conditionally invariant measures describing resonance eigenfunctions. In order to completely understand systems with partial escape it is possible that periodic orbits have to be taken into account. We believe that the singular measures  $\mu_{\underline{p}}$  localizing on periodic orbits  $\underline{p}$ , defined in Sec. 4.3.3, are promising candidates in this regard.

These measures are defined for all periodic orbits of the closed map  $M$ , which leads to two important conclusions. First, recall that the set of all periodic orbits is dense on  $\Gamma$  and gives rise to the uniform distribution according to the sum rule by Hannay and Ozorio de Almeida [206]. Thus it seems likely that replacing the uniform distribution on the periodic orbit  $\underline{p}$  in the sum rule by the conditionally invariant measures  $\mu_{\underline{p}}$  leads, in a similar way, to one (or many) conditional invariant measures supported on the whole of  $\Gamma$  instead of isolated points. Secondly, if the period becomes large,  $p \rightarrow \infty$ , it is likely that the probability to find periodic orbits with decay rate in an interval around  $\gamma_{\text{typ}} \pm \varepsilon$  converges to unity, since most of the periodic orbits cover the phase space uniformly [89, 195]. Hence, there exists at least one classical measure decaying with the typical decay rate, which can be defined as the summation

of periodic orbit measures  $\mu_{\underline{p}}$  in the limit of large periods,

$$\mu_{\text{typ}} = \lim_{p \rightarrow \infty} \sum_{\substack{\underline{p} \text{ p.o.} \\ |\underline{p}|=p}} \mu_{\underline{p}} e^{-\Lambda_{\underline{p}}}, \quad (4.52)$$

where  $e^{-\Lambda_{\underline{p}}}$  is the stability of the periodic orbit. In the limit of a closed system, this limit is equivalent to the sum rule of Ref. [206].

Since in general the computation of periodic orbits with large period is difficult we motivate an approximation of this measure using non-periodic orbits in Appendix C.5. This approximation of  $\mu_{\text{typ}}$  is illustrated together with the average resonance eigenfunctions  $\langle \mathcal{H} \rangle_{\gamma}$  and the corresponding product measures  $\mu_{\xi}$  with the decay rate  $\gamma_{\text{typ}}$  for the chaotic standard map in Fig. 4.35. The qualitative agreement between (a) quantum densities and (b) typical measures improves significantly, compared to the product measures (c). It is a promising and interesting

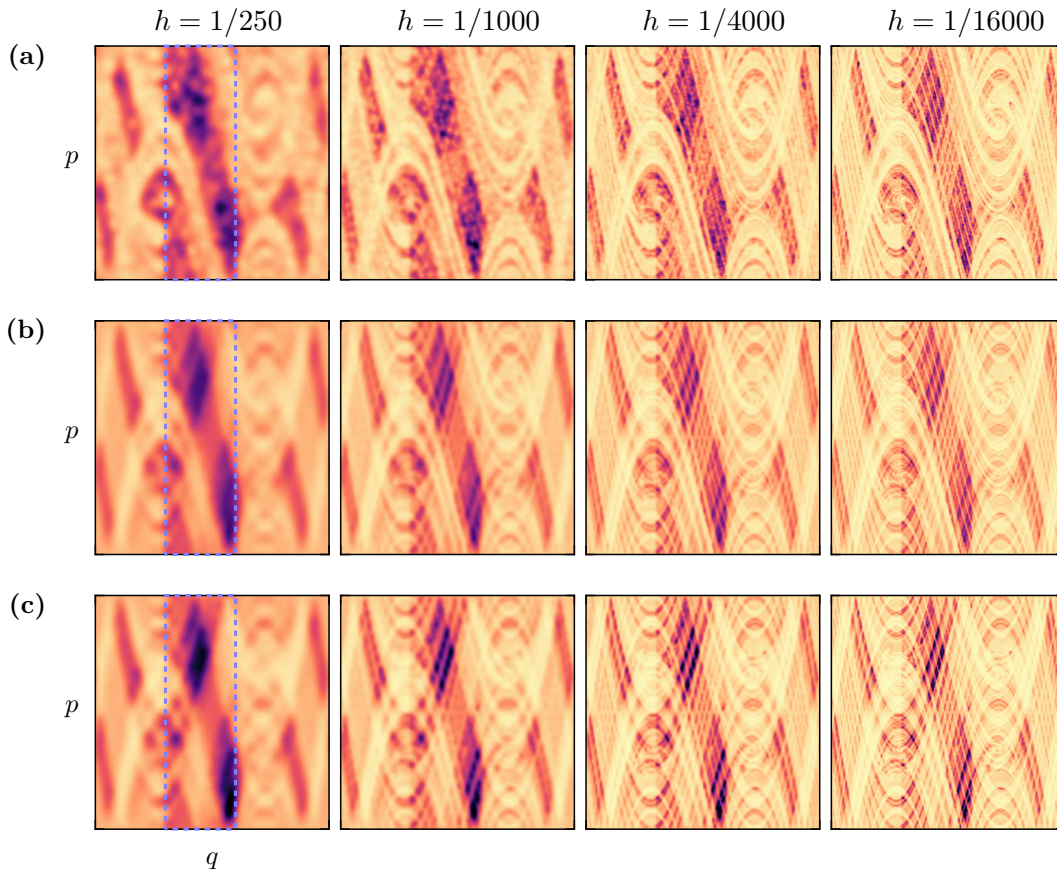


**Figure 4.35:** Quantum-to-classical correspondence for chaotic standard map with partial escape at the typical decay  $\gamma_{\text{typ}}$ . (a) Average Husimi distribution  $\langle \mathcal{H} \rangle_{\gamma}$  for  $h \in \{1/1000, 1/4000, 1/16000\}$  (from left to right) over 50 eigenfunctions. (b) Typical measure  $\mu_{\text{typ}}$ , approximated with  $3000^2$  initial conditions and considering  $n = 20$  time steps, see App. C.5. (c) Corresponding product measure  $\mu_{\xi}$  as before. Individual colormap for each  $h$  with maximum given by the density of  $\mu_{\text{typ}}$ . Dashed blue line indicates the position of the opening  $\Omega$ .

future task to investigate this relation further and generalize this approach to arbitrary decay rates, in order to develop a full understanding of resonance eigenfunctions in maps with partial escape.



# Chapter 5

## Resonance eigenfunctions in maps with full escape

In this chapter we investigate the structure of resonance eigenfunctions for chaotic maps with full escape. This chapter is divided into four sections. In the first section we consider the quantization of maps and their resonances in the limit of full escape. The second section examines resonance eigenfunctions of systems with full escape, which split into long-lived and short-lived eigenfunctions. In particular, we investigate their semiclassical convergence in dependence on the decay rate  $\gamma$ .

In Section 5.3 we discuss different families of classical conditional invariant measures for full escape and discuss their viability as semiclassical limit measures of resonance eigenfunctions. We motivate a new family of measures  $\mu_\gamma^h$  which is based on the temporal distance to the chaotic saddle on the phase space and results in a resonance eigenfunction hypothesis for full escape. For these measures we present a conceptually simple implementation. In the last section we compare resonance eigenfunctions to the proposed classical measures, qualitatively on the phase-space and by their fractal dimensions. This is quantified using the Jensen–Shannon divergence. We find very good agreement between long-lived resonance eigenfunctions and the proposed measures  $\mu_\gamma^h$ . For short-lived resonance eigenfunctions quantum-to-classical agreement is not found. The results of this chapter have been published in Ref. [66].

### 5.1 Quantization for full escape

Classical maps with full escape are characterized by an open subset  $\Omega \subset \Gamma$  where the reflectivity function becomes zero, see Sec. 2.2.4. The simplest case are reflectivity functions  $R(x) = 1 - \mathbb{1}_\Omega(x)$  projecting on the complement of some opening region  $\Omega$ . The quantization for full escape requires an analog correspondence principle as given for partial escape in Sec. 4.1.1, see Ref. [60, Axioms 2]. In the following we first consider the quantization for full escape as the limit of a sequence of quantizations for partial escape. We secondly show results for the convergence of the spectra.

### 5.1.1 Limit of full escape

In order to relate systems with full escape to systems with partial escape let's consider a sequence  $\{R_\alpha\}_{\alpha \in \mathbb{R}_+}$  of reflectivity functions  $R_\alpha : \Gamma \rightarrow \mathbb{R}_+$ , which converges uniformly towards a function  $R_0 : \Gamma \rightarrow \mathbb{R}_{\geq 0}$ ,

$$\limsup_{\alpha \rightarrow 0} \sup_{x \in \Gamma} |R_\alpha(x) - R_0(x)| = 0, \quad (5.1)$$

where  $R_0(\mathbf{x}) = 1 - \mathbb{1}_\Omega(\mathbf{x})$ . Consider further a quantization  $\{\mathcal{U}_{\alpha,N}\}_{N \in \mathbb{N}}$  of the corresponding maps with partial escape for each  $\alpha$ , as discussed in Sec. 4.1. Define the quantum map with full escape as

$$\mathcal{U}_{0,N} := \tilde{\mathcal{U}}_N \mathcal{R}_{0,N} \quad (5.2)$$

where  $\mathcal{R}_{0,N} = \text{Op}_N(R_0^{1/2})$ . Then, for fixed Hilbert-space dimension  $N$  the sequence of quantum maps with partial escape  $\mathcal{U}_{\alpha,N}$  converges towards the quantum map with full escape in operator norm,

$$\lim_{\alpha \rightarrow 0} \|\mathcal{U}_{\alpha,N} - \mathcal{U}_{0,N}\|_\infty = 0. \quad (5.3)$$

A proof of this statement is given in App. C.6.1. This also implies that a correspondence principle between classical and quantum time evolution, as in Eq. (4.1), is satisfied for  $\alpha = 0$ ,

$$\mathcal{U}_{0,N}^\dagger \text{Op}_N(a) \mathcal{U}_{0,N} \sim \text{Op}_N(R_0 \cdot (a \circ M)). \quad (5.4)$$

However, quantum maps with full escape are not invertible. Hence, there is no analogue relation to Eq. (4.6).

The most important consequences of Eq. (5.3) are, that not only the spectrum of  $\mathcal{U}_{\alpha,N}$  converges to the spectrum of  $\mathcal{U}_{0,N}$ , but also the corresponding resonance eigenfunctions for partial escape converge to those for full escape. In this sense, if the semiclassical structure of resonance eigenfunctions of  $\mathcal{U}_\alpha$  is understood for arbitrary small  $\alpha > 0$ , one immediately obtains the semiclassical structure for full escape as well. The investigations for systems with partial escape in Sec. 4.4.5, however, suggested that in this limit the proposed classical measures are not semiclassical limit measures for intermediate decay rates.

### 5.1.2 Resonances in the limit of full escape

Lets consider the chaotic standard map with  $\kappa = 10$  and escape from the opening  $\Omega = (0.3, 0.6) \times [0, 1)$  in terms of the reflectivity functions  $R(q, p) = 1 - (1 - R_\Omega) \mathbb{1}_\Omega(q, p)$ , see Eq. (4.7) in Sec. 4.1.2. The limit of full escape is achieved for  $R_\Omega \rightarrow 0$ , leading to  $R_0(q, p) = 1 - \mathbb{1}_\Omega(q, p)$ . Note that  $R_\Omega$  takes the role of the index  $\alpha$  in the previous section. Quantum mechanically,



these maps can be written as

$$\mathcal{U}_{R_\Omega} = \tilde{\mathcal{U}} \left( \mathbb{1} - \left( 1 - R_\Omega^{1/2} \right) \mathbb{1}_\Omega \right), \quad (5.5)$$

where  $\mathbb{1}_\Omega := \text{Op}(\mathbb{1}_\Omega)$  is the quantum projection on the opening  $\Omega$ . These maps converge in the limit of full escape towards  $\mathcal{U}_0 = \tilde{\mathcal{U}}(\mathbb{1} - \mathbb{1}_\Omega)$ . Let us remark, that we abuse the notation for the classical characteristic function and the quantum projection of the opening,  $\mathbb{1}_\Omega$ , and the meaning should be clear from the context. Note that  $\mathbb{1}_\Omega^2 = \mathbb{1}_\Omega$ .

The spectra of the corresponding quantum map with partial escape are compared to those for full escape in Fig. 5.1 for fixed  $h = 1/1000$ . We illustrate all eigenvalues with  $\gamma \leq 2$  for  $R_\Omega = 10^{-2}$  (blue dots) with  $R_\Omega = 0$  (green crosses) on the  $\theta$ - $\gamma$  plane in (a). Additionally natural decay rate  $\gamma_{\text{nat}}$  (red) and typical decay rate  $\gamma_{\text{typ}}$  (blue) for  $R_\Omega = 10^{-2}$  are indicated as horizontal lines. We observe that around  $\gamma_{\text{nat}}$  most of the eigenvalues agree very well. For larger decay rates there is no agreement of the spectra. The agreement between the spectra improves significantly when smaller  $R_\Omega$  are considered, see (b)–(d). The bulk of eigenvalues

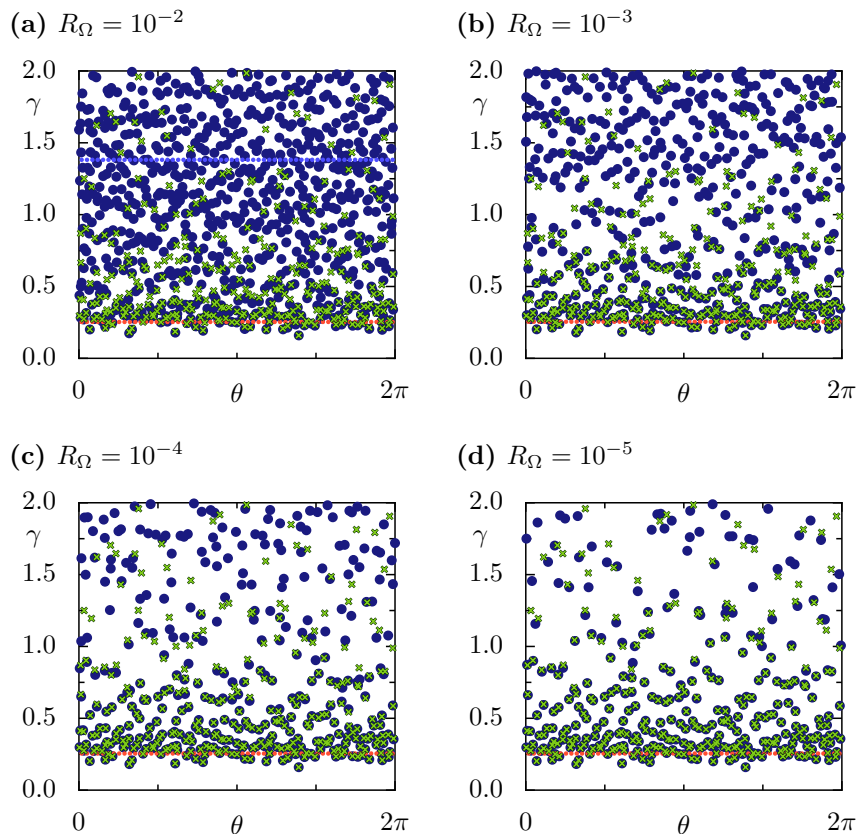


**Figure 5.1:** Eigenvalues of the chaotic standard map in the limit of full escape from  $\Omega = (0.3, 0.6) \times [0, 1)$ . Shown are the spectra  $\mathcal{U}_{R_\Omega}$  in  $\theta$ - $\gamma$  plane with  $\gamma \leq 2$  for  $h = 1/1000$  and (a)  $R_\Omega = 10^{-2}$ , (b)  $R_\Omega = 10^{-3}$  (c)  $R_\Omega = 10^{-4}$ , and (d)  $R_\Omega = 10^{-5}$  (blue markers). Green crosses represent all resonances with  $\gamma < 2$  for the same system with full escape,  $R_\Omega = 0$ . Horizontal lines indicate the natural decay rate  $\gamma_{\text{nat}} \approx 0.25$  for all  $R_\Omega$  (red), and in (a) the typical decay rate  $\gamma_{\text{typ}} \approx 1.38$  (blue).

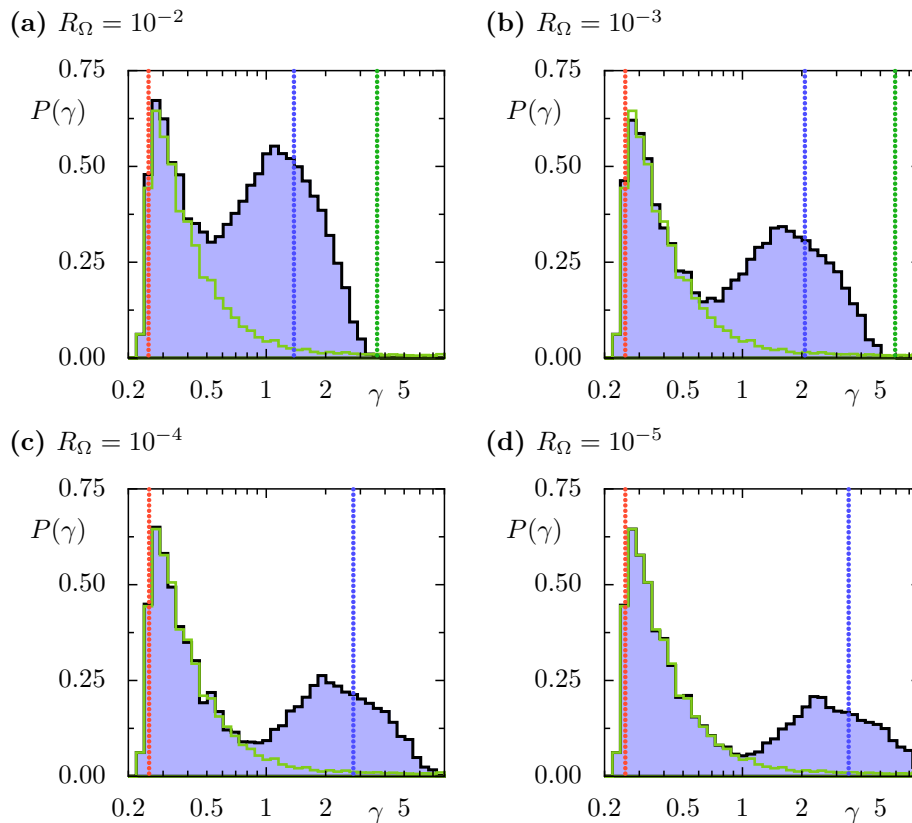


**Figure 5.2:** Distribution of decay rates  $\gamma$  for the chaotic standard map in the limit of full escape. Shown is the normalized probability  $P(\gamma)$  to find the decay rate  $\gamma$  for  $h = 1/1000$  and (a)  $R_\Omega = 10^{-2}$ , (b)  $R_\Omega = 10^{-3}$  (c)  $R_\Omega = 10^{-4}$ , and (d)  $R_\Omega = 10^{-5}$  (blue shaded histogram). The green colored line represents the distribution  $P(\gamma)$  for the same system with full escape,  $R_\Omega = 0$ . Vertical lines indicate classical decay rates for  $\gamma_{\text{nat}} \approx 0.25$  (red),  $\gamma_{\text{typ}} \in \{1.38, 2.07, 2.76, 3.45\}$  (blue), and  $\gamma_{\text{inv}} \in \{3.65, 5.94, 8.24, 10.5\}$  (green) for the given values of  $R_\Omega$ , respectively.

moves to larger  $\gamma$ , while the remaining ones converge towards the eigenvalues for full escape. Note that already for  $R_\Omega = 10^{-3}$  we have  $\gamma_{\text{typ}} > 2$ .

This is further visualized in Fig. 5.2, where the distribution of decay rates  $P(\gamma)$  is compared for  $R_\Omega > 0$  (blue shaded) and  $R_\Omega = 0$  (green) for the same parameters as before. The relevant classical decay rates for partial escape are plotted for comparison as vertical lines. In this representation the movement of the bulk of decay rates around  $\gamma_{\text{typ}} \rightarrow \infty$  becomes clear. The distribution around  $\gamma_{\text{nat}}$  converges to the limiting one for full escape. However, this also shows that for larger decay rates  $\gamma$  one needs to consider much smaller  $R_\Omega$ , in order to achieve the same agreement as for  $\gamma_{\text{nat}}$ . We conclude that resonances of the quantum map with full escape are well approximated by those for finite  $R_\Omega$  under the condition that  $\gamma \ll \gamma_{\text{typ}}(R_\Omega)$ .

Let us now consider the system with full escape,  $R_\Omega = 0$ . For this we illustrate all eigenvalues on the  $\theta$ - $\gamma$  plane in Fig. 5.3 for  $h \in \{1/250, 1/1000, 1/4000, 1/16000\}$ . The smallest decay rates converge towards  $\gamma_{\text{nat}}$  (red line) for decreasing  $h$ . Close to  $\gamma_{\text{nat}}$  there are visibly more eigenvalues than for larger decay rates. Since there exist arbitrarily small eigenvalues, the

range of decay rates is not bounded, as observed for partial escape in Sec. 4.1.2

The growth rate of the number of resonances with finite decay is related to the fractal dimension of the chaotic saddle  $\Gamma_s$  by a fractal Weyl law [56]. For quantum maps with full escape the fractal Weyl law is formulated as follows [57, 78–82]. Consider the number of resonances  $n_{\text{res}}(\gamma_c; N) := |\{\lambda \in \sigma(\mathcal{U}_N) : \gamma = -2 \ln |\lambda| \leq \gamma_c\}|$  with decay rate below some cutoff  $\gamma_c$ . This number grows asymptotically for  $N \rightarrow \infty$  like

$$n_{\text{res}}(\gamma_c; N) \sim s(\gamma_c) \cdot N^{D_0(\Gamma_s)/2} = s(\gamma_c) \cdot h^{-D_0(\Gamma_s)/2}, \quad (5.6)$$

where the so-called shape function  $s(\gamma_c)$  [79] depends only on the chosen cutoff, and  $D_0(\Gamma_s)$  is the box-counting dimension of the chaotic saddle, see Sec. 2.2.5. The shape function is related to the distribution of decay rates in truncated unitary matrices [207], which is heuristically motivated in Ref. [57], and one obtains

$$s(\gamma) = e^{\gamma_{\text{nat}}} \left( 1 - \frac{1 - e^{-\gamma_{\text{nat}}}}{1 - e^{-\gamma}} \right) \quad (5.7)$$

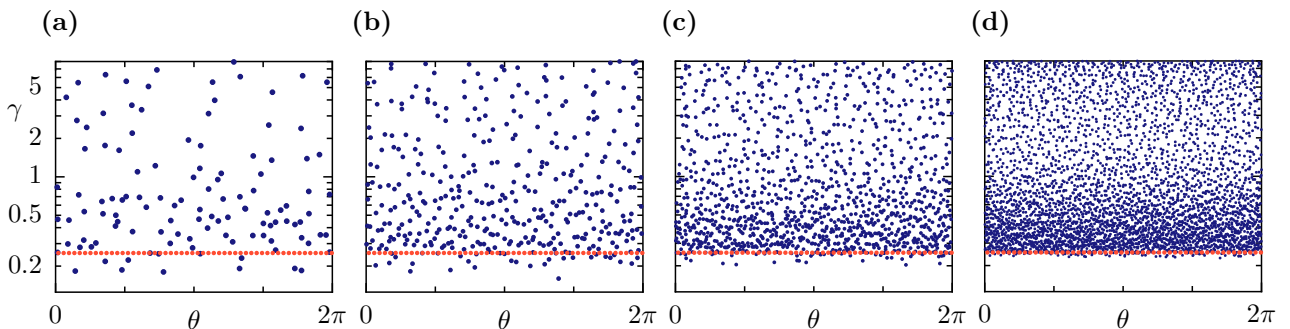


**Figure 5.3:** Eigenvalues of the chaotic standard map with full escape. Shown is the spectrum in  $\theta$ - $\gamma$  plane for (a)  $h = 1/250$ , (b)  $h = 1/1000$  (c)  $h = 1/4000$ , and (d)  $h = 1/16000$ . Red horizontal line indicates the classical natural decay rate  $\gamma_{\text{nat}} \approx 0.25$ .

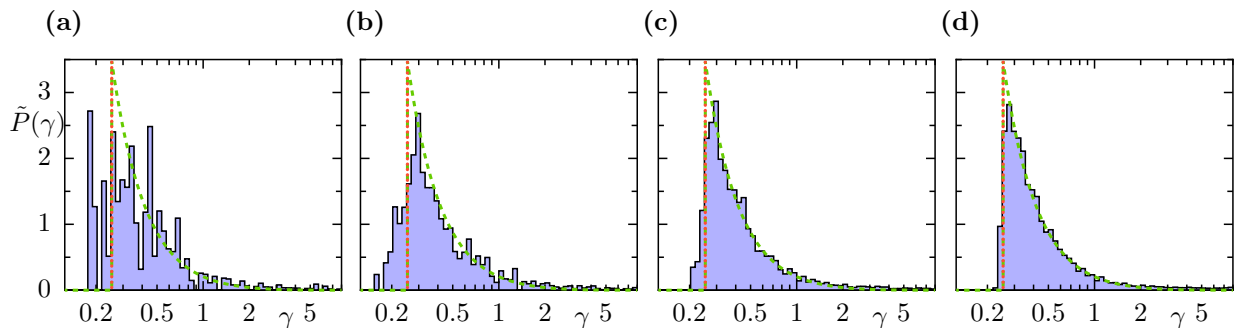


**Figure 5.4:** Rescaled distribution of decay rates  $\gamma$  for the chaotic standard map with full escape. Shown is the rescaled  $\tilde{P}(\gamma) = P(\gamma)/h^{-D_0(\Gamma_s)/2}$  where  $P(\gamma)$  is the probability to find decay rate  $\gamma$  for (a)  $h = 1/250$ , (b)  $h = 1/1000$  (c)  $h = 1/4000$ , and (d)  $h = 1/16000$ . For comparison the rescaled asymptotic expectation, Eq. (5.8) is shown (green dashed line). Red vertical line indicates the classical decay rate  $\gamma_{\text{nat}} \approx 0.25$ .

for  $\gamma \geq \gamma_{\text{nat}}$  and  $s(\gamma) = 0$  else. Hence, in the semiclassical limit the expected probability density to find decay rates  $\gamma$  is given by

$$P(\gamma) = \frac{ds}{d\gamma} \cdot h^{-D_0(\Gamma_s)/2} = \frac{1 - e^{-\gamma_{\text{nat}}}}{e^{-\gamma_{\text{nat}}}} \cdot \frac{e^{-\gamma}}{(1 - e^{-\gamma})^2} \cdot h^{-D_0(\Gamma_s)/2} \quad (5.8)$$

for  $\gamma \geq \gamma_{\text{nat}}$  and  $P(\gamma) = 0$  for  $\gamma < \gamma_{\text{nat}}$ . We illustrate the rescaled probability distribution  $\tilde{P}(\gamma) = P(\gamma)/h^{-D_0(\Gamma_s)/2}$  in Fig. 5.4 for the same parameters as in Fig. 5.3, where the Kantsz-Grassberger relation  $D_0(\Gamma_s)/2 \approx D_1^{(u)}(\Gamma_s) = 1 - \frac{\gamma_{\text{nat}}}{\lambda_L}$ , Eq. (2.52), and  $\lambda_L \approx \ln(\kappa/2)$  [57] have been used. For comparison the (rescaled) asymptotic expectation, Eq. (5.8), is plotted. For larger  $h$  the distribution fluctuates a lot around the predicted behavior, see (a) and (b), but we find very good agreement for small  $h$ , see (c) and (d).

## 5.2 Phase-space distribution for full escape

In this section we discuss the phase-space distribution of resonance eigenfunctions of quantum maps with full escape. First, we show that resonance eigenfunctions for partial escape converge to those of the limit of full escape. Secondly, we illustrate how single resonance eigenfunctions depend on the decay rate  $\gamma$  and how they change as a function of  $h$ . Furthermore, we investigate the convergence of expectation values of observables, which leads to the (not sharp) distinction between long-lived and short-lived resonance eigenfunctions. Finally, we illustrate the average Husimi distribution revealing underlying classical phase-space structures and review some general results about the semiclassical localization of resonance eigenfunctions [59, 60].

### 5.2.1 Eigenfunctions in the limit of full escape

Quantum maps with partial escape converge to the quantum map with full escape, see Sec. 5.1, if the corresponding reflectivity functions converge uniformly, Eq. (5.3). This implies the convergence of the spectra, seen in Sec. 5.1.2, and also of the eigenfunctions. Consider a sequence of eigenvalues  $\{\lambda_\alpha\}_{\alpha>0}$  of  $\mathcal{U}_\alpha$  converging to some eigenvalue  $\lambda_0$  of  $\mathcal{U}_0$ , and let  $\psi_\alpha$  and  $\psi_0$  be the corresponding resonance eigenfunction. Then Eq. (5.3) implies

$$\lim_{\alpha \rightarrow 0} \|\psi_\alpha - \psi_0\|_{\mathbb{H}_N} = 0. \quad (5.9)$$

In the following we consider the quantum maps  $\mathcal{U}_{R_\Omega}$  as in Eq. 5.5, where  $R_\Omega$  takes the role of the parameter  $\alpha$ . As an example we illustrate in Fig. 5.5 the Husimi distributions of two sequences of resonance eigenfunctions for decreasing  $R_\Omega \in \{10^{-2}, 10^{-3}, 10^{-4}, 10^{-5}, 0\}$  (from left to right) for  $h = 1/1000$ . The corresponding eigenvalues  $\lambda_{R_\Omega}$  are chosen closest to some eigenvalue  $\lambda_0$  of the system with full escape. The considered decay rates are  $\gamma \approx 0.666$  in (a) and  $\gamma \approx 1.616$  in (b). In the first case all Husimi distributions are qualitatively very close, even

for  $R_\Omega = 10^{-2}$ , Fig. 5.5(a). For smaller values of  $R_\Omega$  (middle panels) it is hardly possible to distinguish the Husimi distributions from the one at full escape. For the larger decay rate the Husimi distributions show structural differences depending on  $R_\Omega$ , see Fig. 5.5(b). Only for  $R_\Omega = 10^{-5}$  the Husimi distribution has the same main features as the one for full escape. This illustrates that for finite  $R_\Omega$  the agreement between eigenfunctions  $\psi_{R_\Omega}$  and  $\psi_0$  depends on the decay rate  $\gamma$ . For larger decay rates this convergence is seen for even smaller  $R_\Omega$ . Recall that we also observed agreement for the eigenvalues under the condition  $\gamma \ll \gamma_{\text{typ}}(R_\Omega)$ , Fig. 5.1, such that for finite  $R_\Omega$  there is no agreement for  $\gamma \gtrsim \gamma_{\text{typ}}(R_\Omega)$ .

In conclusion long-lived resonance eigenfunctions of systems with full escape show the same features as resonance eigenfunctions of systems with finite but small  $R_\Omega$  for decay rates  $\gamma \ll \gamma_{\text{typ}}(R_\Omega)$ . Fixing  $\gamma$  we can always find an arbitrary but small  $R_\Omega$  such that this condition is satisfied eventually, because  $\gamma_{\text{typ}}(R_\Omega) \rightarrow \infty$  for  $R_\Omega \rightarrow 0$ . Note that semiclassically almost all eigenfunctions have arbitrary large decay rates which is consistent with Refs. [57, 89]. Resonance eigenfunctions with eigenvalues close to zero correspond to so-called ballistically decaying quasimodes [58]. For these a universal classical description is not expected. Instead we are interested in the phase-space distribution of long-lived resonance eigenfunctions with finite decay rates.

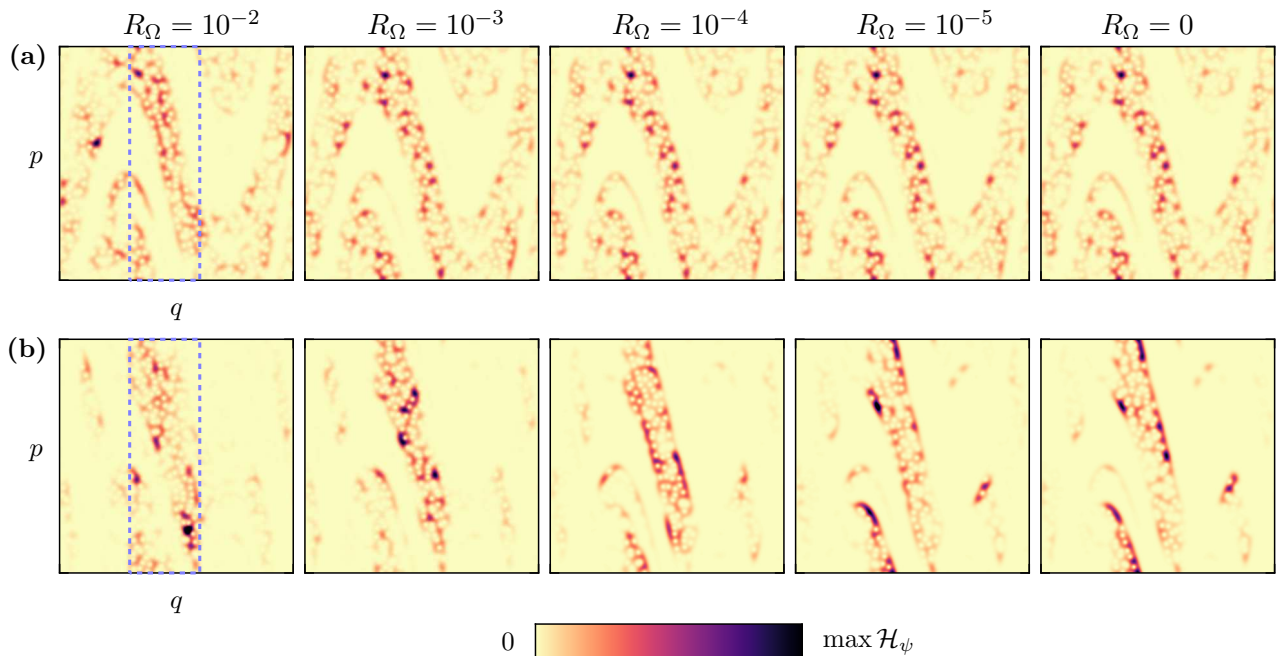


**Figure 5.5:** Husimi distribution  $\mathcal{H}_\psi$  of resonance eigenfunctions  $\psi$  in the limit of full escape. The considered eigenvalues are each closest to (a)  $(\theta, \gamma) \approx (0.05, 0.666)$  and (b)  $(\theta, \gamma) \approx (1.714, 1.616)$  for chaotic standard map with partial escape from  $\Omega$  where  $R_\Omega \in \{10^{-2}, 10^{-3}, 10^{-4}, 10^{-5}, 0\}$  (from left to right) and  $h = 1/1000$ . The considered values of  $(\theta, \gamma)$  correspond to an eigenvalue for  $R_\Omega = 0$ . Dashed blue line indicates the position of the opening  $\Omega = (0.3, 0.6) \times [0, 1)$ .

### 5.2.2 Long-lived resonance eigenfunctions

In the following we investigate properties of resonance eigenfunctions in dependence on their decay rate. For this purpose we illustrate the Husimi distribution of single resonance eigenfunctions  $\mathcal{H}_\gamma$  of the example system with small decay rates  $\gamma \in \{\gamma_{\text{nat}} \approx 0.25, 0.35, 0.5, 0.75, 1\}$  in Fig. 5.6 and with larger decay rates  $\gamma \in \{1.5, 2, 4, 6, 8\}$  in Fig. 5.7 for different values of Planck's constant  $h$ .

The top row of Fig. 5.6 shows long-lived resonance eigenfunctions for  $h = 1/250$ . The

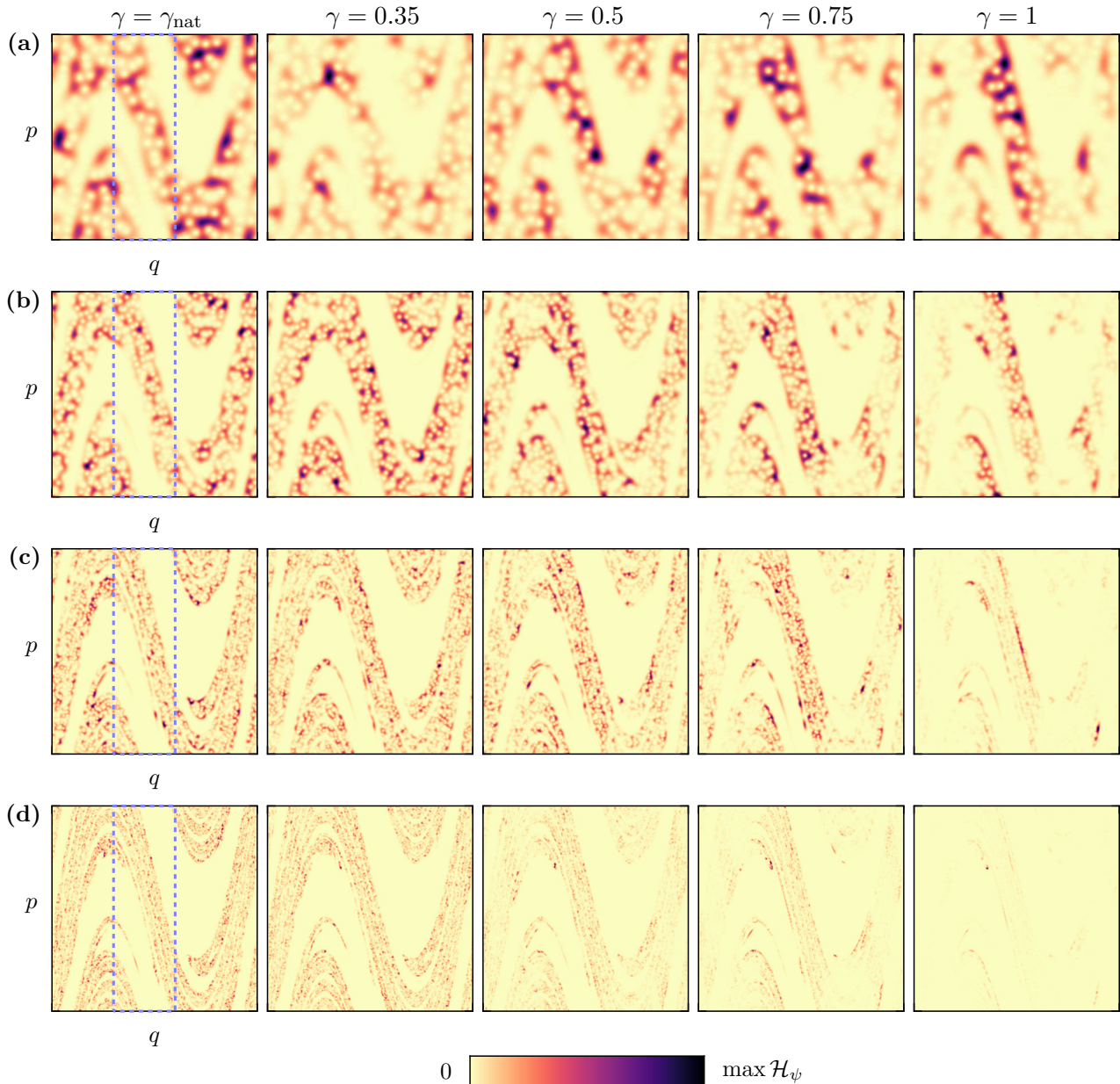


**Figure 5.6:** Husimi distribution  $\mathcal{H}_\psi$  of resonance eigenfunctions  $\psi$  with decay rate closest to  $\gamma \in \{\gamma_{\text{nat}}, 0.35, 0.5, 0.75, 1\}$  for chaotic standard map with full escape from  $\Omega$  and decreasing Planck's constant (a)  $h = 1/250$ , (b)  $h = 1/1000$ , (c)  $h = 1/4000$ , and (d)  $h = 1/16000$ . An individual colormap is used in each panel. Dashed blue line indicates the position of the opening  $\Omega = (0.3, 0.6) \times [0, 1)$ .

distribution is clearly not uniform for all decay rates. We observe one prominent patch on the phase-space, where the density is nearly zero for all decay rates  $\gamma$ . This region is given by the classical image of the opening  $M(\Omega)$ . Moreover, the Husimi distribution is more concentrated on the opening  $\Omega$  for increasing decay rate  $\gamma$ . This becomes more evident for smaller Planck's constant,  $h = 1/1000$ , in Fig. 4.5(b). We find that there are additional regions with zero density for all  $\gamma$ , which are related to further iterates of the opening  $\Omega$ . The support of all long-lived resonance eigenfunctions semiclassically concentrates on the fractal backward trapped set  $\Gamma_b$ , Eq. (2.43), and is zero on the sets  $\Omega_m^-$ , Eq. (2.45), which are iterates of the opening  $\Omega$  [59]. Decreasing  $h$  further to  $h = 1/4000$  and  $h = 1/16000$  in Fig. 4.5(c) and (d), the fractal support is resolved on finer scales. The dependence on the decay rate and the enhanced probability on

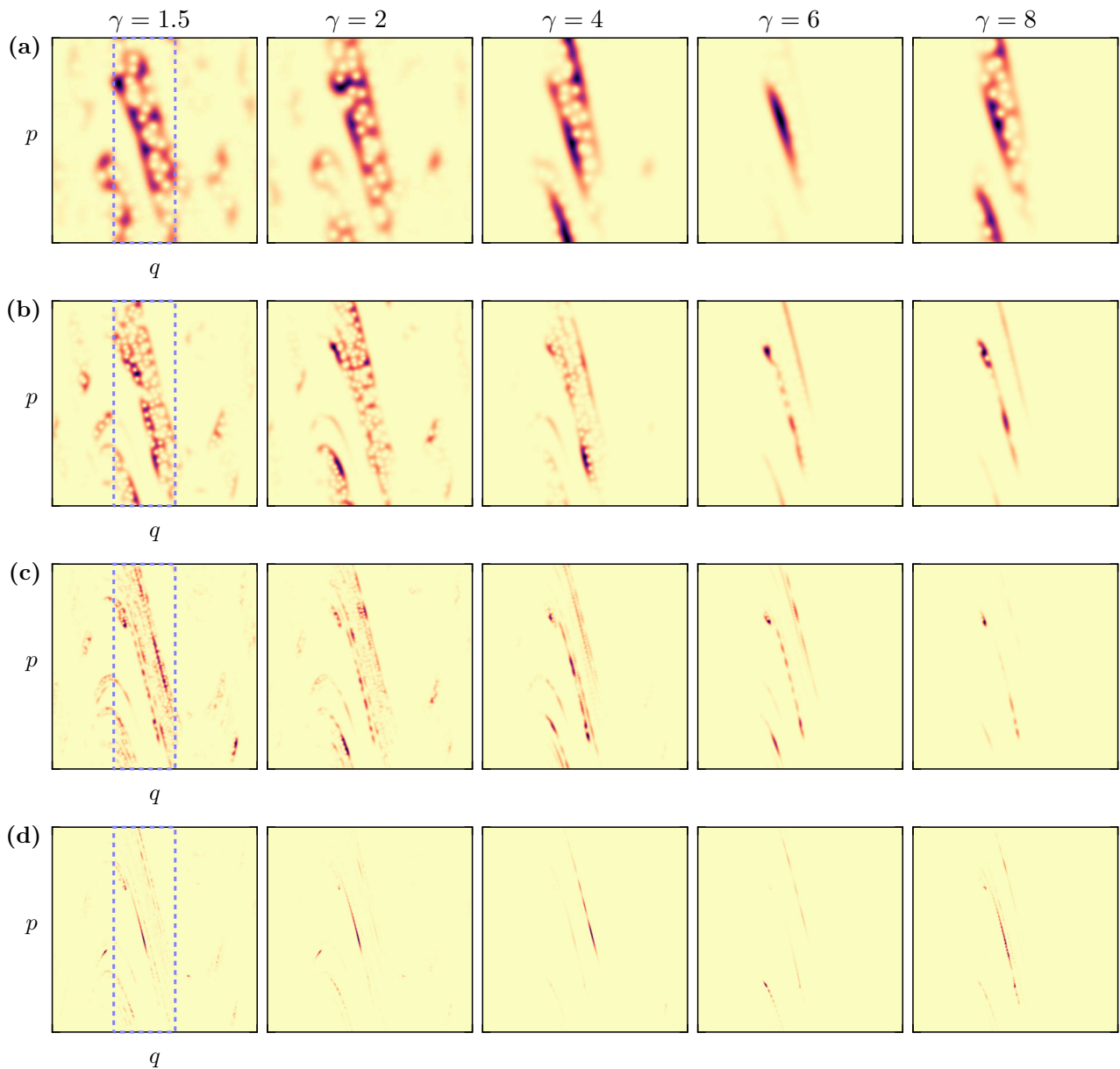


**Figure 5.7:** Same as Fig. 5.6 for larger decay rates  $\gamma \in \{1.5, 2, 4, 6, 8\}$  as indicated considering (a)  $h = 1/250$ , (b)  $h = 1/1000$ , (c)  $h = 1/4000$ , and (d)  $h = 1/16000$ .

$\Omega$  is more pronounced for smaller  $h$ .

We similarly illustrate resonance eigenfunctions with larger decay rates  $\gamma \in \{1.5, 2, 4, 6, 8\}$  in Fig. 5.7 for the same values of  $h$ . Some of these eigenfunctions have a similar structure as before, in particular for  $\gamma = 1.5$ . In contrast, there are also eigenfunctions, which mainly concentrate on single phase-space points, stretched along the unstable direction of the classical map, e.g., for  $h = 1/250$  and  $\gamma = 6$ . Such a behavior is expected for ultra-fast decaying modes [58]. Moreover, for fixed  $\gamma$  and decreasing  $h$  the localization sometimes changes significantly regarding the support and the regions with maximal intensity. This also occurs for fixed  $h$  and increasing  $\gamma$  and could be caused by quantum fluctuations of the single Husimi distributions.

In the next section we investigate if these observations can be quantified by expectation values of some observables. In particular, we are interested if it is possible to distinguish between two different types of resonance eigenfunctions.

### 5.2.3 Convergence of phase-space distribution

The considerations about the limit of full escape, Sec. 5.2.1, implicate that all long-lived resonance eigenfunctions can be seen as the limit of resonance eigenfunctions of systems with partial escape. Therefore we expect that similar to the observations in systems with partial escape, Sec. 4.2.2, long-lived resonance eigenfunctions with the same decay rate  $\gamma$  converge semiclassically to the same distribution, which only depends on the decay rate  $\gamma$ . For short-lived eigenfunctions, however, we do not have this expectation. In the following we quantify this by the same numerical calculations as in Sec. 4.2.2, applied to full escape. First, we calculate expectation values of exemplary observables  $a$  on the phase-space for all resonance eigenfunctions. Secondly, we investigate the average expectation value and the dependence of the standard deviation around this average for decreasing  $h$ .

#### 5.2.3.1 Expectation values of single eigenfunctions

Let us consider the same observables on the phase space  $\Gamma$  as in Sec. 4.2.2, the indicator functions  $a_{1,2,3}(q, p) = \mathbb{1}_{A,B,C}(q, p)$  of the subsets  $A = (0.3, 0.5) \times (0.6, 0.8)$ ,  $B = (0.7, 0.9) \times (0.1, 0.3)$ ,  $C = (0.3, 0.5) \times (0.1, 0.3)$ , and the smooth observable  $a_4(q, p) = \sin^2(2\pi q) \cos(\pi p)$ . The expectation values  $\mathbb{E}_\psi[a_i]$  are calculated according to Eq. (3.10) for all eigenfunctions  $\psi$ .

In Fig. 5.8 we illustrate the expectation values  $\mathbb{E}_\psi[a_i]$  of these observables over the decay rate  $\gamma$  considering all resonance eigenfunctions  $\psi$  for  $h \in \{1/1000, 1/16000\}$ . Results for the observable  $a_1$  are shown for decay rates up to  $\gamma = 2$  in Fig. 5.8(a). At  $h = 1/1000$  (left panel) we observe that the expectation value at  $\gamma_{\text{nat}}$  (red vertical line) is approximately given by the uniform expectation of closed systems,  $\mathbb{E}_{\text{cl}}[a_1] = \mu_L(A) = 0.04$  (gray horizontal line). The expectation values increase with  $\gamma$ . For large decay rates between  $\gamma \in [1, 2]$  there are only a few resonances at this value of  $h$ . The dependence for larger  $\gamma$  can be revealed in a double-logarithmic representation (inset). We observe that  $\mathbb{E}_\psi[a_1]$  increases with  $\gamma$  up to  $\gamma \approx 4$  and



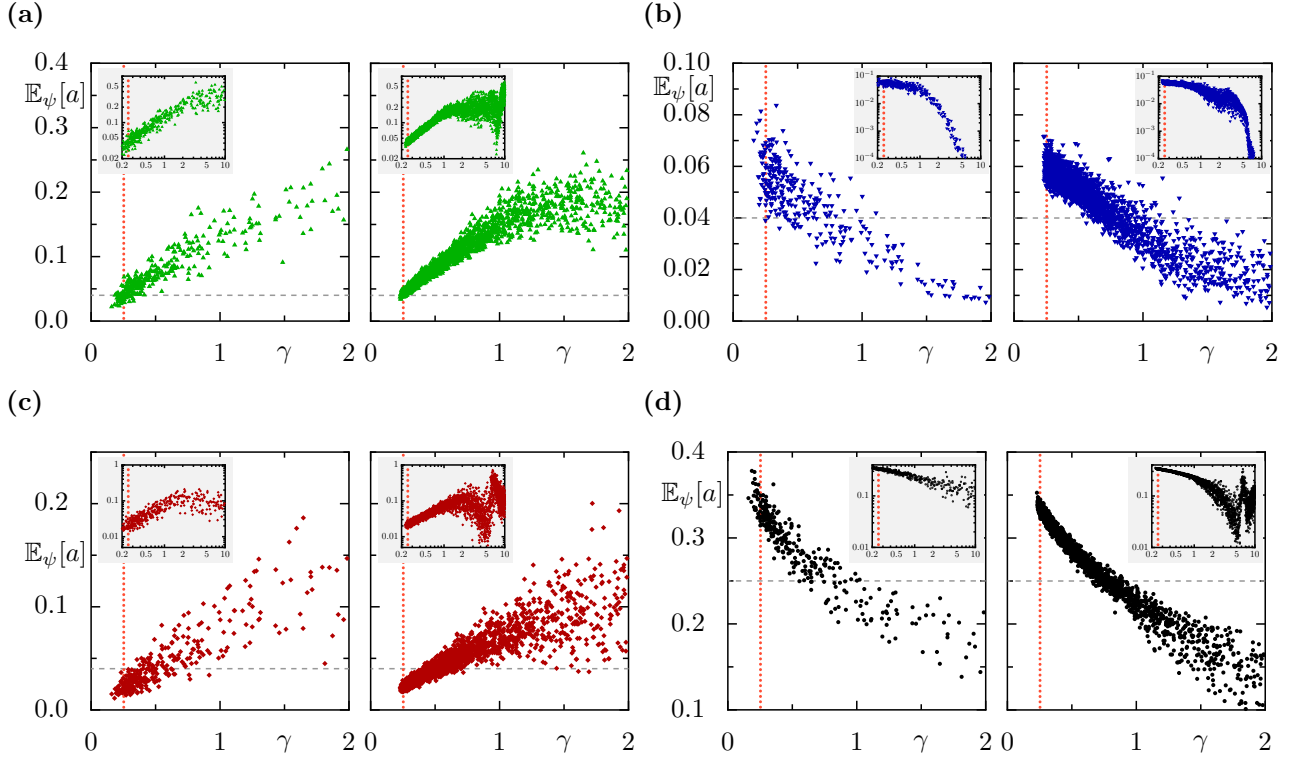


**Figure 5.8:** Expectation values  $\mathbb{E}_\psi[a]$  of different observables  $a$  on  $\Gamma$  for single resonance eigenfunctions  $\psi$  as a function of their decay rate  $\gamma$ . Considered are observables (a)  $a_1 = \mathbb{1}_A$ , (b)  $a_2 = \mathbb{1}_B$ , (c)  $a_3 = \mathbb{1}_C$ , and (d) smooth  $a_4(q, p) = \sin^2(2\pi q) \cos(\pi p)$ , see Fig. 4.7. Planck's constant is  $h = 1/1000$  (left) and  $h = 1/16000$  (right). Gray dashed line indicates  $\mu_L(a_i)$  for each observable. Inset shows the same data for a larger range of decay rates  $\gamma$  in a double-logarithmic plot.

then saturates for larger decay rates. Considering  $h = 1/16000$  (right panel) the dependence on  $\gamma$  is overall the same as for  $h = 1/1000$  for decay rates up to  $\gamma \approx 1$ . For larger decay rates the linear plot shows a saturation of  $\mathbb{E}_\psi[a_1]$ . The double-logarithmic representation in the inset reveals large fluctuations of  $\mathbb{E}_\psi[a_1]$  for decay rates above  $\gamma \approx 2$ . We believe that this indicates the nonuniversal behavior expected for ultra-fast decaying resonance eigenfunctions.

For the second observable  $a_2$  we find a different dependence on the decay rate  $\gamma$ , Fig. 5.8(b). The expectation value decreases with  $\gamma$  and even for  $h = 1/16000$  the observed fluctuations for  $\gamma \gtrsim 2$  are not prominent in the double-logarithmic plot and only visible on smaller scales. Note that the observable  $a_2$  is localized outside of the opening  $\Omega$ , see Fig. 4.7(a). For the third observable the dependence of  $\mathbb{E}_\psi[a_3]$  on  $\gamma$  is very similar to that of  $\mathbb{E}_\psi[a_1]$ , even though the scaling is different. We again find that  $\mathbb{E}_\psi[a_3]$  accumulates around a  $\gamma$ -dependent curve with decreasing  $h$  for decay rates up to  $\gamma \approx 1$ . For larger decay rates the expectation values fluctuate a lot (see inset).

We validate these observations with the results for the smooth observable  $a_4$  in Fig. 5.8(d). Again we observe decreasing expectation values  $\mathbb{E}_\psi[a_4]$  with  $\gamma$ . For  $h = 1/1000$  this behaves nicely even for large  $\gamma$  (left panel). However, for  $h = 1/16000$  there are very strong fluctuations

for decay rates larger than  $\gamma \approx 2$  (right panel, inset). Altogether we confirm that the expectation values of single resonance eigenfunctions behave similar to those of the system with partial escape for decay rates up to  $\gamma \approx 1$ . For these decay rates the results are compatible with a semiclassical convergence. For larger decay rates,  $\gamma \gtrsim 2$ , the presented data indicated that there is no convergence.

### 5.2.3.2 Average expectation values

We quantify these observations by considering average expectation values  $\langle a \rangle_\gamma$  and standard deviations  $\sigma_\gamma(a)$ , defined in Eqs. (4.9) and (4.10), respectively. For this purpose we average over  $S = 50$  resonance eigenfunctions with decay rate close to  $\gamma$  as in Sec. 4.2.2.

First of all we confirm that the mean decay rate  $\langle \gamma \rangle_\gamma$  converges to the specified  $\gamma$  in Fig. 5.9. We illustrate  $\langle \gamma \rangle_\gamma$  over  $h$  (markers) and additionally indicate the standard deviation  $\Delta_\gamma$  of the decay rates as shaded regions (a). For all considered  $\gamma$  the mean value  $\langle \gamma \rangle_\gamma$  converges to the specified value, but we observe larger standard deviations for larger decay rates. This is apparently related to the smaller density of resonances at larger values of  $\gamma$ , see discussion in Sec. 5.1.1 and Fig. 5.4. The standard deviation  $\Delta_\gamma$  is illustrated in a double-logarithmic plot as a function of  $h$  in Fig. 5.9(b). For all decay rates we find a power-law of the form  $\Delta_\gamma \sim h^{D_0(\Gamma_b)}$  (dashed line), which is implied by the fractal Weyl law (5.6). For a derivation see App. C.6.2. This shows that we always average over larger intervals for larger  $\gamma$ , but these regimes converge in the same way for all decay rates.

The convergence of expectation values of the phase-space observables is numerically tested for the smooth observable  $a_4$ . Fig. 5.10(a) illustrates the mean expectation value  $\langle a_4 \rangle_\gamma$  for the same decay rates  $\gamma$  as before. The dashed line is a guide to the eye, and the shaded regions indicate the standard deviation  $\sigma_\gamma(a_4)$ . We observe that the mean expectation value converges only for small decay rates (colored markers). For larger decay rates the mean expectation

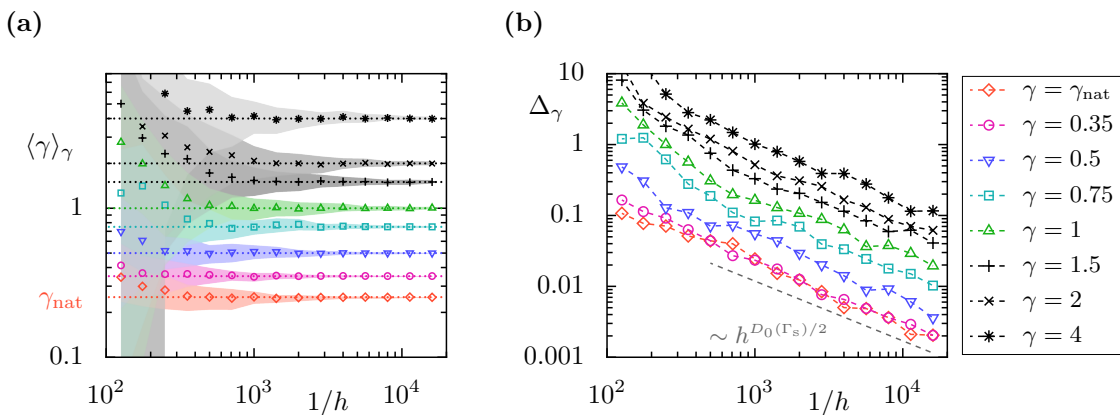


**Figure 5.9:** (a) Average decay rate  $\langle \gamma \rangle_\gamma$  vs.  $h$  for decay rates as specified. The average is taken over  $S = 50$  resonances. Shaded regions indicate standard deviation  $\Delta_\gamma$ . Dotted lines indicate selected  $\gamma$ . (b) Standard deviation  $\Delta_\gamma$  vs.  $h$  for same  $\gamma$  as in (a). Gray dashed line shows scaling  $\sim h^{D_0(\Gamma_s)/2}$ , see App. C.6.2.

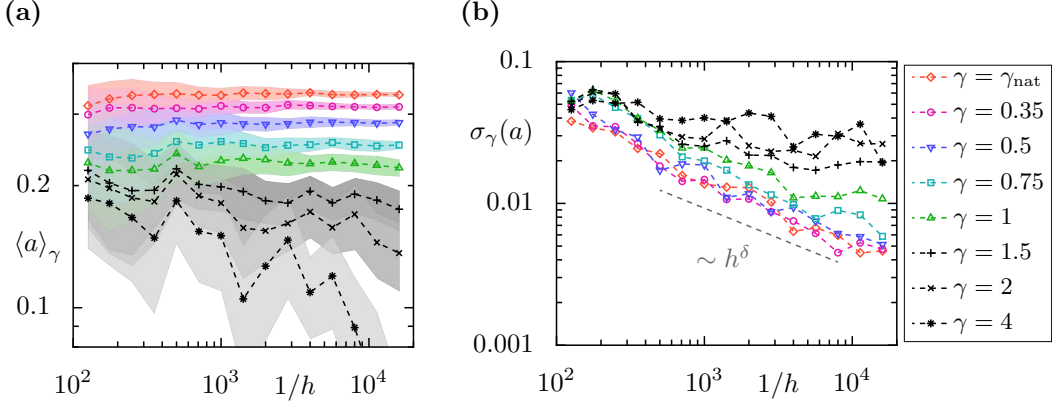


**Figure 5.10:** (a) Mean expectation value  $\langle a \rangle_\gamma$  vs.  $h$  for shown decay rates  $\gamma$  and smooth observable  $a = a_4$ . The average is taken over  $S = 50$  resonance eigenfunctions. Shaded regions indicates the corresponding standard deviation  $\sigma_\gamma(a)$ . (b) Standard deviation  $\sigma_\gamma(a)$  vs.  $h$  for same decay rates. Gray dashed line shows scaling  $\sim h^\delta$  for  $\delta \approx D_0(\Gamma_s)/4$ .

values do not follow a clear trend (black markers). Apparently for  $\gamma = 4$  it decreases and increases again rapidly in between the considered values of  $h$ , which is a strong indication that there is no convergence. This is also seen in the standard deviations  $\sigma_\gamma(a_4)$ , which decrease only for small decay rates. For  $\gamma = \gamma_{\text{nat}}$  we find a power law of the form  $\sigma_\gamma(a_1) \sim h^\delta$  where the exponent approximately satisfies  $\delta \approx D_0(\Gamma_s)/4$ . For decay rates above  $\gamma = 1$  there is no convergence of the standard deviation to zero. This implies, that the fluctuations around the mean value do not vanish semiclassically. Thus, there does not exist a (single) semiclassical limit measure for very short-lived resonance eigenfunctions. Similar results are found for the other observables, presented in App. B.2.

The convergence of all long-lived resonance eigenfunctions is further quantified with help of a similar quantity as in Eq. (4.13) restricted to decay rates smaller than a given cutoff  $\gamma_c$ ,

$$\tilde{S}_k(N, a; \gamma_c) = \frac{1}{n_{\text{res}}(\gamma_c; N)} \sum_{i=1}^{n_{\text{res}}(\gamma_c; N)} |\mathbb{E}_{\gamma_i}[a] - \langle a \rangle_{\gamma_i}|^k, \quad (5.10)$$

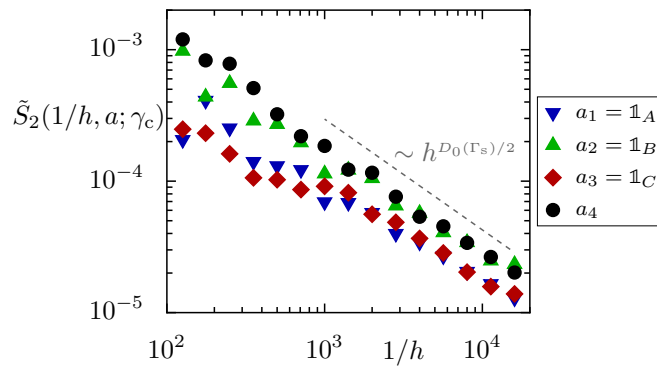


**Figure 5.11:** Convergence of resonance eigenfunctions in terms of the second moment  $\tilde{S}_2(N, a; \gamma_c)$  restricted to decay rates with  $\gamma_c \leq 0.75$ , see Eq. (5.10) shown as a function of  $h$  for the considered observables  $a_{1,2,3,4}$  as in Fig. 4.7.

where  $n_{\text{res}}(\gamma_c; N)$  is the number of eigenvalues with  $\gamma < \gamma_c$ , see the fractal Weyl law in Eq. (5.6). Figure 5.11 illustrates the dependence of  $\tilde{S}_2(N, a; \gamma_c)$  on Planck's constant  $h$  for all considered observables  $a_i$  in a double-logarithmic scaling. In all cases we observe a power law, which approximately satisfies  $\tilde{S}_2 \sim h^{D_0(\Gamma_s)/2}$ . Consistently the expected scaling in closed systems is recovered if the dimension of the chaotic saddle is replaced by the dimension of the whole phase space, see Sec. 3.2.2.

Altogether, we present strong evidence that only long-lived resonance eigenfunctions converge semiclassically. In conclusion, only for long-lived resonance eigenfunctions we expect a universal semiclassical limit measure. On the other hand we find indications, that there is no convergence of single (and average) resonance eigenfunctions for large decay rates  $\gamma$ . The transition between both regimes appears in the considered system at  $\gamma \approx 1$ , but a strict distinction is not observed.

### 5.2.4 Average distribution

The previous section implies, that the phase-space distribution of long-lived resonance eigenfunctions is well described by the average distribution  $\langle \mathcal{H} \rangle_\gamma^S$ , see Eq. (4.14), of the  $S$  closest resonance eigenfunctions. In the following we consider  $S = 50$  as in Sec. 4.2.3 and we omit the index  $S$ .

The average Husimi distributions  $\langle \mathcal{H} \rangle_\gamma$  corresponding to the same parameters as in Fig. 5.6 are illustrated in Fig. 5.12. Even for the largest considered  $h = 1/250$  these distributions are nonuniform, Fig. 5.12(a), and in particular the dependence on  $\gamma$  is clearer than for the single eigenfunctions, see Fig. 5.6(a). The density on the opening  $\Omega$ , indicated by dashed blue lines in the first panel, increases with  $\gamma$ . This is seen in the concentration of the highest intensities (dark red colored) within  $\Omega$  and is well understood [59], see Sec. 5.2.5. For  $h = 1/1000$  we additionally observe that the distribution within the opening also changes with  $\gamma$ , Fig. 5.12(b). For example, compare the densities for  $\gamma = \gamma_{\text{nat}}$  (left) and  $\gamma = 1$  (right) in Fig. 5.12(b): At  $\gamma_{\text{nat}}$  the distribution within  $\Omega$  has only one dominant color-scale on the supported region (dark red), but at  $\gamma = 1$  the density in  $\Omega$  is more concentrated on two smaller regions (black) compared to their surrounding (light orange). Hence at larger decay rates resonance eigenfunctions are less uniform on their support. This effect becomes better visible for smaller values of  $h$ , see (c) and (d). Decreasing  $h$  leads to a finer resolution, such that the average Husimi distribution  $\langle \mathcal{H} \rangle_\gamma$  reveals a fractal support.

Such a fractal support is not seen in the structure of resonance eigenfunctions with large decay rates, illustrated in Fig. 5.13. We notice that for  $h = 1/250$  the averaged distribution for large decay rates  $\gamma$  are almost the same (a), due to the small number of resonances and the definition of  $\langle \mathcal{H} \rangle_\gamma$ . It would be possible to generate more resonances, by changing the quantization or by variation of  $h$ , as done in Ref. [66]. In this thesis we use resonance eigenfunctions from a single quantum map at fixed  $h$ , only, since this effect vanishes semiclassically,

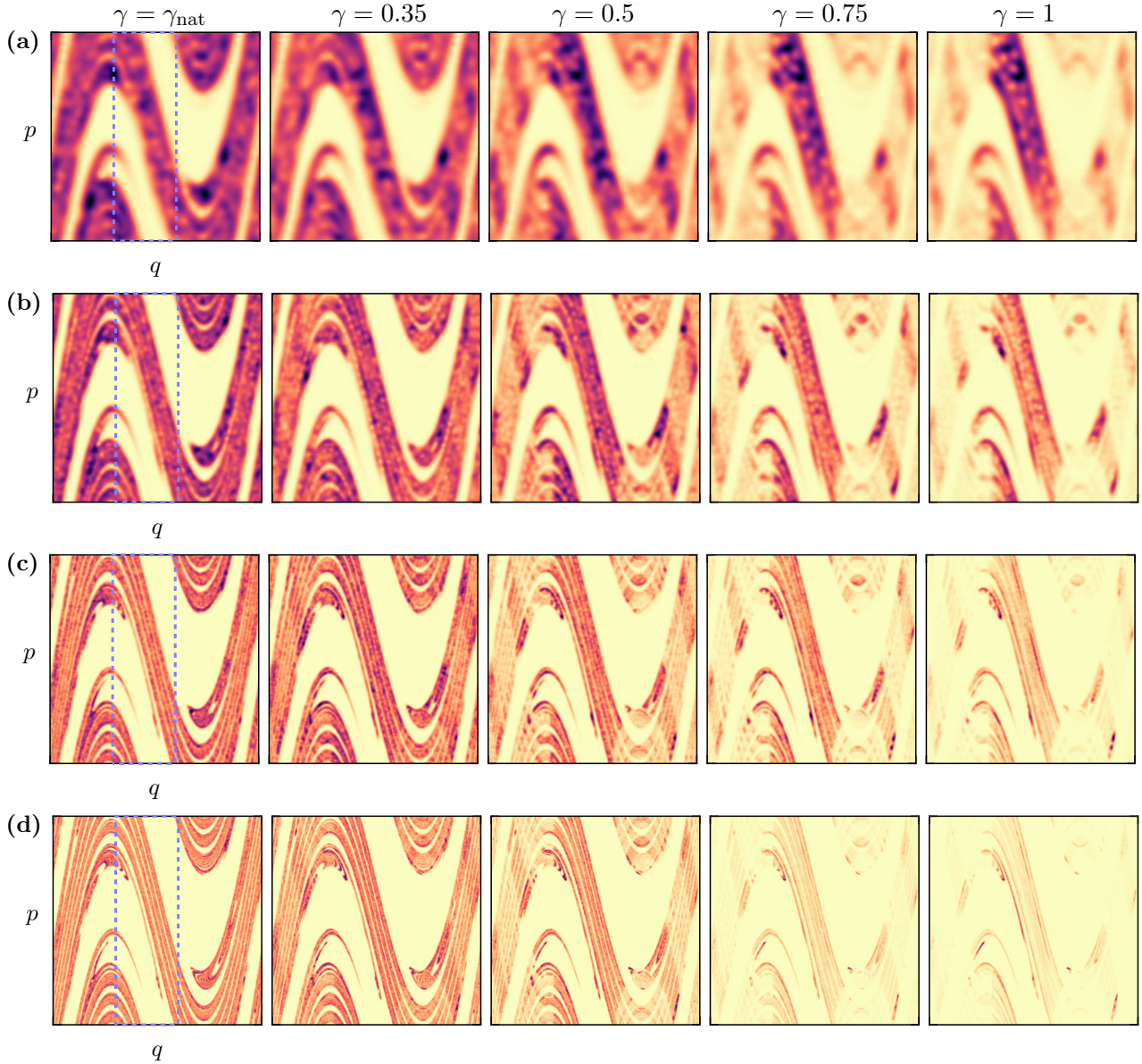


**Figure 5.12:** Average Husimi distribution  $\langle \mathcal{H} \rangle_\gamma$  of resonance eigenfunctions with decay rate closest to  $\gamma \in \{\gamma_{\text{nat}} \approx 0.25, 0.35, 0.5, 0.75, 1\}$  for the chaotic standard map with full escape with (a)  $h = 1/250$ , (b)  $h = 1/1000$ , (c)  $h = 1/4000$ , and (d)  $h = 1/16000$ . The average is taken over  $S = 50$  eigenfunctions. An individual colormap is used in each panel. Dashed blue line indicates the opening  $\Omega$ .

see Fig. 5.10. Apparently the average distribution localizes only on very few and stretched segments on the phase space, e.g., for  $\gamma = 6$  at  $h = 1/1000$  (b). This effect is more pronounced for smaller  $h$ , where the support mainly reduces to a thin filament on the opening, see (c) and (d). There also occur sudden changes in the localization with  $\gamma$ , e.g., for  $h = 1/16000$  the position of the maximum peak changes back and forth between  $\gamma = 4$  and  $\gamma = 8$ .

The latter behavior visualizes the previous observations, that for large decay rates  $\gamma$  the average distribution of resonance eigenfunctions is dominated by fluctuations of single eigenfunctions and is not converging semiclassically. In the following we will therefore mainly focus

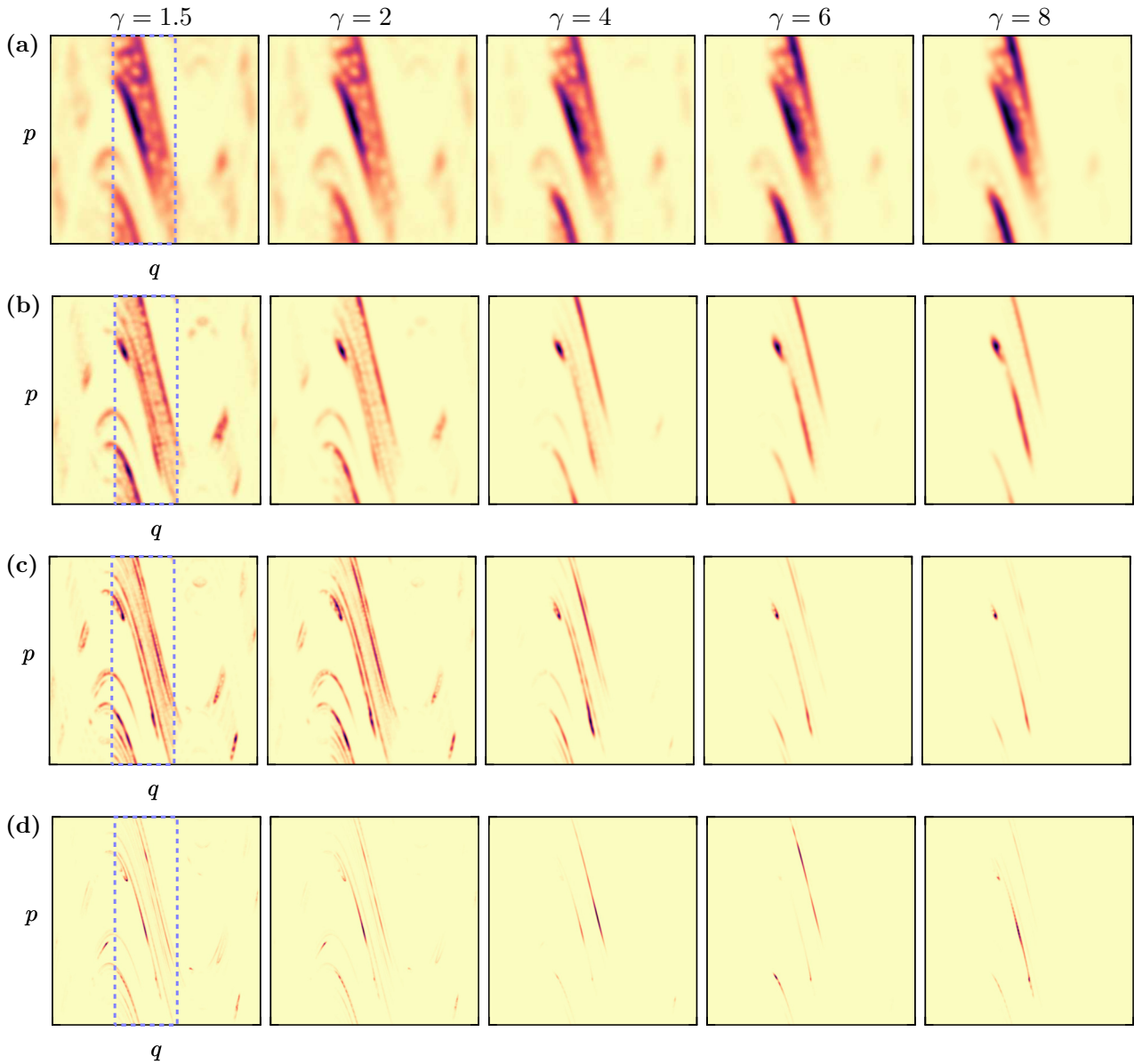


**Figure 5.13:** Same as Fig. 5.12 for larger decay rates  $\gamma \in \{1.5, 2, 4, 6, 8\}$  as indicated considering (a)  $h = 1/250$ , (b)  $h = 1/1000$ , (c)  $h = 1/4000$ , and (d)  $h = 1/16000$ .

on the regime of long-lived resonance eigenfunctions with decay rates up to  $\gamma \lesssim 1$ .

### 5.2.5 Semiclassical expectation for iterations of $\Omega$

As already discussed for partial escape in Sec. 4.2.5 and Sec. 2.2.6 the correspondence principle between quantum and classical time evolution implies certain restrictions on the semiclassical limit measures for eigenfunctions with decay rate  $\gamma$ , see Refs. [59, 60, 208]. We briefly repeat these results in the following.

First, we determine the weight of resonance eigenfunctions on the sets  $\Omega_m^+ = M^{-m}(\Omega) \setminus \bigcup_{i=0}^{m-1} M^{-i}(\Omega)$ , see Eq. (2.44), following the reasoning in Ref. [59]. Recall the definition of the quantum map with full escape,  $\mathcal{U} = \tilde{\mathcal{U}}(\mathbb{1} - \mathbb{1}_\Omega)$ , Eq. (5.5), where  $\mathbb{1}_\Omega$  is a projection on the

opening  $\Omega$ . It satisfies  $\mathcal{U}^\dagger \mathcal{U} = (1 - \mathbb{1}_\Omega)^2 = 1 - \mathbb{1}_\Omega$ , such that the expectation value, i.e., the weight on the opening, for eigenfunctions  $\psi_\gamma$  of  $\mathcal{U}$  with decay rate  $\gamma$  is given by

$$\mathbb{E}_{\psi_\gamma}[\Omega] = \langle \psi_\gamma | \mathbb{1}_\Omega | \psi_\gamma \rangle = \langle \psi_\gamma | \psi_\gamma \rangle - \langle \psi_\gamma | \mathcal{U}^\dagger \mathcal{U} | \psi_\gamma \rangle = 1 - e^{-\gamma}. \quad (5.11)$$

For the expectation on the sets  $\Omega_m^+$  for  $m > 0$  consider the operators  $\text{Op}(\mathbb{1}_{\Omega_m^+})$ , for which the quantum classical correspondence, Eq. (5.4), implies that asymptotically for  $h \rightarrow 0$

$$\mathcal{U}^\dagger \text{Op}(\mathbb{1}_{\Omega_m^+}) \mathcal{U} \sim \text{Op}(R_0 \cdot \mathbb{1}_{\Omega_m^+} \circ M) = \text{Op}((1 - \mathbb{1}_\Omega) \cdot \mathbb{1}_{M^{-1}(\Omega_m^+)}) = \text{Op}(\mathbb{1}_{\Omega_{m+1}^+}). \quad (5.12)$$

The last equality follows from the definition of the sets  $\Omega_m^+$ . This leads to the semiclassical expectation on  $\Omega_m^+$  for maps with full escape [59]

$$\mathbb{E}_{\psi_\gamma}[\Omega_m^+] \xrightarrow{h \rightarrow 0} e^{-m\gamma}(1 - e^{-\gamma}). \quad (5.13)$$

On the other hand, consider the sets which are mapped onto  $\Omega$  under inverse iteration,  $\Omega_m^- = M^m(\Omega) \setminus \bigcup_{i=1}^{m-1} M^i(\Omega)$ , as defined in Eq. (2.45), where  $\Omega_1^- = M(\Omega)$ . The quantization  $\text{Op}(\mathbb{1}_{\Omega_1^-})$  satisfies for  $h \rightarrow 0$  asymptotically [59, 208]

$$\mathcal{U}^\dagger \text{Op}(\mathbb{1}_{\Omega_1^-}) \mathcal{U} \sim \text{Op}(R_0 \cdot \underbrace{\mathbb{1}_{\Omega_1^-} \circ M}_{=\mathbb{1}_{M^{-1}(\Omega_1^-)}=\mathbb{1}_\Omega}) = \text{Op}(\underbrace{(1 - \mathbb{1}_\Omega) \cdot \mathbb{1}_\Omega}_{=0}) = 0 \quad (5.14)$$

which is implied by Eq. (5.4). Similarly follows that  $(\mathcal{U}^\dagger)^m \text{Op}(\mathbb{1}_{\Omega_m^-}) \mathcal{U}^m \sim 0$ . This implies for eigenfunctions with finite decay rates  $\gamma < \infty$ , that the expectation on the sets  $\Omega_m^-$  converges semiclassically to zero [59, 208],

$$\mathbb{E}_{\psi_\gamma}[\Omega_m^-] \xrightarrow{h \rightarrow 0} 0. \quad (5.15)$$

The intuitive implication of the last statement is, that the support of all resonance eigenfunctions with finite  $\gamma < \infty$  converges semiclassically to the fractal backward trapped set,  $\Gamma_b = \Gamma \setminus \bigcup_{m=1}^{\infty} \Omega_m^-$ , see Sec. 2.2.4. Let us remark, that Eq. (5.13) is generalized to partial escape, see Eq. (4.25) in Sec. 4.2.5, where the functions  $T_m^+$  generalize the sets  $\Omega_m^+$ . In contrast, the functions  $T_m^-$  in Eq. (4.26) are similar, but not equivalent to the sets  $\Omega_m^-$ .

The expectation values  $\mathbb{E}_{\psi_\gamma}[\Omega_m^+]$  are illustrated as a function of the modulus of the eigenvalue,  $|\lambda| = e^{-\gamma/2}$ , in Fig. 5.14 for the standard map with full escape. They are obtained by integrating the Husimi distribution of each resonance eigenfunction, evaluated on a  $1024 \times 1024$  grid, over the considered sets  $\Omega_m^+$ . Note that changing the grid size does not change the results, as long as it is fine enough. The insets show  $\Omega_m^+$  on the phase space. For the opening  $\Omega = \Omega_0^+$  in (a), we find very good agreement between the expectation values (colored markers) and the semiclassical prediction, Eq. (5.13), (dashed black line) for all values of  $h$ . The deviations are

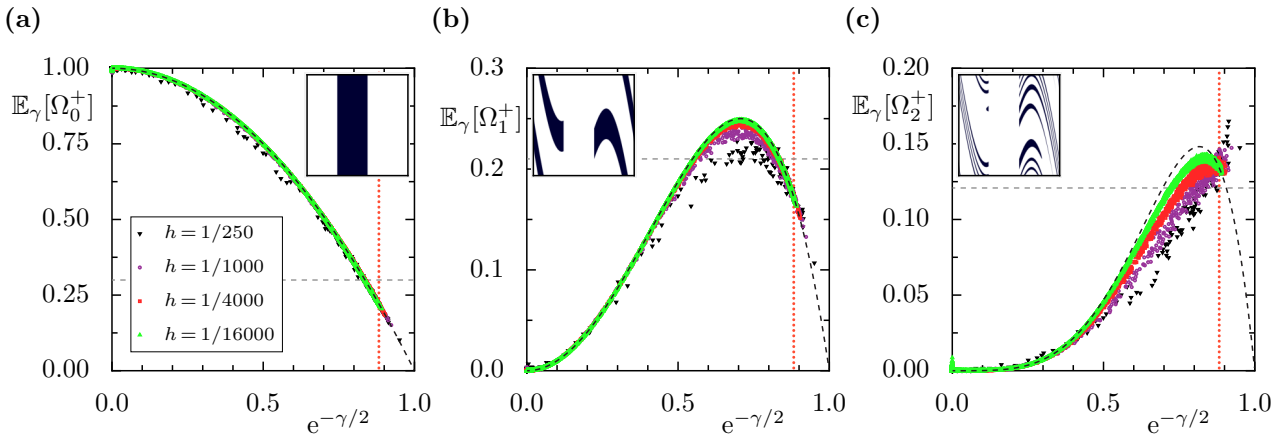


**Figure 5.14:** Expectation values on the sets  $\Omega_n^+$  for (a)  $m = 0$ , (b)  $m = 1$  and (c)  $m = 2$  vs. modulus of eigenvalue  $e^{-\gamma/2}$  for single eigenfunctions at  $h \in \{1/250, 1/1000, 1/4000, 1/16000\}$  (black, violet, red, green) compared to the semiclassical prediction Eq. (5.13) (dashed black lines), and to uniform expectation from closed system,  $\mu_L(\Omega_0^+) = 0.3, \mu_L(\Omega_1^+) \approx 0.21, \mu_L(\Omega_2^+) \approx 0.12$  (gray horizontal lines). Dotted vertical line indicates  $e^{-\gamma_{\text{nat}}/2}$  (red). Inset shows the sets  $\Omega_m^+$  on the phase space  $\Gamma$ .

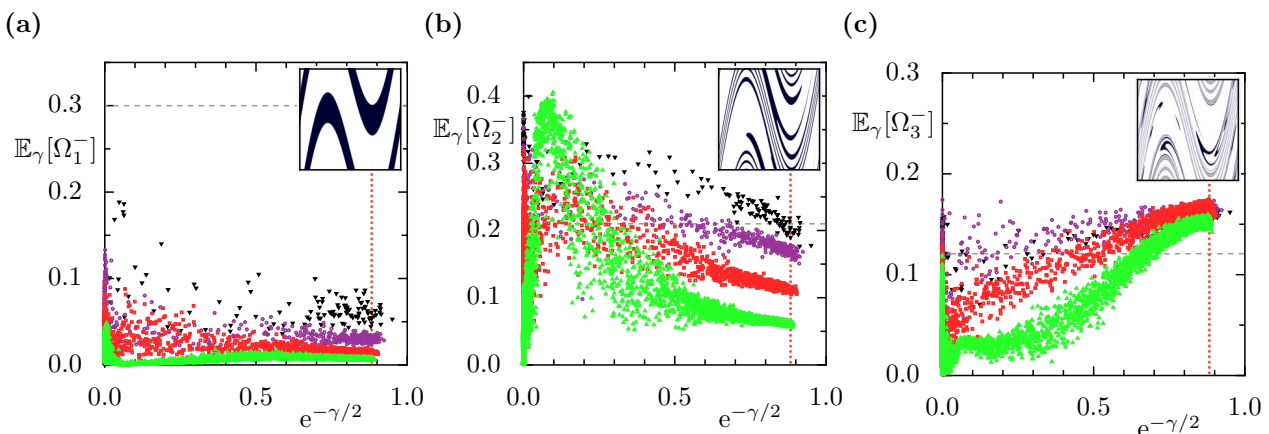


**Figure 5.15:** Same as Fig. 5.14, but showing expectation values on  $\Omega_m^-$  for (a)  $m = 1$ , (b)  $m = 2$  and (c)  $m = 3$ , for which the semiclassical prediction is zero, Eq. (5.15). Shown for comparison is the uniform expectation from the closed system,  $\mu_L(\Omega_1^-) = 0.3, \mu_L(\Omega_2^-) \approx 0.21, \mu_L(\Omega_3^-) \approx 0.12$  (gray horizontal lines). Dotted vertical line indicates  $e^{-\gamma_{\text{nat}}/2}$  (red). Inset shows the sets  $\Omega_m^-$  on the phase space  $\Gamma$ .

due to the finite width of coherent states overlapping with the complement of  $\Omega$ . The gray horizontal line shows for comparison the uniform expectation in the closed system, which is given by the size  $\mu_L(\Omega) = 0.3$ . The expectation values for  $\Omega_1^+$  show deviations to the prediction for  $h = 1/250$  and  $1/1000$ , but there is excellent agreement for all resonance eigenfunctions already at  $h = 1/4000$ , see (b). For  $\Omega_2^+$ , however, there are much larger deviations to the prediction (c). The quantum results approach the classical expectation when  $h$  becomes smaller, but even for  $h = 1/16000$  they do not match precisely. We conclude, that much smaller values of  $h$  are required to resolve the filamentary structure of  $\Omega_2^+$ , shown in the inset. Even for  $h = 1/16000$  the finite width of the coherent states used in the Husimi distribution is not



small enough to resolve this set in detail. Surprisingly, for  $\gamma_{\text{nat}}$  the agreement is similarly good for all  $h$ , see red dotted vertical line. These observations agree with those for partial escape, discussed in Sec. 4.2.5.

Figure 5.15 similarly depicts the expectation values  $\mathbb{E}_{\psi_\gamma}[\Omega_m^-]$  for the same values of  $h$  (colored markers). The insets illustrate the sets  $\Omega_m^-$ . For  $\Omega_1^-$  the semiclassical expectation of zero is confirmed for eigenfunctions with finite decay rate (a). While for  $h = 1/250$  the expectation is significantly larger than zero, it decreases for smaller  $h$ . Similar results are found for  $\Omega_2^-$ , where the expectation value decreases significantly with  $h$  for decay rates close to  $\gamma_{\text{nat}}$  (red vertical line). For  $h = 1/16000$ , however, the expectation value first increases steeply with the modulus of the eigenvalue until it slowly decreases. The peak corresponds to decay rates  $\gamma \approx 4$ , around which the obtained data shows stronger fluctuations for  $e^{-\gamma/2} \lesssim 0.5$ , which corresponds to  $\gamma \gtrsim 1$ . Recall that one condition in Eq. (5.15) is that the decay rate  $\gamma$  is finite. Therefore it may not be applied to ultra-fast decaying eigenfunctions which have eigenvalues close to zero [58]. We already observed in the previous section that the resonance eigenfunctions in these regimes are not strictly separated. Since the expectation value of  $\Omega_2^-$  is not necessarily zero for ultra-fast decaying modes, this explains why we do not observe a convergence to zero in this regime. The filamentary structure becomes much finer for  $\Omega_2^-$  than the quantum mechanical resolution. Hence the expectation values are much larger than zero, even for  $h = 1/16000$  and also around  $\gamma_{\text{nat}}$ .

The class of semiclassical limit measures is restricted by both equations, Eq. (5.13) and Eq. (5.15). More generally, Theorem 1 of Ref. [60] proves that the semiclassical limit measure of any convergent sequence of resonance eigenfunctions is a conditional invariant measure of the classical map with full escape and has the same decay rate  $\gamma$ . For more details we refer to the generalization of this result to maps with partial escape in Sec. 4.2.6.

### 5.3 Conditionally invariant measures for full escape

In this section we introduce and discuss different conditionally invariant measures (c-measures) for classical maps  $\mathcal{M}_\Omega$  with full escape. We first introduce a class of c-measures, which is based on the natural measure and has been successfully applied to explain localization of resonance eigenfunctions in systems with a partial barrier [65]. Secondly, we briefly discuss the limit of full escape for the product measures defined in Sec. 4.3.2. Finally, we motivate a resonance eigenfunction hypothesis based on a uniform distribution on the invariant chaotic saddle  $\Gamma_s$  which is finitely resolved quantum mechanically and therefore decays. This leads to a new class of c-measures depending not only on the decay rate  $\gamma$ , but also on the quantum resolution  $h$ .

#### 5.3.1 $\gamma$ -natural measures

One particularly intuitive class of conditionally invariant measures for maps with full escape are the so-called  $\gamma$ -natural measures  $\mu_\gamma^{\text{nat}}$  [65, 209]. These measures are based on a uniform distribution with respect to the natural measure  $\mu_{\text{nat}}$ , depending on the time to escape from the system. This leads to the following definition. The measures  $\mu_\gamma^{\text{nat}}$  are (i) conditional invariant with decay rate  $\gamma$  and (ii) proportional to the natural measure  $\mu_{\text{nat}}$  on all sets of points with the same temporal distance to the opening  $\Omega$ . These sets are given by  $\Omega_m^+$ , see Eq. (2.44). In particular this leads to a decomposition of the natural measure  $\mu_{\text{nat}}$  as in Eq. (2.68). Using  $\mu_{\text{nat}}(\Omega) = 1 - e^{-\gamma_{\text{nat}}}$  one obtains

$$\begin{aligned} \mu_\gamma^{\text{nat}}(A) &= \frac{1 - e^{-\gamma}}{1 - e^{-\gamma_{\text{nat}}}} \sum_{i=0}^{\infty} e^{-i\gamma} \mu_{\text{nat}}[M^i(A) \cap \Omega] \\ &= \frac{1 - e^{-\gamma}}{1 - e^{-\gamma_{\text{nat}}}} \sum_{i=0}^{\infty} e^{-i(\gamma - \gamma_{\text{nat}})} \mu_{\text{nat}}[A \cap \Omega_i^+], \end{aligned} \quad (5.16)$$

which follows from conditional invariance of  $\mu_{\text{nat}}$ . Thereby a family of conditionally invariant measures is obtained, which are proportional to  $\mu_{\text{nat}}$  on the sets  $\Omega_m^+$  with the same temporal

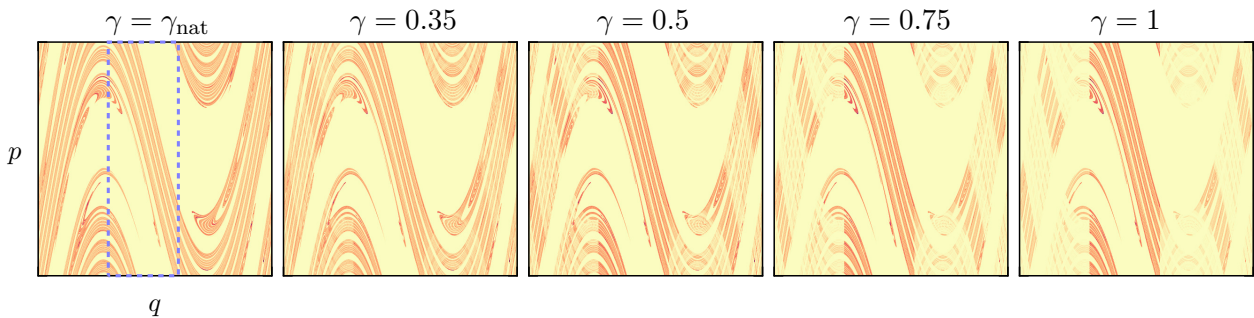


**Figure 5.16:** Measures  $\mu_\gamma^{\text{nat}}$  with  $\gamma \in \{\gamma_{\text{nat}} \approx 0.25, 0.35, 0.5, 0.75, 1\}$  for chaotic standard map with full escape smoothed by a Gaussian of width  $1/500$ . Dashed blue line indicates the opening  $\Omega$ .

distance to  $\Omega$ .

These measures are by definition proportional to  $\mu_{\text{nat}}$  on  $\Omega$  for all decay rates  $\gamma$ , see Fig. 5.16. Hence, there does not occur an additional enhancement within the opening, which we observed for resonance eigenfunctions, e.g., in Fig. 5.12. For this reason the measures  $\mu_{\gamma}^{\text{nat}}$  might be good approximations to the semiclassical limit measures, but this limit necessarily has a more complex structure.

### 5.3.2 Limit of product measures

A second class of conditionally invariant measures follows from the product measures  $\mu_{\xi}$  introduced for partial escape in Chapter 4. Recall that the measures  $\mu_{\xi}$  are defined for reflectivity functions  $R > 0$ , only. In the simple case, where escape only takes place from a region  $\Omega$ ,  $R(\mathbf{x}) = 1 - (1 - R_{\Omega})\mathbb{1}_{\Omega}(\mathbf{x})$ , full escape is characterized by  $R_{\Omega} = 0$ . In this case the map with escape  $\mathcal{M}$  is not invertible, such that  $\mu_{\text{inv}}$  is not defined. Moreover the measures  $\mu_{\xi}$  cannot be constructed directly, but only in the limit where  $R_{\Omega} \rightarrow 0$ . We emphasize that it is important to consider a fixed decay rate  $\gamma$ , as fixing  $\xi > 0$  and taking  $R_{\Omega} \rightarrow 0$  leads to a divergence of the obtained decay rate  $\gamma_{\xi}$ . This follows from Eq. (4.40), since the inverse decay rate  $\gamma_{\text{inv}}[R^{\xi}] \rightarrow \infty$  for any fixed  $\xi > 0$ , when  $R_{\Omega} \rightarrow 0$ .

For a fixed decay rate  $\gamma$ , let  $\mu_{(\xi(\gamma, R_{\Omega}), R_{\Omega})}$  be the product measure of the system with partial escape from  $\Omega$  for reflectivity  $R_{\Omega}$ . This leads to a conditional invariant measure of the system with full escape as the limit

$$\mu_{(\gamma, R_{\Omega}=0)} := \lim_{R_{\Omega} \rightarrow 0} \mu_{(\xi(\gamma, R_{\Omega}), R_{\Omega})}, \quad (5.17)$$

where  $\xi(\gamma, R_{\Omega})$  indicates its dependence on  $\gamma$  and the reflectivity  $R_{\Omega}$ . Note that if the natural decay rate  $\gamma_{\text{nat}}$  of the map with full escape is considered, this sequence converges to the natural measure,  $\mu_{(\gamma_{\text{nat}}, R_{\Omega}=0)} = \mu_{\text{nat}}$ .

As already discussed in Sec. 4.4.5 and illustrated in Fig. 4.30, the agreement between resonance eigenfunctions and product measures  $\mu_{\xi}$  is less good if more escape is allowed from the system, i.e., for smaller  $R_{\Omega}$ . Even though the product measures include a localization effect within the opening  $\Omega$ , it takes place on phase-space regions which are apparently not relevant for the map with full escape. In particular these measures show a strong enhancement on phase-space points  $\mathbf{x} \in \Omega$  whose forward iterates also fall into the opening  $M^i(\mathbf{x}) \in \Omega$ . In the limit of full escape  $R_{\Omega} = 0$ , however, the intensity on future iterations of phase space points is zero, once they enter the opening  $\Omega$ . For this reason these iterates are not relevant for the localization of resonance eigenfunctions in systems with full escape. Thus, the measures  $\mu_{(\gamma, R_{\Omega}=0)}$  are not relevant for the semiclassical phase-space distribution of resonance eigenfunctions. Hence, an entirely different approach is needed to understand resonance eigenfunctions for full escape.

### 5.3.3 Resonance eigenfunction hypothesis for full escape

In the following we heuristically motivate a resonance eigenfunction hypothesis for systems with full escape. It leads to a specific class of measures, which are possible candidates to describe resonance eigenfunctions in systems with full escape. The measures  $\mu_\gamma^{\text{nat}}$  and  $\mu_\xi$  discussed in the previous sections are both missing some of the key elements observed for resonance eigenfunctions in Sec. 5.2: The measures  $\mu_\gamma^{\text{nat}}$  do not include any enhancement within the opening  $\Omega$ , while the measures  $\mu_\xi$  localize on phase-space structures of iterations of  $\Omega$  which are not relevant in the systems with full escape.

#### 5.3.3.1 Simplified escape model

Recall the quantum ergodicity theorem for closed chaotic systems which states that almost all eigenfunctions become uniformly distributed with respect to the invariant uniform measure  $\mu_L$  in the semiclassical limit, Sec. 3.2.2. Thus, it seems reasonable to assume a similar form of uniformity in systems with full escape, but with respect to the uniform measure on the saddle  $\Gamma_s$ . The dynamics on  $\Gamma_s$  is chaotic and  $\Gamma_s$  is invariant under the map with full escape  $\mathcal{M}_\Omega$ . In contrast to the closed system, however, this invariant set is usually a fractal subset of  $\Gamma$ , see 2.2.5. Hence, the quantum mechanical uncertainty relation implies a finite resolution of  $\Gamma_s$  of the order of Planck's constant  $h$ . This leads to a finitely resolved saddle  $\Gamma_s^h$  for the quantum system. A similar approach has been used to motivate the fractal Weyl law of the distribution of resonances [57]. The  $h$ -resolved, or quantum-resolved saddle  $\Gamma_s^h$ , however, is not invariant under time evolution with  $\mathcal{M}_\Omega$ , but decays along the unstable manifold  $\Gamma_u$  of  $\Gamma_s$ . In the following we combine the assumption of uniformity on the saddle and the finite quantum resolution to achieve a conditional invariant measure of the classical system.

We consider a simplified model of the escape mechanism on the phase space, as sketched in Fig. 5.17. The phase space  $\Gamma$  is partitioned by the backward trapped set and the union of the sets  $\Omega_m^-$ , Eq. (2.45), which correspond to forward iterations of  $\Omega$ . The relevant classical

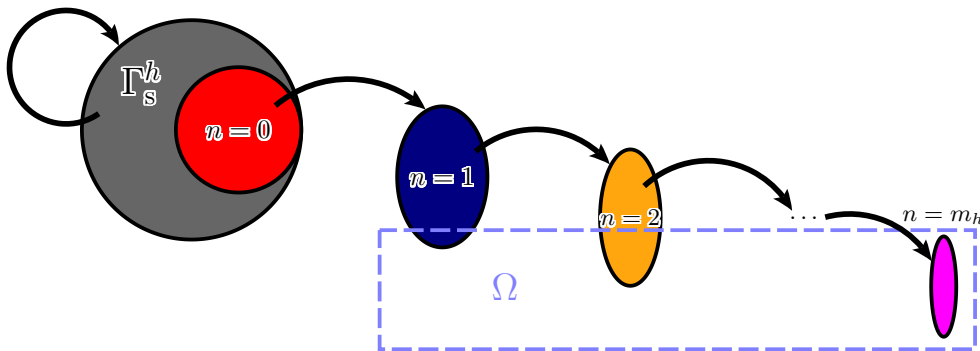


**Figure 5.17:** Sketch of the simplified escape model. Escape from  $h$ -resolved chaotic saddle  $\Gamma_s^h$  takes place from red region ( $n = 0$ ). The iterates of this region ( $n = 1, 2$ ) overlap with the opening  $\Omega$  (dashed blue area). They become smaller and stretched with  $n$ . After some finite time step  $n = m_h$  all iterations of  $n = 0$  have escaped through the opening  $\Omega$ .

dynamics for long times takes place only on the chaotic saddle and the backward trapped set. The  $h$ -resolved chaotic saddle  $\Gamma_s^h$  is a subset of  $\Gamma_b$ , which is illustrated by the large gray circle in Fig. 5.17. This set is not invariant under time evolution. Instead some subset of  $\Gamma_s^h$ , denoted by  $\mathcal{E}_0^h$ , will escape from it after one time step along the unstable manifold, see red circle in Fig. 5.17. Conversely, the set  $\Gamma_s^h \setminus \mathcal{E}_0^h$  is again mapped onto the  $h$ -resolved saddle. Time evolution of  $\mathcal{E}_0^h$  leads to a stretching along  $\Gamma_b$ , and we denote this iterate by  $\mathcal{E}_1^h = M(\mathcal{E}_0^h)$ , which might overlap with the opening  $\Omega$ . Further iterations define the sets  $\mathcal{E}_n^h = M(\mathcal{E}_{n-1}^h \setminus \Omega)$ , each consisting of all points that are mapped onto  $\Gamma_s^h$  in  $n$  backward iterations. Due to the finite size of  $\Gamma_s^h$  for given  $h$  there is a maximal number of iterations  $m_h$ , which satisfies  $\mathcal{E}_{m_h}^h \subset \Omega$ , see Fig. 5.17.

Quantum mechanically let us consider an analog decomposition of the Hilbert space  $\mathbb{H}_N$  for  $N = 1/h$ . Therefore we define the subspaces  $\mathbb{H}_N^{\Omega^-}$  belonging to the union of  $\Omega_m^-$ ,  $\mathbb{H}_N^s$  corresponding to  $\Gamma_s^h$  which includes  $\mathcal{E}_0^h$ , and for  $0 < n \leq m_h$  the spaces  $\mathbb{H}_N^n$  corresponding to the escaping sets  $\mathcal{E}_n^h$ . With this, we obtain  $\mathbb{H}_N = \mathbb{H}_N^s \oplus \mathbb{H}_N^1 \oplus \mathbb{H}_N^2 \dots \oplus \mathbb{H}_N^{m_h} \oplus \mathbb{H}_N^\Omega$ . The dimension of the space  $\mathbb{H}_N^s$  grows with the fractal dimension of the chaotic saddle like  $\sim h^{-D_0(\Gamma_s)/2}$  [57]. Let us remark that a slightly different decomposition is used in Ref. [57] to relate the time evolution on  $\mathbb{H}_N^s$  to truncated random matrices, explaining universal properties of the spectrum and also the fractal Weyl law, see Sec. 5.1.2. Together with the chaotic dynamics on the invariant set, this motivates the assumption, that eigenfunctions of the quantum map restricted to the subspace  $\mathbb{H}_N^s$  are described by truncated random matrices, where the truncation is proportional to the size of  $\mathcal{E}_0^h$ . These eigenfunctions, however, are uniformly distributed.

Therefore, for resonance eigenfunctions of the map with full escape it is reasonable to assume a uniform distribution on the subset of the backward trapped set  $\mathcal{E}_0^h \subset \Gamma_b$  which escapes from the quantum resolved saddle  $\Gamma_s^h$  in one time step. Forward iteration leads to a stretching of the distribution along the unstable manifold. Conditionally invariance further implies a factor proportional to  $e^\gamma$  in each time step, which implies more weight on those sets  $\mathcal{E}_n^h$  with larger number of iterations  $n$  from the  $h$ -resolved chaotic saddle. These considerations are generalized by the following hypothesis about the localization of resonance eigenfunctions in systems with full escape [66].

**Resonance eigenfunction hypothesis for systems with full escape.** *We conjecture that in chaotic systems with full escape through an opening  $\Omega$  the phase-space distribution of resonance eigenfunctions with decay rate  $\gamma$  for effective Planck's constant  $h$  is described by a measure that (i) is conditionally invariant with decay rate  $\gamma$  and (ii) is uniformly distributed on sets with the same temporal distance to the  $h$ -resolved chaotic saddle.*

Combining both properties results in a measure

$$\mu_\gamma^h(A) := \frac{1}{\mathcal{N}} \int_A e^{t_h(\mathbf{x})(\gamma - \gamma_{\text{nat}})} d\mu_{\text{nat}}(\mathbf{x}) \quad (5.18)$$

for all  $A \subset \Gamma$  with normalization constant  $\mathcal{N} = \int_{\Gamma} e^{t_h(\mathbf{x})(\gamma - \gamma_{\text{nat}})} d\mu_{\text{nat}}(\mathbf{x})$  and using a temporal distance  $t_h(\mathbf{x}) \in \mathbb{R}$  to the  $h$ -resolved chaotic saddle  $\Gamma_s^h$ . Such a distance function can be defined from the classical dynamics and needs to satisfy

$$t_h[M^{-1}(\mathbf{x})] = t_h(\mathbf{x}) - 1 \quad (5.19)$$

for almost all  $\mathbf{x} \in \Gamma_b$ . This excludes, e.g., points on the chaotic saddle  $\mathbf{x} \in \Gamma_s$ . This condition is required in order to achieve conditional invariance of  $\mu_{\gamma}^h$ , which is proven in Appendix C.6.3. Let us remark that it is possible to consider a weaker condition, where Eq. (5.19) is assumed only in the semiclassical limit  $h \rightarrow 0$ , i.e., the condition becomes  $\lim_{h \rightarrow 0} (t_h(\mathbf{x}) - t_h[M^{-1}(\mathbf{x})]) = 1$ . In this case the measures  $\mu_{\gamma}^h$  would become conditional invariant only in this limit.

The definition of  $\mu_{\gamma}^h$  has some important implications for its phase-space localization. First of all, for the natural decay rate  $\gamma_{\text{nat}}$  it is equal to the natural measure,  $\mu_{\gamma=\gamma_{\text{nat}}}^h = \mu_{\text{nat}}$ , which is uniformly distributed on the fractal backward trapped set  $\Gamma_b$ . For increasing  $\gamma > \gamma_{\text{nat}}$  the exponential factor in Eq. (5.18) leads to an enhancement of regions of  $\Gamma_b$  with larger temporal distances to the chaotic saddle. Those regions with maximal  $t_h(\mathbf{x})$  experience the strongest enhancement. This maximum is obtained on subsets of the opening  $\Omega$ , because iterating any  $\mathbf{x} \in \Gamma_b$  until it enters  $\Omega$  increases the temporal distance by one for each iteration. Altogether the hypothesis leads to a prediction for the localization observed for resonance eigenfunctions in chaotic systems.

### 5.3.3.2 Implementation of $\mu_{\gamma}^h$

So far we have not specified the precise form of the temporal distance  $t_h(\mathbf{x})$ , restricted only by Eq. (5.19). In the following we present a conceptually and numerically simple implementation of the temporal distance  $t_h(\mathbf{x})$  and of the measures  $\mu_{\gamma}^h$  [66], which is equivalent to the simplified escape model, see Fig. 5.17. Therefore we define the  $h$ -resolved saddle as a symmetric surrounding of the classical saddle,  $\Gamma_s^h = \{\mathbf{x} \in \Gamma : d_{\mathbb{T}^2}(\mathbf{x}, \Gamma_s) < \sqrt{\hbar/2}\}$ . Here we use the Euclidean metric on the two-dimensional torus  $d_{\mathbb{T}^2}(\mathbf{x}, \mathbf{y})$  which is obtained from the usual Euclidean metric by considering periodic boundary conditions. The temporal distance  $t_h(\mathbf{x})$  is defined as the number of backward iterations to enter the  $h$ -resolved saddle for the first time,

$$t_h(\mathbf{x}) = n \Leftrightarrow M^{-n}(\mathbf{x}) \in \Gamma_s^h \quad \text{and} \quad M^{-i}(\mathbf{x}) \notin \Gamma_s^h \quad \forall i < n. \quad (5.20)$$

This implies that points inside of  $\Gamma_s^h$  also obtain negative temporal distances  $t_h(\mathbf{x}) \leq 0$ . For all  $n \in \mathbb{Z}$  define  $\mathcal{E}_n^h := \{\mathbf{x} \in \Gamma_b : t_h(\mathbf{x}) = n\}$  as the set of points which need  $n$  backward iterations to the  $h$ -resolved chaotic saddle. For a fixed value of  $h$  there is a maximal temporal distance  $m_h = \max_{\mathbf{x} \in \Gamma_b} t_h(\mathbf{x}) < \infty$ . Consequently, the sets  $\mathcal{E}_n^h$  with  $n > m_h$  are empty and not considered. The remaining sets do not intersect by definition,  $\mathcal{E}_n^h \cap \mathcal{E}_m^h = \emptyset$  for all  $n, m \in \mathbb{Z}$  with  $n \neq m$ , and they partition the backward trapped set as  $\Gamma_b = \bigcup_{n=0}^{m_h} \mathcal{E}_n^h$ .

Inserting this partition into Eq. (5.18) simplifies the definition of  $\mu_\gamma^h$  to

$$\mu_\gamma^h(A) = \frac{1}{\mathcal{N}} \int_{A \cap \Gamma_b} e^{n(\gamma - \gamma_{\text{nat}})} d\mu_{\text{nat}}(\mathbf{x}) = \frac{1}{\mathcal{N}} \sum_{n=-\infty}^{m_h} \int_{A \cap \mathcal{E}_n^h} e^{n(\gamma - \gamma_{\text{nat}})} d\mu_{\text{nat}}(\mathbf{x}) \quad (5.21)$$

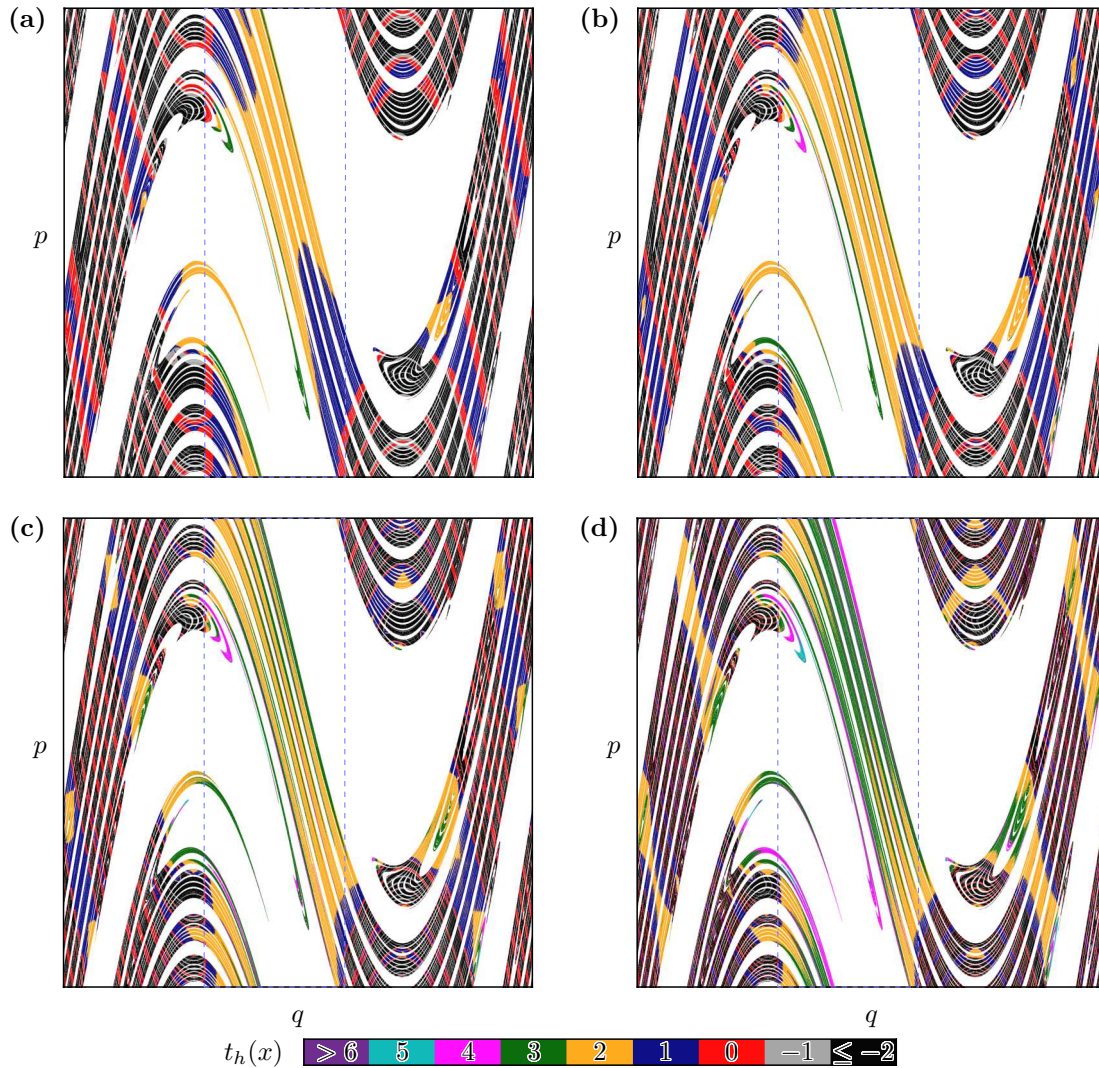
$$= \frac{1}{\mathcal{N}} \sum_{n=-\infty}^{m_h} e^{n(\gamma - \gamma_{\text{nat}})} \mu_{\text{nat}}(A \cap \mathcal{E}_n^h), \quad (5.22)$$

where we used that  $\mu_{\text{nat}}$  is supported only on  $\Gamma_b$ . This implementation of the resonance eigenfunction hypothesis for full escape is numerically simple to investigate.

### 5.3.3.3 Illustration

For the standard map with full escape from  $\Omega = (0.3, 0.6) \times [0, 1)$  the temporal distance  $t_h(\mathbf{x})$  on the backward trapped set is illustrated in Fig. 5.18 for different values of  $h$ . The backward trapped set and the chaotic saddle are calculated as in Sec. 2.2.5. Each point  $\mathbf{x} \in \Gamma_b$  is iterated backwards or forwards, until for some  $n \in \mathbb{Z}$  the condition in Eq. (5.20) is fulfilled. This is,  $d_{\mathbb{T}^2}[M^{-n}(\mathbf{x}), \Gamma_s] \leq \sqrt{\hbar/2}$  and  $d_{\mathbb{T}^2}[M^{-i}(\mathbf{x}), \Gamma_s] > \sqrt{\hbar/2}$  for all  $i < n$ . Thereby we obtain  $t_h(\mathbf{x}) = n \in \mathbb{Z}$  for all  $\mathbf{x} \in \Gamma_b$ . The results for  $h = 1/250$  are shown in Fig. 5.18(a). Each colored subset of  $\Gamma_b$  corresponds to one of the sets  $\mathcal{E}_n^h$ . Note that the white regions are the sets  $M^i(\Omega)$  and thus in the complement of  $\Gamma_b$ . Together the black, gray and red colored region with  $t_h(\mathbf{x}) \leq 0$  correspond to the  $h$ -resolved chaotic saddle. The red region indicates all points which leave the chaotic saddle in one time step, while the gray region needs two iterations and so on. On the other hand we see large stretched blue and yellow regions, which are the first and second iterate of the red region. Because all points are on the backward trapped set, they are stretched along the unstable direction. A close inspection reveals green colored sets with  $t_h(\mathbf{x}) = 3$ . The set with the maximum  $t_h(\mathbf{x}) = 4$  is so small, that it is barely visible in this resolution. In panel (b) we show results for  $h = 1/1000$ . The  $h$ -resolved saddle becomes visibly smaller (black and red). On the opening  $\Omega$  the sets  $\mathcal{E}_1^h$  are less dominant than in (a). Instead those sets  $\mathcal{E}_n^h$  with larger  $t_h(\mathbf{x}) = n$  are more prominent. This process continues for smaller values of  $h$ , see (c) and (d). Comparing (b) and (d), one observes that the regions with large temporal distances  $t_h(\mathbf{x})$  look very similar. For example, compare  $\mathcal{E}_3^h$  (green) and  $\mathcal{E}_4^h$  (magenta) in (b) with  $\mathcal{E}_4^h$  (magenta) and  $\mathcal{E}_5^h$  (petrol) in (d), respectively.

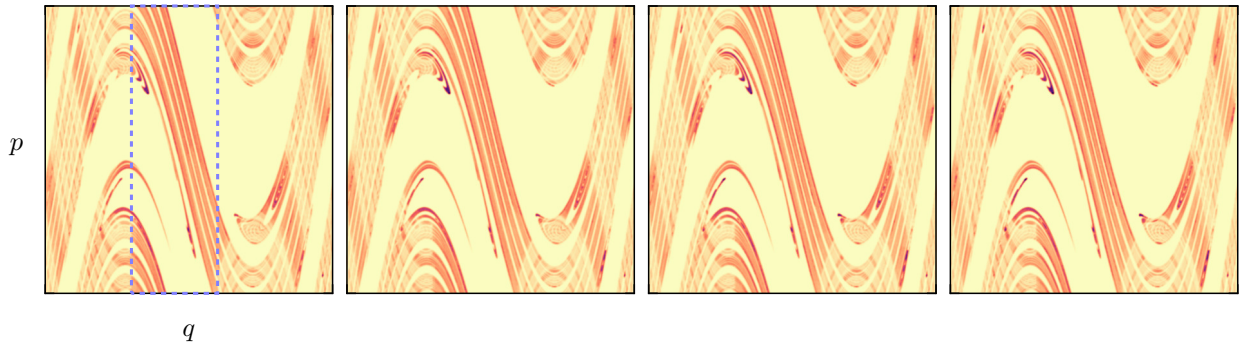
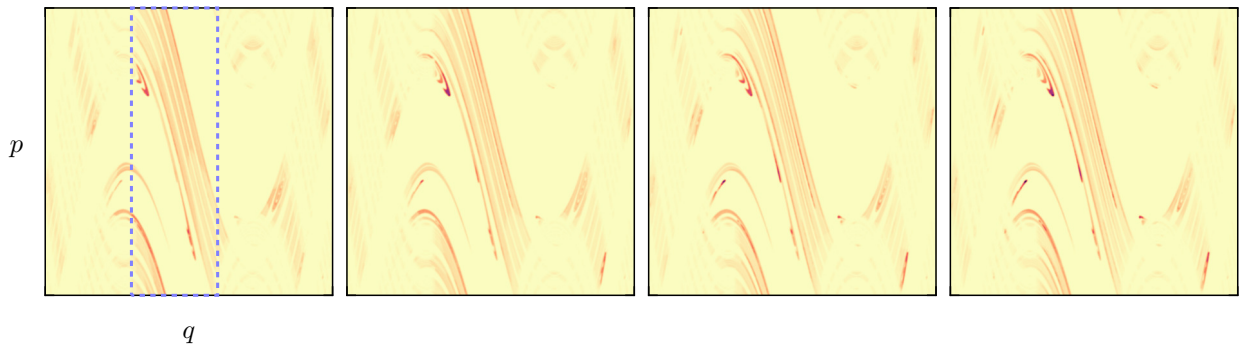
The differences in the saddle distances  $t_h(\mathbf{x})$  shown in Fig. 5.18 have two reasons. First, the geometric distance along the manifold to the  $h$ -resolved chaotic saddle depends obviously on the considered phase-space region. Secondly, the local stretching (or contraction under  $M^{-1}$ ) influences the temporal distance, depending on local Lyapunov exponents. We emphasize that, if for any two  $\mathbf{x}, \mathbf{y} \in \Gamma_b$  the difference  $t_h(\mathbf{x}) - t_h(\mathbf{y})$  remains almost constant for different values of  $h$ , we obtain similar measures. This is easily seen from their definition, Eq. (5.18) and is further discussed later.



**Figure 5.18:** Integer temporal distance  $t_h(\mathbf{x}) \in \mathbb{Z}$  on backward trapped set  $\mathbf{x} \in \Gamma_b$ . Sets of the same color correspond to the sets  $\mathcal{E}_n^h$  with the same temporal distance to  $\Gamma_s^h$  where  $n \leq m_h$  for (a)  $h = 1/250$  with  $m_h = 4$ , (b)  $h = 1/1000$  with  $m_h = 5$ , (c)  $h = 1/4000$  with  $m_h = 6$ , and (d)  $h = 1/16000$  with  $m_h = 7$ . The sets  $\mathcal{E}_n^h$  for  $n = m_h$  are barely visible due to their small size. The opening is indicated by the blue dashed line.

In Figure 5.19 we exemplarily illustrate the measures  $\mu_\gamma^h$  for  $\gamma \in \{0.5, 1\}$  and the same values of  $h$  as in Fig. 5.18. For  $\gamma = 0.5$  the illustrated densities are hard to distinguish, and the underlying structure of the natural measure is still visible. The exponential factor in the definition of  $\mu_\gamma^h$ , Eq. (5.22) leads to similar results for all  $h$ , even though the shown temporal distances  $t_h(\mathbf{x})$  in Fig. 5.18 are different. This indicates that decreasing  $h$  increases the temporal distance for all points on the backward trapped set in a similar way. Considering  $\gamma = 1$  the exponential factor including  $t_h(\mathbf{x})$  becomes more important. Therefore we are able to see differences in the phase-space distributions, see Fig. 5.19(b). For the smallest values of  $h$  the distributions are again very similar (right panels).



(a)  $\gamma = 0.5$ (b)  $\gamma = 1$ 

**Figure 5.19:** Phase-space distribution of the measures  $\mu_\gamma^h$  smoothed by Gaussian of width  $1/500$  for (a)  $\gamma = 0.5$  and (b)  $\gamma = 1$  and  $h \in \{1/250, 1/1000, 1/4000, 1/16000\}$ . The opening is indicated by the blue dashed line.

### 5.3.3.4 Semiclassical limit of $\mu_\gamma^h$

The previous illustrations lead to the question, how the measures  $\mu_\gamma^h$  behave in the limit of small  $h$ . In the following we will heuristically establish a relation to Lyapunov exponents, which indicates convergence of these measures in the semiclassical limit.

At first, consider  $\mathbf{y} \in \Gamma_s$  to be a periodic point of period  $p$  on the chaotic saddle. For all points  $\mathbf{x}$  on the unstable manifold of the periodic orbit  $\{M^i(\mathbf{y})\}_{i=0}^{p-1}$  we are interested in the number of backward iterations, until the distance along the manifold is smaller than some given  $d > 0$ . If the number of iterations is large for any such  $\mathbf{x}$  a local compression on the manifolds occurs by a factor  $e^{-\lambda_{\mathbf{y}}^{(p)}}$ , where  $\lambda_{\mathbf{y}}^{(p)}$  is the finite-time Lyapunov exponent over the period of the orbit. Hence an initial distance  $d_0(\mathbf{x})$  between  $\mathbf{x}$  and  $\mathbf{y}$  becomes smaller than  $d$  after  $n$  steps, if

$$d_0(\mathbf{x}) \cdot e^{-n\lambda_{\mathbf{y}}^{(p)}} < d \quad \Leftrightarrow \quad n \geq t_d(\mathbf{x}) := [\lambda_{\mathbf{y}}^{(p)}]^{-1} \log \frac{d_0(\mathbf{x})}{d}. \quad (5.23)$$

Note that choosing  $d = \sqrt{\hbar/2}$  implies  $t_d(\mathbf{x}) = t_h(\mathbf{x})$  for given  $h$ . Comparing two different

points  $\mathbf{x}$  and  $\tilde{\mathbf{x}}$  on the same manifold we obtain

$$t_d(\mathbf{x}) - t_d(\tilde{\mathbf{x}}) = [\lambda_{\mathbf{y}}^{(p)}]^{-1} \left( \log \frac{d_0(\mathbf{x})}{d} - \log \frac{d_0(\tilde{\mathbf{x}})}{d} \right) = [\lambda_{\mathbf{y}}^{(p)}]^{-1} \log \frac{d_0(\mathbf{x})}{d_0(\tilde{\mathbf{x}})}, \quad (5.24)$$

which is independent of the considered  $d$ . In particular for  $\tilde{\mathbf{x}} = M^{-1}(\mathbf{x})$  we get  $t_d(\mathbf{x}) - t_d(\tilde{\mathbf{x}}) \approx 1$  because  $d_0[M^{-1}(\mathbf{x})] \approx d_0(\mathbf{x})e^{-\lambda_{\mathbf{y}}^{(p)}}$ . Lets compare two points  $\mathbf{x}, \tilde{\mathbf{x}}$  on manifolds of different periodic orbits  $\mathbf{y}, \tilde{\mathbf{y}}$  with periods  $p, \tilde{p}$ , respectively. In this case we get

$$t_d(\mathbf{x}) - t_d(\tilde{\mathbf{x}}) = \log \left( \frac{d_0(\mathbf{x})}{d} \right)^{1/\lambda_{\mathbf{y}}^{(p)}} - \log \left( \frac{d_0(\tilde{\mathbf{x}})}{d} \right)^{1/\lambda_{\tilde{\mathbf{y}}}^{(\tilde{p})}} \quad (5.25)$$

$$= \log \frac{d_0(\mathbf{x})^{1/\lambda_{\mathbf{y}}^{(p)}}}{d_0(\tilde{\mathbf{x}})^{1/\lambda_{\tilde{\mathbf{y}}}^{(\tilde{p})}}} - \left( 1/\lambda_{\mathbf{y}}^{(p)} - 1/\lambda_{\tilde{\mathbf{y}}}^{(\tilde{p})} \right) \log d, \quad (5.26)$$

which is not independent of the chosen distance  $d$ . For decreasing values of  $d$  the difference  $t_d(\mathbf{x}) - t_d(\tilde{\mathbf{x}})$  increases if  $\lambda_{\mathbf{y}}^{(p)} < \lambda_{\tilde{\mathbf{y}}}^{(\tilde{p})}$ , i.e., when the periodic point  $\mathbf{y}$  is on average less expanding along its unstable manifold than  $\tilde{\mathbf{y}}$ .

This could in principle cause trouble when the semiclassical limit  $\hbar \rightarrow 0$  is considered for  $t_h(\mathbf{x})$ , because the measures  $\mu_{\gamma}^h$  depend on the differences in the temporal distances. The periodic points, however, are a set of (fractal) measure zero on the saddle  $\Gamma_s$ . Therefore, some point on the backward trapped set  $\Gamma_b$  will for large times typically not experience the contraction by a factor  $e^{-\lambda_{\mathbf{y}}^{(p)}}$  for a single periodic orbit  $\mathbf{y}$  on the saddle, but on average with a factor  $e^{-\lambda_L}$ . Here  $\lambda_L$  denotes the averaged Lyapunov exponent of all points on the saddle, which also appears in the Kantz-Grassberger relation Eq. (2.52). Lets assume that this average stretching factor is obtained exactly for all iterations after some large number of  $k \gg 1$  iterations. Then if  $m > k$  the initial distance decreases as  $d_0(\mathbf{x}) \cdot \exp\left(-\sum_{i=0}^{k-1} \lambda_i(\mathbf{x}) - (m-k)\lambda_L\right)$ , with  $\lambda_i(\mathbf{x})$  being the stretching exponent at  $M^{-i}(\mathbf{x})$  for  $i < k$ . Similar as above, for some finite  $d > 0$  this defines a temporal distance for any  $\mathbf{x} \in \Gamma_b$  by

$$t_d(\mathbf{x}) = \lambda_L^{-1} \log \left( \frac{d_0(\mathbf{x})e^{-\sum_{i=0}^{k-1} \lambda_i(\mathbf{x})}}{d} \right) + k. \quad (5.27)$$

In this case the temporal distance for any two phase-space points  $\mathbf{x}, \tilde{\mathbf{x}} \in \Gamma_b$  satisfies a similar relation to Eq. (5.24),

$$t_d(\mathbf{x}) - t_d(\tilde{\mathbf{x}}) = \bar{\lambda}^{-1} \log \frac{d_0(\mathbf{x})e^{-\sum_{i=0}^{k-1} \lambda_i(\mathbf{x})}}{d_0(\tilde{\mathbf{x}})e^{-\sum_{i=0}^{k-1} \lambda_i(\tilde{\mathbf{x}})}}, \quad (5.28)$$

which is again independent of the considered  $d$ . This equation means, that the initial distance  $d_0(\mathbf{x})$  is modified by some local finite time Lyapunov exponent  $\lambda_i(\mathbf{x})$  for a finite number of iterations.

These considerations suggest a semiclassical convergence of the measures  $\mu_\gamma^h$ . Note that we considered a specific form for the  $h$ -resolved chaotic saddle for our implementation of  $\mu_\gamma^h$ , which does not play a role in Eq. (5.28). We remark that other implementations of the resonance eigenfunction hypothesis are possible, e.g., by altering the definition of the  $h$ -resolved saddle  $\Gamma_s^h$ . It is not clear, if a limiting result for  $t_h(\mathbf{x})$  like Eq. (5.28), holds in general. Moreover, numerically it is difficult to apply Eq. (5.28), because calculating the initial distance  $d_0(\mathbf{x})$  along the unstable manifold is nontrivial. Therefore, in the following we consider the measures  $\mu_\gamma^h$  for finite  $h$  and in their simplest implementation, only.

## 5.4 Quantum-to-classical comparison

In this section we test the resonance eigenfunction hypothesis for chaotic maps with full escape. For this purpose we compare resonance eigenfunctions and the proposed classical measures  $\mu_\gamma^h$  resulting from the hypothesis. In order to analyze the quantum-to-classical agreement we examine their phase-space distribution qualitatively in Sec. 5.4.1. This is followed by a numerical investigation of effective fractal dimensions of quantum and classical densities in Sec. 5.4.2. We apply the Jensen–Shannon divergence to quantitatively analyze the distance between eigenfunctions and measures, and investigate to which extent they agree in the semiclassical limit, Sec. 5.4.3. Finally we consider different positions and sizes of the opening, Sec. 5.4.5.

### 5.4.1 Qualitative agreement

The average phase-space distribution of long-lived resonance eigenfunctions  $\langle \mathcal{H} \rangle_\gamma$  are illustrated and compared to the classical measures  $\mu_\gamma^h$  in Fig. 5.20. The top row of each sub-panel (a)–(d) shows the quantum distribution, while the bottom row shows the classical one for  $h \in \{1/250, 1/1000, 1/4000, 1/16000\}$ , respectively. The considered decay rates are  $\gamma \in \{\gamma_{\text{nat}}, 0.35, 0.5, 0.75, 1\}$  (from left to right). The classical fractal measures are smoothed with a Gaussian of width  $\sigma = \sqrt{\hbar/2}$  in order to obtain a phase-space density that is comparable to the Husimi distributions.

We observe a remarkable agreement, already for  $h = 1/250$ , see Fig. 5.20(a). For the natural decay rate  $\gamma_{\text{nat}}$  (left panels), both distributions almost perfectly match, even though there are visible fluctuations in the resonance eigenfunctions. Increasing the decay rate  $\gamma$  leads to similar structural changes and localization effects in quantum and classical densities. For  $\gamma = 1$  there appear visible differences, where the classical density experiences stronger enhancement (indicated by darker regions) than for the Husimi distribution. Considering  $h = 1/1000$  in (b) we confirm these observations, but on a finer resolution. Even for  $\gamma = 1$  here it is very difficult to find qualitative differences between quantum and classical densities. The illustrations for  $h = 1/4000$  in (c) and  $h = 1/16000$  in (d) expose the capability of the measures  $\mu_\gamma^h$ , as in all

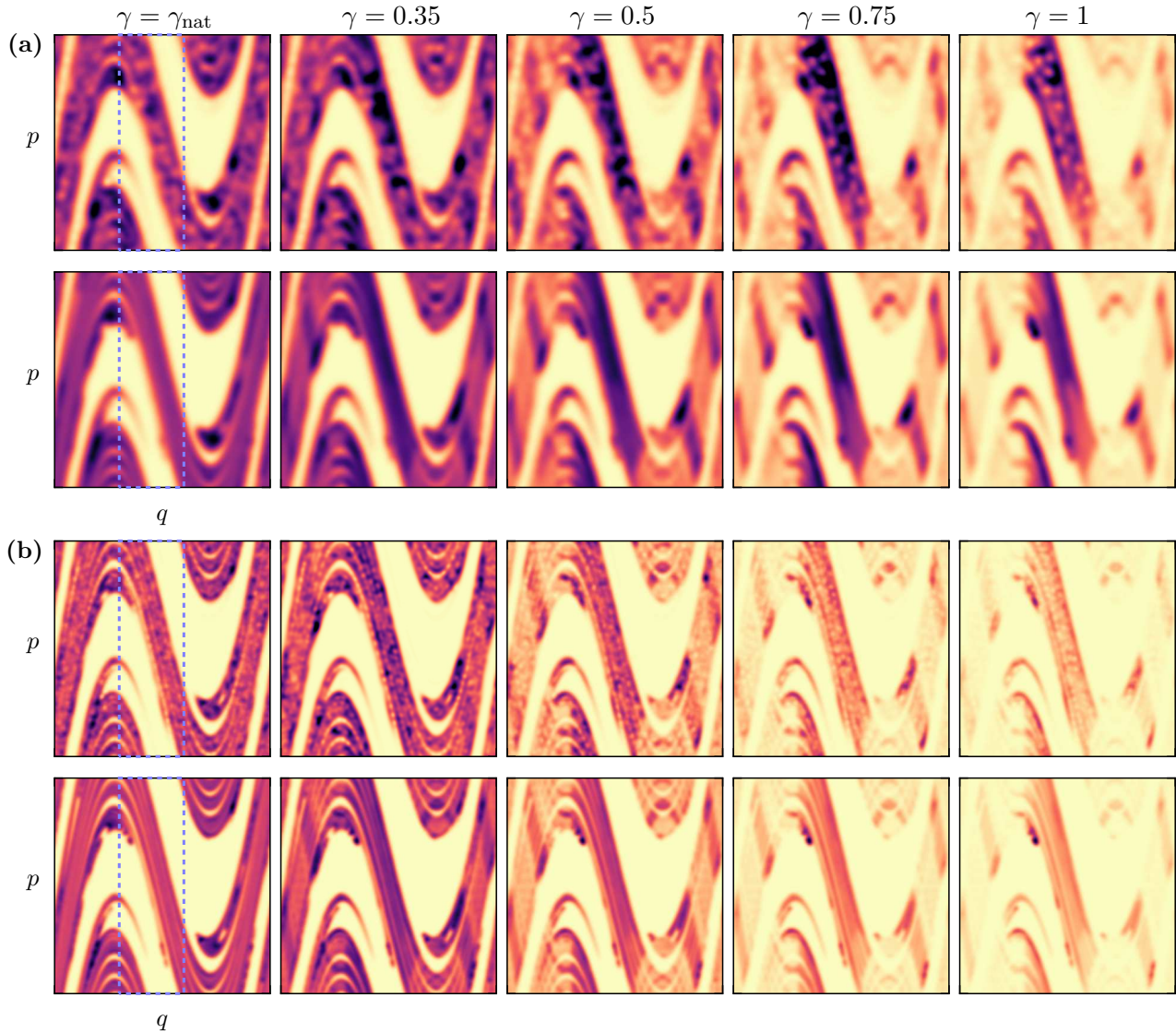


**Figure 5.20:** Quantum-to-classical correspondence for standard map with full escape. Shown are average Husimi distributions  $\langle \mathcal{H} \rangle_\gamma$  of resonance eigenfunctions averaged over 50 resonances for  $\gamma \in \{\gamma_{\text{nat}} \approx 0.25, 0.35, 0.5, 0.75, 1\}$  and (a)  $h = 1/250$ , (b)  $h = 1/1000$ , (c)  $h = 1/4000$ , and (d)  $h = 1/16000$  (top row). Bottom row shows Gaussian smoothed phase-space distribution of the measures  $\mu_\gamma^h$ , Eq. (5.22). The same colormap is used for quantum and classical densities, with the maximum given for each  $h$  and  $\gamma$  individually by the maximum of the classical density. Dashed blue line indicates position of the opening  $\Omega$ .

cases there is excellent agreement on the phase space. The differences are only detected by a careful inspection, and only for the largest decay rates  $\gamma$ .

However, they can be revealed for larger decay rates  $\gamma$ . In analogy to Fig. 5.20 we illustrate phase-space densities of shorter-lived eigenfunctions and measures with  $\gamma \in \{1.5, 2\}$  in Fig. 5.21. We observe that quantum densities and classical measures experience a similar enhancement in the opening  $\Omega$ , but there are differences in the strength and the specific regions. Recall that for such relatively large decay rates convergence of single and average eigenfunctions is not seen, as discussed in Sec. 5.2.3.

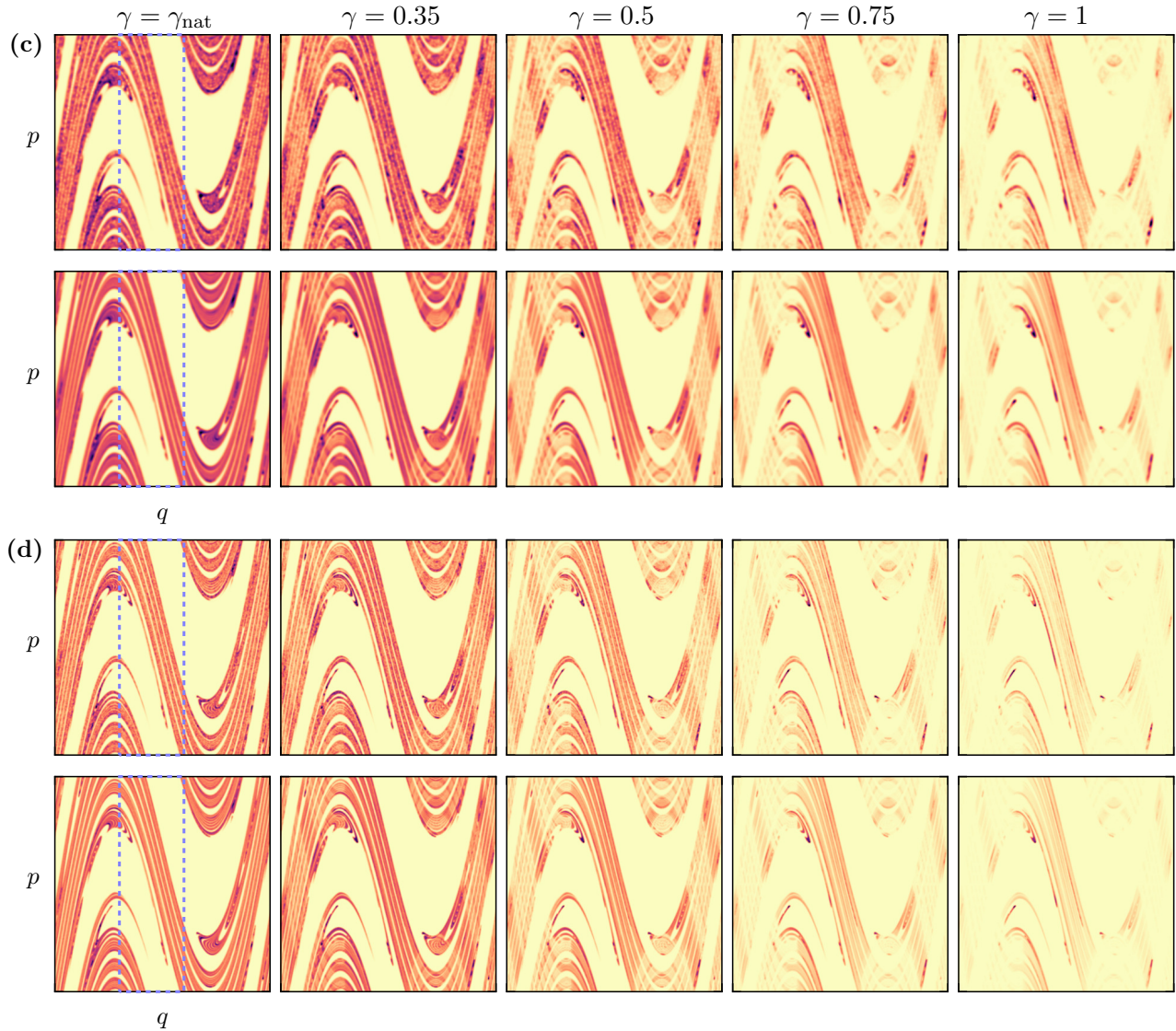


**Figure 5.20 (cont.):** Quantum-to-classical correspondence for standard map with full escape for (a)  $h = 1/250$ , (b)  $h = 1/1000$ , (c)  $h = 1/4000$ , and (d)  $h = 1/16000$ .

In conclusion, the presented phase-space distributions numerically support the resonance eigenfunction hypothesis for full escape postulated in Sec. 5.3.3. Even though the simplest implementation of the measures  $\mu_\gamma^h$  is used, they inherit a similar enhancement of structures within the opening  $\Omega$  for increasing decay rates  $\gamma$ . This leads to the conclusion that the average structural dependence of resonance eigenfunctions on the decay rate  $\gamma$  has a classical origin in the temporal distance to the  $h$ -resolved chaotic saddle. For large decay rates, however, there are visible differences, see Fig. 5.21. In this regime of short-lived eigenfunctions, however, convergence of resonance eigenfunctions is not observed, see Sec. 5.2.3, such that it cannot be expected to find a description in terms of a single classical limit measure. Thus, for large  $\gamma$  it becomes a difficult, if not impossible, task, to determine precisely the single filaments in phase space, on which the Husimi distributions localize.

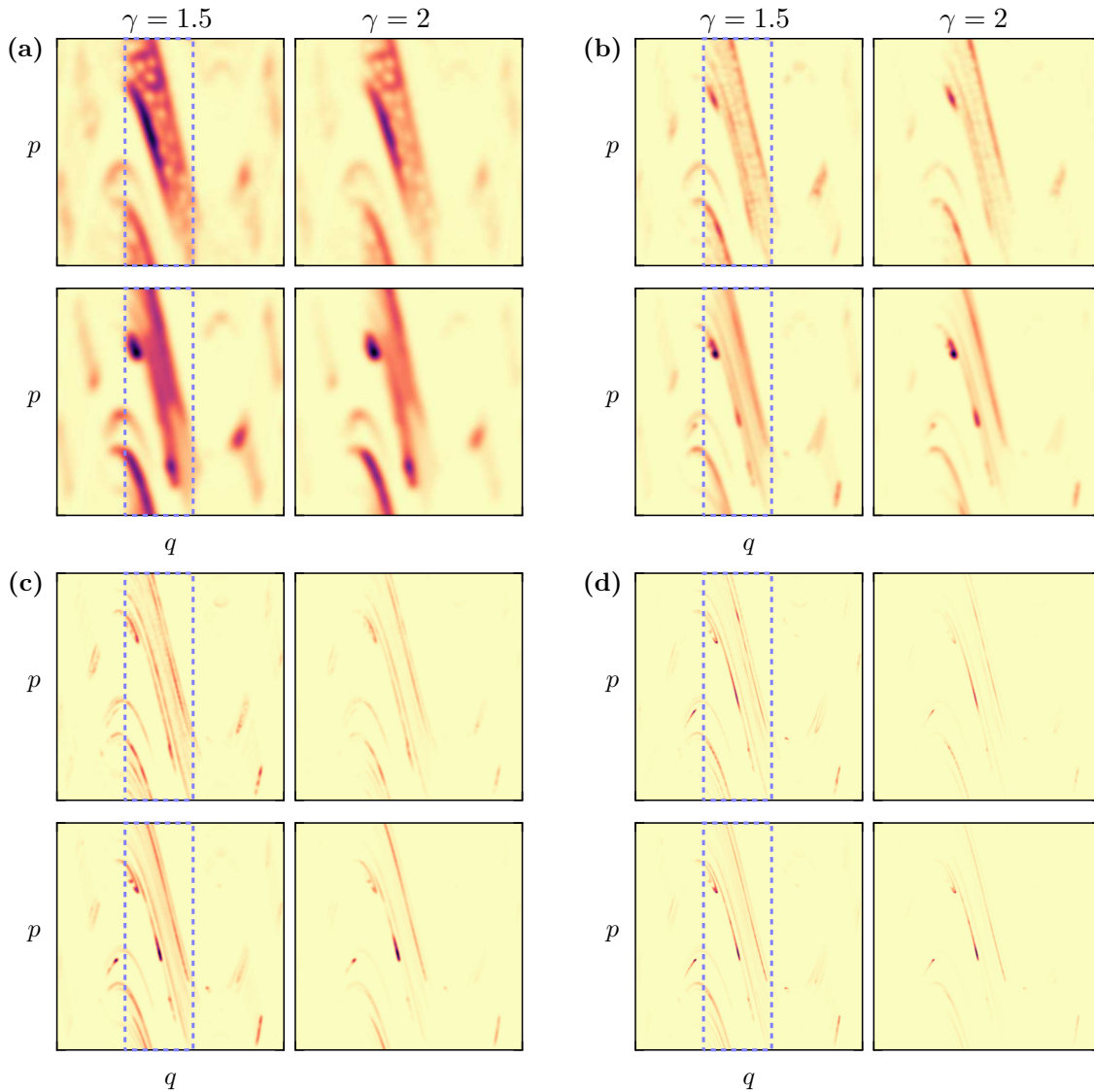


**Figure 5.21:** Quantum-to-classical correspondence at large decay rates for standard map with full escape. Illustrated are  $\langle \mathcal{H} \rangle_\gamma$  (top) and  $\mu_\gamma^h$  (bottom) for  $\gamma \in \{1.5, 2\}$  and (a)  $h = 1/250$ , (b)  $h = 1/1000$ , (c)  $h = 1/4000$ , and (d)  $h = 1/16000$ , as in Fig. 5.20.

## 5.4.2 Fractal dimensions

In this section we compare fractal dimensions of resonance eigenfunctions and classical measures. As discussed in Sec. 4.4.2, a comparison for finite quantum phase-space resolution  $h$  is possible, when effective fractal dimensions  $D_q(\mu, \epsilon)$  are considered for some fixed parameter  $\epsilon \gtrsim \sqrt{h}$ , see Eq. (4.50). Here we apply the same considerations to systems with full escape, numerically investigating the Husimi distributions  $\mathcal{H}_\psi$  of resonance eigenfunctions  $\psi$  and the classical measures  $\mu_\gamma^{\text{nat}}$ , Sec. 5.3.1, and  $\mu_\gamma^h$ , Sec. 5.3.3.

We present in Fig. 5.22 the effective fractal dimensions  $D_q(\gamma, \epsilon) = D_q(\mu_{\psi_\gamma}, \epsilon)$  as a function of the decay rate of the resonance eigenfunction  $\psi_\gamma$  for  $h \in \{1/250, 1/1000, 1/4000, 1/16000\}$  (colored markers). Note that  $\mu_{\psi_\gamma}$  is the Husimi measure of  $\psi_\gamma$ , see Eq. (3.11). For comparison, classical results obtained for  $\mu_\gamma^h$  with  $h = 1/16000$  (green dashed line), as well as for  $\mu_\gamma^{\text{nat}}$  (gray

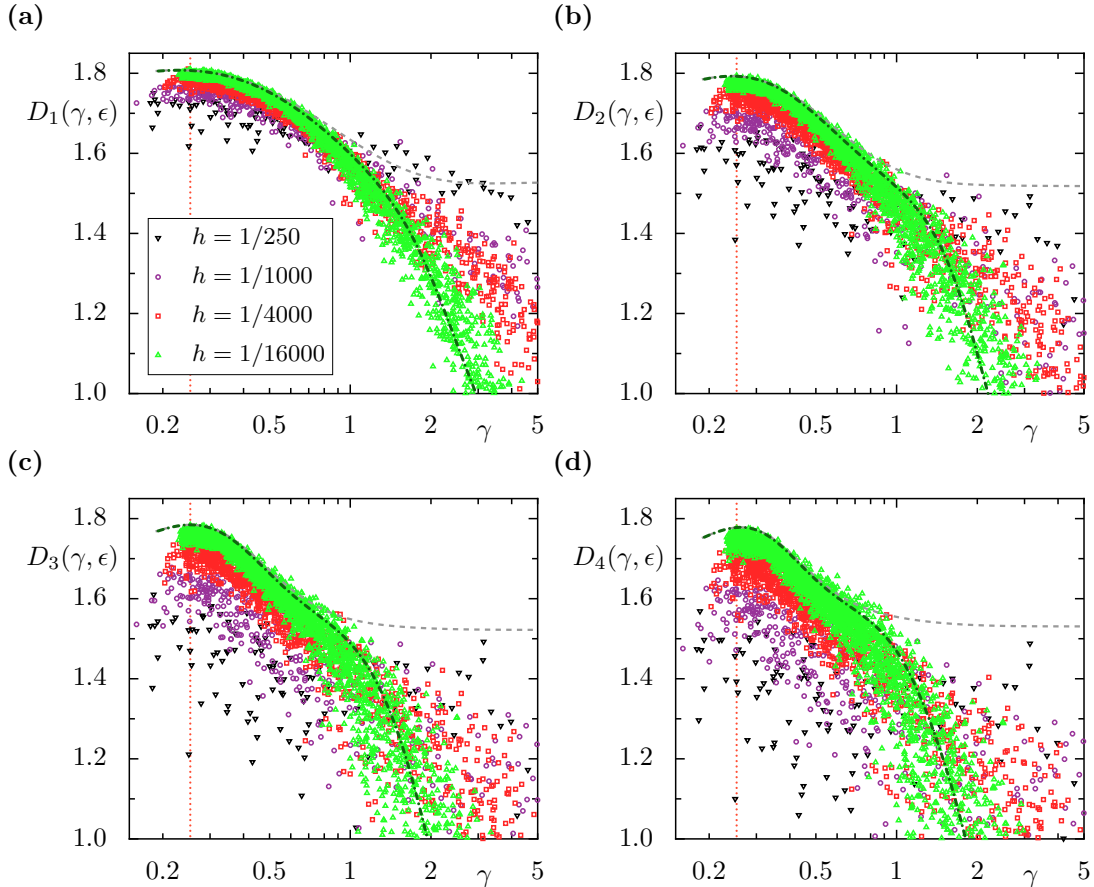


**Figure 5.22:** Fractal dimensions of single resonance eigenfunctions and classical measures for full escape. Shown are effective Rényi-dimensions  $D_q(\gamma, \epsilon)$  of Husimi distribution  $\mathcal{H}_\gamma$  of single resonance eigenfunctions as a function of  $\gamma$  for  $h \in \{1/250, 1/1000, 1/4000, 1/16000\}$  (black, violet, red, green). Considered are dimensions for (a)  $q = 1$ , (b)  $q = 2$ , (c)  $q = 3$ , and (d)  $q = 4$ , while  $\epsilon \in [1/4, 1/16]$ . Results for the classical measures  $\mu_\gamma^h$  with  $h = 1/16000$  (dashed green line) and  $\mu_\gamma^{\text{nat}}$  (dashed gray line) are shown for comparison. Vertical dotted line indicates  $\gamma_{\text{nat}}$ .

dashed line) are shown. The effective information dimension,  $q = 1$ , is shown in (a). Quantum mechanically we observe that  $D_1(\gamma, \epsilon)$  for decay rates around  $\gamma_{\text{nat}}$  increases with decreasing  $h$  and approaches the classical value obtained for  $\mu_{\text{nat}}$ . Note that  $\mu_\gamma^h$  and  $\mu_\gamma^{\text{nat}}$  coincide at the natural decay rate with  $\mu_{\text{nat}}$ . Smaller effective dimensions at large values of  $h$  can be explained by quantum fluctuations of the order of  $\epsilon$ , see discussion for partial escape in App. B.3. For large decay rates,  $\gamma \gtrsim 1$ , we observe that the effective information dimension decreases with  $h$ . The reason lies in the localization of eigenfunctions on a few filaments of the backward trapped set with increasing  $\gamma$ . If  $h$  becomes smaller, the quantum resolution of these filaments is enhanced which implies smaller effective fractal dimensions. For  $h = 1/16000$ , we find excellent agreement between the information dimension of single resonance eigenfunctions and of the corresponding measure  $\mu_\gamma^h$  (green dashed line). We notice that the maximum of  $D_1(\gamma, \epsilon)$  for  $\mu_\gamma^h$  is at  $\gamma_{\text{nat}}$ . The reason is, that these measures become less uniform on the backward trapped set, when  $\gamma$  increases. This non-uniformity leads to smaller information dimensions.

For decay rates larger than  $\gamma \approx 3$ , the information dimension even becomes smaller than one, classically for  $\mu_\gamma^h$  and also for resonance eigenfunctions. This is explained by the localization on only a few, small phase-space filaments. In contrast, comparison with  $\mu_\gamma^{\text{nat}}$  shows disagreement for large  $\gamma$ , especially for smaller values of  $h$ . The information dimension of these measures saturates for large decay rates at finite values  $D_1(\gamma, \epsilon) \approx 1.52$  (gray dashed line). This is not surprising, since the measures  $\mu_\gamma^{\text{nat}}$  are by definition proportional to  $\mu_{\text{nat}}$  on the opening  $\Omega$  and  $\epsilon$  is finite. In the limit  $\epsilon \rightarrow 0$  one expects  $D_1(\mu_\gamma^{\text{nat}}) = D_1(\mu_{\text{nat}})$ . Moreover, this clearly visualizes that the measures  $\mu_\gamma^{\text{nat}}$  are not convenient as the semiclassical limit of resonance eigenfunctions with arbitrary decay rates.

We make similar observations for the effective Rényi dimensions  $D_q(\gamma, \epsilon)$  shown in Fig. 5.22(b)–(d) for  $q \in \{2, 3, 4\}$ . Let us remark, that the effective dimension at the natural decay rate only changes little with increasing  $q$ . For all  $q$  we find that the quantum results agree very well with results for  $\mu_\gamma^h$  when  $h = 1/16000$  is considered. Note that the classical measures also

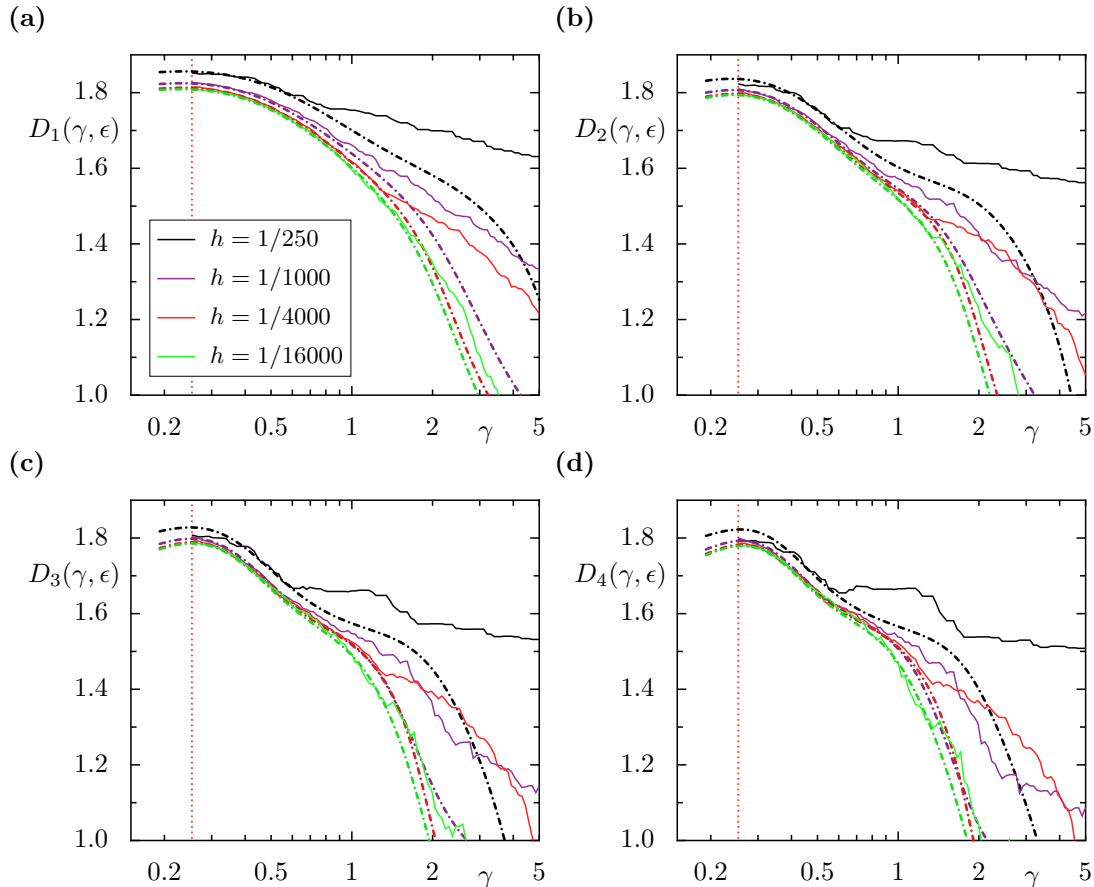


**Figure 5.23:** Fractal dimensions of average resonance eigenfunctions and classical measures for full escape. Shown are effective Rényi-dimensions  $D_q(\gamma, \epsilon)$  as a function of  $\gamma$  considering average Husimi distributions  $\langle \mathcal{H} \rangle_\gamma$  averaged over 50 resonances for  $h \in \{1/250, 1/1000, 1/4000, 1/16000\}$  (black, violet, red, green). The parameter  $q$  is chosen as (a)  $q = 1$ , (b)  $q = 2$ , (c)  $q = 3$ , and (d)  $q = 4$ , while  $\epsilon \in [1/4, 1/16]$ . Results for the corresponding classical measures  $\mu_\gamma^h$ , smoothed by a Gaussian of width  $\sqrt{\hbar/2}$ , are shown for comparison (dashed lines). Vertical dotted line indicates  $\gamma_{\text{nat}}$ .



correctly predict the regime of decay rates  $\gamma$ , for which  $D_q(\gamma, \epsilon)$  becomes smaller than one.

Similarly we calculate effective fractal dimensions using average Husimi distributions  $\langle \mathcal{H} \rangle_\gamma$ . The results are presented in Fig. 5.23, varying the decay rate in the interval  $\gamma_{\text{nat}} \leq \gamma \leq 5$  and averaging over 50 eigenfunctions for each  $\gamma$ . We compare the dimensions  $D_q(\gamma, \epsilon)$  for  $\langle \mathcal{H} \rangle_\gamma$  (solid lines) to those of the corresponding measures  $\mu_\gamma^h$  (dashed lines) using matching colors for the same value of  $h$  and considering  $q \in \{1, 2, 3, 4\}$  in (a)–(d). In order to obtain comparable results we smooth the classical measures on the scale of order  $h$ , as for the qualitative comparison in Fig. 5.20. Note that this mostly effects results for large  $h$ , and without smoothing all classical curves are close to the result for  $h = 1/16000$ . The effective information dimension of averaged Husimi distributions decreases with smaller  $h$  for all considered  $\gamma$  (a), as already observed for partial escape in Fig. 4.24. Taking the average reduces the fluctuations and leads to a smooth quantum distribution. For  $h = 1/250$  this is well approximated by the smooth classical measure  $\mu_\gamma^h$  for decay rates  $\gamma < 0.5$  (black curves). The classical dimension decreases stronger for larger  $\gamma$  than for average eigenfunctions. The latter is influenced by the large intervals in  $\gamma$  used in the average, see discussion of Fig. 5.9, which becomes less relevant for smaller  $h$ . With decreasing  $h$  we find excellent agreement between quantum and classical information dimension. For  $h = 1/1000$  the quantum results follow the classical prediction up to  $\gamma \approx 0.7$  before there is a visible deviation. This region of agreement increases with smaller  $h$ , up to  $\gamma \approx 2$  for  $h = 1/16000$ . We find similar good agreement for the generalized Rényi dimensions in Fig. 5.23(b)–(d).

We further consider the spectrum of Rényi dimensions for a fixed set of decay rates in Fig. 5.24. Here  $D_q(\gamma, \epsilon)$  is shown as a function of  $q$  for the average Husimi distributions  $\langle \mathcal{H} \rangle_\gamma$  (open colored symbols) at  $h = 1/16000$  for different decay rates  $\gamma$ . For comparison the classical results for  $\mu_\gamma^h$  are shown (filled blue symbols). As expected, the box-counting dimension equals

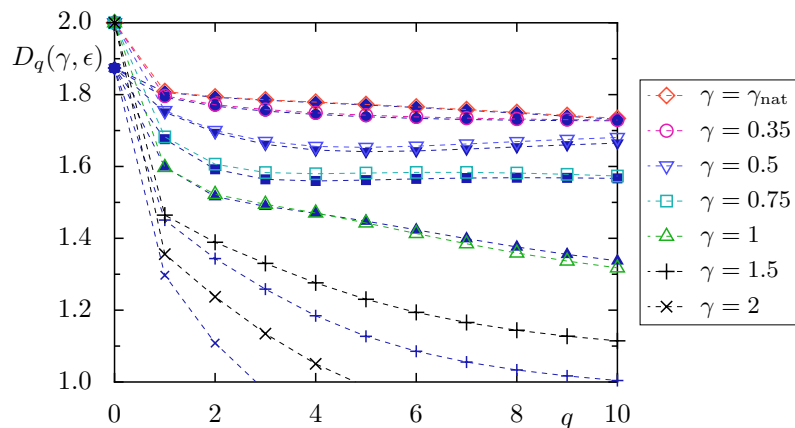


**Figure 5.24:** Fractal dimensions of resonance eigenfunctions and classical measures for full escape. Shown are effective Rényi-dimensions  $D_q(\gamma, \epsilon)$  as a function of  $q$  for decay rates  $\gamma \in \{\gamma_{\text{nat}} \approx 0.25, 0.35, 0.5, 0.75, 1, 1.5, 2\}$  (diamond, circle, lower triangle, square, upper triangle, plus, cross) considering average Husimis  $\langle \mathcal{H} \rangle_\gamma$  of 50 eigenfunctions (open symbols) and the classical measures  $\mu_\gamma^h$  (filled symbols) with  $h = 1/16000$ .

$D_0(\gamma, \epsilon) = 2$  for all Husimi distributions. Since the classical measures  $\mu_\gamma^h$  all localize on  $\Gamma_b$ , their box-counting dimension is independent on  $\gamma$  and equals  $D_0(\gamma, \epsilon) = D_0(\Gamma_b, \epsilon) < 2$ . The presented results in Fig. 5.24 confirm the perfect agreement of the fractal dimensions at  $\gamma = \gamma_{\text{nat}}$  for  $q > 0$ . There is also very good agreement for larger decay rates up to  $\gamma = 1$ , where only small deviations occur for  $q > 5$ . For  $\gamma = 1.5$  (pluses) and  $\gamma = 2$  (crosses) there is a visible deviation between quantum and classical results, already seen in Fig. 5.23. The strong localization of these Husimi densities and classical measures for large  $\gamma$  leads to effective dimensions close to or even smaller than one, if  $q$  increases. Altogether this confirms that the generalized fractal dimensions are well suited as a measure of the localization of resonance eigenfunctions.

### 5.4.3 Jensen–Shannon divergence

In the following we use the Jensen–Shannon divergence  $d_{\text{JS}}$  as a quantitative metric between quantum and classical probability distributions, as defined in Sec. 4.4.3. As in the previous section a finite partition of the phase space into sets of size  $\epsilon^2$  is used with  $\epsilon = 1/16$ . We consider the distances between individual Husimi distributions  $\mathcal{H}_\gamma$  and different classical measures as well as average Husimi distributions  $\langle \mathcal{H} \rangle_\gamma$ .

We illustrate in Fig. 5.25 the Jensen–Shannon divergence between individual Husimi distributions  $\mathcal{H}_\gamma$  and several classical measures as a function of the quantum decay rates  $\gamma$  for  $h \in \{1/1000, 1/4000, 1/16000\}$ . The considered classical measures are the uniform measure  $\mu_L$  (gray circles), the natural measure  $\mu_{\text{nat}}$  (red boxes), the product measures for partial escape  $\mu_\xi := \mu_{(\xi(\gamma, R_\Omega), R_\Omega)}$  for small  $R_\Omega = 10^{-5}$  (black diamonds), the  $\gamma$ -natural measure  $\mu_\gamma^{\text{nat}}$  (green triangles), and the measures  $\mu_\gamma^h$  of the resonance eigenfunction hypothesis (blue diamonds), as defined in Sec. 5.3.3. Results for  $h = 1/1000$  are shown in Fig. 5.25(a). For  $\gamma \approx \gamma_{\text{nat}}$  the distances for all measures obtain values around  $d_{\text{JS}} \approx 0.03$ , except for the uniform measure  $\mu_L$  which shows generally larger  $d_{\text{JS}}$ . The other considered measures all coincide at the natural decay rate, such that we expect a similar dependence in the close vicinity of  $\gamma_{\text{nat}}$ . With increasing decay rate  $\gamma \gtrsim 0.4$  at first the distance for the natural measure  $\mu_{\text{nat}}$  increases (red boxes). This is expected, since the decay rate of  $\mu_{\text{nat}}$  is fixed and not adapted to the quantum decay, such that it certainly is not a semiclassical limit measure for  $\gamma \neq \gamma_{\text{nat}}$  [60]. For decay rates above  $\gamma \gtrsim 0.6$  we find that the distance for the product measures  $\mu_\xi$  increases significantly. This is consistent with the observations in Sec. 4.4.5 that the product measures  $\mu_\xi$  do not agree well with resonance eigenfunctions if  $R_\Omega$  becomes small. For even larger decay rates  $\gamma \gtrsim 1$  we observe that the distances  $d_{\text{JS}}$  for  $\mu_\gamma^{\text{nat}}$  and  $\mu_\gamma^h$  both increase similarly. For  $\mu_\gamma^{\text{nat}}$  this is related to the missing localization effect within the opening  $\Omega$ , see Sec. 5.3.1. For  $\mu_\gamma^h$  we observed in Fig. 5.21 that the strength of the localization effect and the corresponding regions do not perfectly agree between eigenfunctions and measures for large decay rates, which explains why the distance increases. The Jensen–Shannon divergence  $d_{\text{JS}}$  quantifies this observation.

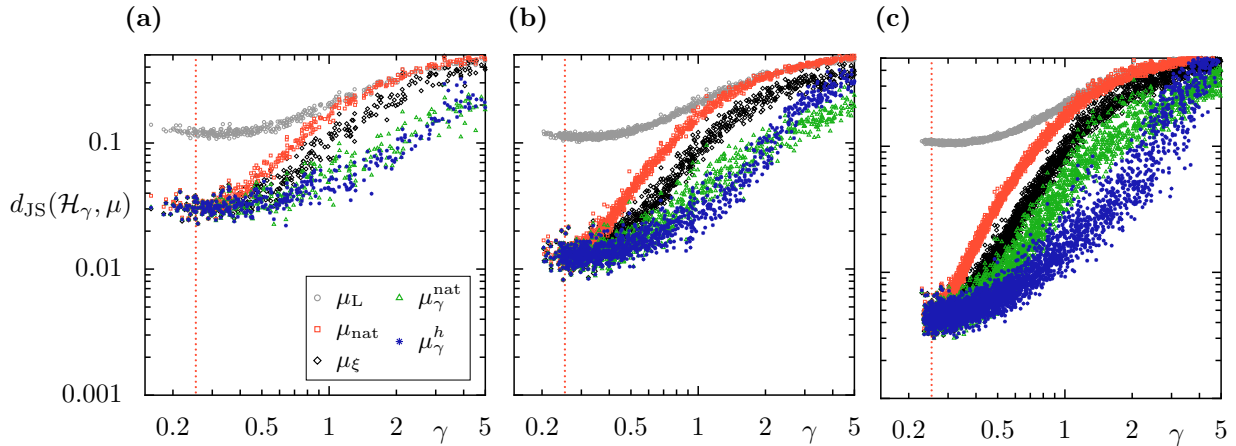


**Figure 5.25:** Jensen–Shannon divergence between single quantum Husimi distributions  $\mathcal{H}_\gamma$  and different classical measures as a function of the decay rate  $\gamma$  for (a)  $h = 1/1000$ , (b)  $h = 1/4000$ , and (c)  $h = 1/16000$  in the system with full escape. The symbols correspond to the considered measures  $\mu_L$  (gray circles),  $\mu_{\text{nat}}$  (red boxes),  $\mu_\xi$  (black diamonds),  $\mu_\gamma^{\text{nat}}$  (green triangles), and  $\mu_\gamma^h$  (blue stars). Red vertical line indicates  $\gamma_{\text{nat}}$ .

Apparently, at this value of  $h$ , it is not possible to properly distinguish the measures  $\mu_\gamma^{\text{nat}}$  and  $\mu_\gamma^h$  based only on the distance  $d_{\text{JS}}$  for the considered scale  $\epsilon$ .

Therefore we consider smaller values of  $h$  in Fig. 5.25(b),  $h = 1/4000$ , and (c),  $h = 1/16000$ . As expected, there is no significant change of the distances for the uniform distribution  $\mu_L$  and it remains of the same order  $d_{\text{JS}} \gtrsim 0.1$  for all considered  $h$ . For the other considered measures we observe that around the natural decay rate  $\gamma_{\text{nat}}$  the distances decrease significantly. With increasing  $\gamma$  the progression of  $d_{\text{JS}}$  is similar as in (a): For  $\mu_{\text{nat}}$  and  $\mu_\xi$  the distances increase significantly at smaller values of  $\gamma$ . The slope at which these distances grow with  $\gamma$  increases between  $h = 1/1000$  and  $h = 1/16000$ . In contrast to (a) there are significant differences between  $\mu_\gamma^{\text{nat}}$  and  $\mu_\gamma^h$ . For  $h = 1/4000$  the distance  $d_{\text{JS}}$  for  $\mu_\gamma^h$  remains slightly smaller than that for  $\mu_\gamma^{\text{nat}}$  up to  $\gamma \approx 2$ . At this point the distances for  $\mu_\gamma^h$  become larger. For large decay rates  $\gamma$  the localization effect predicted by the measures  $\mu_\gamma^h$  apparently does not match the localization effect of resonance eigenfunctions, such that it leads to a worse prediction compared to the missing localization effect for  $\mu_\gamma^{\text{nat}}$ . This is also seen for  $h = 1/16000$ . Here we observe significantly smaller distances than before only for the measures  $\mu_\gamma^h$ . For large decay rates  $\gamma \gtrsim 3$ , however, the distance  $d_{\text{JS}}$  increases to larger values than for the other measures. These results are robust under variation of  $\epsilon > \sqrt{h}$ , which is seen in App. B.4.

In order to validate these observations with a more sensitive test, we consider average resonance eigenfunctions  $\langle \mathcal{H} \rangle_\gamma$ . The Jensen–Shannon divergence between these and the classical measures is illustrated in Fig. 5.26 for the same parameters as in Fig. 5.25. Taking the average reduces the fluctuations of the Husimi distribution, such that we find overall smaller distances. We confirm the much better agreement of resonance eigenfunctions to the measures  $\mu_\gamma^{\text{nat}}$  and  $\mu_\gamma^h$  compared to the other measures for  $h = 1/1000$ , shown in (a). In contrast to  $d_{\text{JS}}$  for the

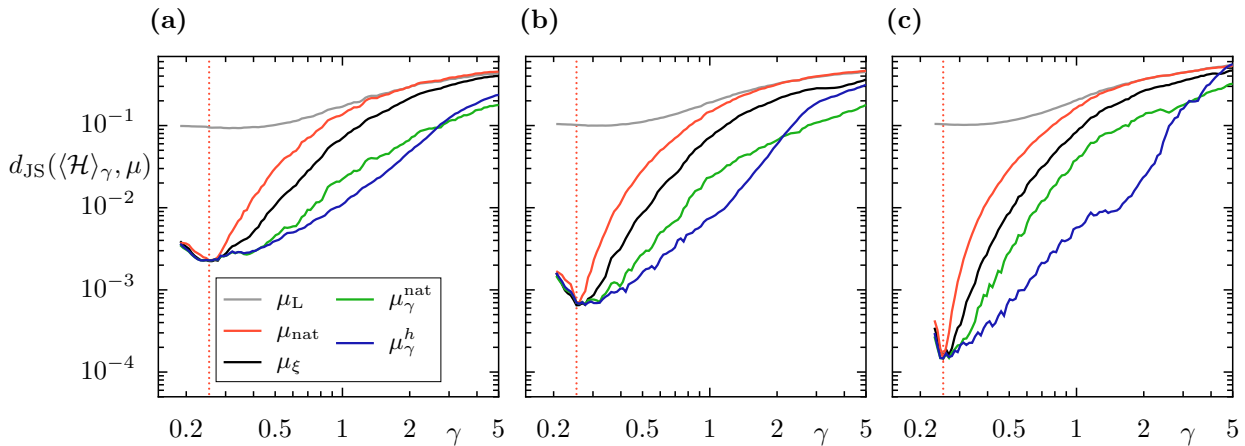


**Figure 5.26:** Jensen–Shannon divergence between average Husimi distributions and different classical measures as a function of the decay rate  $\gamma$  for (a)  $h = 1/1000$ , (b)  $h = 1/4000$ , and (c)  $h = 1/16000$  in the system with full escape. The average in  $\langle \mathcal{H} \rangle_\gamma$  is taken over 50 eigenfunctions. The considered classical measures are  $\mu_L$  (gray circles),  $\mu_{\text{nat}}$  (red boxes),  $\mu_\xi$  (black diamonds),  $\mu_\gamma^{\text{nat}}$  (green triangles), and  $\mu_\gamma^h$  (blue stars). Red vertical line indicates  $\gamma_{\text{nat}}$ .

single Husimi distributions, here we identify a region between  $0.5 \lesssim \gamma \lesssim 2$ , where  $\mu_\gamma^h$  leads to smaller distances which shows that it is better suited to describe quantum mechanics than  $\mu_\gamma^{\text{nat}}$ . This region persists and becomes even larger for smaller values of  $h$ , shown in (b) and (c). For all  $h$  we observe a sharp minimum at  $\gamma = \gamma_{\text{nat}}$  for the natural measure  $\mu_{\text{nat}}$ , which is much more pronounced than in Fig. 5.25. This region of minimal distances  $d_{\text{JS}}$  is slightly broader for the product measure  $\mu_\xi$ , followed by  $\mu_\gamma^{\text{nat}}$  and  $\mu_\gamma^h$ . In all cases this region becomes smaller between (a)  $h = 1/1000$  and (c)  $h = 1/16000$ . A careful inspection of the progression for  $\mu_\gamma^{\text{nat}}$  reveals that for decay rates  $\gamma \gtrsim 0.6$  the distances  $d_{\text{JS}}$  increase with decreasing  $h$ . This rules out the possibility that the measures  $\mu_\gamma^{\text{nat}}$  are semiclassical limit measures of resonance eigenfunctions.

Let us remark that the measures  $\mu_\gamma^{\text{nat}}$  have recently been used to explain the localization transition in chaotic systems with a single partial barrier [65, 210]. In such a system it is also possible to apply the resonance eigenfunction hypothesis and obtain the measures  $\mu_\gamma^h$ . This leads to a change of the predicted weights on either side of the partial barrier. Depending on the size of the opening and the size of the barrier, we find that in most cases both predictions,  $\mu_\gamma^{\text{nat}}$  and  $\mu_\gamma^h$ , lead to similar agreement. The observed deviations in Ref. [210] for systems with very large openings but small partial barriers, however, are not explained with the new approach. One possible reason is, that small partial barriers are not resolved completely by quantum mechanics, which is not taken into account in our definition of the temporal distance. It is also not clear if the observed deviations have a classical origin.

Altogether, the Jensen–Shannon divergence saturates at finite values  $d_{\text{JS}}$  for those classical measures which are not the semiclassical limit of resonance eigenfunctions. This observation holds for individual and averaged Husimi distributions equally and is clearly seen for the

uniform distribution  $\mu_L$  and the natural measure  $\mu_{\text{nat}}$ , when large decay rates  $\gamma$  are considered. Looking more carefully we find that it also holds for  $\mu_\xi$  and for  $\mu_\gamma^{\text{nat}}$  in a regime with  $\gamma > \gamma_{\text{nat}}$ . Conversely, we numerically confirm that it is reasonable to expect  $\mu_{\text{nat}}$  as the semiclassical limit measure for decay rates  $\gamma = \gamma_{\text{nat}}$ . For the proposed measures  $\mu_\gamma^h$  from the resonance eigenfunction hypothesis we find overall the smallest distances  $d_{\text{JS}}$  in the regime of long-lived eigenfunctions. This distance, however, also increases with  $\gamma$  and the semiclassical dependence on  $h$  is not obvious.

#### 5.4.4 Semiclassical limit

In the following we quantify to which extent the measures  $\mu_\gamma^h$  are compatible with a semiclassical distance  $d_{\text{JS}} \rightarrow 0$  in the limit  $h \rightarrow 0$ . We first consider the average Jensen–Shannon divergence  $\langle d_{\text{JS}}(\mathcal{H}_\gamma, \mu_\gamma^h) \rangle$  of individual Husimi distributions and the measures  $\mu_\gamma^h$  as well as  $\langle d_{\text{JS}}(\mathcal{H}_\gamma, \langle \mathcal{H} \rangle_\gamma) \rangle$  between single and average Husimi distributions in Fig. 5.27. All averages are taken over 50 resonances and  $\epsilon = 1/16$ .

Figure 5.27(a) shows the average Jensen–Shannon divergence  $\langle d_{\text{JS}}(\mathcal{H}_\gamma, \mu_\gamma^h) \rangle$  as a function of  $h$  for different decay rates  $\gamma$ . Note that this figure can be obtained by considering the average of single distances  $d_{\text{JS}}(\mathcal{H}_\gamma, \mu_\gamma^h)$  as shown in in Fig. 5.25. For long-lived eigenfunctions with decay rates  $\gamma \lesssim 1$  we observe a power-law decay  $d_{\text{JS}} \sim h^\delta$  where the exponent for  $\gamma = \gamma_{\text{nat}}$  (red diamonds) is approximately  $\delta \gtrsim 0.75$  and becomes larger for smaller decay rates  $\gamma$ . For large decay rates,  $\gamma = 4$ , the Jensen–Shannon divergence increases for smaller  $h$ , such that a semiclassical convergence is ruled out (black stars). For the long-lived eigenfunctions we find distances of similar order and scaling when individual Husimi distributions  $\mathcal{H}_\gamma$  are compared to

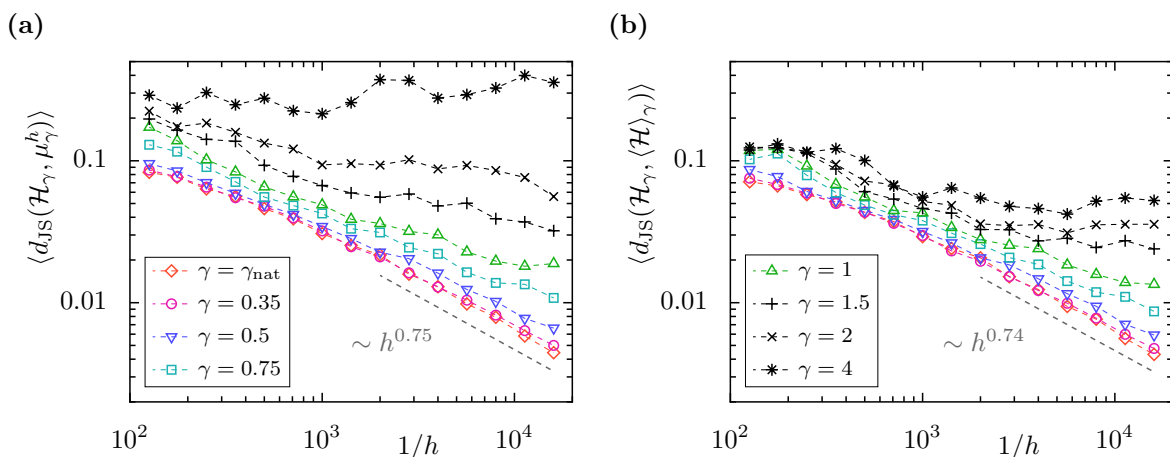


**Figure 5.27:** Quantum-to-classical and quantum-to-average comparison in the semiclassical limit in a system with full escape. (a) Shown is the averaged Jensen–Shannon divergence  $d_{\text{JS}}$  between single Husimi distributions  $\mathcal{H}_\gamma$  and the classical measures  $\mu_\gamma^h$  as a function of  $h$  for  $\gamma \in \{\gamma_{\text{nat}}, 0.35, 0.5, 0.75, 1, 1.5, 2, 4\}$ . (b) Same as (a) considering the averaged  $d_{\text{JS}}$  between single  $\mathcal{H}_\gamma$  and average Husimi distributions  $\langle \mathcal{H} \rangle_\gamma$ . All averages are taken over 50 resonances. Gray line indicates numerical scaling for  $\gamma_{\text{nat}}$ .

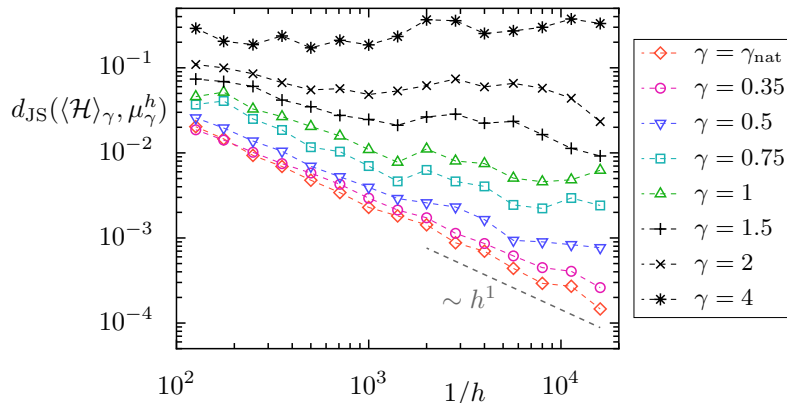


**Figure 5.28:** Quantum-to-classical comparison in the semiclassical limit for average Husimi distributions in a system with full escape. Shown is the Jensen–Shannon divergence  $d_{\text{JS}}$  between average Husimi distributions  $\langle \mathcal{H} \rangle_\gamma$  and the classical measures  $\mu_\gamma^h$  as a function of  $h$  for  $\gamma \in \{\gamma_{\text{nat}}, 0.35, 0.5, 0.75, 1, 1.5, 2, 4\}$ . Gray line indicates numerical scaling for  $\gamma_{\text{nat}}$ .

the averaged Husimi distributions  $\langle \mathcal{H} \rangle_\gamma$ , illustrated in Fig. 5.27(b). This implies that individual long-lived eigenfunctions with  $\gamma \lesssim 1$  are equally well approximated by the classical measures  $\mu_\gamma^h$  and their average distribution  $\langle \mathcal{H} \rangle_\gamma$ . The observations for short-lived eigenfunctions, however, are different. In (a) the distances for  $\gamma > 1$  are overall larger than in (b) and show an entirely different scaling. There is no convergence of single to average eigenfunctions (b), which implies that short-lived single eigenfunctions do not converge semiclassically at all. Thus, it is not surprising, that we do not see convergence in (a). We deduce from Fig. 5.27, that only in the long-lived regime the measures  $\mu_\gamma^h$  are compatible with a semiclassical distance of  $d_{\text{JS}} \rightarrow 0$ . Thus, the resonance eigenfunction hypothesis does not apply to short-lived resonances with very large decay rates. Note that we already discussed the issue of convergence of single to average eigenfunctions in Sec. 5.2.3, and that the results presented in Fig. 5.27 quantify these findings in terms of a distance metric.

In Figure 5.28 we consider the Jensen–Shannon divergence between average Husimi distributions  $\langle \mathcal{H} \rangle_\gamma$  and the proposed measures  $\mu_\gamma^h$ , which leads to a more sensitive test of the hypothesis. We obtain overall smaller distances for all  $\gamma$ , compared to Fig. 5.27(a). For decay rates  $\gamma \lesssim 0.5$ , and in particular for  $\gamma = \gamma_{\text{nat}}$ , we find a power law  $d_{\text{JS}} \sim h^\delta$ . The exponent at  $\gamma_{\text{nat}}$  is approximately given by  $\delta \approx 1$  and there are systematically smaller exponents for larger  $\gamma$ . This numerically supports the resonance eigenfunction hypothesis for long-lived resonances, at least in regime of decay rates around  $\gamma = \gamma_{\text{nat}}$ . Note that the size of the considered interval of decay rates for the averaging process depends on  $\gamma$  but converges semiclassically with the same rate  $\sim h^{D_0(\Gamma_s)/2}$  for all  $\gamma$ , as discussed in Fig. 5.9. It is an interesting open question, if this can be used to derive an analytical expression for the exponent  $\delta$ , at least for the natural decay rate  $\gamma_{\text{nat}}$ . For large decay rates  $\gamma$  we do not observe a power-law decay of  $d_{\text{JS}}$ . Instead, in all cases with  $\gamma \geq 0.75$  we find that the distance  $d_{\text{JS}}$  increases at certain values of  $h$ , e.g., for  $\gamma = 1$  at  $h = 1/2000$  and  $h = 1/8000$  (green triangles). The progression for  $\gamma = 0.75$  indicates

either that there are nonuniversal localization effects even for smaller  $\gamma$ , or that the considered measures  $\mu_\gamma^h$  eventually lead to a finite semiclassical distance.

In conclusion, we find quantitative numerical support for the resonance eigenfunction hypothesis for long-lived eigenfunctions. Moreover, even for short-lived eigenfunctions the proposed measures  $\mu_\gamma^h$  are well-suited to approximate their phase-space representation for finite values of  $h$ . However, we do not expect semiclassical convergence for all decay rates, as the proposed measures increasingly deviate from the resonance eigenfunctions for decay rates  $\gamma \gtrsim 1$ . In these cases there occur two problems: First, the regions and the strength of the localization effect occurring in the measures  $\mu_\gamma^h$  are different from the ones in the phase-space distributions of resonance eigenfunctions. Secondly, we show that there is no convergence of the eigenfunctions themselves, since they are strongly localized on different filaments of the backward trapped set. In the following we present further results for openings  $\Omega$  with different size.

### 5.4.5 Dependence on opening $\Omega$

In this section we present a qualitative quantum-to-classical comparison of the phase-space densities of resonance eigenfunctions and the proposed measures  $\mu_\gamma^h$  for different openings  $\Omega$ . For this purpose we consider the chaotic standard map as before, but with full escape from the smaller opening  $\Omega_1 = (0.2, 0.4) \times [0, 1)$  where  $\gamma_{\text{nat}} \approx 0.21$  and from the larger opening  $\Omega_2 = (0.2, 0.7) \times [0, 1)$  where  $\gamma_{\text{nat}} \approx 0.51$

For the small opening  $\Omega_1$  quantum and classical phase-space densities are illustrated in

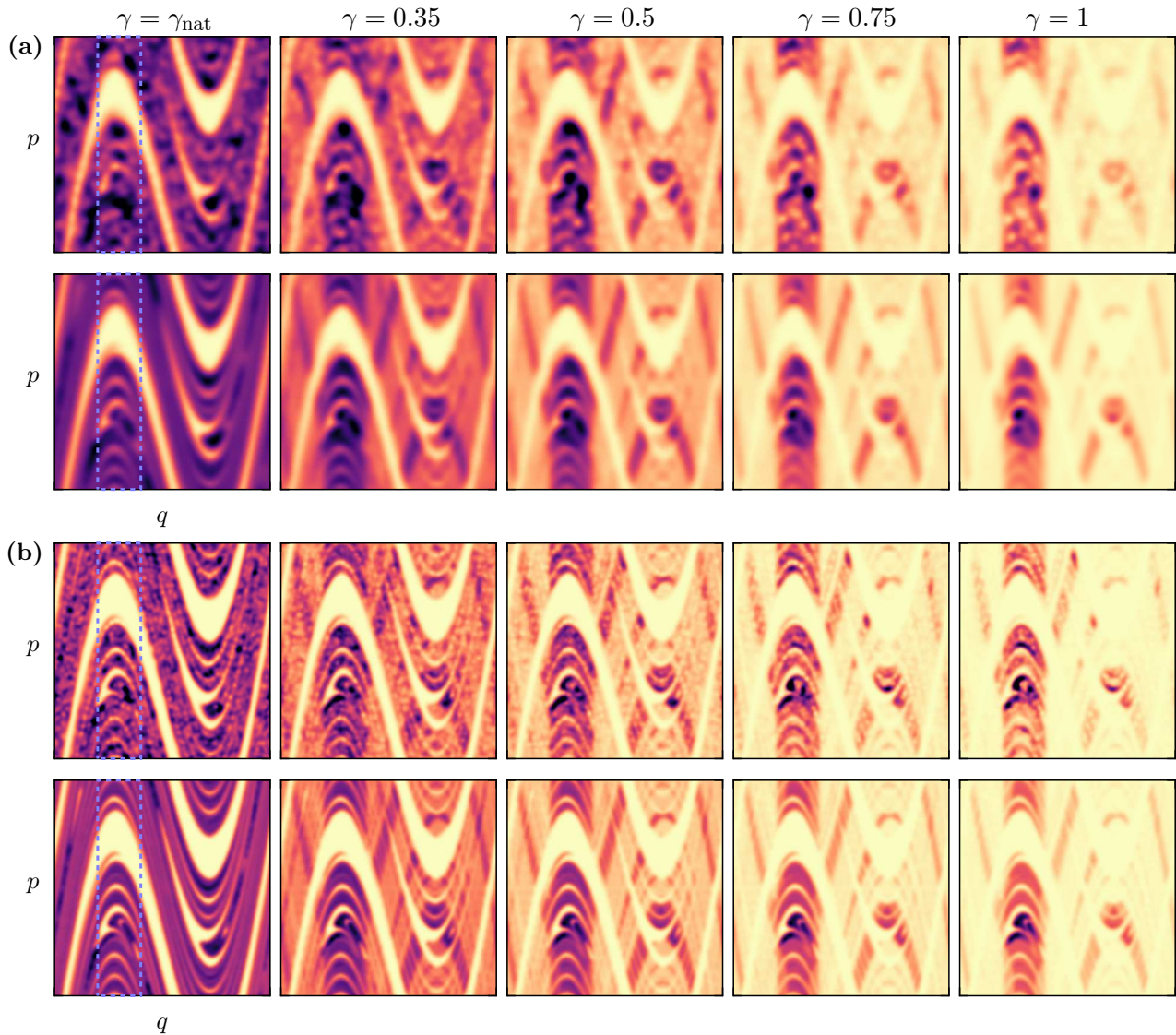


**Figure 5.29:** Quantum-to-classical correspondence for standard map with full escape from  $\Omega = (0.2, 0.4) \times [0, 1)$ . Shown are average Husimi distributions  $\langle \mathcal{H} \rangle_\gamma$  of resonance eigenfunctions averaged over 50 resonances for  $\gamma \in \{\gamma_{\text{nat}} \approx 0.21, 0.35, 0.5, 0.75, 1., 1.5, 2\}$  and (a)  $h = 1/250$ , (b)  $h = 1/1000$ , (c)  $h = 1/4000$ , and (d)  $h = 1/16000$  (top row). Bottom row shows Gaussian smoothed phase-space distribution of the measures  $\mu_\gamma^h$ , Eq. (5.22). The same colormap is used for quantum and classical densities, with the maximum given for each  $h$  and  $\gamma$  individually by the maximum of the classical density. Dashed blue line indicates position of the opening  $\Omega$ .



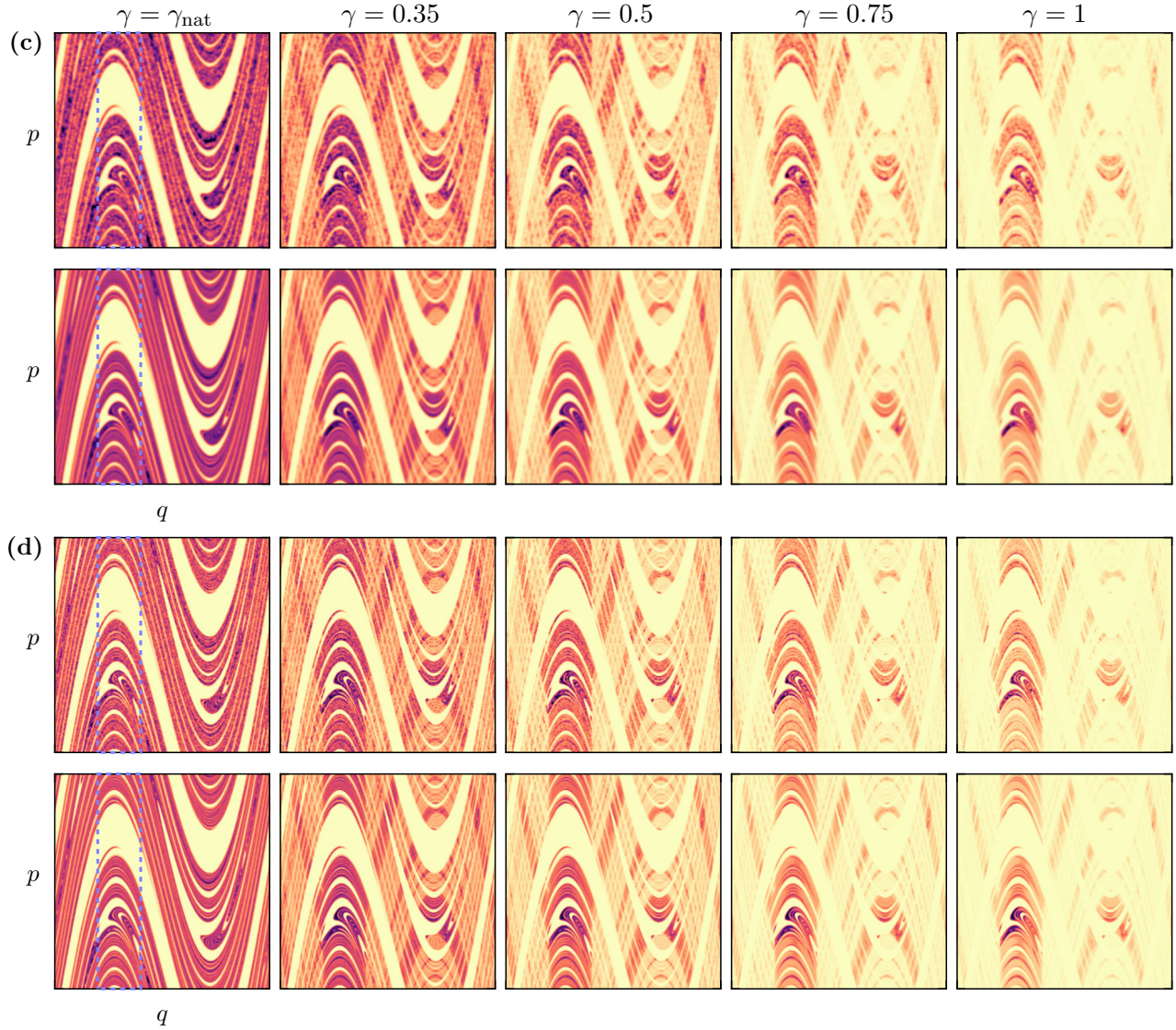


**Figure 5.29 (cont.):** Quantum-to-classical correspondence for standard map with full escape for (a)  $h = 1/250$ , (b)  $h = 1/1000$ , (c)  $h = 1/4000$ , and (d)  $h = 1/16000$ .

Fig. 5.29 and Fig. 5.30 for  $h \in \{1/250, 1/1000, 1/4000, 1/16000\}$ . The long-lived resonance eigenfunctions in Fig. 5.29 qualitatively show excellent agreement with the proposed classical measures. Classically we observe a similar enhancement of the probability with increasing  $\gamma$  in certain subsets of the opening  $\Omega$  as quantum mechanically. For decreasing values of  $h$  we observe a change of the localized regions, e.g., for  $\gamma = 1$ , in both classical and quantum densities, but with a different strength. For larger decay rates shown in Fig. 5.30 we find differences in the specific regions of largest enhancement when  $h$  is large. For smaller values of  $h$  there is still very good quantum-to-classical agreement even for decay rates up to  $\gamma = 2$ . Note that when  $\gamma$  is chosen much larger we do not find agreement (not shown), as discussed in the previous section.

For the larger opening  $\Omega_2$  the system exhibits more decay and  $\gamma_{\text{nat}}$  is much larger. The chaotic saddle and the backward trapped set are here much smaller than for  $\Omega_1$ . Note that

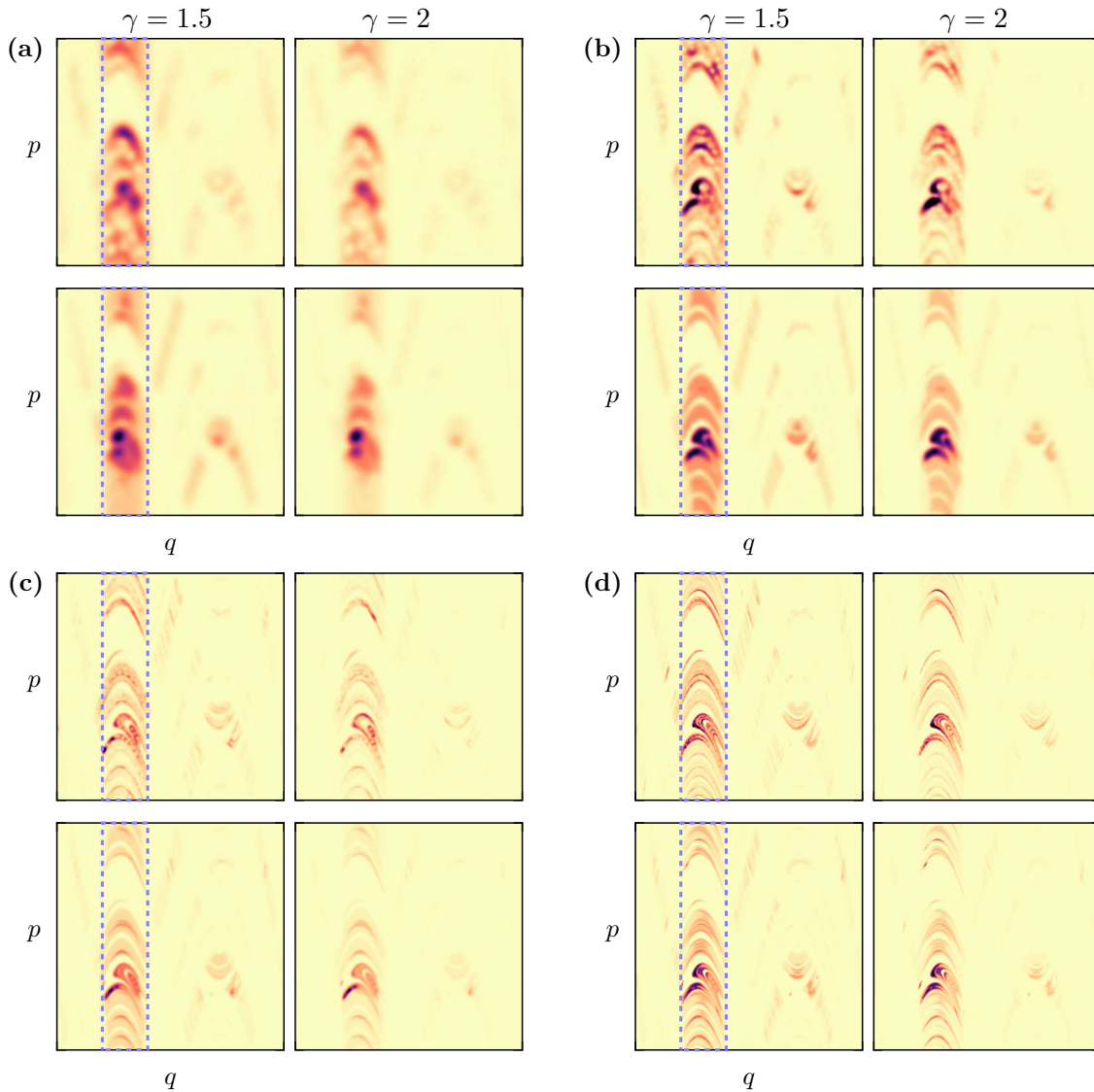


**Figure 5.30:** Quantum-to-classical correspondence at large decay rates for standard map with full escape from  $\Omega = (0.2, 0.4) \times [0, 1]$ . Illustrated are  $\langle \mathcal{H} \rangle_\gamma$  and  $\mu_\gamma^h$  for  $\gamma \in \{1.5, 2\}$  and (a)  $h = 1/250$ , (b)  $h = 1/1000$ , (c)  $h = 1/4000$ , and (d)  $h = 1/16000$ , as in Fig. 5.29

$\Omega_1 \subset \Omega_2$  implies that  $\Gamma_b(\Omega_2) \subset \Gamma_b(\Omega_1)$  by definition Eq. (2.43). This is seen in the support of the quantum and classical phase-space densities illustrated in Fig. 5.31 for the same values of  $h$  as before. Note that here we consider overall larger decay rates compared to Fig. 5.29. Again there is excellent quantum-to-classical agreement even for large  $\gamma$ . Note that we also observe a transition of the maximal intensity when  $h$  changes, e.g., comparing the average Husimi distributions with  $\gamma = 1.5$  or  $\gamma = 2$  between  $h = 1/250$  and  $h = 1/1000$ . Such a transition is in principle also possible classically for larger values of  $h$ , see Sec. 5.3.3, it is here not observed in the considered implementation. Again if even larger  $\gamma$  are considered the agreement declines (not shown).

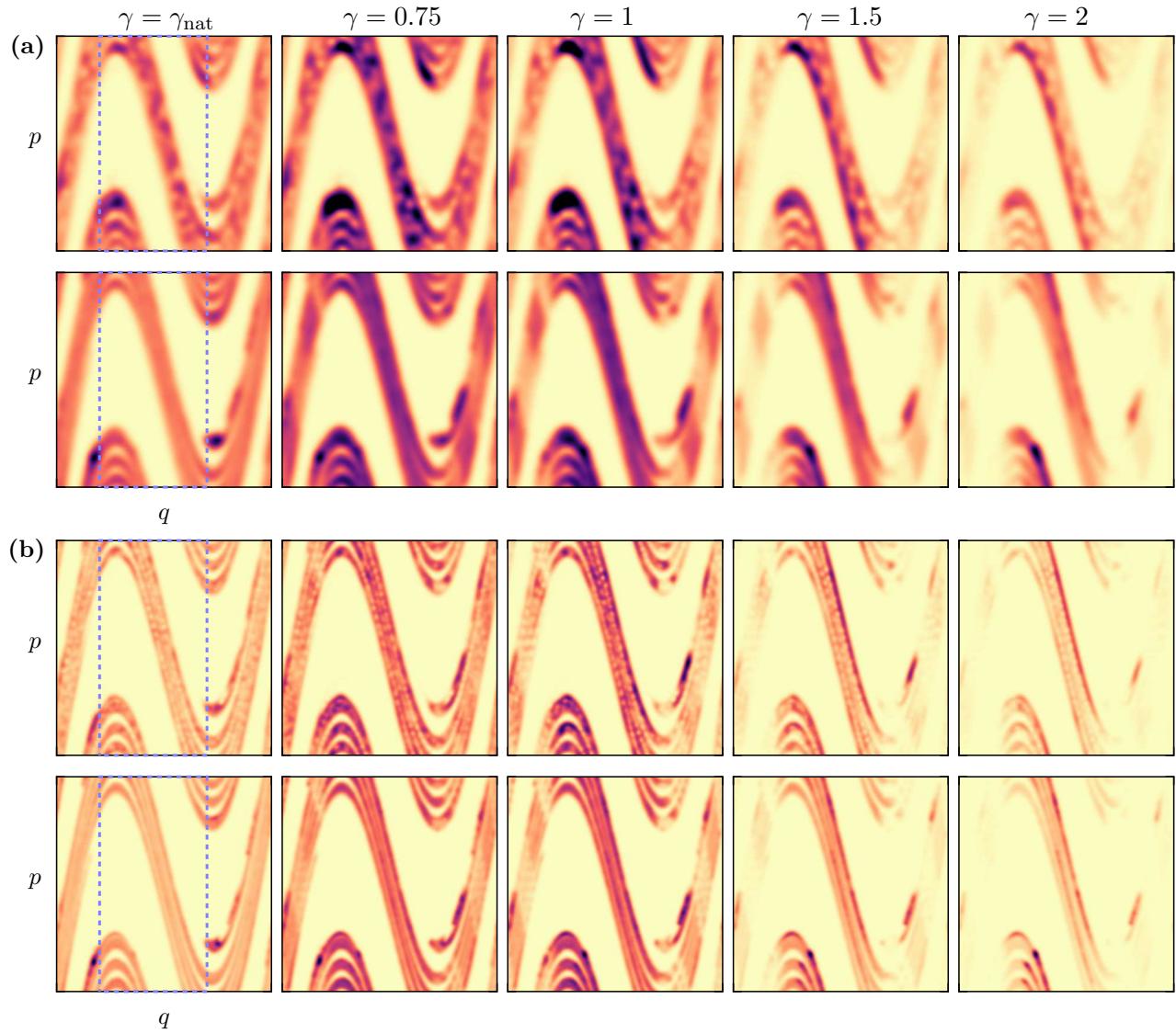


**Figure 5.31:** Quantum-to-classical correspondence for standard map with full escape from  $\Omega = (0.2, 0.7) \times [0, 1)$ . Shown are average Husimi distributions  $\langle \mathcal{H} \rangle_\gamma$  of resonance eigenfunctions averaged over 50 resonances for  $\gamma \in \{\gamma_{\text{nat}} \approx 0.51, 0.75, 1, 1.5, 2\}$  and (a)  $h = 1/250$ , (b)  $h = 1/1000$ , (c)  $h = 1/4000$ , and (d)  $h = 1/16000$  (top row). Bottom row shows Gaussian smoothed phase-space distribution of the measures  $\mu_\gamma^h$ , Eq. (5.22). The same colormap is used for quantum and classical densities, with the maximum given for each  $h$  and  $\gamma$  individually by the maximum of the classical density. Dashed blue line indicates position of the opening  $\Omega$ .

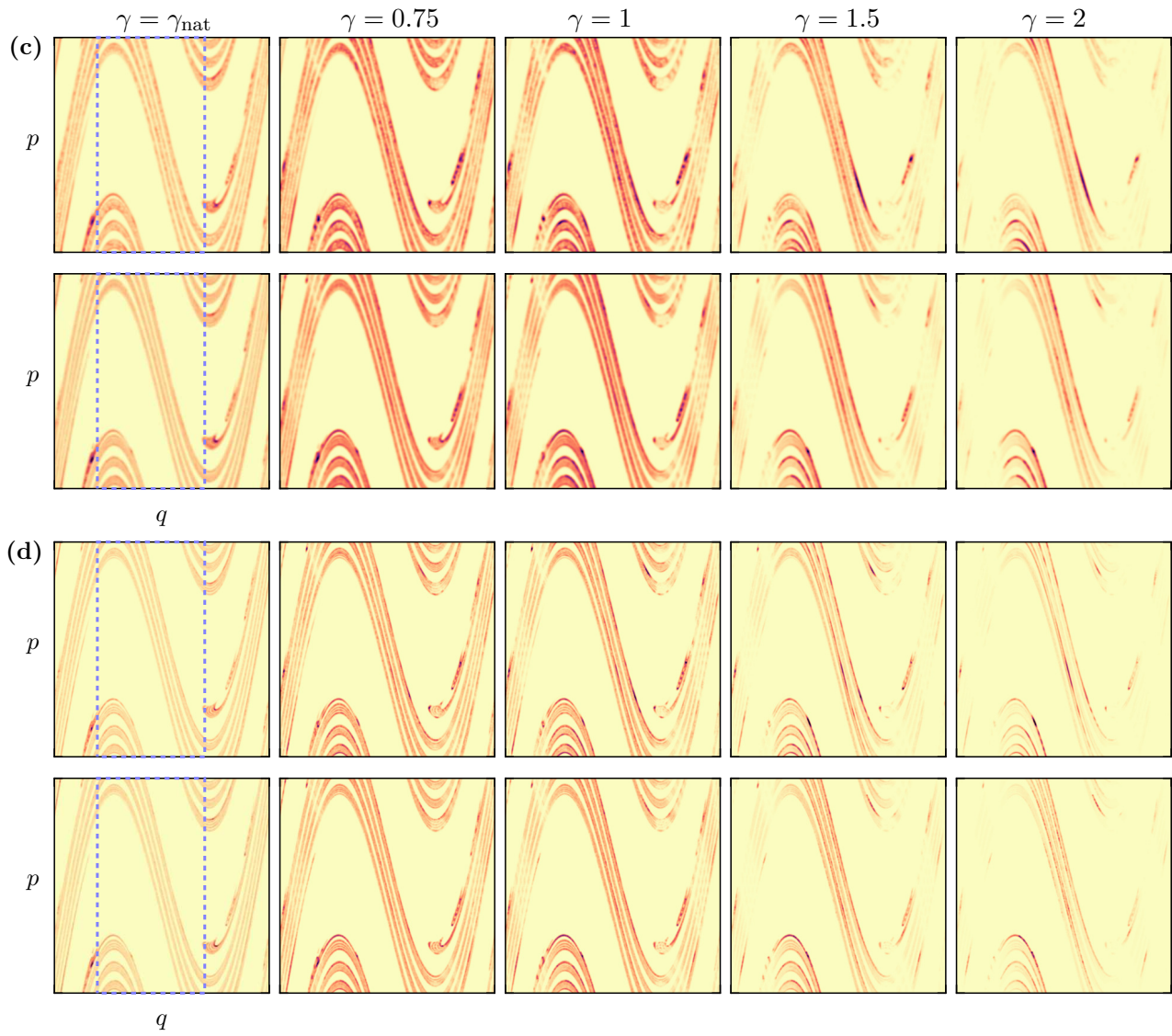


**Figure 5.31 (cont.):** Quantum-to-classical correspondence for standard map with full escape for (a)  $h = 1/250$ , (b)  $h = 1/1000$ , (c)  $h = 1/4000$ , and (d)  $h = 1/16000$ .

## 5.5 Discussion and outlook

Long-lived resonance eigenfunctions of systems with full escape converge semiclassically towards conditionally invariant measures. This convergence is seen numerically for reasonably small decay rates  $\gamma$ , but we do not observe convergence for very large (but still finite) decay rates. For  $\gamma_{\text{nat}}$  we confirm the expectation that resonance eigenfunctions converge towards the natural measure  $\mu_{\text{nat}}$ . We motivate a hypothesis about the semiclassical localization of resonance eigenfunctions which is based on the quantum resolution and instability of the chaotic saddle. This hypothesis implies a class of conditionally invariant measures, for which the simplest implementation qualitatively agrees very well with resonance eigenfunctions in the long-lived regime. Thereby we obtain a classical explanation of the local enhancement of the quantum probability distributions with increasing decay rate  $\gamma$ . Semiclassically we observe that the Jensen–Shannon divergence converges to zero for decay rates close to  $\gamma_{\text{nat}}$ . For large decay rates a semiclassical convergence is not observed. However, in this regime our quantum observations lead to the conclusion that a universal classical description of resonance eigenfunctions cannot be expected.

For this reason the question arises if it is possible to determine definite conditions under which resonance eigenfunctions are expected to converge semiclassically, for example in terms of a limiting decay rate. Furthermore, we emphasize that it is possible to consider more advanced implementations for the resonance eigenfunction hypothesis, e.g., with help of a continuous temporal distance to the chaotic saddle. Our considerations about the limit of these measures, however, suggest that the specific details of the implementation should become less important for  $\hbar \rightarrow 0$ . Nevertheless, for finite  $\hbar$  this could improve the quantum-to-classical agreement for long-lived eigenfunctions. Let us remark that a generalization of the resonance eigenfunction hypothesis to a system with continuous times has been tested for the three-disk scatterer by Roland Ketzmerick with similarly good agreement than presented for the time-discrete map in this thesis (not shown). It would be further interesting to apply this also to potential scattering. Finally, the most important future problem in this regard is to investigate how the different approaches for full and partial escape can be unified.



# Chapter 6

## Summary

Resonance eigenfunctions of non-Hermitian quantum systems play an important role in the description of scattering problems. Their semiclassical phase-space structure is understood for closed systems by a uniform distribution on classically invariant phase-space regions. The structure of eigenfunctions changes drastically when escape from the system is allowed. It is understood that their fractal phase-space structure semiclassically converges towards conditionally invariant measures of the classical dynamics and depends on their decay rate.

In this thesis we perform a detailed investigation about the phase-space structure of resonance eigenfunctions in order to understand the generic case of partial escape and to gain further insight about the limit of full escape. In both cases we relate this structure to conditionally invariant measures of the classical dynamics. For this purpose we investigate a generic chaotic model map with escape.

For chaotic maps with partial escape we observe in the quantum system that single and average resonance eigenfunctions converge in the semiclassical limit to multifractal phase-space distributions. We prove that this semiclassical limit measure must be conditionally invariant. We investigate classical conditionally invariant measures for partial escape in order to obtain an explicit construction depending on the decay rate. For the natural measure  $\mu_{\text{nat}}$  it has been conjectured that it is the semiclassical limit of resonance eigenfunctions with decay rate  $\gamma_{\text{nat}}$  [87]. In addition, we conjecture that the natural measure of the inverse map, the inverse measure  $\mu_{\text{inv}}$ , is the semiclassical limit measure of resonance eigenfunctions with the decay rate  $\gamma_{\text{inv}}$ . Moreover, we propose and construct a class of conditionally invariant measures for chaotic maps with partial escape, based on the hyperbolic phase-space structure. These measures are uniform on subsets which have the same average forward and backward escape under the classical map with partial escape. Qualitatively we find very good quantum-to-classical agreement between the Husimi distribution of resonance eigenfunctions and the proposed measures. Quantitatively, for small decay rates close to the natural decay rate  $\gamma_{\text{nat}}$  and large decay rates close to the inverse decay rate  $\gamma_{\text{inv}}$  our results support the conjectures regarding  $\mu_{\text{nat}}$  and  $\mu_{\text{inv}}$ . For intermediate decay rates, however, we do not find semiclassical convergence of resonance eigenfunctions to the proposed product measures  $\mu_{\xi}$ . Even though for

almost closed systems there is excellent agreement, qualitatively and quantitatively, this does not hold for systems with larger escape. The main results for partial escape are published in Ref. [97]. Let us further remark that we successfully generalized the proposed classical measures to systems with a true time dynamics [211] which is used, e.g., in the description of optical microcavities.

If the nontrivial limit of full escape is considered, there are long-lived resonance eigenfunctions with finite decay rates but also short-lived ones with arbitrary large decay rates. We first investigate the semiclassical convergence of resonance eigenfunctions in dependence on their decay rate. This analysis reveals that there is no universal behavior of resonance eigenfunctions with large (but still finite) decay rates. Thus, semiclassical convergence is not expected for all resonance eigenfunctions. On the other hand, there is a large regime of long-lived eigenfunctions which semiclassically converge towards conditionally invariant measures. Heuristically we motivate a simple model for full escape which leads to a resonance eigenfunction hypothesis based on the quantum resolution and the instability of the invariant chaotic saddle. It states that resonance eigenfunctions in systems with full escape are universally described by conditionally invariant measures which are uniform on sets with the same temporal distance to the quantum-resolved chaotic saddle. This implies a new class of classical conditionally invariant measures for full escape. Qualitatively we find excellent quantum-to-classical agreement of the phase-space structure of resonance eigenfunctions and these measures. Quantitatively, our numerical results support the hypothesis for long-lived eigenfunctions. However, this does not hold for large decay rates, corresponding to shorter-lived eigenfunctions. Thus, it remains an open question if all resonance eigenfunctions with finite decay rates eventually develop universal properties in the semiclassical limit, or if their localization is dominated by fluctuations. The main results about systems with full escape are published in Ref. [66].

For both, partial and full escape, different classes of conditionally invariant measures are presented which lead to an intuitive understanding of the phase-space structure of resonance eigenfunctions based only on simple properties of the classical system. For full escape, the proposed measures are uniform on subsets which escape from the quantum-resolved invariant set. For partial escape, the proposed measures are uniform on subsets which have the same average forward and backward escape. Considering the limit of full escape, however, these intuitive descriptions do not agree with each other. Therefore it remains a challenging open task to unify these approaches and to find the true semiclassical limit measures. In order to advance in this problem a promising class of conditionally invariant measures of the system with partial escape is presented, which is based on periodic orbits. This is left for future research.



# Appendices



# Appendix A

## Generalized baker map

### A.1 Classical baker map

One of the simplest models of chaotic hyperbolic dynamics is the baker map [150–153]. This map implements stretching and folding on the phase space. In general, the phase space is divided into  $M$  parallel rectangles  $A_i$  stretched along the  $p$ -direction with size  $|A_i| = r_i$  for  $\mathbf{r} = (r_0, \dots, r_{M-1}) \in \mathbb{R}_+^M$  with  $\sum_{i=0}^{M-1} r_i = 1$ . The left boundary of the rectangle  $A_i$  is given by  $a_i = \sum_{k=0}^{i-1} r_k$ , where  $a_0 = 0$  and  $a_M = 1$ . It follows that  $A_i = [a_i, a_{i+1}) \times [0, 1)$ . The baker map is then defined as the

$$B_{\mathbf{r}}(q, p) = \left( \frac{q - a_i}{r_i}, r_i \cdot p + a_i \right) \quad \text{for } q \in [a_i, a_{i+1}), \quad (\text{A.1})$$

i.e., it stretches the rectangles  $A_i$  along the  $q$ -direction and compresses in the  $p$ -direction by a factor of  $r_i$ , see Fig. 2.4 for the ternary baker map. The image of such a rectangle is given by  $B_{\mathbf{r}}(A_i) = [0, 1) \times [a_i, a_{i+1})$ . The map  $B_{\mathbf{r}}$  is invertible and symplectic on the torus  $\mathbb{T}^2$ . It is easy to see that it has discontinuities on the boundaries  $\delta A_i$  of the rectangles. Within the rectangle  $A_i$  the Jacobian of  $B_{\mathbf{r}}$  is constant and equals

$$DB_{\mathbf{r}}(q, p) = \begin{pmatrix} 1/r_i & 0 \\ 0 & r_i \end{pmatrix}, \quad \text{for } q \in [a_i, a_{i+1}), \quad (\text{A.2})$$

such that the expansion along the unstable direction is uniform in  $A_i$  with Lyapunov exponent  $\lambda_L = 1/r_i$ . Defining the equally spaced baker map  $B_M := B_{\mathbf{r}}$  for  $\mathbf{r} = (1/M, \dots, 1/M)$  one recovers the two-baker and three-baker maps with  $M = 2$  and  $M = 3$ , respectively. These maps have a uniform Lyapunov exponent  $\lambda_L = 1/M$  on the full phase-space.

The main advantage of the baker map is the simple structure. It has a complete symbolic dynamics in terms of the Markov partition  $\{A_i\}_{i=0}^{M-1}$ . In the following we will briefly recall

this, see e.g., [60]. Consider the symbolic space  $\Sigma = \{0, \dots, M-1\}^{\mathbb{Z}}$ . Any sequence  $\epsilon \in \Sigma$ ,

$$\epsilon = \cdots \epsilon_{-n} \cdots \epsilon_{-2} \epsilon_{-1} \epsilon_0 \epsilon_1 \cdots \epsilon_m \cdots, \quad (\text{A.3})$$

can be mapped onto the phase-space  $\Gamma = \mathbb{T}^2$  via the map  $J_{\mathbf{r}} : \Sigma \rightarrow \mathbb{T}^2$  as

$$J_{\mathbf{r}}(\epsilon) = \left( \sum_{k=0}^{\infty} a_{\epsilon_k} \prod_{l=0}^{k-1} r_{\epsilon_l}, \sum_{k=0}^{\infty} a_{\epsilon_{-(k+1)}} \prod_{l=1}^k r_{\epsilon_{-l}} \right). \quad (\text{A.4})$$

Note that  $J_{\mathbf{r}}$  is not bijective, because e.g., two sequences with  $\epsilon_{i < n} = \tilde{\epsilon}_{i < n}$ ,  $\tilde{\epsilon}_n = \epsilon_n - 1$  and  $\epsilon_{i > n} = 0$  while  $\tilde{\epsilon}_{i > n} = M - 1$  are mapped onto the same point  $(q, p)$ . Excluding all sequences with  $\tilde{\epsilon}_{i > n} = M - 1$  and  $\tilde{\epsilon}_{i < m} = M - 1$  from  $\Sigma$  the restriction of  $J_{\mathbf{r}}$  to this set is bijective.

The symbolic shift  $B^{\Sigma} : \Sigma \rightarrow \sigma$  is defined as

$$B^{\Sigma}(\epsilon) = \cdots \epsilon_{-n} \cdots \epsilon_{-2} \epsilon_{-1} \epsilon_0 \epsilon_1 \cdots \epsilon_m \cdots, \quad (\text{A.5})$$

i.e., the index shifts by one,  $[B^{\Sigma}(\epsilon)]_i = \epsilon_{i+1}$ . The baker map  $B_{\mathbf{r}}$  on the torus  $\mathbb{T}^2$  conjugates with the symbolic shift,

$$B_{\mathbf{r}} = J_{\mathbf{r}} \circ B^{\Sigma} \circ J_{\mathbf{r}}^{-1}, \quad (\text{A.6})$$

such that the dynamics is equivalent on  $\Sigma$  and on the torus.

## A.2 Baker map with escape

Consider the baker map  $B_{\mathbf{r}}$  for some  $\mathbf{r} \in \mathbb{R}_+^M$  with  $\sum_{i=0}^{M-1} r_i = 1$ . The closed map is equivalent to the shift operator  $B^{\Sigma}$  on the set  $\Sigma$  of symbolic sequences, see Eq. (A.6). For the map with escape, let the reflection function be constant on the  $M$  stripes  $A_i$ , and be given by the  $M$ -tuple  $\mathbf{R} = (R_0, \dots, R_{M-1})$  such that for all  $x \in A_i$  one has  $R(x) = R_i$ . This defines the baker map with escape  $\mathcal{B}_{(\mathbf{r}, \mathbf{R})}$  on the set of measures on  $\Gamma = \mathbb{T}^2$  as in Eq. (2.37).

In order to study the dynamics of the baker map with escape, first consider for  $n, m \in \mathbb{N}$  the finite sequence  $\epsilon_-^m \cdot \epsilon_+^n = \epsilon_{-m} \cdots \epsilon_{-1} \epsilon_0 \cdots \epsilon_n$ . This is used to define a so-called cylinder on the symbolic space as  $[\epsilon_-^m \cdot \epsilon_+^n] \subset \Sigma$ , which contains all sequences  $\tilde{\epsilon} \in \Sigma$  with  $\tilde{\epsilon}_i = \epsilon_i$  for  $-m \leq i \leq n$ . This satisfies by construction that  $J_{\mathbf{r}}([\epsilon_-^m \cdot \epsilon_+^n])$  is a rectangle on the torus  $\mathbb{T}^2$  and a subset of  $A_{\epsilon_0}$ . Moreover, applying the inverse baker map to this rectangle yields  $B_{\mathbf{r}}^{-1} \circ J_{\mathbf{r}}([\epsilon_-^m \cdot \epsilon_+^n]) \subset A_{\epsilon_{-1}}$ .

The baker map with escape corresponds to a shift with escape  $\mathcal{B}_{\mathbf{R}}^{\Sigma}$  for measures on the set of symbolic sequences,  $\mu^{\Sigma}$  on  $\Sigma$ . For such a measure  $\mathcal{B}_{\mathbf{R}}^{\Sigma}$  is defined by

$$\mathcal{B}_{\mathbf{R}}^{\Sigma} \mu^{\Sigma}([\epsilon_-^m \cdot \epsilon_+^n]) = R_{\epsilon_{-1}} \cdot \mu^{\Sigma}([\epsilon_{-m} \cdots \epsilon_{-1} \epsilon_0 \cdots \epsilon_n]), \quad (\text{A.7})$$

for all cylinders  $[\epsilon_-^m, \epsilon_+^n] \subset \Sigma$ . This follows from the definition of maps with escape, Eq. (2.37), and the considerations above. Note that due to the conjugacy to the baker map on the torus one can define a measure  $\mu_{\mathbf{r}}$  on the torus for any  $\mu^\Sigma$  as the push-forward measure

$$\mu_{\mathbf{r}} = J_{\mathbf{r}}^* \mu^\Sigma = \mu^\Sigma \circ J_{\mathbf{r}}^{-1}. \quad (\text{A.8})$$

Most importantly the push-forward  $J_{\mathbf{r}}^*$  acts as a semi-conjugacy on the baker map with escape  $\mathcal{B}_{(\mathbf{r}, \mathbf{R})}$  and the shift with escape  $\mathcal{B}_{\mathbf{R}}^\Sigma$ ,

$$J_{\mathbf{r}}^* \mathcal{B}_{\mathbf{R}}^\Sigma = \mathcal{B}_{(\mathbf{r}, \mathbf{R})} J_{\mathbf{r}}^*, \quad (\text{A.9})$$

with the same restrictions to the symbolic space as in Eq. (A.6). Note that in Ref. [60] these restrictions are lowered for the case of full escape in one of the sets  $A_i$ . In order to prove Eq. (A.9) consider  $A \subset \mathbb{T}^2$  and  $[\epsilon] \subset \Sigma$  with  $A = J_{\mathbf{r}}([\epsilon])$  and measures  $\mu^\Sigma$  and  $\mu_{\mathbf{r}}$  with  $\mu_{\mathbf{r}} = \mu^\Sigma \circ J_{\mathbf{r}}^{-1}$ . For these sets and measures

$$J_{\mathbf{r}}^* [\mathcal{B}_{\mathbf{R}}^\Sigma \mu^\Sigma](A) = \mathcal{B}_{\mathbf{R}}^\Sigma \mu^\Sigma \circ J_{\mathbf{r}}^{-1}(A) = \mathcal{B}_{\mathbf{R}}^\Sigma \mu^\Sigma([\epsilon]) \quad (\text{A.10})$$

$$= R_{\epsilon_{-1}} \cdot \mu^\Sigma \left( [B^\Sigma]^{-1}([\epsilon]) \right) = \underbrace{R_{\epsilon_{-1}}}_{=R_{B_{\mathbf{r}}^{-1}(A)}} \cdot \mu^\Sigma \left( \underbrace{[B^\Sigma]^{-1} \circ J_{\mathbf{r}}^{-1}(A)}_{J_{\mathbf{r}}^{-1} \circ B_{\mathbf{r}}^{-1}} \right) \quad (\text{A.11})$$

$$= R_{B_{\mathbf{r}}^{-1}(A)} \cdot [J_{\mathbf{r}}^* \mu^\Sigma](B_{\mathbf{r}}^{-1}(A)) = \mathcal{B}_{(\mathbf{r}, \mathbf{R})} [J_{\mathbf{r}}^* \mu^\Sigma](A), \quad (\text{A.12})$$

holds, which generalizes to arbitrary  $A$  and corresponding subsets of  $\Sigma$ .

### A.3 Quantized baker map

The baker map can be quantized using geometric quantization [151, 152, 174, 212]. In general it is well defined only, if the coefficients of  $\mathbf{r}$  satisfy [60]

$$N_i := N r_i \in \mathbb{N}, \quad \text{for } 0 \leq i < M. \quad (\text{A.13})$$

This condition can be achieved for large enough  $N$  by modification of  $\mathbf{r} \rightarrow \mathbf{r} + \delta \mathbf{r}$ . The  $\delta r_i$  can be chosen arbitrarily small in the limit  $N \rightarrow \infty$ , thus leading to almost the same classical dynamics. The quantization  $\mathcal{B}_{\mathbf{r}}$  on  $\mathbb{H}_N$  is given in position basis by the matrix [151, 152, 212]

$$\mathcal{B}_{\mathbf{r}} = \mathcal{F}_N^{-1} \begin{pmatrix} \mathcal{F}_{N_0} & & & \\ & \mathcal{F}_{N_1} & & \\ & & \ddots & \\ & & & \mathcal{F}_{N_{M-1}} \end{pmatrix}. \quad (\text{A.14})$$

Here  $\mathcal{F}_{\tilde{N}}$  denotes the discrete Fourier transformation between position and momentum states, which is for any  $\tilde{N} \in \mathbb{N}$  and arbitrary Bloch phases  $\vartheta_p, \vartheta_q \in [0, 1]$  defined by the matrix

$$[\mathcal{F}_{\tilde{N}}]_{mn} = \tilde{N}^{-1/2} e^{-2\pi i (m+\vartheta_p)(n+\vartheta_q) / \tilde{N}}. \quad (\text{A.15})$$

In the case of the ternary baker map  $B_3$  choosing the Bloch phases as  $\vartheta_p = \vartheta_q = 1/2$  ensures the same symmetries of classical and quantum map.

# Appendix B

## Additional numerical results

### B.1 Distribution of eigenphases

#### B.1.1 Partial escape.

Consider all eigenvalues  $\lambda = \exp(-i\theta - \gamma/2)$  of a chaotic system with partial escape. Instead of the decay rates  $\gamma$  investigated in Section 4.1.2 here we analyze the distribution of eigenphases  $\theta$ . Therefore we consider the chaotic standard map with partial escape from the region  $\Omega = (0.3, 0.6) \times [0, 1)$  and  $R_\Omega = 0.2$  as in Sec. 4.1.2. We illustrate the distribution of the resonances with respect to their eigenphases  $\theta$  as a histogram in Fig. B.1 for  $h \in \{1/250, 1/1000, 1/4000, 1/16000\}$ . The number of sampling intervals is  $n = 40$  for all  $h$ , leading to better statistics for smaller  $h$  as the number of resonances increases. For  $h = 1/250$  (a) the distribution fluctuates around the uniform distribution, shown for comparison as a red line. With smaller  $h$  the fluctuations become smaller, see (b)–(d).

We conclude that for partial escape in the semiclassical limit all resonances are uniformly distributed with respect to their eigenphase  $\theta$ . This is rigorously proven in Ref. [195], where it

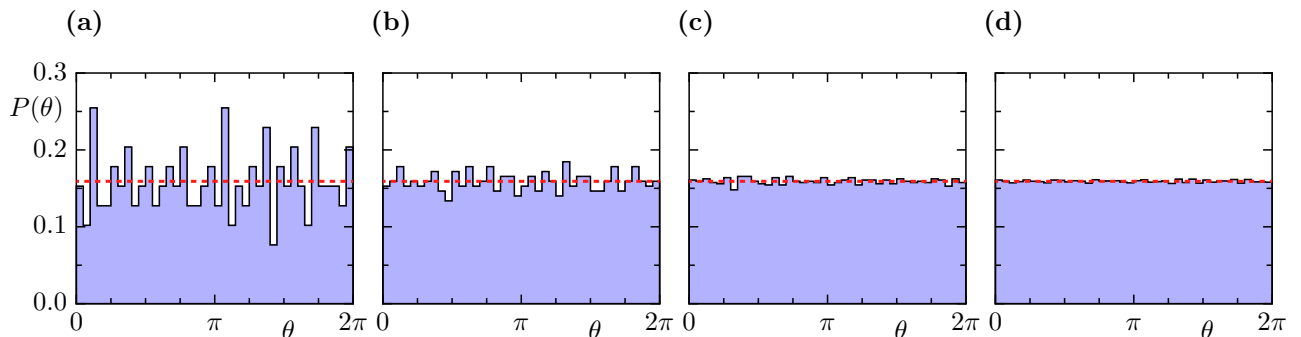


**Figure B.1:** Distribution of eigenphases  $\theta$  for the chaotic standard map with partial escape for  $R_\Omega = 0.2$ . Shown is the normalized probability  $P(\theta)$  for the eigenvalues  $\lambda = \exp(-i\theta - \gamma/2)$  for (a)  $h = 1/250$ , (b)  $h = 1/1000$  (c)  $h = 1/4000$ , and (d)  $h = 1/16000$ . Horizontal line shows the uniform expectation  $P(\theta) = (2\pi)^{-1} \approx 0.16$ . For distribution of decay rates see Fig. 4.2.

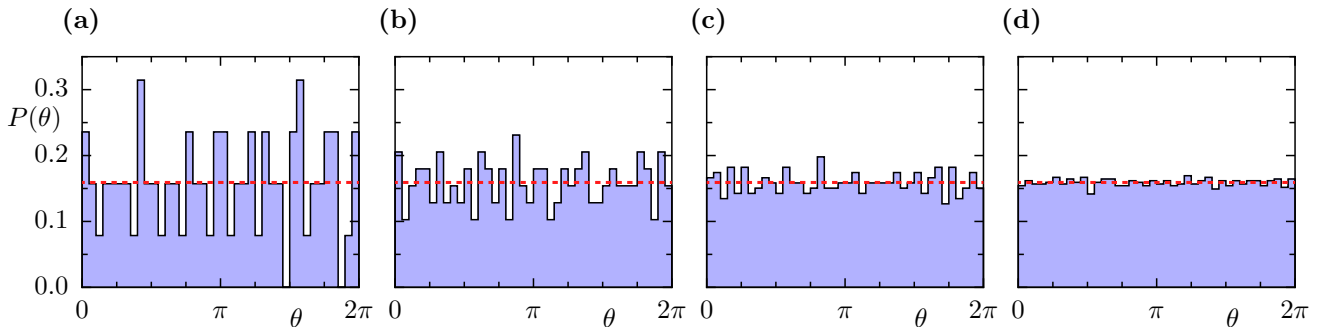


**Figure B.2:** Distribution of eigenphases  $\theta$  for the chaotic standard map with full escape. Shown is the normalized probability  $P(\theta)$  of all eigenvalues  $\lambda = \exp(-i\theta - \gamma/2)$  with  $\gamma \leq 1$  for (a)  $h = 1/250$ , (b)  $h = 1/1000$  (c)  $h = 1/4000$ , and (d)  $h = 1/16000$ . Horizontal line shows the uniform expectation  $P(\theta) = (2\pi)^{-1} \approx 0.16$ . For distribution of decay rates see Fig. 5.4.

is shown that semiclassically almost all resonances have decay rates within  $(\gamma_{\text{typ}} - \epsilon, \gamma_{\text{typ}} + \epsilon)$  and that these resonances are uniformly distributed with respect to their eigenphase. We remark that in Fig. B.1 we analyze all resonances instead of restricting to those close to  $\gamma_{\text{typ}}$ .

### B.1.2 Full escape.

We similarly investigate the eigenphases  $\theta$  of all long-lived resonances with decay rate  $\gamma < 1$  for the system with full escape, i.e.,  $R_\Omega = 0$ . The normalized distribution of  $\theta$  is illustrated in Fig. B.2. We notice stronger fluctuations than in the system with partial escape, which are due to the smaller number of considered resonances. For smaller values of  $h$  these fluctuations vanish and the probability  $P(\theta)$  is almost constant. Note that  $\gamma_{\text{typ}} = \infty$  for full escape which means that the results in Ref. [195] are applicable only for instantaneously decaying resonances.

## B.2 Quantum expectation of observables

For completeness we present in this section the mean expectation value  $\mathbb{E}_\gamma[a]$  and standard deviation  $\sigma_\gamma(a)$  for the observables  $a_{1,2,3} = \mathbb{1}_{A,B,C}$  where  $A = (0.3, 0.5) \times (0.6, 0.8)$ ,  $B = (0.7, 0.9) \times (0.1, 0.3)$ , and  $C = (0.3, 0.5) \times (0.1, 0.3)$ , see Fig. 4.7.

### B.2.1 Partial escape

We present numerical results for the same parameters as in Fig. 4.10 for the observables  $a_{1,2,3} = \mathbb{1}_{A,B,C}$ , defined in Sec. 4.2.2 in Figs. B.3–B.5, respectively. The observations are similar as discussed for the smooth observable  $a_4$  in Sec. 4.2.2.



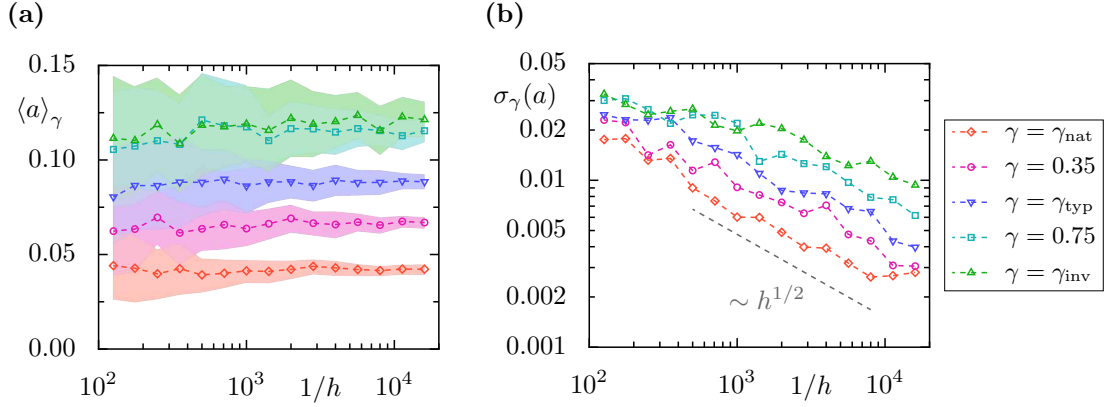


**Figure B.3:** Same as Fig. 4.10 for observable  $a_1 = \mathbb{1}_A$ . (a) Mean expectation value  $\langle a \rangle_\gamma$  vs.  $h$  for  $\gamma \in \{\gamma_{\text{nat}}, 0.35, \gamma_{\text{typ}}, 0.75, \gamma_{\text{inv}}\}$ . The average is taken over  $S = 50$  resonance eigenfunctions. Shaded regions indicate the corresponding standard deviation  $\sigma_\gamma(a)$ . (b) Standard deviation  $\sigma_\gamma(a)$  vs.  $h$  for same  $\gamma$  as in (a). Gray dashed line shows approximate scaling  $\sim h^{1/2}$ .

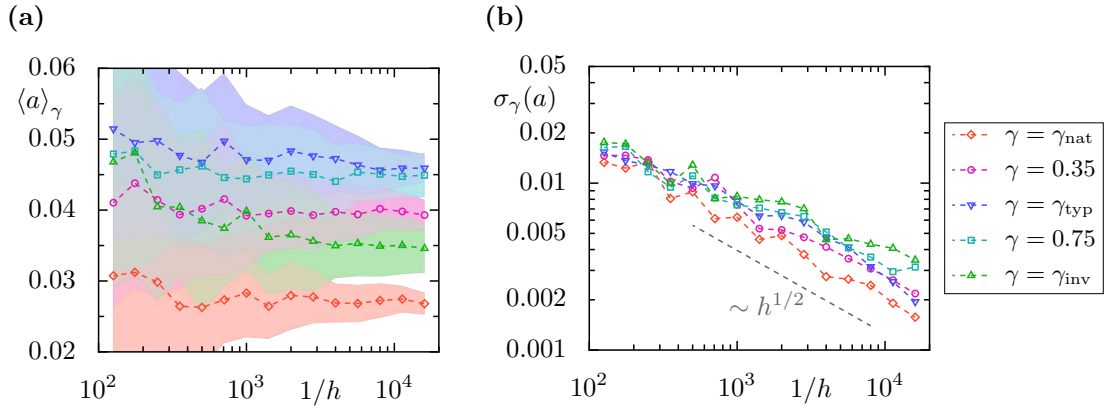


**Figure B.4:** Same as Fig. 4.10 for observable  $a_2 = \mathbb{1}_B$ .

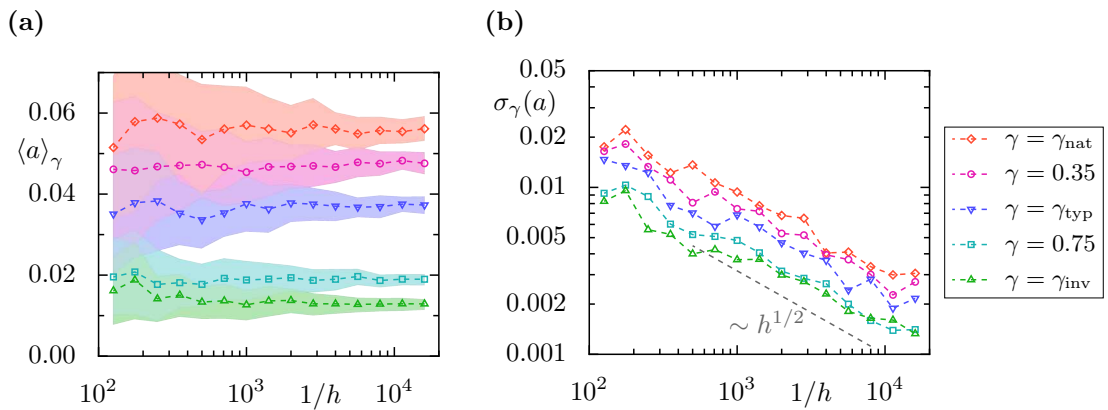


**Figure B.5:** Same as Fig. 4.10 for observable  $a_3 = \mathbb{1}_C$ .

### B.2.2 Full escape

We present numerical results for the same parameters as in Fig. 5.10 for the observables  $a_{1,2,3} = \mathbb{1}_{A,B,C}$  in Figs. B.6–B.8, respectively. The observations are similar as discussed for the

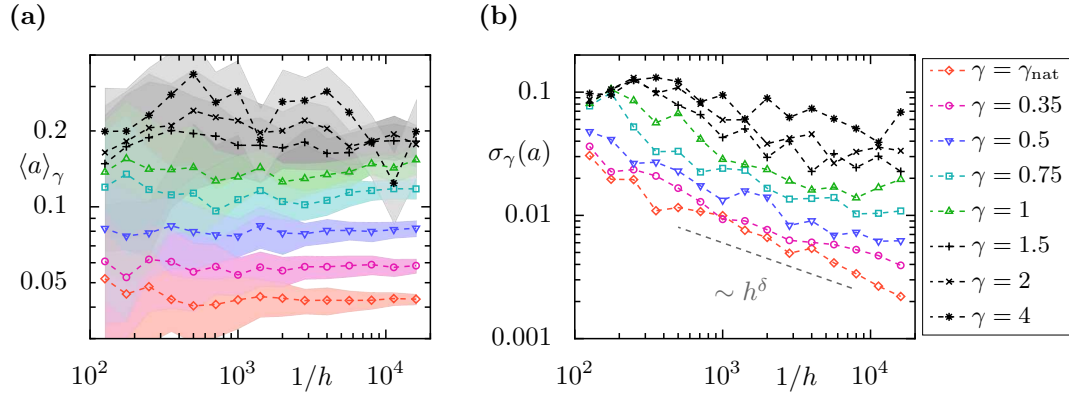


**Figure B.6:** Same as Fig. 5.10 for observable  $a_1 = \mathbb{1}_A$ . (a) Mean expectation value  $\langle a \rangle_\gamma$  vs.  $h$  for shown decay rates  $\gamma$ . The average is taken over  $S = 50$  resonance eigenfunctions. Shaded region indicates standard deviation  $\sigma_\gamma(a)$ . (b) Standard deviation  $\sigma_\gamma(a)$  vs.  $h$  for same decay rates. Gray dashed line shows scaling  $\sim h^\delta$  with  $\delta \approx D_0(\Gamma_s)/4$ .

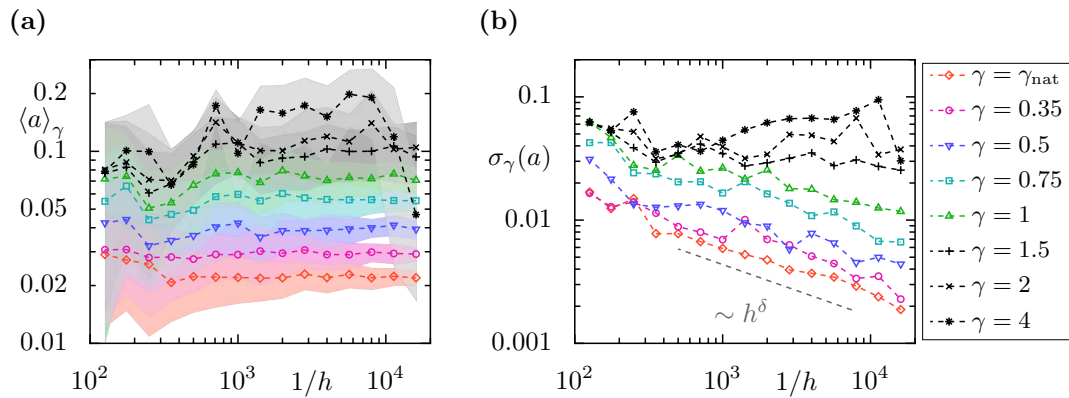


**Figure B.7:** Same as Fig. 5.10 for observable  $a_2 = \mathbb{1}_B$ .

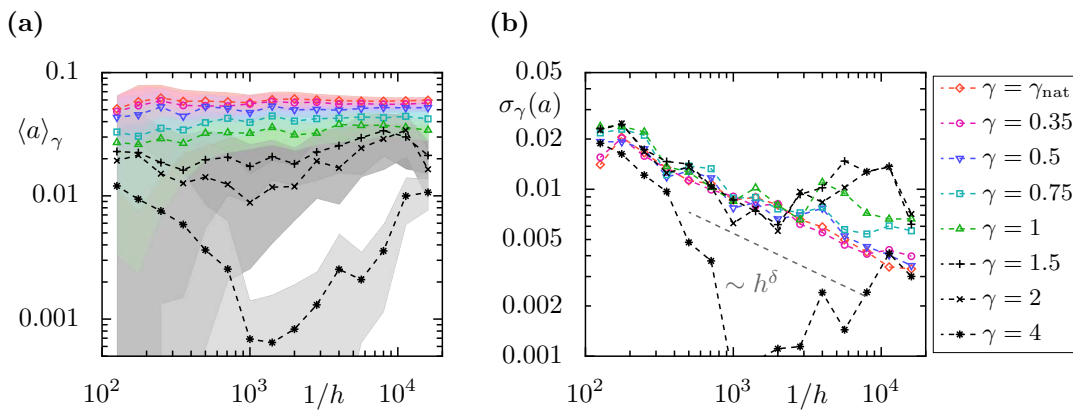


**Figure B.8:** Same as Fig. 5.10 for observable  $a_3 = \mathbb{1}_C$ .

smooth observable  $a_4$  in Sec. 5.2.3.

## B.3 Effective information dimension

We investigate how the effective information dimension  $D_1(\gamma, \epsilon)$ , see Eqs. (2.49) and (4.50), of single Husimi distributions  $\mathcal{H}_\gamma$  depends on the considered parameter  $\epsilon$ . For this purpose we illustrate  $D_1(\gamma, \epsilon)$  as a function of  $\gamma$  for four different values of  $\epsilon \in \{1/8, 1/32, 1/128, 1/512\}$  in Fig. B.9 and different values of Planck's constant  $h$ .

For  $h = 1/250$  and  $h = 1/1000$ , shown in (a) and (b), we observe that first smaller values of  $\epsilon$  lead to smaller effective dimensions, but decreasing  $\epsilon$  further the trivial result  $D_1(\gamma, \epsilon) = 2$  is approached. Similar observations hold for  $h = 1/4000$  and  $h = 1/16000$ , shown in (c) and (d). For the largest considered  $\epsilon = 1/8$  we have almost the same dependence on  $\gamma$  for all values of  $h$ . Due to the limited resolution at the larger value of  $h$  this changes for smaller  $\epsilon$ . Interestingly, we observe a similar progression for  $h = 1/250$  with  $\epsilon = 1/2^5$  and  $h = 1/4000$  with  $\epsilon = 1/2^7$ . This is also seen between  $h = 1/1000$  and  $h = 1/16000$  for the same  $\epsilon$ . In all of these cases the fraction  $\epsilon/\sqrt{h} < 1$  is constant. Altogether, variation of  $\epsilon$  shows that it is necessary to evaluate the results of effective dimensions carefully for fixed values of  $h$ , because there are nontrivial effects in the regime where  $\epsilon$  is of the order of  $\sqrt{h}$  or smaller.

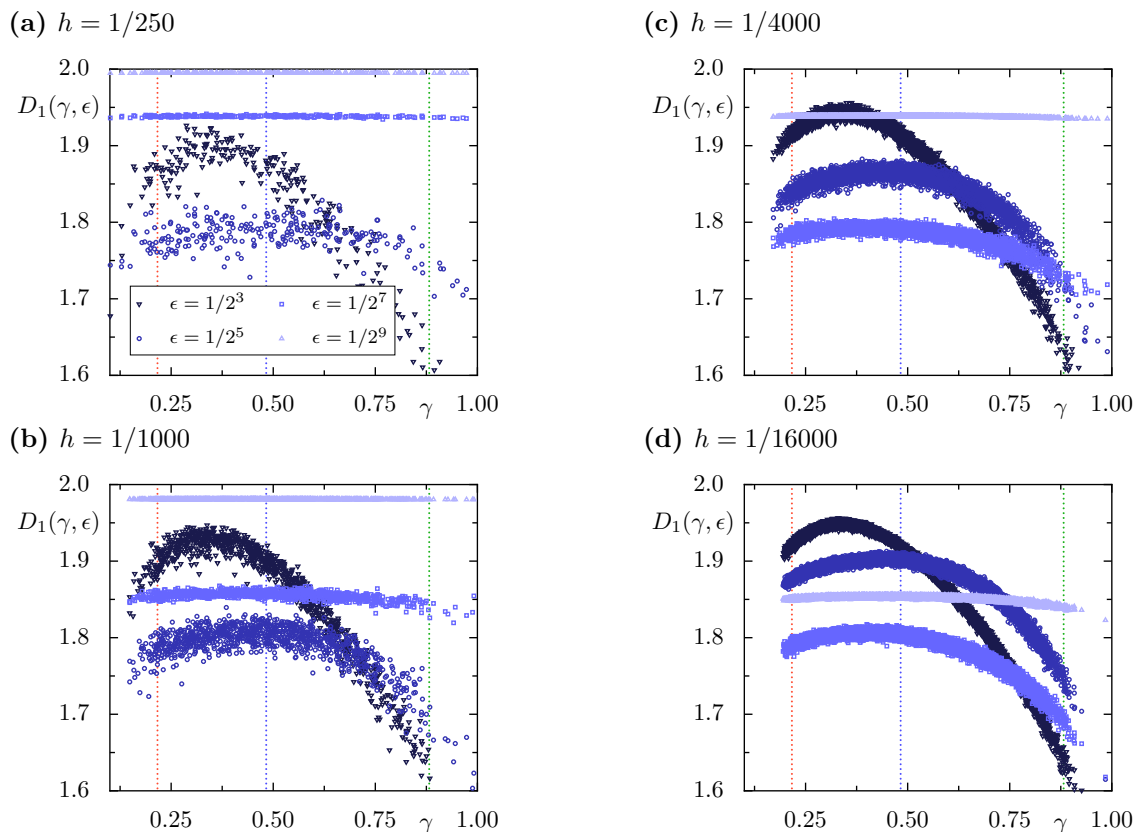


**Figure B.9:** Fractal information dimensions  $D_1(\gamma, \epsilon)$  of single resonance eigenfunctions as a function of their decay rate  $\gamma$ . Considered are four different values of  $\epsilon \in \{1/8, 1/32, 1/128, 1/512\}$  (from dark to light blue) and all eigenfunctions for (a)  $h = 1/250$ , (b)  $h = 1/1000$ , (c)  $h = 1/4000$ , and (d)  $h = 1/16000$ . Vertical dotted lines indicate classical decay rates  $\gamma_{\text{nat}} \approx 0.22$  (red),  $\gamma_{\text{typ}} \approx 0.48$  (blue), and  $\gamma_{\text{inv}} \approx 0.88$  (green).

## B.4 Jensen–Shannon divergence for different scales $\epsilon$

### B.4.1 Partial escape

In this section we illustrate the Jensen–Shannon divergence  $d_{\text{JS}}(\mathcal{H}_\gamma, \mu_\xi)$ , Eq. (4.51), between single Husimi distributions  $\mathcal{H}_\gamma$  and the classical measures  $\mu_\xi$  for the chaotic standard map with partial escape from  $\Omega = (0.3, 0.6) \times [0, 1)$  and  $R_\Omega = 0.2$  for different scales  $\epsilon$ . For  $\epsilon = 1/16$  see Fig. 4.26 in Sec. 4.4.3.

In Figure B.10 we consider larger  $\epsilon = 1/4$ , leading to overall smaller distances. The reason is, that the phase-space distributions are compared on fewer, but larger sets, such that fluctuations and differences can average out. Conversely for smaller  $\epsilon = 1/32$  we find overall larger distances, see Fig. B.11. The general dependence of  $d_{\text{JS}}$  on  $\gamma$  and  $h$  is similar for all three

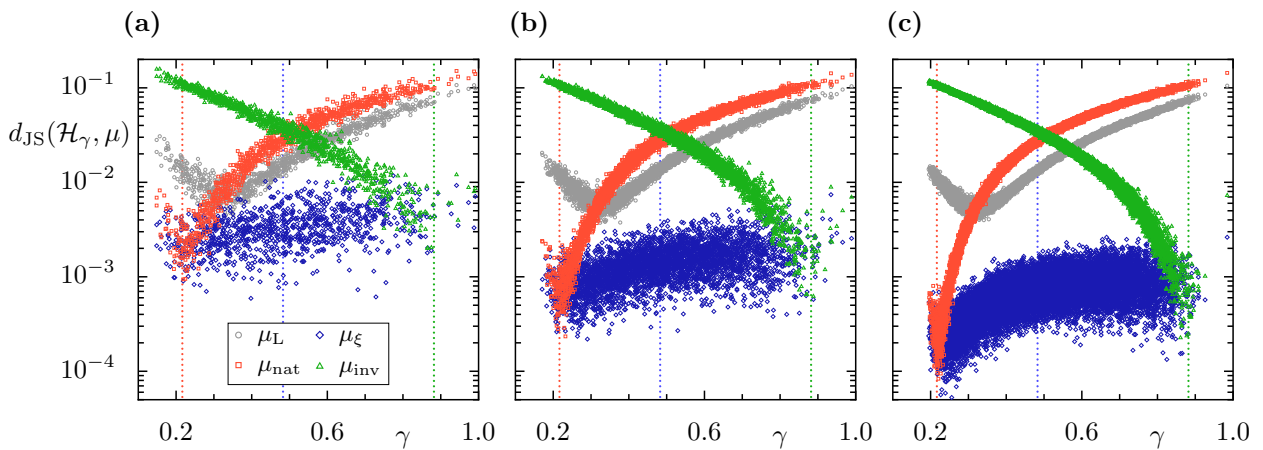


**Figure B.10:** Jensen–Shannon divergence between single quantum Husimi distributions and different classical measures as a function of the decay rate  $\gamma$  for (a)  $h = 1/1000$ , (b)  $h = 1/4000$ , and (c)  $h = 1/16000$ . Same as Fig. 4.26 but using  $\epsilon = 1/4$ . The symbols correspond to the considered measures  $\mu_\xi$  (blue diamonds),  $\mu_{\text{nat}}$  (red boxes),  $\mu_{\text{inv}}$  (green triangles), and  $\mu_L$  (gray circles). Dotted vertical lines indicate  $\gamma_{\text{nat}}$ ,  $\gamma_{\text{typ}}$ , and  $\gamma_{\text{inv}}$  (red, blue, green).

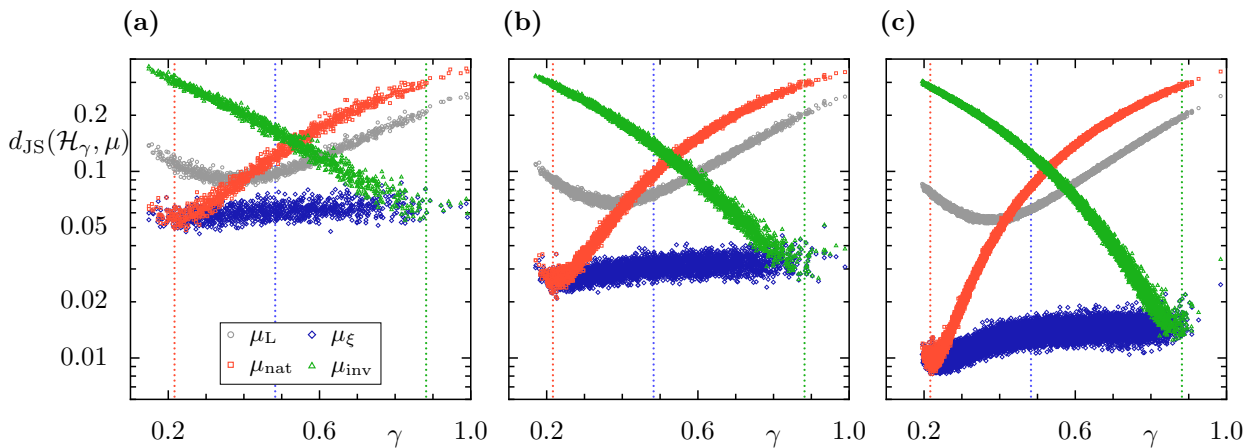


**Figure B.11:** Same as Fig. 4.26 and Fig. B.10 but using  $\epsilon = 1/32$ .

cases and the observations are robust against the specific choice of  $\epsilon$ . In the thesis we select  $\epsilon = 1/16$  since it gives a good phase-space resolution, while at the same time satisfies  $\epsilon > \sqrt{\hbar}$  if  $h$  is smaller than  $h < 1/250$ .

### B.4.2 Full escape

In the following we consider  $d_{\text{JS}}^{\epsilon}(\mathcal{H}_{\gamma}, \mu)$  between single Husimi distributions  $\mathcal{H}_{\gamma}$  and different classical measures  $\mu$  for the chaotic standard map with full escape from  $\Omega = (0.3, 0.6) \times [0, 1)$ , i.e.,  $R_{\Omega} = 0$ , for different scales  $\epsilon$ . For  $\epsilon = 1/16$  see Fig. 5.25 in Sec. 5.4.3. In Fig. B.12 we show analogue results for  $\epsilon = 1/4$  and in Fig. B.13 for  $\epsilon = 1/32$ . As for partial escape, the results are robust against reasonable changes in  $\epsilon$ .

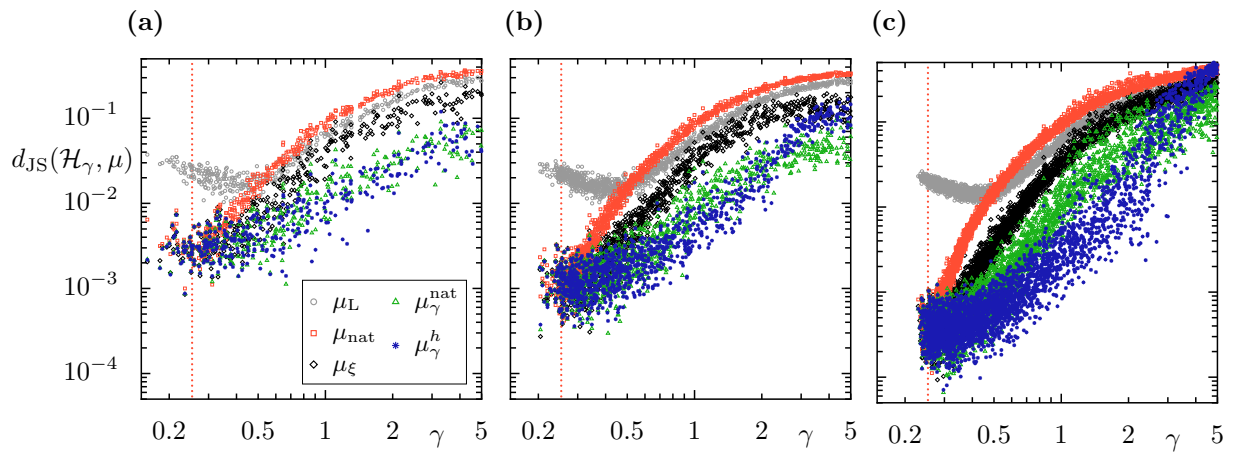


**Figure B.12:** Jensen–Shannon divergence between single quantum Husimi distributions and different classical measures as a function of the decay rate  $\gamma$  for (a)  $h = 1/1000$ , (b)  $h = 1/4000$ , and (c)  $h = 1/16000$  in the system with full escape. Same as Fig. 5.25 but using  $\epsilon = 1/4$ . The symbols correspond to the considered measures  $\mu_L$  (gray circles),  $\mu_{\text{nat}}$  (red boxes),  $\mu_{\xi}$  (black diamonds),  $\mu_{\gamma}^{\text{nat}}$  (green triangles), and  $\mu_{\gamma}^h$  (blue stars). Dotted vertical lines indicate  $\gamma_{\text{nat}}$ ,  $\gamma_{\text{typ}}$ , and  $\gamma_{\text{inv}}$  (red, blue, green).

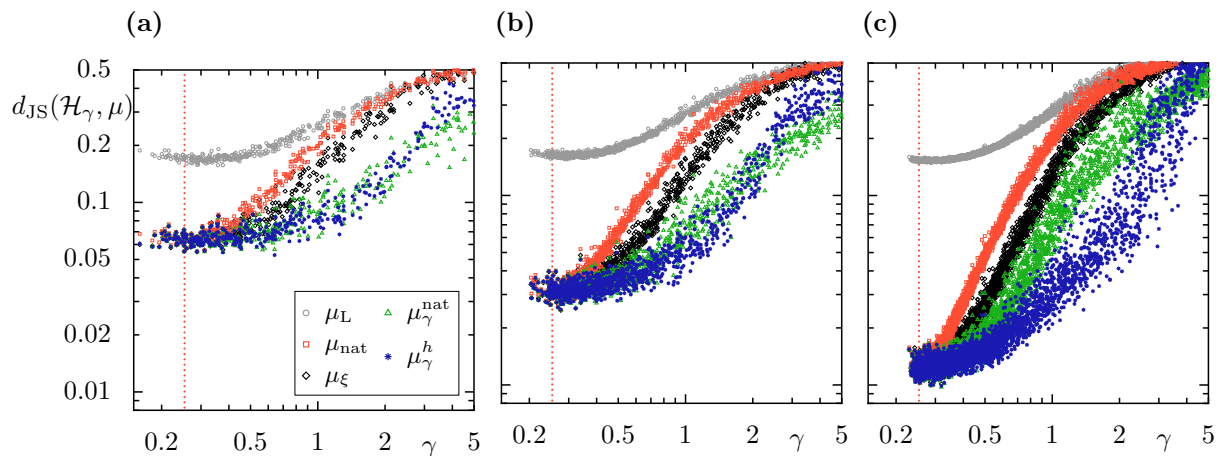


**Figure B.13:** Same as Fig. 5.25 and Fig. B.12 for  $\epsilon = 1/32$ .



# Appendix C

## Miscellaneous proofs

### C.1 Expectation for iterations of $R$ for c-measures

In the following we show that if  $\mu$  is a conditionally invariant probability measure,  $\mathcal{M}\mu = e^{-\gamma}\mu$ , Eq. (2.54), and  $\mu(\Gamma) = 1$ , the expectation value of the functions  $T_n^+$  and  $T_m^-$  defined in Sec. 4.2.5 satisfy

$$\mu(T_n^+) = e^{-n\gamma}(1 - e^{-\gamma}) \quad \text{and} \quad \mu(T_m^-) = e^{m\gamma}(e^\gamma - 1), \quad (\text{C.1})$$

which corresponds to the semiclassical results Eqs. (4.25) and (4.26) and is shown as follows.

Recall the notation  $\mathcal{M}\mu(f) = \mu(R \cdot [f \circ M])$ , Eq. (2.38). Applying the map with escape  $n$  times one obtains

$$\mathcal{M}^n \mu(f) = \mu(R \cdot [R \circ M] \cdots [R \circ M^{n-1}] \cdot [f \circ M^n]) \quad (\text{C.2})$$

$$= \mu \left( \prod_{i=0}^{n-1} R \circ M^i \cdot f \circ M^n \right). \quad (\text{C.3})$$

Inserting the function  $f(x) = \mathbb{1}_\Gamma(x) = 1$  and using conditional invariance of  $\mu$ , we get

$$\mu \left( \prod_{i=0}^{n-1} R \circ M^i \right) = \mathcal{M}^n \mu(\mathbb{1}_\Gamma) \stackrel{(2.54)}{=} e^{-n\gamma} \mu(\mathbb{1}_\Gamma) = e^{-n\gamma}. \quad (\text{C.4})$$

Applying this towards  $T_n^+ = \prod_{i=0}^{n-1} R \circ M^i - \prod_{i=0}^n R \circ M^i$  we get

$$\mu(T_n^+) = \mu \left( \prod_{i=0}^{n-1} R \circ M^i \right) - \mu \left( \prod_{i=0}^n R \circ M^i \right) = e^{-n\gamma}(1 - e^{-\gamma}), \quad (\text{C.5})$$

which proves the first part of Eq. (C.1). The second part follows similarly from the inverse time evolution Eq. (2.58),  $\mathcal{M}^{-1}\mu(f) = \mu(R^{-1} \circ M^{-1} \cdot f \circ M^{-1})$ , applied  $m$  times to  $f = \mathbb{1}_\Gamma$  and using conditional invariance,  $\mathcal{M}^{-1}\mu = e^\gamma\mu$ .

## C.2 Comparison of natural and inverse decay rate

Here we show that for natural and inverse decay rate  $\gamma_{\text{nat}} < \gamma_{\text{inv}}$  holds. Heuristically the idea is quite simple: Assume a finite approximation of the Perron-Frobenius operator, i.e., a positive matrix mapping phase-space densities onto phase-space densities. The Perron-Frobenius theorem implies that the largest eigenvalue  $\Lambda_+^{\text{fwd}}$  is non-degenerate and positive, and it is associated with the natural decay rate  $\Lambda_+^{\text{fwd}} = e^{-\gamma_{\text{nat}}}$ . Thus any other eigenvalue must be smaller than  $\Lambda_+^{\text{fwd}}$  implying larger decay rates. In particular  $\gamma_{\text{inv}} > \gamma_{\text{nat}}$ . Consistently, the largest eigenvalue  $\Lambda_+^{\text{inv}}$  of the Perron-Frobenius approximation of the inverse map is associated with the inverse decay rate as,  $\Lambda_+^{\text{inv}} = e^{\gamma_{\text{inv}}}$ . Any other eigenvalue must be smaller than  $\Lambda_+^{\text{inv}}$ , leading to smaller decay rates.

In the following we first prove the statement  $\gamma_{\text{nat}} < \gamma_{\text{inv}}$  for the generalized bakers map with escape, followed by a generalization to arbitrary maps with escape.

*Proof for bakers map.* Consider the generalized bakers map  $B_{\mathbf{r}}$  with  $\mathbf{r} \in \mathbb{R}_+^N$ , such that  $\sum_i r_i = 1$ , see App. A.1. Let the reflectivity function be constant on the rectangles  $A_i$  as defined in Sec. A.2,  $R(x) = R_i$  for all  $x \in A_i$ . In this case it is easy to see that

$$e^{-\gamma_{\text{nat}}} = \sum_i r_i R_i, \quad \text{and} \quad e^{\gamma_{\text{inv}}} = \sum_i r_i \frac{1}{R_i}. \quad (\text{C.6})$$

In order to show that  $\gamma_{\text{nat}} < \gamma_{\text{inv}}$  we show that  $e^{-\gamma_{\text{nat}}} > e^{-\gamma_{\text{inv}}}$ ,

$$e^{-\gamma_{\text{nat}}}/e^{-\gamma_{\text{inv}}} = \sum_i r_i R_i \cdot \sum_j r_j \frac{1}{R_j} = \sum_{i,j} r_i r_j \frac{R_i}{R_j} \quad (\text{C.7})$$

$$= \frac{1}{2} \sum_{i,j} \left( \underbrace{r_i r_j \frac{R_i}{R_j} + r_j r_i \frac{R_j}{R_i}}_{=r_i r_j \left( \frac{R_i}{R_j} + \frac{R_j}{R_i} \right) \geq 2r_i r_j} \right) \geq \sum_{i,j} r_i r_j = \sum_i r_i \sum_j r_j = 1. \quad (\text{C.8})$$

However, equality is only obtained if  $R_i = R_j$  for all  $i, j$ , which relates to the trivial case of a global factor. For all other cases this proves for the generalized Bakers map that the natural decay rate is always smaller than the inverse decay rate.  $\square$



In order to prove this statement for an arbitrary (hyperbolic) map we follow the ideas and use notation as in Refs. [67,162], where Eq. (2.53) as a generalization of the Kantsz-Grassberger relation Eq. (2.52) is derived.

*Proof for arbitrary map with escape.* Consider the  $n$ -th image and preimage of a region of interest  $\Gamma$  under the closed map  $M$ . We will consider  $\Gamma$  to be the whole phase space later. If  $n$  is large enough,  $n \gg 1$ , then one can always *identify a set of narrow "columns" in the unstable direction and narrow "strips" along the stable direction*, see Fig. 2 in Ref. [162] and Ref. [137] Chp. 9. Each of these columns and strips contain a periodic point  $y$  with period  $p = n$  [137, Chp. 9] such that  $M^n(y) = y$ .

Let  $y$  be such a periodic point with period  $p = n$  at the intersection of strip  $j$  with column  $i$ . The width of column  $i$  and strip  $j$  are determined by the Lyapunov exponents around the cycle point,  $\varepsilon_i^{(n)} = e^{\lambda_y^{(n)}}$  and  $\varepsilon_j^{(n)} = e^{-\lambda_y^{(n)}}$  [162], where in our case of a volume preserving map contraction and expansion rate are the same,  $-\lambda_y^{(n)} = \lambda_y^{(n)} > 0$ . Note that  $n\lambda_y^{(n)}$  is the total expansion after one period of  $y$ . Consider a uniform distribution of density one in the strip  $j$  (giving a total weight of  $\varepsilon_j^{(n)}$ ). This distribution is mapped under the closed map  $M$  in  $n$  steps onto the column  $i$ . The points in  $j$  stay close to the periodic point, such that on average they obtain a decay with  $R_y^{(n)} = (\prod_{k=1}^n R[M^k(y)])^{1/n}$  in each time step. Thus after  $n$  iterations the weight on the  $i$ -th column is given by [162]

$$\mu_i^{(n)} = \prod_{k=1}^n R[M^k(y)] \cdot \varepsilon_j^{(n)} = e^{n[\ln R_y^{(n)} - \lambda_y^{(n)}]}. \quad (\text{C.9})$$

For the natural decay rate  $\gamma = \gamma_{\text{nat}}$  the sum over all columns satisfies

$$e^{-n\gamma_{\text{nat}}} = \sum_i \mu_i^{(n)} = \sum_{y \text{ p.p.: } p=kn} e^{n[\ln R_y^{(n)} - \lambda_y^{(n)}]} \quad (\text{C.10})$$

and can be written as a sum over periodic orbits. Similar considerations for the inverse map  $\mathcal{M}^{-1}$  lead to a mapping of a density on column  $i$  onto the strip  $j$ , which experiences an average growth with  $\frac{1}{R_y^{(n)}}$ . Thus the weight accumulating on strip  $j$  equals

$$\mu_j^{(n)} = e^{n[-\ln R_y^{(n)} - \lambda_y^{(n)}]} \quad (\text{C.11})$$

and one obtains an exponential growth for the corresponding c-measure as

$$e^{n\gamma_{\text{inv}}} = \sum_j \mu_j^{(n)} = \sum_{y \text{ p.p.: } p=kn} e^{n[-\ln R_y^{(n)} - \lambda_y^{(n)}]}. \quad (\text{C.12})$$

Altogether we get

$$e^{-n\gamma_{\text{nat}}}/e^{-n\gamma_{\text{inv}}} = \sum_{y \text{ p.p.: } p=kn} e^{n[\ln R_y^{(n)} - \lambda_y^{(n)}]} \sum_{z \text{ p.p.: } p=kn} e^{n[-\ln R_z^{(n)} - \lambda_z^{(n)}]} \quad (\text{C.13})$$

$$= \sum_{y,z \text{ p.p.: } p=kn} e^{-n\lambda_y^{(n)}} e^{-n\lambda_z^{(n)}} \underbrace{\left[ e^{n \ln R_y^{(n)}} e^{-n \ln R_z^{(n)}} \right]}_{\left( \frac{R_y^{(n)}}{R_z^{(n)}} \right)^n} \quad (\text{C.14})$$

$$= \frac{1}{2} \sum_{y,z \text{ p.p.: } p=kn} e^{-n\lambda_y^{(n)}} e^{-n\lambda_z^{(n)}} \underbrace{\left[ \left( \frac{R_y^{(n)}}{R_z^{(n)}} \right)^n + \left( \frac{R_z^{(n)}}{R_y^{(n)}} \right)^n \right]}_{\geq 2} \quad (\text{C.15})$$

$$\geq \left( \sum_{y \text{ p.p.: } p=kn} e^{-n\lambda_y^{(n)}} \right) \left( \sum_{z \text{ p.p.: } p=kn} e^{-n\lambda_z^{(n)}} \right) \xrightarrow{n \rightarrow \infty} 1. \quad (\text{C.16})$$

Taking the limit in the last step gives unity because we sum over terms  $e^{-n\lambda_y^{(n)}}$ , corresponding to one divided by the magnitude of the expanding eigenvalue of the linearization around the periodic orbit, as for example is given in Ref. [137] (Eq. (9.42), page 367). This corresponds to the sum rule by Hannay and Ozorio de Almeida [206]. Note that in case of the baker map the result is already exact for  $n = 1$  due to exact self similarity.  $\square$

## C.3 Conditional invariance of product measures

In this section we first rigorously prove conditional invariance for the product measures  $\mu_\xi$  constructed for the generalized baker map with partial escape. Secondly we consider general hyperbolic maps and heuristically derive conditional invariance.

### C.3.1 Generalized baker map

In this section we prove conditional invariance for the measures  $\mu_\xi$  for the uniformly hyperbolic baker map with escape, defined in App. A.2. For this purpose, let us consider the specific class of Bernoulli measures [60]. Therefore we define a weight distribution  $\mathbf{P} = (P_0, P_1, \dots, P_M)$  satisfying  $0 \leq P_i \leq 1$  for all  $i < M$  and  $\sum_{i=0}^{M-1} P_i = 1$ . For any such  $\mathbf{P}$  consider the Bernoulli measure  $\nu_{\mathbf{P}}^{\Sigma_+}$ , which is defined on one sided cylinders  $[\cdot, \epsilon_+] \subset \Sigma_+$  as [60]

$$\nu_{\mathbf{P}}^{\Sigma_+}([\cdot, \epsilon_+^n]) = \prod_{k=0}^{n-1} P_{\epsilon_k}. \quad (\text{C.17})$$

This measure can be pushed similar as defined in Eq. (A.8) onto the interval  $[0, 1)$  by  $\nu_{\mathbf{r}, \mathbf{P}} = \nu_{\mathbf{P}}^{\Sigma_+} \circ J_{\mathbf{r}}^{-1}$ . Note that for  $\mathbf{P} = \mathbf{r}$  the uniform measure on the unit interval  $\nu_{\mathbf{L}}$  is obtained, and in all other cases the measure  $\nu_{\mathbf{r}, \mathbf{P}}$  is not absolutely continuous to the uniform measure, i.e.,

it has no density [60]. Similarly one defines  $\nu_{\mathbf{P}}^{\Sigma^-}$  on the set of cylinders  $[\epsilon_-] \subset \Sigma_-$ .

In the following we generalize Proposition 3 in Ref. [60], given for full escape from one rectangle  $A_i$ , to arbitrary escape: For any weight distribution  $\mathbf{P}$  and given any reflectivity  $\mathbf{R}$  on the sets  $A_i$  there exists a unique auxiliary weight distribution  $\mathbf{P}^* = (P_0^*, \dots, P_{M-1}^*)$ , defined by  $P_i^* := R_i P_i \left( \sum_{j=0}^{M-1} R_j P_j \right)^{-1}$ , such that the measure

$$\mu_{\mathbf{P}, \mathbf{R}}^{\Sigma} := \nu_{\mathbf{P}}^{\Sigma^+} \times \nu_{\mathbf{P}^*}^{\Sigma^-} \quad (\text{C.18})$$

is conditional invariant under the baker shift with escape  $\mathcal{B}_{\mathbf{R}}^{\Sigma}$ . The corresponding measure  $\mu_{\mathbf{r}, \mathbf{P}, \mathbf{R}} := \mu_{\mathbf{P}, \mathbf{R}}^{\Sigma} \circ J_{\mathbf{r}}^{-1}$  is a conditional invariant measure of the baker map with escape  $B_{\mathbf{r}}$  on the torus.

*Proof.* In order to see conditional invariance, consider

$$\mathcal{B}_{\mathbf{R}}^{\Sigma} \mu_{\mathbf{P}, \mathbf{R}}^{\Sigma}([\epsilon_-^m \cdot \epsilon_+^n]) \stackrel{(\text{A.7})}{=} R_{\epsilon_{-1}} \cdot \mu_{\mathbf{P}, \mathbf{R}}^{\Sigma}([\epsilon_{-m} \cdots \epsilon_{-2} \cdot \epsilon_{-1} \epsilon_0 \cdots \epsilon_n]) \quad (\text{C.19})$$

$$\stackrel{(\text{C.18})}{=} R_{\epsilon_{-1}} \nu_{\mathbf{P}^*}^{\Sigma^-}([\epsilon_{-m} \cdots \epsilon_{-2} \cdot]) \cdot \nu_{\mathbf{P}}^{\Sigma^+}([\epsilon_{-1} \epsilon_0 \cdots \epsilon_n]) \quad (\text{C.20})$$

$$\stackrel{(\text{C.17})}{=} \underbrace{R_{\epsilon_{-1}} P_{\epsilon_{-1}}}_{=(\sum_{j=0}^{M-1} R_j P_j) P_{\epsilon_{-1}}^*} \prod_{k=2}^m P_{\epsilon_{-k}}^* \prod_{l=0}^n P_{\epsilon_l} \quad (\text{C.21})$$

$$= \left( \sum_{j=0}^{M-1} R_j P_j \right) \mu_{\mathbf{P}, \mathbf{R}}^{\Sigma}([\epsilon_-^m \cdot \epsilon_+^n]), \quad (\text{C.22})$$

where the definition of  $P_{\epsilon_{-1}}^*$  has been used in the last step. This proves that the measure  $\mu_{\mathbf{P}, \mathbf{R}}^{\Sigma}$  is an eigenmeasure of  $\mathcal{B}_{\mathbf{R}}^{\Sigma}$  with eigenvalue  $\Lambda_{\mathbf{P}, \mathbf{R}} = \sum_{j=0}^{M-1} R_j P_j$ , implying the decay rate  $\gamma_{\mathbf{P}, \mathbf{R}} = -\ln \Lambda_{\mathbf{P}, \mathbf{R}}$ . Due to the semi-conjugacy of baker map and baker shift with escape this also proves that  $\mu_{\mathbf{r}, \mathbf{P}, \mathbf{R}}$  is conditionally invariant under  $\mathcal{B}_{(\mathbf{r}, \mathbf{R})}$  with the same decay rate,

$$\mathcal{B}_{(\mathbf{r}, \mathbf{R})} \mu_{\mathbf{r}, \mathbf{P}, \mathbf{R}}(A) = \mathcal{B}_{(\mathbf{r}, \mathbf{R})} [J_{\mathbf{r}}^* \mu_{\mathbf{P}, \mathbf{R}}^{\Sigma}](A) = J_{\mathbf{r}}^* [\mathcal{B}_{\mathbf{R}}^{\Sigma} \mu_{\mathbf{P}, \mathbf{R}}^{\Sigma}](A) = e^{-\gamma_{\mathbf{P}, \mathbf{R}}} [J_{\mathbf{r}}^* \mu_{\mathbf{P}, \mathbf{R}}^{\Sigma}](A) \quad (\text{C.23})$$

$$= e^{-\gamma_{\mathbf{P}, \mathbf{R}}} \mu_{\mathbf{r}, \mathbf{P}, \mathbf{R}}(A). \quad (\text{C.24})$$

□

The natural measure  $\mu_{\text{nat}}$  is given by  $\mathbf{P}_{\text{nat}} = \mathbf{r} = (r_0, \dots, r_{M-1})$ , i.e., the measure along the unstable direction is the uniform measure  $\nu_{\text{L}}$ , while the distribution along the stable direction is given by the fractal measure  $\nu_{\text{nat}} := \nu_{\mathbf{r}, \mathbf{P}^*}$  with  $P_{\text{nat}, i}^* = R_i r_i \Lambda_{\text{nat}}^{-1}$  and  $\Lambda_{\text{nat}} = \sum_{i=0}^{M-1} R_i r_i$ . Let us remark that this fractal distribution at a given phase-space point  $x$  depends on the backward iterations  $B_{\mathbf{r}}^{-1}$  and is proportional to the accumulated reflectivity  $\prod_{i=1}^n R[M^{-i}(x)]$ , which follows from multiplication of terms  $P_{\text{nat}, j}^*$  as in Eq. (C.17) for  $\mathbf{P}^*$ . This is in accordance to the finite approximation of  $\mu_{\text{nat}}$  as in Eq. (4.33). Recalling Eq. (C.18) it turns out that we

can write

$$\mu_{\text{nat}} = \nu_{\text{L}} \times \nu_{\text{nat}}, \quad (\text{C.25})$$

which is understood for rectangles  $A = A_q \times A_p \subset \mathbb{T}^2$  as  $\mu_{\text{nat}}(A) = \nu_{\text{L}}(A_q) \cdot \nu_{\text{nat}}(A_p)$ . The natural measure  $\mu_{\text{nat}}$  is uniformly distributed along the unstable manifold. Note that the fractal distribution along the stable manifold depends on  $\mathbf{r}$  and on the reflectivity  $\mathbf{R}$ .

Conversely, the inverse measure  $\mu_{\text{inv}}$  is uniform along the stable manifold, such that  $\mathbf{P}_{\text{inv}}^* = \mathbf{r}$ . This implies a fractal distribution  $\nu_{\text{inv}} := \nu_{\mathbf{r}, \mathbf{P}}$  along the unstable manifold determined by  $P_{\text{inv},i} = \frac{r_i}{R_i} \left( \sum_{k=0}^{M-1} \frac{r_k}{R_k} \right)^{-1}$ , such that the eigenvalue is  $\Lambda_{\text{inv}} = \left( \sum_{k=0}^{M-1} \frac{r_k}{R_k} \right)^{-1}$ . The fractal distribution at some phase-space point  $x$  depends on the forward iterates of and is proportional to  $\prod_{i=0}^n R^{-1}[M^i(x)]$ , see Eq. (C.17) and compare with Eq. (4.34). Similar to  $\mu_{\text{nat}}$ , the inverse measure is given by the product of  $\nu_{\text{inv}}$  and  $\nu_{\text{L}}$ ,

$$\mu_{\text{inv}} = \nu_{\text{inv}} \times \nu_{\text{L}}. \quad (\text{C.26})$$

For the product measures  $\mu_{\xi}$  we assumed that their distribution along the unstable direction is determined by the natural measure for the reflection function  $R^{1-\xi}$ , while the distribution along the stable direction is given by the inverse measure obtained for  $R^{\xi}$ . For the baker map with partial escape defined by  $\mathbf{R}$  as above consider  $\mathbf{R}^{\beta} := (R_0^{\beta}, \dots, R_{M-1}^{\beta})$  for  $\beta \in \{\xi, 1 - \xi\}$ . Consider the Bernoulli measure defined by  $\mathbf{P}_{\xi}$  with

$$P_{\xi,i} := P_{\text{nat},i}^{1-\xi} P_{\text{inv},i}^{\xi} \cdot \left( \sum_{k=0}^{M-1} P_{\text{nat},k}^{1-\xi} P_{\text{inv},k}^{\xi} \right)^{-1} = r_i R_i^{-\xi} \left( \sum_{k=0}^{M-1} r_k R_k^{-\xi} \right)^{-1}, \quad (\text{C.27})$$

which corresponds to the product of the weight distributions  $\mathbf{P}_{\text{nat}}(\mathbf{R}^{1-\xi})$  and  $\mathbf{P}_{\text{inv}}(\mathbf{R}^{\xi})$ . This implies that  $\mathbf{P}_{\xi}^*$  is given by

$$P_{\xi,i}^* = R_i P_{\xi,i} \left( \sum_{k=0}^{M-1} R_k P_{\xi,k} \right)^{-1} = \dots = r_i R_i^{1-\xi} \left( \sum_{k=0}^{M-1} r_k R_k^{1-\xi} \right)^{-1}, \quad (\text{C.28})$$

which corresponds to  $P_{\xi,i}^* = (P_{\text{nat},i}^*)^{1-\xi} (P_{\text{inv},i}^*)^{\xi} \cdot \left( \sum_{k=0}^{M-1} (P_{\text{nat},k}^*)^{1-\xi} (P_{\text{inv},k}^*)^{\xi} \right)^{-1}$ , which is the product of the weight distributions  $\mathbf{P}_{\text{nat}}^*(\mathbf{R}^{1-\xi})$  and  $\mathbf{P}_{\text{inv}}^*(\mathbf{R}^{\xi})$ . The corresponding measure  $\mu_{\xi} := \mu_{\mathbf{r}, \mathbf{P}_{\xi}, \mathbf{R}}$  is a conditionally invariant Bernoulli measure as discussed above. Its eigenvalue is thus given by

$$\Lambda_{\xi} = \sum_{i=0}^{M-1} R_i P_{\xi,i} = \frac{\sum_{i=0}^{M-1} r_i R_i^{1-\xi}}{\sum_{k=0}^{M-1} r_k R_k^{-\xi}} \equiv \frac{\Lambda_{\text{nat}}^{\mathbf{R}^{1-\xi}}}{(\Lambda_{\text{inv}}^{\mathbf{R}^{\xi}})^{-1}} \quad (\text{C.29})$$

$$= e^{-\gamma_{\text{inv}}[\mathbf{R}^{\xi}] - \gamma_{\text{nat}}[\mathbf{R}^{1-\xi}]} = e^{-\gamma_{\xi}} \quad (\text{C.30})$$

where the decay rate  $\gamma_\xi = \gamma_{\text{inv}}[\mathbf{R}^\xi] + \gamma_{\text{nat}}[\mathbf{R}^{1-\xi}]$  is given by the sum of natural decay rate using  $\mathbf{R}^{1-\xi}$  and inverse decay rate for  $\mathbf{R}^\xi$ . We emphasize that Eq. (C.28) corresponds to the fractal measures  $\nu_{\text{nat}}^{\mathbf{R}^{1-\xi}}$  along the unstable direction. Similarly Eq. (C.27) corresponds to  $\nu_{\text{inv}}^{\mathbf{R}^\xi}$  along the stable direction on the phase-space. Thus for the generalized baker map with partial escape the product measures  $\mu_\xi$  are exactly of the form

$$\mu_\xi = \nu_{\text{inv}}^{\mathbf{R}^\xi} \times \nu_{\text{nat}}^{\mathbf{R}^{1-\xi}}, \quad (\text{C.31})$$

i.e., the fractal distribution along the stable manifold is characterized by the inverse measure for  $\mathbf{R}^\xi$ , while the fractal distribution along the unstable manifold is characterized by the natural measure obtained for  $\mathbf{R}^{1-\xi}$ . Loosely written this justifies the representation of the product measures as  $\mu_\xi = \mu_{\text{inv}}^{\mathbf{R}^\xi} \times \mu_{\text{nat}}^{\mathbf{R}^{1-\xi}}$ .

Let us emphasize that in general it is possible to construct other c-measures by a similar approach as in Eq. (C.31). However, in the case where escape takes place from a single strip, only, we expect all of these product-like c-measures of the baker map to be the same. Such measures are illustrated for the triadic baker map  $B_3$  and for the asymmetric  $B_r$  with  $\mathbf{r} = (0.25, 0.3, 0.45)$  in Fig. C.1 and Fig. C.2. Let us remark that the measures constructed and

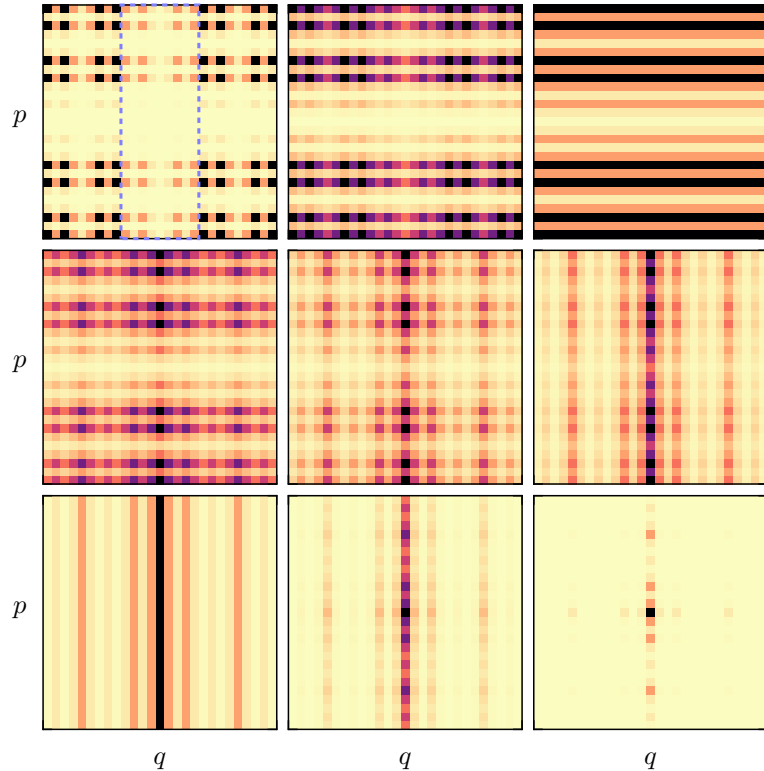


**Figure C.1:** Product measures  $\mu_\xi$  for triadic baker map  $B_3$  with partial escape from the middle strip,  $\mathbf{R} = (1, 0.2, 1)$ , for  $\xi \in \{-1, -0.25, 0, 0.25, 0.5, 0.75, 1, 1.25, 2\}$  (from top left to bottom right). Top right and bottom left panels correspond to  $\gamma_{\text{nat}}$  ( $\xi = 0$ ) and  $\gamma_{\text{inv}}$  ( $\xi = 1$ ), respectively. The number of steps for construction is  $n = 3$ . Dashed blue line indicates the position of the opening  $\Omega$ .

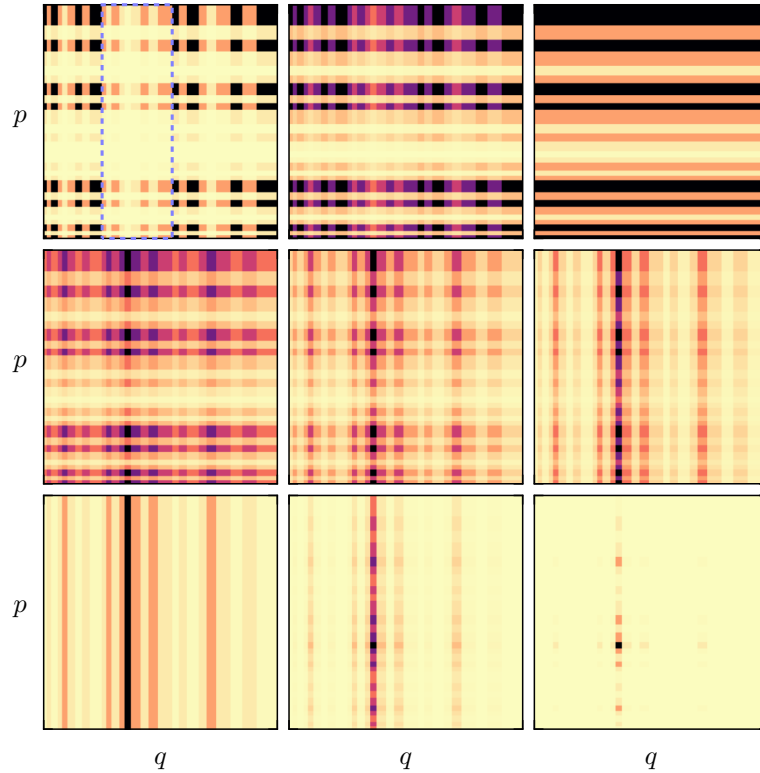


**Figure C.2:** Product measures  $\mu_\xi$  for asymmetric baker map  $B_{\mathbf{r}}$  with  $\mathbf{r} = (0.25, 0.3, 0.45)$  and partial escape from the middle strip,  $\mathbf{R} = (1, 0.2, 1)$ , for  $\xi$  as in Fig. C.1. The number of steps for construction is  $n = 3$ . Dashed blue line indicates the position of the opening  $\Omega$ .

numerically investigated in Ref. [205] for the special case of the triadic baker map with escape from the middle strip as  $\mathbf{R} = (1, \alpha, 1)$  are equivalent to the product measures  $\mu_\xi$  presented here. If full escape from the middle strip is considered,  $\mathbf{R} = (1, 0, 1)$ , these measures are equivalent to the Bernoulli measures discussed in Refs. [60, 213].

### C.3.2 Hyperbolic maps

In this section we motivate that  $\mu_\xi$  is conditionally invariant,  $\mathcal{M}\mu_\xi = e^{-\gamma\xi}\mu_\xi$ , if the considered closed map  $M$  is uniformly hyperbolic. Note that this condition is rather restrictive and is not satisfied by the standard map. The main idea is to use the local decomposition into stable and unstable direction. In this sense, the measures can locally be written as  $\mu_\xi = \mu_{\text{nat}}[R^{1-\xi}] \times \mu_{\text{inv}}[R^\xi]$ , as discussed below. The additional factor  $R$  from the time evolution  $\mathcal{M}$ , see Eq. (2.37), is split into two factors  $R^{1-\xi}$  and  $R^\xi$ , being compensated by the fractal measure along stable and unstable direction, leading to the decay rates  $\gamma_{\text{nat}}[R^{1-\xi}]$  and  $\gamma_{\text{inv}}[R^\xi]$  in Eq. (4.40).

Let  $M$  be hyperbolic. Consider a foliation of the phase space  $\Gamma$  under  $n$  forward and  $m$  backward iterations. This leads to a partition  $\Gamma$  into cells  $C_k$  where the boundary of each cell has stable and unstable manifold segments, see [214] or [137, Sec. 9.5]. If  $n$  and  $m$  are large enough, the cells are approximately parallelograms, each containing a periodic point  $y_k$

of period  $p \leq n + m$ . Lets consider the phase-space density of  $\mu_{\text{nat}}$  and  $\mu_{\text{inv}}$ , which is up to normalization and approximated with a finite number of steps given by

$$\mathcal{B}_m(x) := \prod_{i=1}^m R[M^{-i}(x)], \quad \mathcal{F}_n(x) := \prod_{j=0}^{n-1} R^{-1}[M^j(x)]. \quad (\text{C.32})$$

The reflectivity  $R$  is evaluated at the backward iterates approximating  $\mu_{\text{nat}}$ , and  $R^{-1}$  at the forward iterates, respectively. For all points in  $C_k$  which are on the unstable manifold of the periodic point  $x \in \Gamma_{y_k}^u$ , the distance  $d(M^{-i}(x), M^{-i}(y_k))$  decreases with increasing  $i \in \mathbb{N}$ , such that  $\mathcal{B}_m(x) \approx \mathcal{B}_m(y_k)$ . Similarly for points on the stable manifold  $x \in \Gamma_{y_k}^s$  we obtain  $\mathcal{F}_n(x) \approx \mathcal{F}_n(y_k)$ .

For each of the cells  $C_k$  there exists a local coordinate transformation  $h_k : \Gamma \rightarrow \mathbb{R}^2$  from the phase-space to the tangential space, such that the parallelogram  $C_k$  is mapped onto a rectangle as follows. Let the periodic point be mapped onto the origin,  $h_k(y_k) = (0, 0)$ , and its unstable and stable manifolds onto first and second coordinate, respectively. Thus, for all  $x \in \Gamma_{y_k}^u$  we have  $h_k(x) = (x_u, 0)$  and for all  $x \in \Gamma_{y_k}^s$  we have  $h_k(x) = (0, x_s)$  for some  $x_s, x_u \in \mathbb{R}$ . Last but not least  $h_k$  is assumed to preserve the volume between the phase space  $\Gamma$  and  $\mathbb{R}^2$  as  $\mu_L(C_k) = \mu_L(h_k(C_k))$ .

From the considerations above, the mapping  $\mathcal{B}_n \circ h_k^{-1}(0, x_u) \approx \mathcal{B}_n(y_k)$  is constant along the first coordinate, while  $\mathcal{F}_m \circ h_k^{-1}(x_s, 0) \approx \mathcal{F}_m(y_k)$  is constant along the second coordinate. Let  $h_k(C_k) = I_u \times I_s$  for some intervals  $I_{u,s} \subset \mathbb{R}$ . The previous considerations motivate, that the natural measure can be written as

$$\mu_{\text{nat}} = \nu_L \times \nu_{\text{nat}}, \quad (\text{C.33})$$

$$\mu_{\text{nat}}(C_k) = \nu_L \times \nu_{\text{nat}}[h_k(C_k)] = \int_{I_u} dx_u \cdot \int_{I_s} d\nu_{\text{nat}} = |I_u| \int_{I_s} d\nu_{\text{nat}} \quad (\text{C.34})$$

while the inverse measure on  $C_k$  can be written as

$$\mu_{\text{inv}} = \nu_{\text{inv}} \times \nu_L, \quad (\text{C.35})$$

$$\mu_{\text{inv}}(C_k) = \nu_{\text{inv}} \times \nu_L[h_k(C_k)] = \int_{I_u} d\nu_{\text{inv}} \cdot \int_{I_s} dx_s = |I_s| \int_{I_u} d\nu_{\text{inv}} \quad (\text{C.36})$$

similar to the baker map, Sec. C.3.1. Since the map  $M$  is volume preserving the preimage of  $C_k$  is compressed in the unstable, and stretched along the stable direction of  $y_k$  by a factor  $e^{-\lambda_{y_k}}$ , such that  $h_{k-1}(M^{-1}(C_k)) = e^{-\lambda_{y_k}} I_u \times e^{\lambda_{y_k}} I_s$ . Equations C.33 and C.35 are thus related

to conditional invariance of  $\mu_{\text{nat}}$  and  $\mu_{\text{inv}}$  as follows,

$$e^{-\gamma_{\text{nat}}} \mu_{\text{nat}}(C_k) = \mathcal{M} \mu_{\text{nat}}(C_k) = R[M^{-1}(y_k)] \cdot \nu_{\text{L}} \times \nu_{\text{nat}}[h_{k-1}(M^{-1}(C_k))] \quad (\text{C.37})$$

$$= R[M^{-1}(y_k)] \cdot e^{-\lambda y_k} |I_{\text{u}}| \cdot \int_{e^{\lambda y_k} I_{\text{s}}} d\nu_{\text{nat}}, \quad (\text{C.38})$$

and

$$e^{-\gamma_{\text{inv}}} \mu_{\text{inv}}(C_k) = \mathcal{M} \mu_{\text{inv}}(C_k) = R[M^{-1}(y_k)] \cdot \nu_{\text{inv}} \times \nu_{\text{L}}[h_{k-1}(M^{-1}(C_k))] \quad (\text{C.39})$$

$$= R[M^{-1}(y_k)] \cdot e^{\lambda y_k} |I_{\text{s}}| \int_{e^{-\lambda y_k} I_{\text{u}}} d\nu_{\text{inv}}. \quad (\text{C.40})$$

This allows to define the product measure  $\mu_{\xi}$  on the sets  $C_k$  as

$$\mu_{\xi} := \nu_{\text{inv}}[R^{\xi}] \times \nu_{\text{nat}}[R^{1-\xi}]. \quad (\text{C.41})$$

Applying the map with escape to this measure yields

$$\mathcal{M} \mu_{\xi}(C_k) = R[M^{-1}(y_k)] \cdot \int_{e^{-\lambda y_k} I_{\text{u}}} d\nu_{\text{inv}}[R^{\xi}] \cdot \int_{e^{\lambda y_k} I_{\text{s}}} d\nu_{\text{nat}}[R^{1-\xi}] \quad (\text{C.42})$$

$$= \underbrace{R^{\xi}[M^{-1}(y_k)] \int_{e^{-\lambda y_k} I_{\text{u}}} d\nu_{\text{inv}}[R^{\xi}]}_{=e^{-\gamma_{\text{inv}}[R^{\xi}]} \cdot \int_{I_{\text{u}}} d\nu_{\text{inv}}[R^{\xi}] \cdot e^{-\lambda y_k}} \cdot \underbrace{R^{1-\xi}[M^{-1}(y_k)] \int_{e^{\lambda y_k} I_{\text{s}}} d\nu_{\text{nat}}[R^{1-\xi}]}_{=e^{-\gamma_{\text{nat}}[R^{1-\xi}]} \cdot \int_{I_{\text{s}}} d\nu_{\text{nat}}[R^{1-\xi}] \cdot e^{\lambda y_k}} \quad (\text{C.43})$$

$$= e^{-(\gamma_{\text{inv}}[R^{\xi}] + \gamma_{\text{nat}}[R^{1-\xi}])} \cdot \mu_{\xi}(C_k), \quad (\text{C.44})$$

such that the measure  $\mu_{\xi}$  is conditionally invariant on the sets  $C_k$  with decay rate  $\gamma_{\xi} := \gamma_{\text{inv}}[R^{\xi}] + \gamma_{\text{nat}}[R^{1-\xi}]$ . We emphasize that this is not a rigorous proof. However, we find strong numerical evidence presented in Sec. C.3.3 that the approximation of the product measures  $\mu_{\xi}$  for finite time steps  $n$ , Eq. (4.42), converge weakly to conditional invariant measures for  $n \rightarrow \infty$ .

### C.3.3 Construction and convergence of product measures

In this section we present, how the product measures  $\mu_{\xi}$  are approximated numerically for chaotic maps with escape  $\mathcal{M}$ . We further check numerically their convergence depending on the construction parameters. These considerations are taken from Ref. [97].

**Numerical construction** First, consider a fixed number  $n$  of time steps for the approximation  $\tilde{\mu}_{\xi}^n$ , see Eq. (4.42). Secondly, select a set  $X_c$  of  $N_c$  initial conditions is selected. These initial conditions can be chosen randomly uniform on  $\Gamma$ . In this thesis we consider a  $\sqrt{N_c} \times \sqrt{N_c}$  grid of phase-space points, such that the distance to the next nearest point is given by  $1/\sqrt{N_c}$ .



This distance defines the minimal classical resolution for some subset of interest  $A \subset \Gamma$ . The typical scale of  $A$ , e.g., its diameter, should be much larger than  $1/\sqrt{N_c}$ , such that the number of initial points within  $A$  is much larger than one,  $|X_c \cap A| \gg 1$ . In particular, for comparison with quantum mechanics this implies the condition  $1/\sqrt{N_c} \ll \sqrt{\hbar}$ . For each grid point  $x \in X_c$  we compute the orbit  $\{M^k(x)\}_{k=-n}^{n-1}$ , which is used in Eq. (4.42) and end with the sum of all contributions of points  $x \in X_c \cap A$ ,

$$\tilde{\mu}_\xi^n(A) \approx \frac{1}{|X_c \cap A|} \sum_{x \in X_c \cap A} \prod_{i=1}^n R^{1-\xi}[M^{-i}(x)] \prod_{j=0}^{n-1} R^{-\xi}[M^j(x)]. \quad (\text{C.45})$$

Finally, this measure is normalized with  $\|\tilde{\mu}_\xi^n\| = \tilde{\mu}_\xi^n(\Gamma)$ . We stress that fixing the number of steps  $n$  and increasing  $N_c$  improves the approximation of  $\tilde{\mu}_\xi^n$ . On the other hand, for a fixed number of initial conditions  $N_c$  the number of construction steps  $n$  obtains an optimal value due to the smallest spacing of sampling points, discussed in detail in Ref. [197].

**Convergence of construction** In the following we report properties of the classical measures regarding their conditional invariance, their convergence with  $n$ , and the accuracy of the classical construction used in this paper. This is illustrated in Figs. C.3 and C.4 for  $N_c = 8192^2$  initial phase-space points. Conditional invariance is investigated with the Jensen–Shannon divergence  $d_{\text{JS}}$  between approximation  $\mu_\xi^n$  and its normalized iterate  $\mathcal{M}\mu_\xi^n/\|\mathcal{M}\mu_\xi^n\|$ , see Fig. C.3(a). Increasing values of  $n$  lead to a decreasing  $d_{\text{JS}}$  for all considered values of  $\xi \in \{0, 0.3, 0.5, 0.7, 1\}$ , up to a maximal number  $\tilde{n}$ . Thus  $\mu_\xi^n$  satisfies conditional invariance, Eq. (2.54), with increasing  $n$ . The limiting construction time step  $\tilde{n}$  can be explained by the finite phase-space resolution due to the fixed number of points  $N_c$ . Secondly, we numerically

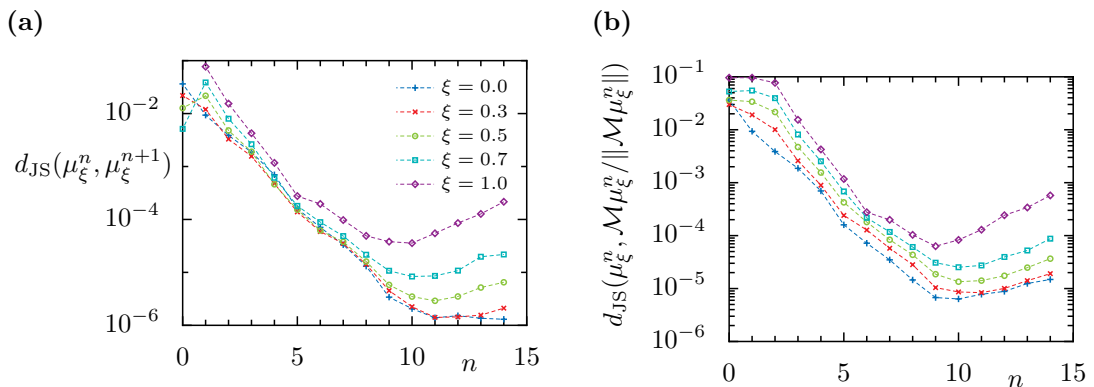


**Figure C.3:** Numerical estimation of conditional invariance and convergence for classical construction of product measures  $\mu_\xi$  for fixed number of initial conditions  $N_c = 8192^2$ . (a) Shown is the Jensen–Shannon divergence  $d_{\text{JS}}(\mu_\xi^n, \mu_\xi^{n+1})$  with  $\epsilon = 1/16$ , see Eq. (4.51), between numerical constructions with increasing number of time-steps  $n$  as a function of the number of construction time steps  $n$  for  $\xi \in \{0, 0.3, 0.5, 0.7, 1\}$ . (b) Considered is  $d_{\text{JS}}$  between  $\mu_\xi^n$  and its normalized iterate  $\mathcal{M}\mu_\xi^n/\|\mathcal{M}\mu_\xi^n\|$  over number of time-steps  $n$  for same  $\xi$  as in (a).

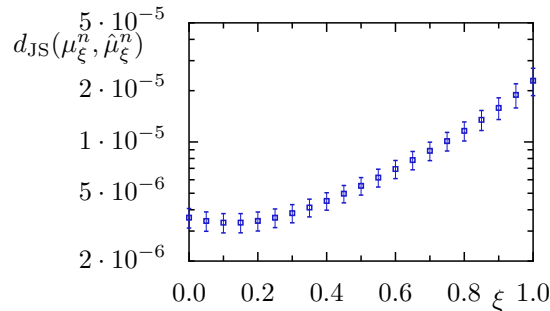


**Figure C.4:** Numerical estimation of accuracy for classical construction of product measures  $\mu_\xi$  for fixed number of initial conditions  $N_c = 8192^2$ . Shown is the average Jensen–Shannon divergence of  $d_{\text{JS}}(\mu_\xi^n, \hat{\mu}_\xi^n)$  with  $\epsilon = 1/16$ , see Eq. (4.51), and the standard deviation between  $\mu_\xi^n$  and 10 different realizations of  $\hat{\mu}_\xi^n$  with random-uniform initial points on  $\Gamma$  for fixed  $n = 8$ .

show that  $d_{\text{JS}}(\mu_\xi^n, \mu_\xi^{n+1})$  decreases with  $n$  for all considered  $\xi$ , see Fig. C.3(b). This indicates weak convergence of  $\mu_\xi^n$ . The same restrictions due to finite  $N_c$  apply here. Based on these results we use  $\mu_\xi^n$  with  $n = 8$  as an approximation for  $\mu_\xi$  throughout the paper.

Moreover, we calculate the Jensen–Shannon divergence  $d_{\text{JS}}$  between two different numerical approximations, first  $\mu_\xi^n$  defined above with  $N_c$  grid-points (which is used in this thesis), and second  $\hat{\mu}_\xi^n$  with  $N_c$  random-uniform initial conditions. This allows to numerically test the magnitude of classical fluctuations due to the finite sample size. The results are presented in Fig. C.4, where the average of the distances  $d_{\text{JS}}(\mu_\xi^n, \hat{\mu}_\xi^n)$  is shown as a function of  $\xi$  for 10 realizations of the random-uniform initial distributions. Additionally the corresponding standard deviation for the considered realizations is shown. We observe that for  $\xi = 0$  (i.e., at  $\gamma_{\text{nat}}$ ) the accuracy is nearly one magnitude smaller than for  $\xi = 1$  ( $\gamma_{\text{inv}}$ ), and that the dependence is continuous. In all cases the errors are much smaller than the quantum-to-classical distances investigated in Sec. 4.4.3.

## C.4 Conditional invariance of periodic orbit measures

In the following we prove that the measures  $\mu_{\underline{p}}$  defined in Eq. (4.47) for any periodic orbit  $\underline{p} = \{y_i\}_{i=0}^{p-1}$  of length  $|\underline{p}| = p$  are conditionally invariant with decay rate  $\gamma_{\underline{p}} = -\frac{1}{p} \sum_{j=0}^{p-1} \ln R_j$ , where all  $y_i \in \Gamma$  and  $R_i = R(y_i)$ . Recall the definition

$$\mu_{\underline{p}}(A) := \frac{1}{C} \sum_{i=0}^{p-1} c_i \delta_{y_i}, \quad \text{with} \quad c_i = \left( \prod_{j=0}^{p-1} R_j^{(j-i) \bmod p} \right)^{1/p}, \quad (4.47)$$

where for all  $k \in \mathbb{N}$  we have  $-k \bmod p = (p - k) \bmod p$ , e.g.,  $-1 \bmod p = p - 1$ .

*Proof conditional invariance.* In order to prove conditional invariance we want to show that

for any measurable  $A \subset \Gamma$

$$\mathcal{M} \left( \sum_{i=0}^{p-1} c_i \delta_{y_i}(A) \right) = \sum_{i=0}^{p-1} c_i R_i \delta_{y_{(i+1) \bmod p}}(A) \stackrel{!}{=} e^{-\gamma \underline{p}} \sum_{i=0}^{p-1} c_i \delta_{y_i}(A). \quad (\text{C.46})$$

Therefore it is sufficient to show that  $c_i R_i = e^{-\gamma \underline{p}} c_{i+1}$  for all  $i < p-1$  and  $c_{p-1} R_{p-1} = e^{-\gamma \underline{p}} c_0$ .

We obtain for  $i < p-1$

$$c_i R_i = \left( R_i^p \prod_{j=0}^{p-1} R_j^{(j-i) \bmod p} \right)^{1/p} = \left( R_i^p \prod_{k=0}^{p-1} R_k \prod_{j=0}^{p-1} R_j^{[(j-i) \bmod p]-1} \right)^{1/p} \quad (\text{C.47})$$

$$= \underbrace{\prod_{k=0}^{p-1} R_k^{1/p}}_{=e^{-\gamma \underline{p}}} \left( R_i^p \prod_{\substack{j=0 \\ j \neq i}}^{p-1} R_j^{(j-[i+1]) \bmod p} \cdot R_i^{-1} \right)^{1/p} = e^{-\gamma \underline{p}} \left( \prod_{j=0}^{p-1} R_j^{(j-[i+1]) \bmod p} \right)^{1/p}, \quad (\text{C.48})$$

$$= e^{-\gamma \underline{p}} c_{i+1}, \quad (\text{C.49})$$

where for  $j \neq i$  we used  $[(j-i) \bmod p] - 1 = (j - [i+1]) \bmod p$ . The equivalent relation for  $i = p-1$  is shown similarly. This proves that  $\mu_p$  is a c-measure of  $\mathcal{M}$ .  $\square$

*Proof of uniqueness.* In order to see that there exists only one c-measure for any given periodic orbit consider the following sets of linear equations for the normalized coefficients  $c_i/C$  (which we will call  $c_i$  again in the following). We have for  $0 \leq i < p-1$  that  $c_i R_i = \Lambda_{\underline{p}} c_{i+1}$  with  $\Lambda_{\underline{p}} := e^{-\gamma \underline{p}} = \prod_{i=0}^{p-1} R_i^{1/p}$ . Note that  $\Lambda_{\underline{p}}$  cannot be chosen freely, as  $p$ -fold application of the map with escape leads to this factor (to the power of  $p$ ) for each of the points on the considered periodic orbit. We first show, that this already implies that  $c_{p-1} R_{p-1} = \Lambda_{\underline{p}} c_0$ ,

$$\Lambda_{\underline{p}} c_0 = \frac{\Lambda_{\underline{p}}^2 c_1}{R_0} = \frac{\Lambda_{\underline{p}}^3 c_2}{R_0 R_1} = \dots = \frac{\Lambda_{\underline{p}}^p c_{p-1}}{\prod_{i=0}^{p-2} R_i} = \frac{\prod_{i=0}^{p-1} R_i c_{p-1}}{\prod_{i=0}^{p-2} R_i} = R_{p-1} c_{p-1}, \quad (\text{C.50})$$

so that we remove this condition from the linear system of equations. Together with the normalization  $\sum_{i=0}^{p-1} c_i = 1$  we obtain the linear equation

$$\underline{K} \cdot \underline{c} := \begin{pmatrix} R_0 & -\Lambda_{\underline{p}} & 0 & \dots & & \\ 0 & R_1 & -\Lambda_{\underline{p}} & 0 & \dots & \\ 0 & 0 & R_2 & -\Lambda_{\underline{p}} & 0 & \dots \\ \vdots & & & \ddots & \ddots & \\ 0 & \dots & & 0 & R_{p-2} & -\Lambda_{\underline{p}} \\ 1 & \dots & & 1 & 1 & \mathbf{1} \end{pmatrix} \cdot \begin{pmatrix} c_0 \\ c_1 \\ c_2 \\ \vdots \\ c_{p-2} \\ c_{p-1} \end{pmatrix} = \begin{pmatrix} 0 \\ 0 \\ 0 \\ \vdots \\ 0 \\ 1 \end{pmatrix}, \quad (\text{C.51})$$

implicitly defining the coefficient matrix  $\underline{K}$ . This equation has exactly one solution, if the

determinant of the matrix satisfies  $\det(\underline{K}) \neq 0$ . Evaluation of the determinant with Laplace's formula applied to the last column of the matrix (highlighted in red) gives using that  $\underline{K}$  is  $p$ -dimensional

$$\det(\underline{K}) = (-1)^{p+p} \cdot \mathbf{1} \cdot \det \begin{pmatrix} R_0 & -\Lambda_{\underline{p}} & 0 & \dots & \\ 0 & R_1 & -\Lambda_{\underline{p}} & 0 & \dots \\ \vdots & & \ddots & \ddots & \\ 0 & & 0 & R_{p-3} & -\Lambda_{\underline{p}} \\ 0 & \dots & & 0 & R_{p-2} \end{pmatrix} \quad (\text{C.52})$$

$$+ \underbrace{(-1)^{p+(p-1)}}_{=-1} \cdot (-\Lambda_{\underline{p}}) \cdot \det \begin{pmatrix} R_0 & -\Lambda_{\underline{p}} & 0 & \dots & \\ 0 & R_1 & -\Lambda_{\underline{p}} & 0 & \dots \\ \vdots & & \ddots & \ddots & \\ 0 & \dots & 0 & R_{p-3} & -\Lambda_{\underline{p}} \\ 1 & \dots & & 1 & 1 \end{pmatrix} \quad (\text{C.53})$$

$$= \prod_{i=0}^{p-2} R_i + \Lambda_{\underline{p}} \cdot \det \underbrace{\begin{pmatrix} R_0 & -\Lambda_{\underline{p}} & 0 & \dots & \\ 0 & R_1 & -\Lambda_{\underline{p}} & 0 & \dots \\ \vdots & & \ddots & \ddots & \\ 0 & \dots & 0 & R_{p-3} & -\Lambda_{\underline{p}} \\ 1 & \dots & & 1 & \mathbf{1} \end{pmatrix}}_{:=\underline{K}_{p-1}} \quad (\text{C.54})$$

Thus we iteratively by obtain similarly defining  $\underline{K}_{p-n}$

$$\det(\underline{K}) = \prod_{i=0}^{p-2} R_i + \Lambda_{\underline{p}} \cdot \left( \prod_{i=0}^{p-3} R_i + \Lambda_{\underline{p}} \cdot \det(\underline{K}_{p-2}) \right) \quad (\text{C.55})$$

$$= \prod_{i=0}^{p-2} R_i + \Lambda_{\underline{p}} \prod_{i=0}^{p-3} R_i + \Lambda_{\underline{p}}^2 \cdot \left( \prod_{i=0}^{p-4} R_i + \det(\underline{K}_{p-3}) \right) \quad (\text{C.56})$$

$$= \dots = \sum_{j=1}^{p-1} \Lambda_{\underline{p}}^{j-1} \prod_{i=0}^{p-1-j} R_i + \Lambda_{\underline{p}}^{p-1}, \quad (\text{C.57})$$

which satisfies  $\det(\underline{K}) > 0$  if all  $R_i > 0$ . This is the case for all strictly positive reflection functions  $R > 0$ . Thus for any periodic orbit, there exists only one c-measure, defined by the solution of Eq. (C.52). This solution is given in Eq. (4.47).  $\square$

## C.5 Measures on arbitrary orbits

In order to approximate the typical measure defined in Eq. (4.52) we consider arbitrary orbits instead of periodic orbits in the following. Consider the orbit  $\mathbf{y} = \{y_i\}_{i=-\infty}^{\infty}$  of all (forward and backward) iterations  $y_i = M^i(y_0)$  of some initial point  $y_0$ . Let  $R_i := R(y_i)$  for all  $i \in \mathbb{Z}$ . For the finite subset  $\mathbf{y}_n := \{y_{-n}, \dots, y_{-1}, y_0, y_1, \dots, y_{n-1}\}$  of  $n$  backward and forward iterates of  $y_0$  with length  $2n$  define a measure in analogy to periodic orbits, Eq. (4.47),

$$\mu_{[\mathbf{y},n]} = 1/C \sum_{i=-n}^{n-1} c_{n,i} \delta_{y_i} \quad \text{with} \quad (C.58)$$

$$c_{n,i} := \prod_{k=-n}^{i-1} R_k \prod_{j=-n}^{n-1} R_j^{\frac{j-i}{2n}} = \prod_{j=-n}^{n-1} R_j^{\frac{(j-i) \bmod (2n)}{2n}}, \quad (C.59)$$

where  $C = \sum_{i=-n}^{n-1} c_{n,i}$  normalizes the measure. Before discussing their conditional invariance in the limit of large  $n$  in Sec. C.5.2, consider the average decay of such an orbit,

$$\gamma_{\mathbf{y}} = - \lim_{n \rightarrow \infty} \ln \prod_{k=-n}^{n-1} R_k^{\frac{1}{2n}} \quad (C.60)$$

$$= - \lim_{n \rightarrow \infty} \frac{1}{2n} \sum_{k=-n}^{n-1} \ln R(M^k(y_0)) \stackrel{(2.29)}{=} - \int_{\Gamma} \ln R d\mu_L = \gamma_{\text{typ}}, \quad (C.61)$$

which is given by the typical decay rate for almost all initial conditions, see Eq. (2.67) and [89]. Hence, averaging over many initial conditions, these measures could be used to construct an approximation to the measure  $\mu_{\text{typ}}$ , defined in Eq. (4.52).

### C.5.1 Approximation for typical measure

Consider the measures  $\mu_{\mathbf{y}}$  for many initial conditions on the phase space, such that each of these measures decays with rate  $\gamma_{\text{typ}}$ . If these initial conditions are distributed uniformly it is sufficient to consider the contribution at the initial point  $y_0$  for each of these measures. Taking their average still gives a classical measure with decay rate  $\gamma_{\text{typ}}$ . The numerical simplest implementation is achieved by taking a finite sample  $X_c$  of initial conditions uniformly on the phase space  $\Gamma$  and considering  $\mu_{[\mathbf{y},n]}$  restricted to the initial point  $y_0$  for a finite number of time steps  $n$ . The resulting measure is determined by

$$\mu_{\text{typ}}^{\{n, X_c\}}(A) = \frac{1}{|X_c|} \sum_{y_0 \in X_c \cap A} \frac{c_{n,y_0}}{C_{[\mathbf{y},n]}}. \quad (C.62)$$

Establishing the relation to the measure conjectured in Eq. (4.52) is an interesting task which remains for future research.

### C.5.2 Conditional invariance

By definition, as for the periodic orbits, we obtain for all  $-n \leq i \leq n-1$

$$c_{n,i} R_i = e^{-\gamma[\mathbf{y},n]} c_{n,i+1}, \quad \text{where} \quad e^{-\gamma[\mathbf{y},n]} := \prod_{k=-n}^{n-1} R_k^{\frac{1}{2^n}}. \quad (\text{C.63})$$

Thus we get

$$\mathcal{M}\mu_{[\mathbf{y},n]} = 1/C_n \sum_{i=-n}^{n-1} c_{n,i} R_i \delta_{y_{i+1}} = 1/C_n \sum_{i=-n}^{n-1} e^{-\gamma[\mathbf{y},n]} c_{n,i+1} \delta_{y_{i+1}} \quad (\text{C.64})$$

$$= e^{-\gamma[\mathbf{y},n]} / C_n \left( \sum_{i=-n+1}^{n-1} c_{n,i} \delta_{y_i} + c_{n,n} \delta_{y_n} + c_{n,-n} \delta_{y_{-n}} - c_{n,-n} \delta_{y_{-n}} \right) \quad (\text{C.65})$$

$$= e^{-\gamma[\mathbf{y},n]} \mu_{[\mathbf{y},n]} + e^{-\gamma[\mathbf{y},n]} (c_{n,n} \delta_{y_n} - c_{n,-n} \delta_{y_{-n}}) / C_n, \quad (\text{C.66})$$

which is not conditionally invariant due to the terms  $c_{n,\pm n}/C_n$ . These terms come from the end points  $y_{-n}$  and  $y_n$  of the finite orbit. In order to show that the limit  $\mu_{\mathbf{y}} = \lim_{n \rightarrow \infty} \mu_{[\mathbf{y},n]}$  is conditionally invariant, it is necessary to show that  $\lim_{n \rightarrow \infty} c_{n,\pm n}/C_n = 0$ . Note that for a periodic orbit with length  $2n$  the endpoints coincide,  $y_{-n} = y_n$ , and both terms cancel each other.

In order to show the convergence recall the coefficients  $c_{n,i} = \prod_{k=-n}^{i-1} R_k \prod_{j=-n}^{n-1} R_j^{\frac{j-i}{2^n}}$ . In order to simplify the calculation we divide each coefficient with the global factor  $\tilde{c} = \prod_{j=-n}^{n-1} R_j^{\frac{1}{2} + \frac{j}{2^n}}$  and obtain the rescaled coefficients

$$a_{n,i} := c_{n,i} / \tilde{c} = \prod_{k=-n}^{i-1} R_k \prod_{j=-n}^{n-1} R_j^{\frac{-i}{2^n}} \prod_{j=-n}^{n-1} R_j^{-\frac{1}{2}} = \prod_{k=-n}^{i-1} R_k^{\frac{1}{2}} \prod_{j=-n}^{n-1} R_j^{\frac{-i}{2^n}} \prod_{k=i}^{n-1} R_k^{-\frac{1}{2}}. \quad (\text{C.67})$$

For  $i = -n$  and  $i = n$  we get

$$a_{n,-n} = \prod_{j=-n}^{n-1} R_j^{\frac{n}{2^n}} \prod_{k=-n}^{n-1} R_k^{-\frac{1}{2}} = 1 \quad \text{and} \quad a_{n,n} = \prod_{k=-n}^{n-1} R_k^{\frac{1}{2}} \prod_{j=-n}^{n-1} R_j^{\frac{-n}{2^n}} = 1, \quad (\text{C.68})$$

respectively. Hence, in order to achieve conditional invariance it is sufficient to show that  $\lim_{n \rightarrow \infty} 1/A_n = 0$  with the rescaled normalization factor

$$A_n = \sum_{i=-n}^{n-1} a_{n,i} = \sum_{i=-n}^{n-1} \prod_{k=-n}^{i-1} R_k \prod_{j=-n}^{n-1} R_j^{-\frac{i+n}{2^n}} = \sum_{i=0}^{2n-1} \left( \prod_{k=0}^{i-1} R_k^{\frac{1}{2}} \right)^i \left( \prod_{j=0}^{2n-1} R_j^{\frac{1}{2^n}} \right)^{-i} \quad (\text{C.69})$$

$$= \sum_{i=0}^{2n-1} \left( \frac{\langle \{R_k\}_{k=-n}^{i-n} \rangle_{\text{geom}}}{\langle \{R_k\}_{k=-n}^{n-1} \rangle_{\text{geom}}} \right)^i, \quad (\text{C.70})$$

where an index shift is used in the third equality. In the last step the geometric mean  $\langle \cdot \rangle_{\text{geom}}$  of a finite set is applied to the two products. This sum itself looks similar to a geometric sequence  $\sum_{i=0}^{2n-1} r^i$ , which diverges for  $r \geq 1$ . However,  $r$  is not constant here, but depends on  $i$ . Thus  $1/A_n \rightarrow 0$  if the number of summands with  $\frac{\langle \{R_k\}_{k=-n}^{i-n} \rangle_{\text{geom}}}{\langle \{R_k\}_{k=-n}^{n-1} \rangle_{\text{geom}}} > 1$  grows with  $n$ .

As an example consider the case that all  $R_k = \alpha$  for some  $\alpha$ . Then the geometric mean of these  $\{R_k\}$  equals  $\alpha$  in both cases, such that  $1/A_n = 1/\sum_{i=0}^{2n-1} 1 = (2n)^{-1} \rightarrow 0$ . In general this is not satisfied. However, ergodicity implies that for almost all initial conditions the orbit encounters every phase-space region proportional to its size. This means that the average decay rate of almost all orbits converges to  $\gamma_{\text{typ}} = -\int_{\Gamma} \ln R d\mu_L$ . For example, if  $R(x \in \Omega) = R_\Omega$  and  $R(x \notin \Omega) = 1$ , the probability  $P(R_k = R_\Omega) = \mu_L(\Omega)$  and  $P(R_k = 1) = 1 - \mu_L(\Omega)$  for arbitrary long orbits. Intuitively this leads to divergence of  $A_n$  with increasing  $n$  (as the geometric means are of the same order for large  $i$ ), and we are able to numerically support this statement (not shown), even though a rigorous proof cannot be given.

Because the considered system is chaotic it is reasonable to apply these results to (typical) arbitrary long orbits. In conclusion, if the number of iterations  $n \rightarrow \infty$  we expect

$$\|\mathcal{M}\mu_{[\mathbf{y},n]} - e^{-\gamma[\mathbf{y},n]}\mu_{[\mathbf{y},n]}\| = e^{-\gamma[\mathbf{y},n]}\|(\delta_{y_n} - \delta_{y_{-n}})/A_n\| \quad (\text{C.71})$$

$$\leq e^{-\gamma[\mathbf{y},n]} \left( \|\delta_{y_n}\| + \|\delta_{y_{-n}}\| \right) \cdot |1/A_n| \quad (\text{C.72})$$

$$= 2e^{-\gamma[\mathbf{y},n]}/A_n \xrightarrow{n \rightarrow \infty} 0, \quad (\text{C.73})$$

which means that for any  $\mathbf{y}$  the measure  $\mu_{[\mathbf{y},n]}$  converges to a c-measure of the map with partial escape  $\mathcal{M}$  with decay rate  $\gamma = -\lim_{n \rightarrow \infty} \frac{1}{2n} \ln \prod_{k=-n}^{n-1} R_k = \gamma_{\text{typ}}$ , which is the typical decay rate, see Eq. (2.67) and Ref. [89].

## C.6 Full escape

### C.6.1 Convergence of quantum map in limit of full escape

In the following we show that the quantum propagator for partial escape converges in the limit of full escape to the corresponding propagator in operator norm. Consider for fixed  $N$  the operators  $R_\alpha$ ,  $\mathcal{R}_\alpha$ ,  $\mathcal{U}_\alpha$  and  $\mathcal{U}_0$  as in Sec. 5.1.1. The statement

$$\lim_{\alpha \rightarrow 0} \|\mathcal{U}_{\alpha,N} - \mathcal{U}_{0,N}\|_\infty = 0. \quad (5.3)$$

The statement follows directly from

$$\|\mathcal{U}_\alpha - \mathcal{U}_0\|_\infty = \|\tilde{\mathcal{U}}(\mathcal{R}_\alpha - \mathcal{R}_0)\|_\infty = \|\tilde{\mathcal{U}}\|_\infty \|\mathcal{R}_\alpha - \mathcal{R}_0\|_\infty = \|\mathcal{R}_\alpha - \mathcal{R}_0\|_\infty \quad (C.74)$$

and from

$$\lim_{\alpha \rightarrow 0} \|\mathcal{R}_\alpha - \mathcal{R}_0\|_\infty = 0 \quad (C.75)$$

with operator norm  $\|\cdot\|_\infty$ , and where  $\{R_\alpha\}_{\alpha \in \mathbb{R}_+}$  is a set of reflection functions such that  $\lim_{\alpha \rightarrow 0} R_\alpha = R_0 := 1 - \mathbb{1}_\Omega$  converges uniformly.

Equation (C.75) is shown as follows. For fixed  $N$  let  $\mathcal{R}_\alpha = \text{Op}\sqrt{R_\alpha}$  denote the anti-Wick quantization of the reflection operator of  $R_\alpha$ . Then

$$\lim_{\alpha \rightarrow 0} \|\mathcal{R}_\alpha - \mathcal{R}_0\|_\infty = \lim_{\alpha \rightarrow 0} \sup_{\psi \in \mathbb{H}_N, \|\psi\| \leq 1} \|\mathcal{R}_\alpha \psi - \mathcal{R}_0 \psi\|_{\mathbb{H}_N} \quad (C.76)$$

$$= \lim_{\alpha \rightarrow 0} \sup_{\psi \in \mathbb{H}_N, \|\psi\| \leq 1} \|(\text{Op}\sqrt{R_\alpha} - \text{Op}\sqrt{R_0})\psi\|_{\mathbb{H}_N} \quad (C.77)$$

$$= \lim_{\alpha \rightarrow 0} \sup_{\psi \in \mathbb{H}_N, \|\psi\| \leq 1} \left\| \left( \int \sqrt{R_\alpha(x)} |x\rangle \langle x| dx - \int \sqrt{R_0(x)} |x\rangle \langle x| dx \right) \psi \right\|_{\mathbb{H}_N} \quad (C.78)$$

$$= \lim_{\alpha \rightarrow 0} \sup_{\psi \in \mathbb{H}_N, \|\psi\| \leq 1} \left\| \underbrace{\int \left[ \sqrt{R_\alpha(x)} - \sqrt{R_0(x)} \right] |x\rangle \langle x| dx}_{\leq \|\sqrt{R_\alpha} - \sqrt{R_0}\|_\infty} \psi \right\|_{\mathbb{H}_N} \quad (C.79)$$

$$\leq \lim_{\alpha \rightarrow 0} \|\sqrt{R_\alpha} - \sqrt{R_0}\|_\infty \sup_{\psi \in \mathbb{H}_N, \|\psi\| \leq 1} \underbrace{\left\| \int |x\rangle \langle x| dx \right\|_{\mathbb{H}_N}}_{=1} \quad (C.80)$$

$$\leq \lim_{\alpha \rightarrow 0} \|\sqrt{R_\alpha} - \sqrt{R_0}\|_\infty = 0, \quad (C.81)$$

where the last equality follows from uniform convergence of  $R_\alpha$ , and continuity of the square root.



### C.6.2 Scaling of $\gamma$ -interval for fixed number of states

Here we show that the interval in  $\gamma$  used for calculation of the average distribution for a fixed number of resonances  $S$  scales as  $\Delta_\gamma \sim h^{D_0(\Gamma_s)/2}$ . The fractal Weyl law, discussed in Sec. 5.1.2 states that the number of resonance states with decay rate  $\gamma < \gamma_c$  grows asymptotically with  $h$  like, Eq. (5.6),

$$n_{\text{res}}(\gamma_c) \sim s(\gamma_c) \cdot h^{-D_0(\Gamma_s)/2}. \quad (\text{C.82})$$

The derivative of  $n_{\text{res}}$  with respect to  $\gamma$  can be expressed as

$$\frac{d}{d\gamma} n_{\text{res}}(\gamma) = \frac{d}{d\gamma} s(\gamma) \cdot h^{-D_0(\Gamma_s)/2} = s'(\gamma) \cdot h^{-D_0(\Gamma_s)/2} \quad (\text{C.83})$$

$$\approx \frac{n_{\text{res}}(\gamma) - n_{\text{res}}(\gamma + \Delta_\gamma)}{\Delta_\gamma}, \quad (\text{C.84})$$

where the difference in the denominator  $n_{\text{res}}(\gamma) - n_{\text{res}}(\gamma + \Delta_\gamma)$  is equal to the number of states with decay rates in the interval  $[\gamma, \gamma + \Delta_\gamma]$ . If we consider a fixed number  $S$  of decay rates within the interval  $[\gamma, \gamma + \Delta_\gamma]$ , i.e., we consider  $S = 50$  throughout the thesis, then we obtain the following scaling for the width  $\Delta_\gamma$ ,

$$\Delta_\gamma \approx \frac{n_{\text{res}}(\gamma) - n_{\text{res}}(\gamma + \Delta_\gamma)}{s'(\gamma)} \cdot h^{D_0(\Gamma_s)/2} = \frac{S}{s'(\gamma)} \cdot h^{D_0(\Gamma_s)/2}, \quad (\text{C.85})$$

which corresponds to the observed scaling  $\sim h^{D_0(\Gamma_s)/2}$  in Fig. 5.9. The prefactor is explained by the shape function  $s(\gamma)$ , Eq. (5.7), leading to larger intervals  $\Delta_\gamma$  for larger decay rates.

### C.6.3 Conditional invariance of measures $\mu_\gamma^h$

The measures  $\mu_\gamma^h$  defined in Eq. (5.18) are conditionally invariant under the map with full escape  $\mathcal{M}$  and have decay rate  $\gamma$ .

*Proof.* Consider a measurable set  $A \subset \Gamma$ . The definition of  $\mu_\gamma^h$ , Eq. (5.18), implies that

$$\mu_\gamma^h(A) = \frac{1}{\mathcal{N}} \int \mathbb{1}_A(x) \cdot e^{t_h(\mathbf{x})(\gamma - \gamma_{\text{nat}})} d\mu_{\text{nat}}(x) = \mu_{\text{nat}}[\mathbb{1}_A \cdot e^{t_h(\gamma - \gamma_{\text{nat}})}], \quad (\text{C.86})$$

where in the last equality the temporal distance is considered as a function on  $\Gamma$ . The property of the temporal distance, Eq. (5.19), implies that  $t_h[M(x)] = t_h(\mathbf{x}) - 1$  for almost all points on the backward trapped set, which are not in the opening  $\Omega$ . This is important in the following, where the reflection function for full escape,  $R = 1 - \mathbb{1}_\Omega$ , excludes all phase-space points  $x \in \Omega$ .

Altogether we obtain

$$\mathcal{M}\mu_\gamma^h(A) = \mathcal{M}\mu_\gamma^h(\mathbb{1}_A) \stackrel{(2.38)}{=} \mu_\gamma^h(R \cdot \mathbb{1}_A \circ M) \quad (\text{C.87})$$

$$\stackrel{(C.86)}{=} \mu_{\text{nat}}[(1 - \mathbb{1}_\Omega) \cdot \mathbb{1}_A \circ M \cdot e^{t_h(\gamma - \gamma_{\text{nat}})}] \quad (\text{C.88})$$

$$= \mu_{\text{nat}}[(1 - \mathbb{1}_\Omega) \cdot \mathbb{1}_A \circ M \cdot e^{(t_h \circ M^{-1})(\gamma - \gamma_{\text{nat}})}] \quad (\text{C.89})$$

$$= e^{-(\gamma - \gamma_{\text{nat}})} \mu_{\text{nat}}[(1 - \mathbb{1}_\Omega) \cdot \mathbb{1}_A \circ M \cdot e^{t_h \circ M(\gamma - \gamma_{\text{nat}})}] \quad (\text{C.90})$$

$$\stackrel{(2.38)}{=} e^{-(\gamma - \gamma_{\text{nat}})} \mathcal{M}\mu_{\text{nat}}[\mathbb{1}_A \cdot e^{t_h(\gamma - \gamma_{\text{nat}})}] \quad (\text{C.91})$$

$$= e^{-(\gamma - \gamma_{\text{nat}})} e^{-\gamma_{\text{nat}}} \mu_{\text{nat}}[\mathbb{1}_A \cdot e^{t_h(\gamma - \gamma_{\text{nat}})}] = e^{-\gamma} \mu_\gamma^h(A), \quad (\text{C.92})$$

proving that the measures  $\mu_\gamma^h$  are conditionally invariant measures of the map with full escape  $\mathcal{M}$  and have decay rate  $\gamma$ .

□

# List of Figures

|      |  |    |
|------|--|----|
| 2.1  | Sketch of scattering problem. . . . .  | 6  |
| 2.2  | Phase-space portrait of the standard map. . . . .  | 17 |
| 2.3  | Local unstable and stable directions on phase space for chaotic standard map. . . . .  | 18 |
| 2.4  | Phase-space portrait of the ternary baker map. . . . .   | 18 |
| 2.5  | Classical sets of ternary baker map with escape from the middle strip. . . . .   | 22 |
| 2.6  | Classical sets of chaotic standard map with full escape from $\Omega = (0.3, 0.6) \times [0, 1)$ . . . . .                   | 23 |
| 3.1  | Regular and chaotic eigenfunctions for the closed standard map with a mixed phase space. . . . .                             | 36 |
| 3.2  | Typical eigenfunctions for the standard map with a chaotic phase space. . . . .  | 37 |
| 4.1  | Eigenvalues of the chaotic standard map with partial escape for $R_\Omega = 0.2$ . . . . .                                   | 42 |
| 4.2  | Distribution of decay rates $\gamma$ for the chaotic standard map with partial escape for $R_\Omega = 0.2$ . . . . .         | 42 |
| 4.3  | Eigenvalues and distribution of decay rates for the chaotic standard map with partial escape for $R_\Omega = 0.8$ . . . . .  | 43 |
| 4.4  | Eigenvalues and distribution of decay rates for the chaotic standard map with partial escape for $R_\Omega = 0.05$ . . . . . | 43 |
| 4.5  | Husimi distribution $\mathcal{H}_\gamma$ of single resonance eigenfunctions for partial escape. . . . .                      | 45 |
| 4.6  | Husimi distribution of single resonance eigenfunctions with the same decay rate. . . . .                                     | 46 |
| 4.7  | Illustration of considered observables on the phase space. . . . .   | 46 |
| 4.8  | Expectation values of different observables for single resonance eigenfunctions. . . . .                                     | 47 |
| 4.9  | Average decay rate as a function of $h$ . . . . .  | 49 |
| 4.10 | Mean expectation value of smooth observable as a function of $h$ . . . . .   | 50 |
| 4.11 | Convergence of resonance eigenfunctions in terms of the second moment $\tilde{S}_2(N, a)$ . . . . .                          | 51 |
| 4.12 | Average Husimi distribution of resonance eigenfunctions for partial escape. . . . .  | 52 |
| 4.13 | Rescaled Husimi distribution of resonance eigenfunctions revealing their fluctuations. . . . .                               | 53 |
| 4.14 | Probability distribution of fluctuations of rescaled Husimi. . . . .   | 54 |
| 4.15 | Expectation values of backward iterations of $R$ . . . . .   | 57 |
| 4.16 | Expectation values of forward iterations of $R$ . . . . .  | 57 |
| 4.17 | Finite approximations of natural and inverse measure for partial escape. . . . .   | 62 |
| 4.18 | Natural and inverse decay rate from time evolution. . . . .  | 62 |

|      |  |     |
|------|--|-----|
| 4.19 | Construction of product measures $\mu_\xi$ . . . . .   | 65  |
| 4.20 | Decay of product measures $\mu_\xi$ . . . . .  | 66  |
| 4.21 | Classical decay rates $\gamma_\xi$ as a function of $\xi$ . . . . .  | 66  |
| 4.22 | Quantum-to-classical correspondence on the phase space for standard map with partial escape. . . . .   | 69  |
| 4.23 | Fractal dimensions of single resonance eigenfunctions and classical measures for partial escape. . . . .   | 73  |
| 4.24 | Fractal dimensions of average resonance eigenfunctions and classical measures for partial escape. . . . .  | 74  |
| 4.25 | Fractal dimensions of resonance eigenfunctions and classical measures for partial escape. Dependence on considered dimension. . . . .                      | 75  |
| 4.26 | Jensen–Shannon divergence between single quantum Husimi distributions and different classical measures as a function of the decay rate $\gamma$ . . . . .  | 76  |
| 4.27 | Jensen–Shannon divergence between average quantum Husimi distributions and different classical measures as a function of the decay rate $\gamma$ . . . . . | 77  |
| 4.28 | Quantum-to-classical comparison in the semiclassical limit for single eigenfunctions. . . . .  | 79  |
| 4.29 | Quantum-to-classical comparison in the semiclassical limit for average Husimi distributions. . . . .   | 79  |
| 4.30 | Quantum-to-classical correspondence for standard map with partial escape considering different $R_\Omega$ . . . . .  | 82  |
| 4.31 | Quantum-to-classical and quantum-to-average comparison in the semiclassical limit depending on $R_\Omega$ . . . . .  | 85  |
| 4.32 | Quantum-to-classical comparison in the semiclassical limit for average Husimi distributions depending on $R_\Omega$ . . . . .                              | 87  |
| 4.33 | Quantum-to-classical correspondence for standard map with partial escape considering different openings $\Omega$ . . . . .                                 | 88  |
| 4.34 | Quantum-to-classical correspondence for baker map with partial escape. . . . .   | 89  |
| 4.35 | Quantum-to-classical correspondence for partial escape at the typical decay $\gamma_{\text{typ}}$ . . . . .  | 92  |
| 5.1  | Eigenvalues of the chaotic standard map in the limit of full escape. . . . .   | 97  |
| 5.2  | Distribution of decay rates $\gamma$ for the chaotic standard map in the limit of full escape. . . . .   | 98  |
| 5.3  | Eigenvalues of the chaotic standard map with full escape. . . . .  | 99  |
| 5.4  | Rescaled distribution of decay rates $\gamma$ for the chaotic standard map with full escape. . . . .   | 99  |
| 5.5  | Husimi distribution of resonance eigenfunctions in the limit of full escape. . . . .   | 101 |
| 5.6  | Husimi distribution of long-lived resonance eigenfunctions for full escape. . . . .  | 102 |
| 5.7  | Same as Fig. 5.6 for larger decay rates. . . . .   | 103 |
| 5.8  | Expectation values of different observables for single resonance eigenfunctions. . . . .   | 105 |
| 5.9  | Average decay rate as a function of $h$ . . . . .  | 106 |
| 5.10 | Mean expectation value of smooth observable as a function of $h$ . . . . .   | 107 |

---

|      |   |     |
|------|---|-----|
| 5.11 | Convergence of resonance eigenfunctions in terms of $\tilde{S}_2(N, a; \gamma_c)$ . . . . .   | 107 |
| 5.12 | Average Husimi distribution of resonance eigenfunctions for full escape. . . . .  | 109 |
| 5.13 | Same as Fig. 5.12 for larger decay rates. . . . .   | 110 |
| 5.14 | Expectation values on the preimages of $\Omega$ for full escape. . . . .  | 112 |
| 5.15 | Expectation values on the images of $\Omega$ for full escape. . . . .   | 112 |
| 5.16 | Measures $\mu_\gamma^{\text{nat}}$ for the chaotic standard map with full escape. . . . .   | 114 |
| 5.17 | Sketch of the simplified escape model for full escape. . . . .  | 116 |
| 5.18 | Temporal distance on backward trapped set. . . . .  | 120 |
| 5.19 | Phase-space distribution measures $\mu_\gamma^h$ . . . . .  | 121 |
| 5.20 | Quantum-to-classical correspondence on the phase space for standard map with full escape. . . . .   | 124 |
| 5.21 | Quantum-to-classical correspondence on the phase space at large decay rates for standard map with full escape. . . . .  | 126 |
| 5.22 | Fractal dimensions of single resonance eigenfunctions and classical measures for full escape. . . . .   | 127 |
| 5.23 | Fractal dimensions of average resonance eigenfunctions and classical measures for full escape. . . . .  | 128 |
| 5.24 | Fractal dimensions of resonance eigenfunctions and classical measures for full escape. Dependence on considered dimension. . . . .                                      | 129 |
| 5.25 | Jensen–Shannon divergence between single quantum Husimi distributions and different classical measures as a function of the decay rate $\gamma$ . Full escape. . . . .  | 131 |
| 5.26 | Jensen–Shannon divergence between average quantum Husimi distributions and different classical measures as a function of the decay rate $\gamma$ . Full escape. . . . . | 132 |
| 5.27 | Quantum-to-classical comparison in the semiclassical limit for single eigenfunctions for full escape. . . . .   | 133 |
| 5.28 | Quantum-to-classical comparison in the semiclassical limit for average Husimi distributions for full escape. . . . .  | 134 |
| 5.29 | Quantum-to-classical correspondence for standard map with full escape from $\Omega = (0.2, 0.4) \times [0, 1)$ . . . . .  | 136 |
| 5.30 | Quantum-to-classical correspondence at large decay rates for standard map with full escape from $\Omega = (0.2, 0.4) \times [0, 1)$ . . . . .                           | 138 |
| 5.31 | Quantum-to-classical correspondence for standard map with full escape from $\Omega = (0.2, 0.7) \times [0, 1)$ . . . . .  | 139 |
| B.1  | Distribution of eigenphases $\theta$ for the chaotic standard map with partial escape. . . . .  | 151 |
| B.2  | Distribution of eigenphases $\theta$ for the chaotic standard map with full escape. . . . .   | 152 |
| B.3  | Same as Fig. 4.10 for observable $a_1 = \mathbb{1}_A$ . . . . .   | 153 |
| B.4  | Same as Fig. 4.10 for observable $a_2 = \mathbb{1}_B$ . . . . .   | 153 |
| B.5  | Same as Fig. 4.10 for observable $a_3 = \mathbb{1}_C$ . . . . .   | 153 |

---

|      |   |     |
|------|---|-----|
| B.6  | Same as Fig. 5.10 for observable $a_1 = \mathbb{1}_A$ . . . . .   | 154 |
| B.7  | Same as Fig. 5.10 for observable $a_2 = \mathbb{1}_B$ . . . . .   | 154 |
| B.8  | Same as Fig. 5.10 for observable $a_3 = \mathbb{1}_C$ . . . . .   | 154 |
| B.9  | Fractal information dimensions of single resonance eigenfunctions as a function of their decay rate $\gamma$ for different $\epsilon$ . . . . .   | 155 |
| B.10 | Jensen–Shannon divergence between single quantum Husimi distributions and different classical measures as a function of the decay rate $\gamma$ . . . . .                                       | 156 |
| B.11 | Same as Fig. 4.26 and Fig. B.10 but using $\epsilon = 1/32$ . . . . .   | 156 |
| B.12 | Jensen–Shannon divergence between single quantum Husimi distributions and different classical measures as a function of the decay rate $\gamma$ for full escape and $\epsilon = 1/4$ . . . . .  | 157 |
| B.13 | Jensen–Shannon divergence between single quantum Husimi distributions and different classical measures as a function of the decay rate $\gamma$ for full escape and $\epsilon = 1/32$ . . . . . | 157 |
| C.1  | Product measures $\mu_\xi$ for triadic baker map $B_3$ with partial escape from the middle strip. . . . .   | 165 |
| C.2  | Product measures $\mu_\xi$ for asymmetric baker map $B_r$ with partial escape from the middle strip. . . . .  | 166 |
| C.3  | Estimation of conditional invariance and convergence for construction of product measures. . . . .  | 169 |
| C.4  | Estimation of accuracy for construction of product measures. . . . .  | 170 |

---

All figures in this thesis are generated with PyXGraph, which simplifies the usage of PyX.

# Bibliography

- [1] O. Bohigas, M. J. Giannoni, and C. Schmit: *Characterization of Chaotic Quantum Spectra and Universality of Level Fluctuation Laws*, Phys. Rev. Lett. **52** (1984), 1–4. Cited on page 1.
- [2] M. V. Berry: *Semiclassical Theory of Spectral Rigidity*, Proc. R. Soc. Lon. A **400** (1985), 229–251. Cited on page 1.
- [3] M. Sieber and K. Richter: *Correlations between periodic orbits and their rôle in spectral statistics*, Phys. Scripta **2001** (2001), 128–133. Cited on page 1.
- [4] S. Müller, S. Heusler, P. Braun, F. Haake, and A. Altland: *Semiclassical Foundation of Universality in Quantum Chaos*, Phys. Rev. Lett. **93** (2004), 014103. Cited on page 1.
- [5] M. V. Berry: *Regular and irregular semiclassical wavefunctions*, J. Phys. A **10** (1977), 2083–2091. Cited on pages 1, 34, and 35.
- [6] A. Voros: *Asymptotic  $\hbar$ -expansions of stationary quantum states*, Ann. Inst. Henri Poincaré A **26** (1977), 343–403. Cited on pages 1, 34, and 35.
- [7] M. V. Berry: *Semiclassical mechanics of regular and irregular motion*, in: *Comportement Chaotique des Systèmes Déterministes — Chaotic Behaviour of Deterministic Systems* (Eds. G. Iooss, R. H. G. Helleman and R. Stora), 171–271, (North-Holland, Amsterdam), (1983). Cited on pages 1, 34, and 35.
- [8] A. I. Shnirelman: *Ergodic properties of eigenfunctions* (in Russian), Usp. Math. Nauk **29** (1974), 181–182. Cited on pages 1, 34, and 36.
- [9] Y. Colin de Verdière: *Ergodicité et fonctions propres du laplacien* (in French), Commun. Math. Phys. **102** (1985), 497–502. Cited on pages 1, 34, and 36.
- [10] S. Zelditch: *Uniform distribution of eigenfunctions on compact hyperbolic surfaces*, Duke. Math. J. **55** (1987), 919–941. Cited on pages 1, 34, and 36.
- [11] S. Zelditch and M. Zworski: *Ergodicity of eigenfunctions for ergodic billiards*, Commun. Math. Phys. **175** (1996), 673–682. Cited on pages 1, 34, and 36.

- 
- [12] S. Zelditch: *Index and Dynamics of Quantized Contact Transformations*, Ann. Inst. Fourier **47** (1997), 305–363. Cited on pages 1, 34, and 36.
- [13] S. Nonnenmacher and A. Voros: *Chaotic Eigenfunctions in Phase Space*, J. Stat. Phys. **92** (1998), 431–518. Cited on pages 1, 34, 36, and 54.
- [14] A. Bäcker, R. Schubert, and P. Stifter: *Rate of quantum ergodicity in Euclidean billiards*, Phys. Rev. E **57** (1998), 5425–5447, ; erratum ibid. **58** (1998) 5192. Cited on pages 1, 34, 36, and 38.
- [15] S. De Bièvre: *Quantum chaos: a brief first visit*, in: *Second Summer School in Analysis and Mathematical Physics (Cuernavaca, 2000)* (Eds. S. Pérez-Esteva and C. Villegas-Blas), Contemp. Math. **289**, 161–218. Amer. Math. Soc., Providence, RI, (2001). Cited on pages 1, 34, and 36.
- [16] D. Belkić: *Principles of Quantum Scattering Theory*, Series in Atomic and Molecular Physics, (Institute of Physics Publishing, Bristol), (2004). Cited on pages 1, 5, 6, and 7.
- [17] P. Gaspard: *Quantum Chaotic Scattering*, (2014), Scholarpedia **9**(6): 9806. Cited on pages 1, 5, and 6.
- [18] J. M. Seoane and M. A. F. Sanjuán: *New developments in classical chaotic scattering*, Rep. Prog. Phys. **76** (2013), 016001. Cited on page 1.
- [19] M. Hénon and J.-M. Petit: *Series Expansions for Encounter-Type Solutions of Hill's Problem*, Celestial Mech. **38** (1986), 67–100. Cited on page 1.
- [20] P. T. Boyd and S. L. W. McMillan: *Chaotic Scattering in the Gravitational Three-body Problem*, Chaos **3** (1993), 507–523. Cited on page 1.
- [21] C. C. Rankin and W. H. Miller: *Classical S Matrix for Linear Reactive Collisions of  $H + Cl_2$* , J. Chem. Phys. **55** (1971), 3150–3156. Cited on page 1.
- [22] D. W. Noid, S. K. Gray, and S. A. Rice: *Fractal Behavior in Classical Collisional Energy Transfer*, J. Chem. Phys. **84** (1986), 2649–2652. Cited on pages 1 and 5.
- [23] J. N. Bardsley and F. Mandl: *Resonant Scattering of Electrons by Molecules*, Rep. Prog. Phys. **31** (1968), 471–531. Cited on page 1.
- [24] T. Yamamoto and K. Kaneko: *Helium Atom as a Classical Three-Body Problem*, Phys. Rev. Lett. **70** (1993), 1928–1931. Cited on page 1.
- [25] G. E. Mitchell, A. Richter, and H. A. Weidenmüller: *Random Matrices and Chaos in Nuclear Physics: Nuclear Reactions*, Rev. Mod. Phys. **82** (2010), 2845–2901. Cited on page 1.



- [26] S. W. Jones and H. Aref: *Chaotic Advection in Pulsed Source–Sink Systems*, *Physics of Fluids* **31** (1988), 469–485. Cited on page 1.
- [27] C. Jung and E. Ziemniak: *Hamiltonian Scattering Chaos in a Hydrodynamical System*, *J. Phys. A* **25** (1992), 3929–3943. Cited on page 1.
- [28] C. Jung, T. Tél, and E. Ziemniak: *Application of Scattering Chaos to Particle Transport in a Hydrodynamical Flow*, *Chaos* **3** (1993), 555–568. Cited on page 1.
- [29] H.-J. Stöckmann: *Quantum Chaos: An Introduction*, (Cambridge University Press, Cambridge), (1999). Cited on page 1.
- [30] N. Moiseyev: *Non-Hermitian Quantum Mechanics*, (Cambridge University Press), (2011). Cited on pages 1, 8, and 11.
- [31] Y. V. Fyodorov and H.-J. Sommers: *Statistics of resonance poles, phase shifts and time delays in quantum chaotic scattering: Random matrix approach for systems with broken time-reversal invariance*, *J. Math. Phys.* **38** (1997), 1918–1981. Cited on pages 1 and 8.
- [32] H. Schomerus: *From scattering theory to complex wave dynamics in non-Hermitian  $\mathcal{PT}$ -symmetric resonators*, *Phil. Trans. R. Soc. A* **371** (2013), 20120194. Cited on pages 1 and 8.
- [33] D. C. Brody and E.-M. Graefe: *Mixed-State Evolution in the Presence of Gain and Loss*, *Phys. Rev. Lett.* **109** (2012), 230405. Cited on pages 1 and 8.
- [34] I. Yusipov, T. Lapyteva, S. Denisov, and M. Ivanchenko: *Localization in Open Quantum Systems*, *Phys. Rev. Lett.* **118** (2017), 070402. Cited on pages 1 and 8.
- [35] E. M. Graefe, B. Longstaff, T. Plastow, and R. Schubert: *Lindblad Dynamics of Gaussian States and Their Superpositions in the Semiclassical Limit*, *J. Phys. A* **51** (2018), 365203. Cited on pages 1 and 8.
- [36] I. I. Yusipov, O. S. Vershinina, S. Denisov, S. P. Kuznetsov, and M. V. Ivanchenko: *Quantum Lyapunov Exponents beyond Continuous Measurements*, *Chaos* **29** (2019), 063130. Cited on pages 1 and 8.
- [37] S. Malzard, C. Poli, and H. Schomerus: *Topologically Protected Defect States in Open Photonic Systems with Non-Hermitian Charge-Conjugation and Parity-Time Symmetry*, *Phys. Rev. Lett.* **115** (2015), 200402. Cited on page 1.
- [38] H. Shen, B. Zhen, and L. Fu: *Topological Band Theory for Non-Hermitian Hamiltonians*, *Phys. Rev. Lett.* **120** (2018), 146402. Cited on page 1.

- [39] Z. Gong, Y. Ashida, K. Kawabata, K. Takasan, S. Higashikawa, and M. Ueda: *Topological Phases of Non-Hermitian Systems*, Phys. Rev. X **8** (2018), 031079. Cited on page 1.
- [40] S. Yao and Z. Wang: *Edge States and Topological Invariants of Non-Hermitian Systems*, Phys. Rev. Lett. **121** (2018), 086803. Cited on page 1.
- [41] F. K. Kunst, E. Edvardsson, J. C. Budich, and E. J. Bergholtz: *Biorthogonal Bulk-Boundary Correspondence in Non-Hermitian Systems*, Phys. Rev. Lett. **121** (2018), 026808. Cited on page 1.
- [42] D. J. Luitz and F. Piazza: *Exceptional Points and the Topology of Quantum Many-Body Spectra*, Physical Review Research **1** (2019), 033051. Cited on page 1.
- [43] H. Cao and J. Wiersig: *Dielectric microcavities: Model systems for wave chaos and non-Hermitian physics*, Rev. Mod. Phys. **87** (2015), 61–111. Cited on pages 1 and 27.
- [44] J. U. Nöckel and A. D. Stone: *Ray and wave chaos in asymmetric resonant optical cavities*, Nature **385** (1997), 45–47. Cited on page 1.
- [45] C. Gmachl, F. Capasso, E. E. Narimanov, J. U. Nöckel, A. D. Stone, J. Faist, D. L. Sivco, and A. Y. Cho: *High-Power Directional Emission from Microlasers with Chaotic Resonators*, Science **280** (1998), 1556–1564. Cited on page 1.
- [46] J. U. Nöckel and R. K. Chang: *2D Microcavities: Theory and Experiments*, in: *Experimental Methods in the Physical Sciences* (Eds. R. D. van Zee and J. P. Looney), vol. 40 of *Cavity-Enhanced Spectroscopies*, 185–226, (Academic Press), (2003). Cited on page 1.
- [47] S.-Y. Lee, S. Rim, J.-W. Ryu, T.-Y. Kwon, M. Choi, and C.-M. Kim: *Quasiscattered Resonances in a Spiral-Shaped Microcavity*, Phys. Rev. Lett. **93** (2004), 164102. Cited on pages 1, 2, 27, and 79.
- [48] J. Wiersig and J. Main: *Fractal Weyl law for chaotic microcavities: Fresnel’s laws imply multifractal scattering*, Phys. Rev. E **77** (2008), 036205. Cited on pages 1, 2, 27, and 41.
- [49] J. Wiersig and M. Hentschel: *Combining Directional Light Output and Ultralow Loss in Deformed Microdisks*, Phys. Rev. Lett. **100** (2008), 033901. Cited on page 1.
- [50] J.-B. Shim, S.-B. Lee, S. W. Kim, S.-Y. Lee, J. Yang, S. Moon, J.-H. Lee, and K. An: *Uncertainty-Limited Turnstile Transport in Deformed Microcavities*, Phys. Rev. Lett. **100** (2008), 174102. Cited on page 1.

- [51] S. Shinohara, T. Harayama, and T. Fukushima: *Fresnel Filtering of Gaussian Beams in Microcavities*, Optics Letters **36** (2011), 1023–1025. Cited on page 1.
- [52] S. Shinohara, T. Harayama, T. Fukushima, M. Hentschel, S. Sunada, and E. E. Narimanov: *Chaos-assisted emission from asymmetric resonant cavity microlasers*, Phys. Rev. A **83** (2011), 053837. Cited on page 1.
- [53] J.-B. Shim, J. Wiersig, and H. Cao: *Whispering gallery modes formed by partial barriers in ultrasmall deformed microdisks*, Phys. Rev. E **84** (2011), 035202. Cited on page 1.
- [54] T. Harayama and S. Shinohara: *Ray-Wave Correspondence in Chaotic Dielectric Billiards*, Phys. Rev. E **92** (2015), 042916. Cited on pages 1, 2, and 27.
- [55] J. Kullig and J. Wiersig: *Frobenius–Perron eigenstates in deformed microdisk cavities: non-Hermitian physics and asymmetric backscattering in ray dynamics*, New J. Phys. **18** (2016), 015005. Cited on pages 1 and 2.
- [56] W. T. Lu, S. Sridhar, and M. Zworski: *Fractal Weyl Laws for Chaotic Open Systems*, Phys. Rev. Lett. **91** (2003), 154101. Cited on pages 2 and 99.
- [57] H. Schomerus and J. Tworzydło: *Quantum-to-Classical Crossover of Quasibound States in Open Quantum Systems*, Phys. Rev. Lett. **93** (2004), 154102. Cited on pages 2, 99, 100, 101, 116, and 117.
- [58] H. Schomerus and P. Jacquod: *Quantum-to-classical correspondence in open chaotic systems*, J. Phys. A **38** (2005), 10663–10682. Cited on pages 2, 101, 104, and 113.
- [59] J. P. Keating, M. Novaes, S. D. Prado, and M. Sieber: *Semiclassical Structure of Chaotic Resonance Eigenfunctions*, Phys. Rev. Lett. **97** (2006), 150406. Cited on pages 2, 39, 55, 56, 100, 103, 108, 110, and 111.
- [60] S. Nonnenmacher and M. Rubin: *Resonant eigenstates for a quantized chaotic system*, Nonlinearity **20** (2007), 1387–1420. Cited on pages 2, 30, 39, 40, 58, 59, 95, 100, 110, 113, 130, 148, 149, 162, 163, and 166.
- [61] S. Nonnenmacher and M. Zworski: *Quantum decay rates in chaotic scattering*, Acta Math. **203** (2009), 149–233. Cited on page 2.
- [62] L. Ermann, G. G. Carlo, and M. Saraceno: *Localization of Resonance Eigenfunctions on Quantum Repellers*, Phys. Rev. Lett. **103** (2009), 054102. Cited on page 2.
- [63] M. Novaes: *Resonances in open quantum maps*, J. Phys. A **46** (2013), 143001. Cited on page 2.

- [64] T. Weich, S. Barkhofen, U. Kuhl, C. Poli, and H. Schomerus: *Formation and interaction of resonance chains in the open three-disk system*, New J. Phys. **16** (2014), 033029. Cited on page 2.
- [65] M. J. Körber, A. Bäcker, and R. Ketzmerick: *Localization of Chaotic Resonance States due to a Partial Transport Barrier*, Phys. Rev. Lett. **115** (2015), 254101. Cited on pages 2, 114, and 132.
- [66] K. Clauß, M. J. Körber, A. Bäcker, and R. Ketzmerick: *Resonance Eigenfunction Hypothesis for Chaotic Systems*, Phys. Rev. Lett. **121** (2018), 074101. Cited on pages 2, 3, 95, 108, 117, 118, and 144.
- [67] E. G. Altmann, J. S. E. Portela, and T. Tél: *Leaking chaotic systems*, Rev. Mod. Phys. **85** (2013), 869–918. Cited on pages 2, 19, 20, 23, 25, 27, 29, and 161.
- [68] P. Gaspard and S. A. Rice: *Hamiltonian mapping models of molecular fragmentation*, J. Phys. Chem. **93** (1989), 6947–6957. Cited on page 2.
- [69] J. A. Ramilowski, S. D. Prado, F. Borondo, and D. Farrelly: *Fractal Weyl law behavior in an open Hamiltonian system*, Phys. Rev. E **80** (2009), 055201. Cited on pages 2, 5, and 20.
- [70] Y.-C. Lai and T. Tél: *Transient Chaos: Complex Dynamics on Finite Time Scales*, no. 173 in Applied Mathematical Sciences, (Springer Verlag, New York), 1st edn., (2011). Cited on pages 2 and 23.
- [71] G. Pianigiani and J. A. Yorke: *Expanding Maps on Sets Which Are Almost Invariant: Decay and Chaos*, Trans. Amer. Math. Soc. **252** (1979), 351–366. Cited on pages 2 and 26.
- [72] H. Kantz and P. Grassberger: *Repellers, semi-attractors, and long-lived chaotic transients*, Physica D **17** (1985), 75–86. Cited on pages 2 and 25.
- [73] T. Tél: *Escape rate from strange sets as an eigenvalue*, Phys. Rev. A **36** (1987), 1502–1505. Cited on page 2.
- [74] M. F. Demers and L.-S. Young: *Escape rates and conditionally invariant measures*, Nonlinearity **19** (2006), 377–397. Cited on pages 2, 26, 27, and 30.
- [75] J. Sjöstrand: *Geometric Bounds on the Density of Resonances for Semiclassical Problems*, Duke Math. J. **60** (1990), 1–57. Cited on page 2.
- [76] J. Lin: *Divergence Measures Based on the Shannon Entropy*, IEEE Transactions on Information Theory **37** (1991), 145–151. Cited on pages 2, 75, and 76.

- 
- [77] M. Zworski: *Dimension of the limit set and the density of resonances for convex co-compact hyperbolic surfaces*, *Invent. math.* **136** (1999), 353–409. Cited on page 2.
- [78] S. Nonnenmacher and M. Zworski: *Fractal Weyl laws in discrete models of chaotic scattering*, *J. Phys. A* **38** (2005), 10683. Cited on pages 2 and 99.
- [79] S. Nonnenmacher: *Fractal Weyl Law for Open Chaotic Maps*, in: *Mathematical Physics of Quantum Mechanics* (Eds. J. Asch and A. Joye), vol. 690 of *Lect. Notes Phys.*, 435–450, (Springer Berlin Heidelberg), (2006). Cited on pages 2 and 99.
- [80] S. Nonnenmacher and M. Zworski: *Distribution of Resonances for Open Quantum Maps*, *Commun. Math. Phys.* **269** (2007), 311–365. Cited on pages 2 and 99.
- [81] G. G. Carlo, D. A. Wisniacki, L. Ermann, R. M. Benito, and F. Borondo: *Classical transients and the support of open quantum maps*, *Phys. Rev. E* **87** (2013), 012909. Cited on pages 2 and 99.
- [82] S. Nonnenmacher, J. Sjöstrand, and M. Zworski: *Fractal Weyl law for open quantum chaotic maps*, *Annals of Mathematics* **179** (2014), 179–251. Cited on pages 2 and 99.
- [83] M. Kopp and H. Schomerus: *Fractal Weyl laws for quantum decay in dynamical systems with a mixed phase space*, *Phys. Rev. E* **81** (2010), 026208. Cited on page 2.
- [84] A. Eberspächer, J. Main, and G. Wunner: *Fractal Weyl law for three-dimensional chaotic hard-sphere scattering systems*, *Phys. Rev. E* **82** (2010), 046201. Cited on page 2.
- [85] L. Ermann and D. L. Shepelyansky: *Ulam method and fractal Weyl law for Perron-Frobenius operators*, *Eur. Phys. J. B* **75** (2010), 299–304. Cited on page 2.
- [86] M. J. Körber, M. Michler, A. Bäcker, and R. Ketzmerick: *Hierarchical Fractal Weyl Laws for Chaotic Resonance States in Open Mixed Systems*, *Phys. Rev. Lett.* **111** (2013), 114102. Cited on page 2.
- [87] G. Casati, G. Maspero, and D. L. Shepelyansky: *Quantum fractal eigenstates*, *Physica D* **131** (1999), 311–316. Cited on pages 2, 63, 79, 91, and 143.
- [88] E. G. Altmann, J. S. E. Portela, and T. Tél: *Chaotic Systems with Absorption*, *Phys. Rev. Lett.* **111** (2013), 144101. Cited on pages 2 and 25.
- [89] S. Nonnenmacher and E. Schenck: *Resonance distribution in open quantum chaotic systems*, *Phys. Rev. E* **78** (2008), 045202. Cited on pages 2, 26, 29, 41, 42, 43, 49, 91, 101, 173, and 175.

- 
- [90] A. Potzuweit, T. Weich, S. Barkhofen, U. Kuhl, H.-J. Stöckmann, and M. Zworski: *Weyl asymptotics: From closed to open systems*, Phys. Rev. E **86** (2012), 066205. Cited on page 2.
- [91] B. Gutkin and V. A. Osipov: *Universality in spectral statistics of open quantum graphs*, Phys. Rev. E **91** (2015), 060901. Cited on pages 2, 41, and 43.
- [92] M. Schönwetter and E. G. Altmann: *Quantum signatures of classical multifractal measures*, Phys. Rev. E **91** (2015), 012919. Cited on pages 2, 43, 49, and 72.
- [93] G. G. Carlo, R. M. Benito, and F. Borondo: *Theory of Short Periodic Orbits for Partially Open Quantum Maps*, Phys. Rev. E **94** (2016), 012222. Cited on page 2.
- [94] C. A. Prado, G. G. Carlo, R. M. Benito, and F. Borondo: *Role of Short Periodic Orbits in Quantum Maps with Continuous Openings*, Phys. Rev. E **97** (2018), 042211. Cited on page 2.
- [95] D. Lippolis, J.-W. Ryu, S.-Y. Lee, and S. W. Kim: *On-manifold localization in open quantum maps*, Phys. Rev. E **86** (2012), 066213. Cited on page 2.
- [96] D. Lippolis, J.-W. Ryu, and S. W. Kim: *Localization in chaotic systems with a single-channel opening*, Phys. Rev. E **92** (2015), 012921. Cited on page 2.
- [97] K. Clauß, E. G. Altmann, A. Bäcker, and R. Ketzmerick: *Structure of Resonance Eigenfunctions for Chaotic Systems with Partial Escape*, Phys. Rev. E **100** (2019), 052205. Cited on pages 3, 39, 63, 64, 75, 80, 144, and 168.
- [98] T.-Y. Wu and T. Ohmura: *Quantum Theory of Scattering*, Prentice-Hall International Series in Physics, (Prentice-Hall Inc., Englewood Cliffs, New Jersey), (1962). Cited on pages 5 and 7.
- [99] R. G. Newton: *Scattering Theory of Waves and Particles*, Texts and Monographs in Physics, (Springer-Verlag, New York/Heidelberg/Berlin), 2nd edn., (1982). Cited on pages 5, 7, and 8.
- [100] B. A. Lippmann and J. Schwinger: *Variational Principles for Scattering Processes. I*, Phys. Rev. **79** (1950), 469–480. Cited on pages 5 and 6.
- [101] B. Eckhardt and C. Jung: *Regular and Irregular Potential Scattering*, J. Phys. A **19** (1986), L829–L833. Cited on page 5.
- [102] C. Mahaux and H. A. Weidenmüller: *Shell-Model Approach to Nuclear Reactions*, (North-Holland, Amsterdam), (1969). Cited on pages 5 and 8.

- [103] J. A. Beswick, G. Delgado-Barrio, and J. Jortner: *Vibrational predissociation lifetimes of the van der Waals molecule HeI<sub>2</sub>*, J. Chem. Phys. **70** (1979), 3895–3901. Cited on page 5.
- [104] V. V. Baturó, I. N. Cherepanov, S. S. Lukashov, S. A. Poretsky, and A. M. Pravilov: *The ArI<sub>2</sub>(ion-Pair States) van der Waals complexes*, Chem. Phys. Lett. **647** (2016), 161–164. Cited on page 5.
- [105] D. Mulherin and I. I. Zinnes: *Coulomb Scattering. I. Single Channel*, J. Math. Phys. **11** (1970), 1402–1408. Cited on page 6.
- [106] W. Heisenberg: *Die „beobachtbaren Größen“ in der Theorie der Elementarteilchen*, Z. Phys. **120** (1943), 513–538. Cited on page 6.
- [107] M. Reed and B. Simon: *Methods of Modern Mathematical Physics IV: Analysis of Operators*, (Academic Press), (1978). Cited on page 7.
- [108] M. Reed and B. Simon: *Methods of Modern Mathematical Physics III: Scattering Theory*, (Academic Press), (1979). Cited on page 7.
- [109] J. Aguilar and J. M. Combes: *A Class of Analytic Perturbations for One-body Schrödinger Hamiltonians*, Commun. Math. Phys. **22** (1971), 269–279. Cited on page 8.
- [110] E. Balslev and J. M. Combes: *Spectral Properties of Many-body Schrödinger Operators with Dilatation-analytic Interactions*, Commun. Math. Phys. **22** (1971), 280–294. Cited on page 8.
- [111] W. P. Reinhardt: *Chaotic dynamics, semiclassical quantization, and mode-mode energy transfer: the Boulder view*, J. Phys. Chem. **86** (1982), 2158–2165. Cited on page 8.
- [112] N. Moiseyev: *Quantum theory of resonances: calculating energies, widths and cross-sections by complex scaling*, Phys. Rep. **302** (1998), 212–293, 00634. Cited on page 8.
- [113] B. Simon: *Resonances in n-Body Quantum Systems With Dilatation Analytic Potentials and the Foundations of Time-Dependent Perturbation Theory*, Annals of Mathematics **97** (1973), 247–274. Cited on page 8.
- [114] S.-I. Chu and W. P. Reinhardt: *Intense Field Multiphoton Ionization via Complex Dressed States: Application to the H Atom*, Phys. Rev. Lett. **39** (1977), 1195–1198. Cited on page 8.

- 
- [115] K. Yajima: *Resonances for the AC-Stark effect*, Commun. Math. Phys. **87** (1982), 331–352. Cited on page 8.
- [116] J. S. Howland: *Complex scaling of ac Stark Hamiltonians*, J. Math. Phys. **24** (1983), 1240–1244. Cited on page 8.
- [117] A. Maquet, S.-I. Chu, and W. P. Reinhardt: *Stark ionization in dc and ac fields: An  $L^2$  complex-coordinate approach*, Phys. Rev. A **27** (1983), 2946–2970. Cited on page 8.
- [118] N. Moiseyev and H. J. Korsch: *Metastable quasienergy positions and widths for time-periodic Hamiltonians by the complex-coordinate method*, Phys. Rev. A **41** (1990), 498–501. Cited on page 8.
- [119] N. Mertig and A. Shudo: *Open Quantum Maps from Complex Scaling of Kicked Scattering Systems*, Phys. Rev. E **97** (2018), 042216. Cited on pages 8 and 20.
- [120] C. Mahaux and H. A. Weidenmüller: *Comparison between the R-Matrix and Eigenchannel Methods*, Phys. Rev. **170** (1968), 847–856. Cited on page 8.
- [121] T. J. Christiansen and M. Zworski: *A mathematical formulation of the Mahaux–Weidenmüller formula for the scattering matrix*, J. Phys. A **42** (2009), 415202. Cited on page 8.
- [122] K. Pichugin, H. Schanz, and P. Šeba: *Effective coupling for open billiards*, Phys. Rev. E **64** (2001), 056227. Cited on page 8.
- [123] G. Akguc and L. E. Reichl: *Effect of Evanescent Modes and Chaos on Deterministic Scattering in Electron Waveguides*, Phys. Rev. E **64** (2001), 056221. Cited on page 8.
- [124] Y. V. Fyodorov and H.-J. Sommers: *Spectra of Random Contractions and Scattering Theory for Discrete-Time Systems*, J. Exp. Theor. Phys. Lett. **72** (2000), 422–426. Cited on pages 8, 9, and 10.
- [125] G. D. Birkhoff: *On the Periodic Motions of Dynamical Systems*, Acta Math. **50** (1927), 359–379. Cited on pages 9 and 16.
- [126] P. Gaspard: *Chaos, Scattering and Statistical Mechanics*, no. 9 in Cambridge Nonlinear Science Series, (Cambridge University Press, Cambridge, United Kingdom), (1998). Cited on pages 9, 13, 14, 16, 21, and 41.
- [127] B. V. Chirikov: *Research concerning the theory of non-linear resonance and stochasticity*, (CERN, Geneva), (1971), Translated at CERN from the Russian Preprint N 267, Institute of Nuclear Physics, Novosibirsk (1969). Cited on page 9.



- [128] J. Tworzydło, A. Tajic, H. Schomerus, and C. W. J. Beenakker: *Dynamical model for the quantum-to-classical crossover of shot noise*, Phys. Rev. B **68** (2003), 115313. Cited on page 9.
- [129] H. Schomerus: *Random Matrix Approaches to Open Quantum Systems*, arXiv:1610.05816 [cond-mat.dis-nn] (2016). Cited on pages 9 and 10.
- [130] M. Reed and B. Simon: *Methods of modern mathematical Physics I: Functional Analysis*, (Academic Press), (1980). Cited on page 11.
- [131] D. C. Brody: *Biorthogonal Quantum Mechanics*, J. Phys. A **47** (2013), 035305. Cited on pages 11 and 12.
- [132] V. I. Arnold: *Mathematical Methods of Classical Mechanics*, (Springer, New York), 2nd edn., (1989). Cited on pages 13 and 15.
- [133] H. Narnhofer and W. Thirring: *Canonical Scattering Transformation in Classical Mechanics*, Phys. Rev. A **23** (1981), 1688–1697. Cited on page 13.
- [134] B. Eckhardt: *Fractal Properties of Scattering Singularities*, J. Phys. A **20** (1987), 5971–5979. Cited on page 13.
- [135] P. Gaspard and S. A. Rice: *Scattering from a classically chaotic repeller*, J. Chem. Phys. **90** (1989), 2225–2241. Cited on page 13.
- [136] G. Troll and U. Smilansky: *A simple model for chaotic scattering: I. Classical theory*, Physica D **35** (1989), 34–64. Cited on pages 13 and 16.
- [137] E. Ott: *Chaos in Dynamical Systems*, (Cambridge University Press, Cambridge, United Kingdom), 2nd edn., (2002). Cited on pages 14, 16, 17, 23, 161, 162, and 166.
- [138] J. Moser: *Stable and random motions in dynamical systems*, no. 77 in Annals of mathematics studies, (Princeton Univ. Press, Princeton NJ), (1973). Cited on page 14.
- [139] B. V. Chirikov and D. L. Shepelyansky: *Correlation properties of dynamical chaos in Hamiltonian systems*, Physica D **13** (1984), 395–400. Cited on page 14.
- [140] J. D. Meiss and E. Ott: *Markov Tree Model of Transport in Area-Preserving Maps*, Physica D **20** (1986), 387–402. Cited on page 14.
- [141] Y.-C. Lai, M. Ding, C. Grebogi, and R. Blümel: *Algebraic decay and fluctuations of the decay exponent in Hamiltonian systems*, Phys. Rev. A **46** (1992), 4661–4669. Cited on page 14.

- 
- [142] R. L. Devaney: *An Introduction to Chaotic Dynamical Systems*, (Addison-Wesley, Reading Mass.), (1989). Cited on page 14.
- [143] D. K. Arrowsmith and C. M. Place: *an introduction to Dynamical Systems*, (Cambridge University Press, Cambridge), 3rd edn., (1994). Cited on pages 14 and 18.
- [144] B. Hasselblatt and Y. Pesin: *Hyperbolic Dynamics*, (2008), Scholarpedia **3**(6): 2208. Cited on page 14.
- [145] P. Walters: *An Introduction to Ergodic Theory*, Graduate Texts in Mathematics, (Springer-Verlag, New York), (1982). Cited on pages 15, 16, 19, 20, 27, and 38.
- [146] P. Ehrenfest and T. Ehrenfest: *Begriffliche Grundlagen der Statistischen Auffassung in der Mechanik* (in german), in: *Encyklopädie der mathematischen Wissenschaften mit Einschluss ihrer Anwendungen: Mechanik* (Eds. F. Klein and C. Müller), 773–860, (Vieweg+Teubner Verlag, Wiesbaden), (1911). Cited on page 15.
- [147] B. V. Chirikov: *A universal instability of many-dimensional oscillator systems*, Phys. Rep. **52** (1979), 263–379. Cited on page 17.
- [148] H. Poincaré: *Sur un théorème de géométrie*, Rend. Cir. Mat. Palermo **33** (1912), 375–407. Cited on page 17.
- [149] G. D. Birkhoff: *Proof of Poincaré’s geometric theorem*, Trans. Amer. Math. Soc. **14** (1913), 14–22. Cited on page 17.
- [150] V. I. Arnold and A. Avez: *Ergodic Problems of Classical Mechanics*, (Benjamin, NewYork), (1968). Cited on pages 18, 19, and 147.
- [151] N. L. Balazs and A. Voros: *The Quantized Baker’s Transformation*, Ann. Phys. **190** (1989), 1–31. Cited on pages 18, 32, 147, and 149.
- [152] M. Saraceno: *Classical structures in the quantized baker transformation*, Ann. Phys. (N.Y.) **199** (1990), 37–60. Cited on pages 18, 32, 147, and 149.
- [153] J. H. Hannay, J. P. Keating, and A. M. Ozorio de Almeida: *Optical realization of the baker’s transformation*, Nonlinearity **7** (1994), 1327–1342. Cited on pages 18 and 147.
- [154] E. Ott and T. Tél: *Chaotic scattering: An introduction*, Chaos **3** (1993), 417. Cited on page 23.
- [155] B. Mandelbrot: *How Long is the Coast of Britain? Statistical Self-Similarity and Fractional Dimension*, Science **156** (1967), 636–638. Cited on page 23.

- [156] B. Mandelbrot: *The Fractal Geometry of Nature*, (W. H. Freeman and Company, New York), (1982). Cited on page 23.
- [157] W. Hurewicz and H. Wallman: *Dimension theory*, (Princeton University Press, Princeton), Revised edn., (1974). Cited on page 23.
- [158] G. Edgar: *Measure, Topology, and Fractal Geometry*, Undergraduate Texts in Mathematics, (Springer-Verlag, New York), 2nd edn., (2008). Cited on page 24.
- [159] H. G. E. Hentschel and I. Procaccia: *The Infinite Number of Generalized Dimensions of Fractals and Strange Attractors*, *Physica D* **8** (1983), 435–444. Cited on page 24.
- [160] P. Grassberger: *Generalized Dimensions of Strange Attractors*, *Phys. Lett. A* **97** (1983), 227–230. Cited on page 24.
- [161] T. Tél and M. Gruiz: *Chaotic Dynamics – An Introduction Based on Classical Mechanics*, (Cambridge University Press, Cambridge, United Kingdom), (2006). Cited on page 25.
- [162] E. G. Altmann, J. S. E. Portela, and T. Tél: *Chaotic explosions*, *EPL* **109** (2015), 30003. Cited on pages 25, 26, 27, 28, and 161.
- [163] T. Tél: *The joy of transient chaos*, *Chaos* **25** (2015), 097619. Cited on page 26.
- [164] N. Chernov and R. Markarian: *Ergodic properties of Anosov maps with rectangular holes*, *Bol. Soc. Bras. Mat* **28** (1997), 271–314. Cited on page 26.
- [165] N. Chernov, R. Markarian, and S. Troubetzkoy: *Conditionally Invariant Measures for Anosov Maps with Small Holes*, *Ergodic Theory Dynam. Systems* **18** (1998), 1049–1073. Cited on page 26.
- [166] S. M. Ulam: *A collection of mathematical problems*, in: *Interscience tracts in pure and applied Mathematics* (Eds. L. Bers, R. Courant and J. J. Stoker), vol. 8, 73–75, New York, (1960), Interscience. Cited on pages 27 and 28.
- [167] L. Ermann and D. L. Shepelyansky: *Incommensurate Standard Map*, *Phys. Rev. E* **99** (2019), 012215. Cited on pages 27 and 28.
- [168] A. Bouzouina and S. De Bièvre: *Equipartition of the eigenfunctions of quantized ergodic maps on the torus*, *Commun. Math. Phys.* **178** (1996), 83–105. Cited on page 31.
- [169] M. Degli Esposti and S. Graffi: *Mathematical aspects of quantum maps*, in: *The Mathematical Aspects of Quantum Maps* [173], 49–90. Cited on pages 31 and 32.

- [170] J. Marklof, S. O’Keefe, and S. Zelditch: *Weyl’s law and quantum ergodicity for maps with divided phase space (with an appendix Converse quantum ergodicity)*, *Nonlinearity* **18** (2005), 277–304. Cited on pages 31 and 58.
- [171] A. Bäcker: *Numerical aspects of eigenvalues and eigenfunctions of chaotic quantum systems*, in: Degli Esposti and Graffi [173], 91–144. Cited on page 32.
- [172] F. Haake: *Quantum Signatures of Chaos*, (Springer-Verlag, Berlin), 3rd edn., (2010). Cited on page 32.
- [173] M. Degli Esposti and S. Graffi (eds.): *The Mathematical Aspects of Quantum Maps*, vol. 618 of *Lect. Notes Phys.*, (Springer-Verlag, Berlin), (2003). Cited on pages 195 and 196.
- [174] S. De Bièvre, M. Degli Esposti, and R. Giachetti: *Quantization of a Class of Piecewise Affine Transformations on the Torus*, *Commun. Math. Phys.* **176** (1996), 73–94. Cited on pages 32 and 149.
- [175] M. V. Berry, N. L. Balazs, M. Tabor, and A. Voros: *Quantum maps*, *Ann. Phys. (N.Y.)* **122** (1979), 26–63. Cited on page 32.
- [176] S.-J. Chang and K.-J. Shi: *Evolution and exact eigenstates of a resonant quantum system*, *Phys. Rev. A* **34** (1986), 7–22. Cited on page 32.
- [177] E. P. Wigner: *On the quantum correction for thermodynamic equilibrium*, *Phys. Rev.* **40** (1932), 749–759. Cited on pages 33 and 34.
- [178] R. J. Glauber: *Coherent and Incoherent States of the Radiation Field*, *Phys. Rev.* **131** (1963), 2766–2788. Cited on page 33.
- [179] E. C. G. Sudarshan: *Equivalence of Semiclassical and Quantum Mechanical Descriptions of Statistical Light Beams*, *Phys. Rev. Lett.* **10** (1963), 277–279. Cited on page 33.
- [180] K. Husimi: *Some formal properties of the density matrix*, *Proc. Phys. Math. Soc. Jpn.* **22** (1940), 264–314. Cited on page 33.
- [181] H.-W. Lee: *Theory and Applications of the Quantum Phase-Space Distribution Functions*, *Phys. Rep.* **259** (1995), 147–211. Cited on page 33.
- [182] G. Haag: *Quanten-Abbildungen auf dem Zwei-Torus mit und ohne Spin 1/2*, Ph.D. thesis, Universität Ulm, Abteilung Theoretische Physik, (2002). Cited on pages 33 and 38.
- [183] G. B. Folland: *Harmonic Analysis in Phase Space*, vol. 122 of *Annals of Mathematics Studies*, (Princeton University Press, Princeton), (1989). Cited on page 33.

- [184] M. V. Berry: *Semi-classical mechanics in phase space: A study of Wigner's function*, Phil. Trans. R. Soc. A **287** (1977), 237–271. Cited on pages 34 and 35.
- [185] A. Voros: *Semi-classical ergodicity of quantum eigenstates in the Wigner representation*, in: *Stochastic Behavior in Classical and Quantum Hamiltonian Systems* (Eds. G. Casati and J. Ford), vol. 93 of *Lecture Notes in Physics*, 326–333, (Springer Berlin Heidelberg, Berlin), (1979). Cited on page 34.
- [186] N. D. Cartwright: *A Non-Negative Wigner-Type Distribution*, Physica A **83** (1976), 210–212. Cited on page 34.
- [187] I. C. Percival: *Semiclassical theory of bound states*, vol. 36, 1–61, (John Wiley & Sons, Inc.), (1977). Cited on page 35.
- [188] S. Zelditch: *On the Rate of Quantum Ergodicity I: Upper Bounds*, Commun. Math. Phys. **160** (1994), 81–92. Cited on page 38.
- [189] S. Zelditch: *On the Rate of Quantum Ergodicity II: Lower Bounds*, Communications in Partial Differential Equations **19** (1994), 1565–1579. Cited on page 38.
- [190] R. Aurich and M. Taglieber: *On the Rate of Quantum Ergodicity on Hyperbolic Surfaces and for Billiards*, Physica D **118** (1998), 84–102. Cited on page 38.
- [191] B. Eckhardt, S. Fishman, J. Keating, O. Agam, J. Main, and K. Müller: *Approach to ergodicity in quantum wave functions*, Phys. Rev. E **52** (1995), 5893–5903. Cited on page 38.
- [192] T. A. Brody, J. Flores, J. B. French, P. A. Mello, A. Pandey, and S. S. M. Wong: *Random-matrix physics: spectrum and strength fluctuations*, Rev. Mod. Phys. **53** (1981), 385–479. Cited on page 38.
- [193] D. L. Shepelyansky: *Fractal Weyl law for quantum fractal eigenstates*, Phys. Rev. E **77** (2008), 015202. Cited on page 41.
- [194] M. Novaes: *Supersharp resonances in chaotic wave scattering*, Phys. Rev. E **85** (2012), 036202. Cited on page 42.
- [195] E. Schenck: *Weyl Laws for Partially Open Quantum Maps*, Ann. Henri Poincaré **10** (2009), 711–747. Cited on pages 42, 43, 49, 91, 151, and 152.
- [196] F. Kunzmann: *Statistical Analysis for Eigenfunctions of Quantum Maps with Escape*, Bachelor thesis, Technische Universität Dresden, Fakultät Physik, (2019). Cited on pages 53, 54, and 55.

- [197] M. Schönwetter: *Fractal Dimensions in Classical and Quantum Mechanical Open Chaotic Systems*, Dissertation, Technische Universität Dresden, Fachrichtung Physik, (2016). Cited on pages 72 and 169.
- [198] X. Huang, S. Li, and Y. Wang: *Jensen-Shannon Boosting Learning for Object Recognition*, in: *2005 IEEE Computer Society Conference on Computer Vision and Pattern Recognition (CVPR'05)*, vol. 2, 144–149, (2005). Cited on page 75.
- [199] D. Das, D. Chen, A. F. T. Martins, N. Schneider, and N. A. Smith: *Frame-Semantic Parsing*, *Computational Linguistics* **40** (2013), 9–56. Cited on page 75.
- [200] P. Bernaola-Galván, R. Román-Roldán, and J. L. Oliver: *Compositional Segmentation and Long-Range Fractal Correlations in DNA Sequences*, *Phys. Rev. E* **53** (1996), 5181–5189. Cited on page 75.
- [201] I. Grosse, P. Bernaola-Galván, P. Carpena, R. Román-Roldán, J. Oliver, and H. E. Stanley: *Analysis of Symbolic Sequences Using the Jensen-Shannon Divergence*, *Phys. Rev. E* **65** (2002), 041905. Cited on page 75.
- [202] K. W. Boyack and R. Klavans: *Co-Citation Analysis, Bibliographic Coupling, and Direct Citation: Which Citation Approach Represents the Research Front Most Accurately?*, *Journal of the American Society for Information Science and Technology* **61** (2010), 2389–2404. Cited on page 75.
- [203] M. Xia and Z. Xu: *Entropy/Cross Entropy-Based Group Decision Making under Intuitionistic Fuzzy Environment*, *Information Fusion* **13** (2012), 31–47. Cited on page 75.
- [204] D. Endres and J. Schindelin: *A New Metric for Probability Distributions*, *IEEE Transactions on Information Theory* **49** (2003), 1858–1860. Cited on page 76.
- [205] T. Becker: *Bedingt invariante Maße der partiell geöffneten Baker-Abbildung*, Bachelor thesis, Technische Universität Dresden, Fachrichtung Physik, (2016). Cited on pages 90 and 166.
- [206] J. H. Hannay and A. M. Ozorio De Almeida: *Periodic Orbits and a Correlation Function for the Semiclassical Density of States*, *J. Phys. A* **17** (1984), 3429–3440. Cited on pages 91, 92, and 162.
- [207] K. Życzkowski and H.-J. Sommers: *Truncations of random unitary matrices*, *J. Phys. A* **33** (2000), 2045–2057. Cited on page 99.
- [208] M. Sieber: *Resonance eigenfunctions in chaotic scattering systems*, *Pramana* **73** (2009), 543–551. Cited on pages 110 and 111.

- 
- [209] K. Clauß: *Localization of Resonance States in Open Chaotic Quantum Maps*, Masterthesis, Technische Universität Dresden, Fachrichtung Physik, (2015). Cited on page 114.
- [210] M. Körber: *Phase-Space Localization of Chaotic Resonance States due to Partial Transport Barriers*, Ph.D. thesis, Technische Universität Dresden, Fachrichtung Physik, (2016). Cited on page 132.
- [211] J. Lötfering: *Klassische Vorhersage von Resonanzmoden in optischen Mikrokavitäten*, Bachelorarbeit, Technische Universität Dresden, Fakultät Physik, (2019). Cited on page 144.
- [212] N. L. Balazs and A. Voros: *The Quantized Baker's Transformation*, Europhys. Lett. **4** (1987), 1089–1094. Cited on page 149.
- [213] J. P. Keating, S. Nonnenmacher, M. Novaes, and M. Sieber: *On the resonance eigenstates of an open quantum baker map*, Nonlinearity **21** (2008), 2591–2624. Cited on page 166.
- [214] C. Grebogi, E. Ott, and J. A. Yorke: *Unstable periodic orbits and the dimensions of multifractal chaotic attractors*, Phys. Rev. A **37** (1988), 1711–1724. Cited on page 166.





# Acknowledgements

First of all I would like to thank Roland Ketzmerick for managing all the chaos, for countless discussions, inspirational input, for his neverending patience and the ongoing support. I am thankful for all the fruitful ideas and advice from Arnd Bäcker and also for all the technical necessities for making beautiful figures. I would like to thank Eduardo Altmann for the great opportunity to collaborate, for all the inputs and improvements, for the great stay Sydney, and for reviewing this thesis.

This work would not have been started without Martin Körber who supported me in the beginning and undoubtedly always raised my motivation to tackle this problem. It would not have been completed, if there had not been Markus Firmbach, Felix Fritzs, Alexander Schnell, Jonas Stöber, and Franziska Onken proofreading and improving the manuscript. I am deeply indebted to all of you!

I am thankful for the opportunity to work in the Computational Physics group which would not be running without Gundula Schädlich. In particular I enjoyed all the discussions with Normann Mertig, Martin Richter, Clemens Löbner, Julius Kullig, Tom Schilling, and all the active group members. It also was a great pleasure and experience to supervise the Bachelor thesis and work together with Tobias Becker, Jakob Lötfering, and Felix Kunzmann. During all the coffee breaks I always found an open ear with Alexander Schnell, Felix Fritzs, and Markus Firmbach, not only about scientific questions but also personally. I am very thankful for all of your patience and help.

I gratefully acknowledge financial support from the TU Dresden Graduate Academy, the IMPRS-MPSSE and from the German Research Foundation.

Finally, I would like to thank all of my friends and my whole family for believing in me and supporting me emotionally in all these years.

# Erklärung

Hiermit versichere ich, dass ich die vorliegende Arbeit ohne unzulässige Hilfe Dritter und ohne Benutzung anderer als der angegebenen Quellen angefertigt habe; die aus fremden Quellen direkt oder indirekt übernommenen Gedanken sind als solche kenntlich gemacht. Die Arbeit wurde bisher weder im Inland noch im Ausland in gleicher oder ähnlicher Form einer anderen Prüfungsbehörde vorgelegt.

Die vorliegende Dissertation wurde unter der Betreuung von Prof. Dr. Roland Ketzmerick am Institut für Theoretische Physik der Technischen Universität Dresden angefertigt. Es haben keine früheren erfolglosen Promotionsverfahren stattgefunden. Ich erkenne die Promotionsordnung des Bereiches Mathematik und Naturwissenschaften an der Technischen Universität Dresden vom 23. Februar 2011 mitsamt der Änderungen vom 15. Juni 2011, vom 18. Juni 2014, sowie vom 23. Mai 2018 an.

Konstantin Clauß  
Dresden, 28. März 2020